Finite Element Analysis of Short-Term and Long-Term Building Response to Tunnelling



Wing Nam Yiu

Balliol College

University of Oxford

A thesis submitted for the degree of

Doctor of Philosophy

Trinity 2018

Finite Element Analysis of Short-Term and Long-Term Building Response to Tunnelling

Wing Nam Yiu
Balliol College, University of Oxford

A thesis submitted for the degree of Doctor of Philosophy
Trinity 2018

Abstract

Tunnelling in urban areas causes short-term and long-term ground movements under existing buildings. Finite element analysis provides a useful option for assessing the likely extent of damage induced in these buildings. Although finite element analysis is suggested to be used in the later phases of the building damage assessment procedures employed in practice, only the effect of short-term ground movements is typically considered and there are no detailed guidelines on the specification and complexity of the modelling. This thesis addresses the tunnel-soil-building interaction problem and the effect of long-term consolidation, as well as demonstrating the application of 3D finite element analysis with appropriate simplifications for practical assessment purposes.

Finite element models are developed to quantify the effect of shallow tunnelling on an example masonry building founded on strip footings, considering both single- and twin-tunnel scenarios in a typical London soil profile. Total stress and effective stress analyses are adopted with specific modelling procedures to focus on the short-term and long-term response respectively. The analyses use a non-linear model for the masonry, and allow slippage and gapping at the soil-footing interface. Two advanced constitutive models for the soil (the extended Mohr-Coulomb model and the modified two-surface kinematic hardening model) are implemented with customized stress update schemes.

The finite element results present the interaction between the soil and the building by comparing with the greenfield ground response. The horizontal coupling between the foundation and the ground is shown to be relatively weak. The dominant deformation mode of the building varies with the tunnel configuration (i.e. single or twin tunnels) and the tunnel eccentricity. Strain localization is found around the explicitly modelled window and door openings. The long-term consolidation is sensitive to the permeability of the tunnel lining. The building response to long-term ground movements is further affected by the tunnel-tunnel interaction in the case of twin-tunnel configuration.

Performing 3D analysis of a single facade and foundation provides useful damage predictions, without the need to model a complete building. The proposed result processing methods such as characteristic strain and damage bar chart are practical tools for assessment. The study highlights some limitations of the elastic beam assessment method, which is often adopted in the early phase of the damage assessment process.

Acknowledgements

First and foremost, I would like to thank my supervisors, Prof. Harvey Burd and Prof. Chris Martin, for their guidance and supervision throughout the course of this DPhil. In particular, I would like to thank Harvey for his valuable insights, shared knowledge and boundless patience. I am also really grateful to Chris for his useful advices on learning focuses, and his objective and crucial feedback on written work. I am very appreciative of being able to work with them during my time at Oxford. I am extremely thankful to my examiners, Prof. Lidija Zdravković and Prof. Manolis Chatzis, for reviewing my thesis and conducting an intellectually stimulating viva voce.

I would like to express my gratitude to the Clarendon Fund and Balliol College for funding my research and living in Oxford. I would also like to acknowledge the University of Oxford Advanced Research Computing for providing computational resources for conducting some of the simulations included in the thesis. My appreciation goes to Alison May for her administrative assistance.

I am grateful to have met many amazing academic peers in the Civil Engineering Research Group, with whom I have had diversified and enlightening conversations. I would like to especially thank Christelle Abadie, Maria Garcia Espinosa, Yiling He, Aidan Wimshurst and Stephen Suryasentana for motivating each other and for sharing numerous enjoyable moments inside and outside the office.

I would also like to thank my friends whom I have met in Oxford outside the Department of Engineering Science. I am delighted to be part of the Oxford University Pistol Club. I would like to thank all my fellow shooters for sharing joy during practice and for being cheerful during competitions. Thanks also go to my close friends from the Hong Kong community in Oxford and the Oxford University Hong Kong Scholars Association for having thought-provoking discussions and for saving me from homesickness. I would also like to thank my three-year neighbours in the Dellal Building for being caring and thoughtful. My Oxford journey would not be unique and complete without any of these great people.

Sincere thanks to my parents, Winnie Wai Mei Wu and Louis Kwok Chung Yiu, my aunt, Monica Wai Chun Woo, my sisters, Rebecca Wing Tung Yiu and Angela Wing Hang Yiu, and my brothers-in-law, Evan Yuk Chuen Liu and Victor Chun Yu Lee, for their inexhaustible love and support. Special thanks to my best friend, Bernadette Cheng, and my boyfriend, Kai Chiu Wu, for providing unlimited encouragement.

— Wing Nam (Coco)

Contents

Abstract i
Nomenclature for stress and strain viii

1 Introduction **1**
1.1 Background 1
1.2 Objectives 4
1.3 Scope of research 4
1.4 Publications 5

2 Literature review **6**
2.1 Volume loss 6
2.2 Observed greenfield data and empirical estimation 7
2.2.1 Short-term ground movements 8
2.2.2 Long-term ground movements 9
2.2.3 Advantages and limitations of empirical estimation 11
2.3 Current building damage assessment procedure 11
2.3.1 Cause of building damage 11
2.3.2 Field observation and centrifuge testing 12
2.3.3 Building damage classification 14
2.3.4 Current phased assessment procedure 14
2.3.5 Advantages and limitations of current methods 15
2.4 Finite element analysis of short-term greenfield settlement 16
2.4.1 Two-dimensional (2D) tunnel modelling 19
2.4.2 Three-dimensional (3D) tunnel modelling 20
2.4.3 Soil constitutive models 21
2.4.3.1 Mechanical behaviour 22
2.4.3.2 Advanced constitutive models 23
2.4.4 Lateral stresses 25
2.5 Finite element analysis of long-term greenfield settlement 25
2.5.1 Modelling approach 25
2.5.2 Soil model 26
2.5.3 Soil permeability 27

2.5.4 Lining permeability . . . 27
2.5.5 Hydraulic condition . . . 28
2.6 Finite element analysis of tunnel-soil-building interaction . . . 28
2.6.1 Modelling approach of the building . . . 29
2.6.1.1 Two-dimensional modelling . . . 29
2.6.1.2 Three-dimensional modelling . . . 31
2.6.1.3 Masonry constitutive model . . . 32
2.6.1.4 Soil-building interface . . . 33
2.6.2 Effect of tunnel excavation on building . . . 34
2.6.3 Influence of building features . . . 34
2.7 Concluding remarks . . . 36

3 Finite element modelling procedure 38
3.1 Specification of the scenario . . . 39
3.1.1 Building . . . 39
3.1.2 Foundation . . . 40
3.1.3 Geological conditions . . . 40
3.1.4 Tunnel configuration . . . 41
3.2 Building modelling approach . . . 42
3.3 Foundation-facade interface . . . 43
3.4 Soil-foundation interface . . . 44
3.5 Total stress and effective stress analyses . . . 44
3.6 Constitutive models . . . 46
3.6.1 Masonry building . . . 46
3.6.2 Lintel . . . 47
3.6.3 Footing . . . 47
3.6.4 Terrace Gravel . . . 48
3.6.4.1 Identification of problem and selection of constitutive models . . . 48
3.6.4.2 Features of the extended Mohr-Coulomb model . . . 49
3.6.5 London Clay . . . 51
3.6.5.1 Identification of problem and selection of constitutive models . . . 51
3.6.5.2 Features of multiple von Mises yield surface kinematic hardening model . . . 52
3.6.5.3 Features of modified two-surface kinematic hardening model . . . 54
3.6.6 Lining . . . 56
3.6.7 Ghost membrane . . . 56

3.7 Element types and mesh boundary . . . 56
3.8 Calculation procedure: total stress analysis . . . 57
3.8.1 Main assumptions . . . 57
3.8.2 Tunnel modelling procedure . . . 57
3.8.3 Simulation steps . . . 59
3.9 Calculation procedure: effective stress analysis . . . 60
3.9.1 Main assumptions . . . 60
3.9.2 Tunnel modelling procedure . . . 62
3.9.3 Simulation steps . . . 64
3.10 Result processing . . . 66
3.10.1 Displacement and strain profile . . . 68
3.10.2 Contact traction profile . . . 68
3.10.3 Tensile strain field . . . 68
3.10.4 Characteristic strain . . . 68
3.10.5 Damage bar chart . . . 69
3.10.6 Facade opening distortion . . . 70

4 Extended Mohr-Coulomb (EMC) model for Terrace Gravel 71
4.1 Overview of the model . . . 71
4.2 Implementation . . . 73
4.2.1 Consistency in presentation . . . 73
4.2.2 Overview of the integration scheme . . . 73
4.2.3 Challenges and modifications . . . 77
4.2.3.1 Yield surface intersection . . . 77
4.2.3.2 Elastoplastic unloading . . . 78
4.2.3.3 Numerical integration at non-differentiable singularities 79
4.2.3.4 Stress and hardening parameter correction . . . 80
4.2.3.5 Numerical integration at the minimum size of substep 81
4.2.3.6 Constitutive matrix . . . 81
4.2.4 Additional considerations . . . 82
4.2.4.1 Error check for each substep . . . 82
4.2.4.2 Initialisation of the size of the yield surface . . . 82
4.2.4.3 Typographical errors in Doherty & Muir Wood (2013) 82
4.3 Validation . . . 84
4.3.1 Reduction to elastic, perfectly plastic Mohr-Coulomb . . . 84
4.3.2 Triaxial test simulations . . . 86
4.3.3 Footing test simulations . . . 89
4.4 Calibration to the Terrace Gravel . . . 93
4.5 Limitations . . . 95

Appendix . . . 97
A. ε_J corresponding to the beginning of hardening . . . 97

5 Implementation of the M2-SKH model for London Clay 99
5.0.1 Nomenclature of substepping in implementation . . . 100
5.1 Overview of the model . . . 100
5.1.1 MCC model . . . 100
5.1.2 Elastic behaviour . . . 100
5.1.3 Yield, bounding and plastic potential surfaces . . . 101
5.1.4 Measure of proximity of the YS to the BS . . . 102
5.2 Implementation . . . 105
5.2.1 Model parameters . . . 106
5.2.2 State variables . . . 107
5.2.3 Stress update algorithm . . . 107
5.2.3.1 Elastic stress update routine . . . 109
5.2.3.2 Yield surface stress update routine . . . 111
5.2.3.3 Bounding surface stress update routine . . . 116
5.2.3.4 Constitutive matrix . . . 118
5.3 Calibration . . . 118
5.3.1 Normal consolidation and swelling lines . . . 120
5.3.2 Shape of yield and bounding surfaces in deviatoric plane . . . 122
5.3.3 Shape of plastic potential surface in deviatoric plane . . . 125
5.3.4 Hardening parameter . . . 126
5.3.5 Correlations between the hardening parameter, K_0 profile and overburden stress . . . 127
5.3.6 Summary of the adopted parameters . . . 129
5.4 Validation with greenfield response induced by tunnelling modelled in plane strain . . . 131
5.4.1 Short-term ground response . . . 134
5.4.2 Medium-term ground response . . . 135
5.4.3 Long-term ground response . . . 137

6 Total stress analysis of building response to tunnelling 138
6.1 Calculations and example meshes . . . 138
6.2 Short-term greenfield analysis . . . 140
6.2.1 Displacement and horizontal strain profiles . . . 143
6.2.2 Effect of constitutive model for the Terrace Gravel . . . 146
6.3 Short-term isolated facade analysis . . . 151
6.3.1 Soil-building interaction . . . 151
6.3.2 Importance of facade openings . . . 156

6.3.3 Effect of constitutive model for the Terrace Gravel 161
6.3.4 Effect of tunnel eccentricity 162
6.3.5 Soil-foundation interaction sensitivity study 163
6.3.5.1 Footing properties 165
6.3.5.2 Frictional soil-foundation interface 167
6.3.6 Evaluation of elastic beam assessment (EBA) method 175
6.3.6.1 Conventional EBA_A approach 175
6.3.6.2 Modified EBA_B approach 177
6.3.6.3 Comparison with finite element analysis results 178
6.4 Short-term complete building analysis 180
6.4.1 Orthogonal tunnel 180
6.4.2 Skew tunnel 184
6.5 Concluding remarks 187

7 Effective stress analysis of building response to tunnelling 189
7.1 List of calculations and meshes 190
7.2 Greenfield analysis 194
7.2.1 Base case 194
7.2.2 Effect of tunnel configuration 197
7.2.3 Effect of lining permeability 199
7.2.4 Effect of model calibration 202
7.3 Isolated facade analysis 204
7.3.1 Base case 207
7.3.2 Effect of tunnel configuration 209
7.3.3 Effect of lining permeability 212
7.3.4 Effect of model calibration 216
7.4 Concluding remarks 222

8 Conclusions 223
8.1 Contributions 223
8.1.1 Implementation of advanced constitutive models 223
8.1.2 Understanding of tunnel-soil-building interaction 224
8.1.3 Understanding of time-dependent effects on ground and building response 226
8.1.4 Finite element analysis for building damage assessment in practice 227
8.1.5 Evaluation of the current building damage assessment procedure 229
8.2 Recommendations for future work 229

References 230

Nomenclature for stress and strain

(tension positive)

In triaxial stress space, following Muir Wood (2004),

σ_{a}	axial stress	
σ_{r}	radial stress	
p	mean stress	$(\sigma_{\mathrm{a}} + 2\sigma_{\mathrm{r}})/3$
q	deviator stress	$\sigma_{\mathrm{a}} - \sigma_{\mathrm{r}}$
ε_{a}	axial strain	
ε_{r}	radial strain	
$\delta\varepsilon_p$	volumetric strain increment	$\delta\varepsilon_{\mathrm{a}} + 2\delta\varepsilon_{\mathrm{r}}$
$\delta\varepsilon_q$	distortional strain increment	$\frac{2}{3}(\delta\varepsilon_{\mathrm{a}} - \delta\varepsilon_{\mathrm{r}})$

In 3D general stress space,

$\hat{\boldsymbol{\sigma}}$	stress (tensor form)	$\begin{bmatrix} \sigma_{xx} & \tau_{xy} & \tau_{xz} \\ \tau_{yx} & \sigma_{yy} & \tau_{yz} \\ \tau_{zx} & \tau_{zy} & \sigma_{zz} \end{bmatrix}$
$\boldsymbol{\sigma}$	stress (Voigt form)	$\{\sigma_{xx}, \sigma_{yy}, \sigma_{zz}, \tau_{xy}, \tau_{yz}, \tau_{zx}\}^{\mathrm{T}}$
$\hat{\boldsymbol{s}}$	deviatoric stress (tensor form)	$\begin{bmatrix} s_{xx} & \tau_{xy} & \tau_{xz} \\ \tau_{yx} & s_{yy} & \tau_{yz} \\ \tau_{zx} & \tau_{zy} & s_{zz} \end{bmatrix} = \begin{bmatrix} \sigma_{xx} - p & \tau_{xy} & \tau_{xz} \\ \tau_{yx} & \sigma_{yy} - p & \tau_{yz} \\ \tau_{zx} & \tau_{zy} & \sigma_{zz} - p \end{bmatrix}$
$\boldsymbol{s}$	deviatoric stress (Voigt form)	$\{s_{xx}, s_{yy}, s_{zz}, \tau_{xy}, \tau_{yz}, \tau_{zx}\}^{\mathrm{T}}$
p	mean stress	$(\sigma_{xx} + \sigma_{yy} + \sigma_{zz})/3$
J	deviatoric stress invariant	$\sqrt{\frac{1}{6}[(\sigma_{xx} - \sigma_{yy})^2 + (\sigma_{yy} - \sigma_{zz})^2 + (\sigma_{zz} - \sigma_{xx})^2] + \tau_{xy}^2 + \tau_{yz}^2 + \tau_{zx}^2}$ $= \frac{1}{2}(\hat{\boldsymbol{s}} : \hat{\boldsymbol{s}})^{1/2}$
J_3		$s_{xx}s_{yy}s_{zz} + 2\tau_{xy}\tau_{yz}\tau_{zx} - s_{xx}\tau_{yz}^2 - s_{yy}\tau_{zx}^2 - s_{zz}\tau_{xy}^2$
θ	Lode angle	$\frac{1}{3}\sin^{-1}(\frac{-3\sqrt{3}J_3}{2J^3})$ $= -\frac{1}{3}\sin^{-1}\left[\frac{3\sqrt{3}}{2}\frac{\det(\hat{\boldsymbol{s}})}{\{[\frac{1}{2}(\hat{\boldsymbol{s}}:\hat{\boldsymbol{s}})]^{1/2}\}^3}\right]$
$\hat{\boldsymbol{\varepsilon}}$	strain (tensor form)	$\begin{bmatrix} \varepsilon_{xx} & \varepsilon_{xy} & \varepsilon_{xz} \\ \varepsilon_{yx} & \varepsilon_{yy} & \varepsilon_{yz} \\ \varepsilon_{zx} & \varepsilon_{zy} & \varepsilon_{zz} \end{bmatrix}$
$\boldsymbol{\varepsilon}$	strain (Voigt form)	$\{\varepsilon_{xx}, \varepsilon_{yy}, \varepsilon_{zz}, \gamma_{xy}, \gamma_{yz}, \gamma_{zx}\}^{\mathrm{T}}$ $= \{\varepsilon_{xx}, \varepsilon_{yy}, \varepsilon_{zz}, 2\varepsilon_{xy}, 2\varepsilon_{yz}, 2\varepsilon_{zx}\}^{\mathrm{T}}$
$\delta\varepsilon_p$	volumetric strain increment	$\delta\varepsilon_{xx} + \delta\varepsilon_{yy} + \delta\varepsilon_{zz}$
$\delta\varepsilon_J$	distortional strain increment	$\sqrt{\frac{2}{3}[(\delta\varepsilon_{xx} - \delta\varepsilon_{yy})^2 + (\delta\varepsilon_{yy} - \delta\varepsilon_{zz})^2 + (\delta\varepsilon_{zz} - \delta\varepsilon_{xx})^2] + \delta\gamma_{xy}^2 + \delta\gamma_{yz}^2 + \delta\gamma_{zx}^2}$

Chapter 1

Introduction

1.1 Background

The construction of shallow tunnels in soil (e.g. for a new underground transportation system) inevitably generates local ground deformations. When low-permeability soil is involved, tunnel excavation causes further ground movements beyond the construction period. In an urban environment, these deformations may cause damage to any nearby buildings on the ground surface. Damage may be particularly significant for load-bearing masonry structures, which typically behave in a brittle manner, and even minor damage is undesirable in high heritage-value buildings. During the planning of new urban tunnelling projects, detailed calculation procedures are therefore required to identify buildings at risk and to make reliable assessments of the likely extent of any tunnel-induced structural damage for timely implementation of mitigation measures.

Current methods for assessing masonry buildings at risk of tunnel-induced settlement damage are typically based on a phased sequence of calculations of increasing detail and sophistication and decreasing conservatism (e.g. Mair et al. 1996, Burland et al. 2001, Harris & Franzius 2006, Crossrail Ltd 2008, Burland et al. 2012). Greenfield assessments, which neglect the presence of surface and subsurface structures, are first applied to identify influence zones of potentially high risk along the tunnel alignment. Initial building assessments are then conducted for buildings located inside these influence zones using a relatively simple analytical approach in which the building is

modelled as an elastic beam that deforms according to the greenfield tunnel-induced ground movements (Burland & Wroth 1975, Boscardin & Cording 1989). This procedure is referred to the 'elastic beam assessment' method in the thesis. If this approach (which is generally assumed to be conservative (e.g. Mair et al. 1996)) indicates a risk of significant damage, then further, more refined, calculations are conducted using numerical analysis to obtain more detailed damage assessments.

Finite element analysis provides a means of conducting refined assessments. However, although there are examples in the literature comparing finite element modelling results with field data for buildings that have been affected by tunnelling (e.g. Amorosi et al. 2014, Fargnoli et al. 2015, Bilotta et al. 2017), there are no obvious signs that this type of computational modelling is being undertaken routinely in civil engineering practice for project-based assessment purposes. It appears that the various practical difficulties that need to be addressed, notably uncertainties as to how the soil and building material models should be specified and calibrated, combined with an apparent cautious conservatism among practitioners and clients, limit the application and development of finite element-based procedures for tunnel-induced damage assessments. As a consequence, the use of finite element analysis on such projects does not appear to be standardized yet, and no thorough guideline for the use of computational modelling has been set out for project-based assessment purposes in civil engineering practice. The assessment results are likely to be highly dependent on the individual's choice of modelling approaches, material constitutive models, initial stress and hydraulic states, boundary conditions and so on.

Given the efficiency of the modern computation and considering that a large number of surface buildings may be involved in project-based assessments, a simple, expeditious yet rigorous finite element analysis procedure can be exploited as an intermediate prediction between the relatively simple elastic beam assessment method and highly detailed 3D numerical models. Robust modelling procedures are required to incorporate the key features of the problem to obtain results that are sufficiently reliable. The simplification of the problem and the development of appropriate finite element

modelling procedures, while avoiding undue complexity for practical building damage risk assessment purposes, remain challenging subjects for research.

A separate issue to be considered is that current building damage assessment procedures focus on the immediate displacements and strains impact induced by tunnelling. Although additional settlements and increases in slope are observed after construction in some cases (Nyren et al. 2001, Hover et al. 2015), assessments of the transient and long-term effects of tunnel excavation on the building are not mandatory in current design procedures.

Tunnel-induced ground movements in low-permeability soil include both short-term settlement and long-term consolidation settlement. The short-term settlement is often caused by over-excavation and shear deformation of soil induced by the excavation process. The long-term consolidation settlement results from the equilibration of effective stresses and excess pore pressures around the excavated tunnel. The redistribution of stresses depends on the drainage properties of the soil and the tunnel lining. Finite element analysis carried out by Wongsaroj et al. (2013) shows that the long-term settlement of low-permeability soil following tunnel excavation can be substantial. Mair (2008) points out that despite the larger magnitude of settlement, the subsequent differential settlement and hence the impact on buildings caused by long-term settlement is likely to be less influential as the settlement trough becomes wider. However, Bowers et al. (1996) computed an increase in deflection ratio in the structure under hogging in the long term. Harris (2002) also considers that long-term settlement might increase the curvature within the settlement trough and suggests that making reliable predictions of consolidation settlement is difficult. Peck (1969) remarks on the possible long-term damage caused by soil remoulded in construction. To avoid disputes among stakeholders and to provide appropriate mitigation measures regarding any possible long-term damage to buildings, it is therefore necessary to improve understanding of the time-dependent settlement process and the associated building response.

1.2 Objectives

The need to develop reliable and efficient finite element modelling procedures in the context of building damage assessments, and the requirement for improved understanding of tunnel-soil-building interaction over time, have motivated the current research. The thesis aims to promote the application and development of finite element-based procedures with an appropriate balance of complexity and efficiency for practical tunnelling-induced building damage assessments. The main objectives of the current research are:

i. To enhance the scientific knowledge about tunnel-soil-building interaction mechanisms;
ii. To improve the understanding of long-term tunnel-induced ground movements and the associated effects on existing buildings;
iii. To identify essential modelling parameters for simulating tunnel-soil-building interaction for the purpose of building damage assessments; and
iv. To evaluate the conventional elastic beam assessment method used in the current building damage assessment procedure.

1.3 Scope of research

Finite element analysis is exploited to study short-term and long-term building response to tunnelling. This research is concerned with shallow tunnel construction (single tunnel or twin tunnels) in geological conditions similar to central London, underneath a pre-existing masonry building founded on continuous strip footing foundations. The existence of any pre-existing underground infrastructure is not considered. The area of interest is usually at or above the level of building foundation, in the transverse direction of the tunnel. As the profile of surface settlement is affected by the tunnel volume loss but not the actual tunnelling method, the simulation of tunnelling in the current model is adopted to provide representation of the tunnel volume loss rather than the detailed tunnel excavation process.

The finite element analysis software Abaqus is used. Advanced constitutive models

(implemented as user subroutines) are employed for the soil. A non-linear model with a tension cut-off is adopted for the masonry. The building foundation is explicitly modelled to investigate the soil-foundation interface behaviour and to enable potential occurrence of gapping. Both total stress analysis and effective stress analysis are considered. A range of modelling approaches for the building and the tunnel excavation are explored. Several data processing procedures are developed to interpret the data computed from the finite element analysis for practical damage assessment purposes.

The thesis offers a systematic selection of essential components that should be considered in efficient finite element modelling by conducting detailed parametric studies. Due to the unavailability of high-quality data, no case study is included. Moreover, complicating factors in real conditions such as pre-existing cracks in masonry and the use of compensation grouting are beyond the scope of the thesis.

1.4 Publications

Part of the research work regarding the short-term building response to tunnelling has been published during the course of the DPhil. The publication is summarized below.

Yiu et al. (2017*b*) presents the results in Sections 6.3.2 and 6.3.5.1 which focus on the damage in a plain facade and a facade with openings via isolated facade analyses, and study the sensitivity of the footing properties for building damage assessments.

Yiu et al. (2017*a*) covers the study of the various damage that are active in the particular tunnel-soil-building interaction scenario via numerical results, explores the extent to which isolated facade models provide an acceptable expedient for practical damage assessment purposes, and provides a basis for understanding the nature and impact of some of the simplifications and assumptions inherent in the elastic beam assessment method. The paper collects and condenses the findings from Chapter 6.

Yiu et al. (2018) focuses particularly on modelling the soil-foundation contact behaviour. The results, which are included in Section 6.3.5.2 of the thesis, highlight the sensitivity of the traction redistribution and relative horizontal movement between the footing and the surrounding soil to the assumed friction coefficient value.

Chapter 2

Literature review

Previous research can largely be classified into three sub-topics, which are (i) greenfield ground response in the short term after tunnelling, (ii) greenfield ground response in the long term after tunnelling, and (iii) immediate building damage induced by tunnelling. Substantial findings have been obtained by means of field measurements, laboratory experiments and numerical analyses. This chapter starts with observations from short-term and long-term greenfield monitoring data and their empirical estimation. It is followed by the performance of pre-existing masonry buildings above the tunnel alignment and the current building damage assessment process. Attention is then drawn to the modelling approaches developed for finite element analysis of tunnelling in greenfield conditions in the short term and the long term, and tunnelling underneath a masonry building. The key results have established the basis of the current work and facilitate the choice of finite element analysis procedures adopted in the later chapters.

2.1 Volume loss

The excavated volume of soil in tunnel construction is typically larger than the final tunnel volume owing to mechanical effects such as surrounding soil moving towards the tunnel void and for practical reasons such as allowance for lining installation. This extra volume of excavated soil is termed 'tunnel volume loss', $V_{\mathrm{L}}^{\mathrm{T}}$, and it is usually expressed

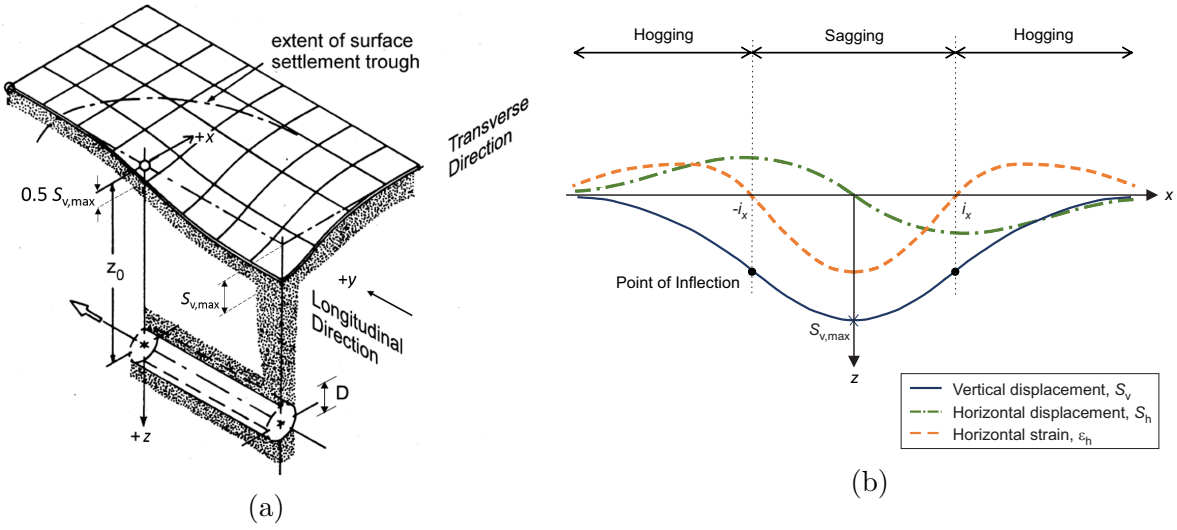


Figure 2.1: Typical greenfield settlement: (a) above advancing tunnel heading (after Attewell et al. 1986); (b) idealization of transverse surface displacement and strains shortly after tunnelling (after O'Reilly & New 1982)

as a percentage of the designed tunnel volume and used as a measurement parameter of soil disturbance caused by the tunnel construction. The tunnelling-induced volume loss and the change in soil stress state cause ground movements. The typical surface settlement trough above and in front of an advancing single tunnel heading in the greenfield condition is illustrated in Fig. 2.1(a). The 'settlement volume loss', V_L^S, is computed from the volume of the settlement trough (as a percentage of the designed tunnel volume). Under undrained conditions, the settlement volume loss is equal to the tunnel volume loss.

2.2 Observed greenfield data and empirical estimation

Two phases of ground movements induced by tunnelling are recognised (Rankin 1988) — an immediate phase occurring with tunnel construction and a time-dependent post-construction phase.

2.2.1 Short-term ground movements

Initial settlement related to loss of ground is caused mainly by stress relaxation and over-excavation. The short-term ground surface response to tunnelling in greenfield conditions for several major projects in London were monitored, and documented in previous literature: the Heathrow Express Trial Tunnel (Bowers et al. 1996), the Jubilee Line Extension (JLE) project at St James's Park (Nyren et al. 2001), the Channel Tunnel Rail Link (CTRL) project in Essex (Standing & Selemetas 2013), and the Crossrail project at Hyde Park (Wan et al. 2017).

Transverse direction. The short-term ground surface vertical displacement profile, S_{v}, in the transverse direction, induced by a single tunnel, is commonly described by a Gaussian distribution curve, first proposed by Peck (1969):

$$S_{\mathrm{v}}(x) = S_{\mathrm{v,max}} \exp(-\frac{x^2}{2i^2}) \tag{2.1}$$

where x is the horizontal distance from tunnel centre, $S_{\mathrm{v,max}}$ is the maximum settlement above the tunnel axis, and i is the distance from the tunnel axis to the point of inflection, as illustrated in Fig. 2.1(b). O'Reilly & New (1982) suggested a linear relationship between i and the depth of tunnel, z_{o}:

$$i = K z_{\mathrm{o}} \tag{2.2}$$

where K is the trough width parameter, with recommended values of 0.4 to 0.7 for stiff to soft clay and 0.2 to 0.3 for granular materials based on case histories.

The approximation of the transverse short-term surface vertical displacement profile using a Gaussian curve is achieved satisfactorily by Withers (2001*c*), Standing & Selemetas (2013) and Wan et al. (2017) while processing field measurements.

The horizontal displacement, S_{h}, can be estimated by assuming that the resultant vectors of ground movement are directed towards the tunnel axis (O'Reilly & New

1982), and expressed as

$$S_{\mathrm{h}} = \frac{S_{\mathrm{v}} x}{z_{\mathrm{o}}} \tag{2.3}$$

The field measurements of surface horizontal displacement recorded in Wan et al. (2017) support this assumption (termed 'point-sink' assumption); however, the field data in Standing & Selemetas (2013) indicate no unique focal point for the resultant vectors of the measured displacements.

The field study in Standing & Selemetas (2013) further indicates that operational variables such as the face and tail-skin grouting pressures of an earth pressure balanced tunnel boring machine (TBM) strongly affect the ground response, compared to an open-face TBM. These variables, which affect the ground conditions, might lead to a greenfield ground response deviating from the Gaussian model.

Longitudinal direction. Empirically, the shape of the longitudinal settlement profile above the tunnel centreline follows a cumulative normal distribution function as the tunnel head advances (Rankin 1988). The ground surface settlement directly above the tunnel face corresponds to the point of inflection in the longitudinal profile and its magnitude is assumed as $0.5S_{\mathrm{v,max}}$ (Fig. 2.1(a)).

2.2.2 Long-term ground movements

Additional long-term settlements occur due to consolidation caused by excess pore water pressure dissipation and creep. Clough et al. (1983) recorded a local rapid rise in excess pore pressure ahead of the tunnelling. Ward & Pender (1981) and Wongsaroj et al. (2007) report that the pore water pressure in the soil just above the crown rises when the tunnelling shield approaches, followed by a drop as the shield passes, and the pore pressure increases close to its initial level thereafter. The trend of the change in the pore water pressure in the soil at the tunnel springline level depends on the proximity to the tunnel.

The three-year measurements of ground movement at the Heathrow Express Trial Tunnel (Bowers et al. 1996) and the five-year measurement data at St James's Park

induced by the JLE construction (Nyren et al. 2001) indicate significant long-term settlements with extended transverse trough. Consolidation is still taking place at St James's Park 15 years after the JLE construction, as shown in Avgerinos et al. (2016). The vertical displacement after a year at the CTRL site is not substantial, attributed to the grouted lining (Standing & Selemetas 2013).

Evidenced by the wet tunnel wall in the JLE project recorded in Harris (2002), a new drainage path is introduced by the excavated tunnel, with the inner face of the lining assumed at atmospheric pressure, driving the ground consolidation process. Ward & Pender (1981) and Soga et al. (2017) conclude from other case studies that all tunnels eventually act as drains, either fully or partially, despite grouting, causing further long-term settlement and squatting of the tunnel. The monitoring data in Nyren (1998) show that the fluid inflow from the soil towards a tunnel is greater at the bottom of the tunnel than at the crown.

In the case of twin tunnels, the study of their long-term behaviour in London Clay conducted by Laver (2010) suggests that the second tunnel not only introduces another drainage boundary to the system, but also interacts with the first tunnel by restricting flow supply and compressing the soil column in between.

On the basis of field monitoring data, the factors affecting long-term consolidation induced by tunnelling include the following (Mair & Taylor 1999, Wongsaroj et al. 2007, 2013, Soga et al. 2017):

i. the magnitude and distribution of excess pore pressure developed by construction;
ii. pore water pressure distribution in the system throughout the lifetime;
iii. geological ground profile and drainage boundary conditions;
iv. soil permeability and compressibility; and
v. lining permeability.

Empirical estimation. Unlike the short-term settlements, the normal Gaussian curve does not match the long-term surface settlement profile satisfactorily, especially near the edges of the trough (Bowers et al. 1996). Also, the consolidation settlement does not follow a linear relationship against log time, but fitting a line at the maxi-

mum rate of movement after construction on a log time plot gives an upper bound of possible further movements (Harris 2002). The modified Gaussian equation suggested by Vorster et al. (2005) allows better fitting of long-term settlement data from field measurements (Wongsaroj et al. 2013).

2.2.3 Advantages and limitations of empirical estimation

Although empirical methods are simple to use and the Gaussian expression for short-term greenfield settlement can be applied with some confidence, the assumptions of the shape and width of the settlement profile limit their application to single-tunnel cases at greenfield sites. The accuracy of superposing Gaussian profiles in the case of multiple tunnels remains uncertain. The use of Gaussian curves for estimating long-term settlements remains an area of doubt.

2.3 Current building damage assessment procedure

Shallow tunnelling in urban areas raises concern about its impact on existing surface structures. Building damage assessment and classification have been used to evaluate the risks to buildings which may reach serviceability or even ultimate limit state.

2.3.1 Cause of building damage

The critical cause of building damage is not the overall subsidence but the differential settlement which induces strain from bending and shearing deformation of the building. As masonry has a low tensile strength (and high compressive strength), tensile cracks tend to form along the minor principal strain direction (taking tension positive). Tensile strains can be induced by bending and shearing deformation, which may occur simultaneously (Burland & Wroth 1975). The corners of openings for windows and doors in building facades in turn intensify stresses, similar to the apexes of sharp notches (see e.g. Hills & Dini 2011).

2.3.2 Field observation and centrifuge testing

Field observation. Frischmann et al. (1994) present crack surveys of the Mansion House during construction of the Waterloo and City Line link tunnel. There was no intervention measure such as compensation grouting applied for the building. The location of the building (directly above the centreline of the tunnel) and the extremely large windows are regarded to be liable for the increase in cracking.

Multiple brick-masonry buildings were monitored during and after the JLE construction. Despite the application of pre-treatment and corrective grouting, differential settlements and deteriorated serviceability were recorded in some cases.

The movements of the sub-basement of the brick-masonry Treasury were compared with the greenfield data from St James's Park in Viggiani & Standing (2001). The short-term vertical displacements of the building were shallower and flatter than the greenfield site. The horizontal strains measured on the building (of the order of 70 $\mu\varepsilon$ (microstrain)) were significantly smaller than the greenfield data (of the order of 1200 $\mu\varepsilon$ in compression and 400 $\mu\varepsilon$ in tension). The maximum vertical displacement of the building tripled four years after the end of construction work, with increased slopes.

Measurements on the masonry buildings on Moodkee Street, which are made of load-bearing brick founded on shallow strip foundations, indicated horizontal strains of less than 100 $\mu\varepsilon$ (Withers 2001*b*). These strains are also lower than had been estimated from empirical assessments based on greenfield displacements. The effect of sequential tunnelling and the higher flexibility of buildings deforming in sagging than those in hogging are also observed in the measurements in Withers (2001*b*).

Substantial immediate settlements and noticeable long-term settlements were measured in the masonry London Bridge Post Office; however, the slope of total settlements in the long term remains approximately the same as that of the immediate settlements (Petrova et al. 2001). New cracks were recorded in the building after tunnelling.

New cracks and widened existing cracks were also found in the load-bearing brickwork and masonry cladding of the Royal Institution of Chartered Surveyors and the

Institution of Civil Engineers on Great George Street after tunnelling (Gupta et al. 2001).

Withers (2001*a*) surveyed the load-bearing masonry walls in Keetons Estate and recorded doors and windows sticking to cracked windows, worsening of existing cracks and initiation of new cracks. Other observations such as insignificant horizontal strains of the facades ($< 150\ \mu\varepsilon$) and long-term movements with approximately the same slopes as the short-term movements are consistent with other buildings.

Centrifuge testing. Centrifuge modelling, which can reproduce in situ stress conditions, is often used to study the tunnel-soil-structure interaction problem experimentally (e.g. Farrell et al. 2014, Ritter et al. 2017*a*).

Farrell et al. (2014) studied the response of two types of buildings, represented by aluminium beams (elastic) and micro concrete and masonry with cement-based mortar beams (inelastic), to tunnelling in sand using a geotechnical centrifuge. A gap between the beam and the soil was observed due to the difference in vertical settlements. Building load redistribution towards the building edges was recorded and the settlements of the building edges were greater than the greenfield values in those regions. The horizontal strains in the building models were measured to be negligible for various tunnel eccentricities.

Ritter et al. (2017*a*) conducted centrifuge tests on a single shallow tunnel excavation in dense sand underneath a 3D-printed building of typical masonry properties with facade openings, internal walls and a rough soil-structure interface. The experimental data show that, compared to greenfield data, the ground surface vertical settlements are smaller when the building is situated symmetrically above the tunnel, and greater when the structure is located at one side of the tunnel. The soil horizontal displacements are shown to be restrained by the presence of the building, but the extent of the modification is less sensitive to the tunnel eccentricity. The results also indicate a decrease in trough width parameter when the building is away from the tunnel centreline or when the tunnel volume loss increases. The effect of building characteristics was studied by testing various 3D building models. An increase in the area of openings of

Table 2.1: Building damage classification (after Burland et al. (1977) and Boscardin & Cording (1989))

Category of damage	Normal degree of severity	Ease of repair of visible damage	Typical crack width (mm)	Limiting tensile strain (ε_{lim}) ($\mu\varepsilon$)
0	Negligible	No need	< 0.1	$0 - 500$
1	Very slight	Normal decoration	$0.1 - 1$	$500 - 750$
2	Slight	Fill and repoint	$1 - 5$	$750 - 1500$
3	Moderate	Small replacement	$5 - 15$	$1500 - 3000$
4	Severe	Extensive replacement	$15 - 25$	> 3000
5	Very severe	Rebuilding	> 25	> 3000

the facade increases its flexibility and reduces the modification of soil movements from the greenfield profile. Measurements of the building indicate that buildings experiencing both sagging and hogging suffer from greater deflection than those under sagging or hogging only, evidenced by earlier cracking, as presented in Ritter et al. (2017*b*).

2.3.3 Building damage classification

Burland et al. (1977) proposed a system of damage categorization for brickwork or stone masonry based on the ease of repair of visible damage and typical crack widths, which could however be subjective. Boscardin & Cording (1989) improved this with a quantitative system by relating the damage categories to the concept of limiting tensile strain, ε_{lim}, based on case records, as summarized in Table 2.1.

2.3.4 Current phased assessment procedure

In the United Kingdom, the phased building damage assessment described by Burland (2001) is typically adopted during the design stage of major tunnelling projects such as Jubilee Line Extension and Crossrail (Burland 2001, Crossrail Ltd 2008). Buildings in the vicinity of tunnel construction are screened at each phase using assessment methods with increasing detail but reducing conservatism.

In Phase 1, greenfield settlements are computed to represent the uncoupled building subsidence along the tunnel alignment. Buildings that lie outside the contour of a certain settlement or slope are deemed to have negligible risk. These buildings are

excluded from further assessment. In Phase 2, a simple analytical approach based on beam theory, developed by Burland & Wroth (1975), is adopted to predict the maximum tensile strain in the building. The ground surface horizontal strains are included in the maximum tensile strain by direct superposition (Boscardin & Cording 1989). This method, where the building is modelled as a simple elastic beam conforming to the greenfield settlement profile, is referred to in this thesis as the 'elastic beam assessment' (EBA) method. The concept of relative stiffness was first considered by Potts & Addenbrooke (1997), in terms of the relative axial stiffness and bending stiffness between the structure and soil, to account for the reduction in deflection ratio and horizontal strain from the greenfield values due to the presence of the building. The relative stiffness method is commonly employed in a further phase known as Phase 2b. There are other variants of Phase 2b such as those described in Mair & Taylor (2001), Franzius et al. (2005*b*) and Harris & Franzius (2006). The maximum tensile strain computed from Phase 2 classifies the building risk level according to the damage categories in Table 2.1. Buildings predicted to have Damage Category 3 or above, and heritage or other high value buildings, are further assessed in Phase 3, where numerical analysis such as finite element analysis is employed. Details such as soil behaviour, tunnelling processes, structural features, 3D effects and tunnel-soil-building interaction can be considered at this stage.

2.3.5 Advantages and limitations of current methods

The conventional EBA method often leads to over-conservative solutions because the structural response and soil deformation are assumed to be uncoupled (Miliziano et al. 2002, Farrell et al. 2014). Although the relative stiffness method improves the empirical prediction, the resulting deformation is limited to be expressed as a modification of the greenfield settlements, which neglects the possibility of a fundamentally different mechanism of behaviour caused by the presence of the building. Over-conservative assessment could lead to unnecessary and costly mitigation measures (such as compensation grouting) on the basis of misleading damage estimates. Meanwhile, there is

no available standard or guideline for the use of numerical modelling (such as finite element analysis) for damage assessment purposes. Finite element assessment procedures rely on individual judgement for the input data, ranging from mesh detail to constitutive model choice and calibration, which are subject to a wide spectrum of possible complexity. The implementation of a full, complex 3D numerical model is often constrained for practical reasons by the available time and computational resources.

Furthermore, the prediction of building damage induced by long-term consolidation is not mandatory in the current assessment procedures. Although a substantial increase in long-term differential settlements has not yet been recorded in the field, deterioration in building serviceability has been observed despite the fact that grouting had already been applied before tunnel construction in some cases (e.g. Viggiani & Standing 2001, Petrova et al. 2001, Withers 2001*a*).

2.4 Finite element analysis of short-term greenfield settlement

Numerical analysis offers the advantages of high flexibility, high resolution and relatively low cost compared to field measurements and centrifuge model tests. Previous researchers have attempted to reproduce the commonly assumed Gaussian settlement profile in the transverse plane using finite element analysis, which is also of interest to this thesis. A transverse cross-section plane strain model is the most commonly used model for predicting short-term greenfield response. Recently, three-dimensional models have been employed to incorporate multiple 3D effects. Table 2.2 and Table 2.3 summarise some 2D and 3D examples from the literature. The predicted ground response has been found to be affected by several factors including the tunnel modelling approach, the material constitutive models and the initial conditions.

Finite element analysis can be used to model the response to different assumed values of volume loss (termed 'volume loss control approach') or, alternatively, to estimate volume loss from excavation details provided (termed 'indirect approach').

Table 2.2: Examples of 2D finite element modelling of tunnelling problems

Reference	Drainage condition	Analysis approach	Tunnel process modelling	Lining/ Grout/ Shield	Element type	Soil type	Soil model
Rowe et al. (1983)	coupled	direct	nodal force approach	Y/-/-	soil: 8-node quadrilateral	soft-firm soil & clay	elastoplastic (MC)
Addenbrooke & Potts (1996)	coupled	1st tunnel: direct; 2nd tunnel: indirect	load reduction method (2nd tunnel: use λ obtained from the 1st)	Y/-/-	soil: 8-node quadrilateral; lining: 3-node Mindlin beam	sand, Terrace Gravel & London Clay	sand: linear elastic; gravel & clay: non-linear elastic
Kovacevic et al. (1996)	coupled	indirect	λ-factor approach	Y/-/-	soil: 8-node quadrilateral with reduced integration; lining: 3-node Mindlin beam	made ground, Terrace Gravel, London Clay & bed clay	made ground: linear elastic; others: non-linear elastic & perfectly plastic (MC)
Addenbrooke et al. (1997)	coupled	direct	load reduction method	Y/-/-	soil & lining: quadrilateral	made ground, Terrace Gravel & London Clay	made ground: linear elastic; others: non-linear elastic & perfectly plastic (MC)
Liu et al. (2000)	undrained	indirect	load reduction method	-/-/-	6-node triangle	London Clay	multiple surface plasticity
Karakus & Fowell (2003)	undrained	indirect	hypothetical modulus of elasticity soft lining method	Y/-/-	soil: 8-node quadrilateral with reduced integration; lining: 3-node quadratic beam	made ground, Terrace Gravel & London Clay	made ground & gravel: linear elastic & perfectly plastic (Drucker-Prager); clay: modified Cam Clay
Franzius et al. (2005*a*)	undrained	direct	load reduction method	-/-/-	8-node quadrilateral	London Clay	non-linear elastic & perfectly plastic (MC)
Amorosi et al. (2014)	undrained	direct	displacement field method	-/-/-	8-node quadrilateral	clayey soil	linear elastic & perfectly plastic (MC)
Avgerinos et al. (2016)	coupled	direct	nodal force approach	Y/-/-	soil: 8-node quadrilateral; lining: 3-node beam	made ground, Terrace Gravel & London Clay	made ground: linear elastic; gravel: non-linear elastic perfectly plastic (MC); clay: M2-SKH

MC: Mohr-Coulomb

Table 2.3: Examples of 3D finite element modelling of tunnelling problems

Reference	Drainage	Approach	Tunnel process modelling	L_{exc}	Lining/ Grout/ Shield	Element type	Soil type	Soil model
Guedes de Melo & Santos Pereira (2000)	-	indirect	case 1: SBS, lining after 1 step; case 2: SBS, face pressure, grout pressure, lining 2 rings behind	2 m	case 1: Y/-/-; case 2: Y/Y/Y	soil & lining: 20-node hexahedral	-	linear elastic
Augarde & Burd (2001)	undrained	direct	SBS; lining shrinkage method by force	6 m	Y/-/-	soil: 10-node tetrahedral; lining: solid or shell	over-consolidated soil	multiple surface plasticity
Franzius et al. (2005*a*)	undrained	direct (vary L_{exc})	SBS; lining 1 ring behind	2.5 m	Y/-/-	soil: 20-node hexahedral; lining: shell	London Clay	non-linear elastic & plastic (Mohr-Coulomb)
Wisser et al. (2005)	undrained	direct	SBS with lining shrinkage method by strain	5/ 12.5 m	Y/Y/-	soil & lining: 10-node tetrahedral	over-consolidated clay	multiple surface plasticity
Wongsaroj et al. (2007)	coupled	indirect	SBS; lining 3 rings behind	2 m	Y/-/-	soil: 8-node or 20-node hexahedral; lining: 8-node shell	made ground, Terrace Gravel, London Clay & Beds Clay	subloading surface model
Losacco et al. (2014)	undrained	direct	SBS; face pressure; shield & tail: displacement field method; lining 3 rings behind	2.5 m	Y/-/Y	soil, shield & lining: 20-node hexahedral	made ground & clay	non-linear elastic & perfectly plastic (Mohr-Coulomb)
Fargnoli et al. (2015)	drained	direct	SBS; face pressure; tail: displacement field method; grout pressure; lining 2 ring behind	1.4 m	Y/Y/Y	soil: 10-node tetrahedral; lining & shield: 6-node triangular plate	gravelly sand & sandy silt	hardening with small-strain stiffness (HSsmall)
Bloodworth & Houlsby (2017)	undrained	direct	single-staged; lining shrinkage method by strain	-	Y/-/-	soil: tetrahedral; lining: shell	stiff clay	multiple surface plasticity

Volume loss control (direct) approach. The tunnel volume loss, $V_{\mathrm{L}}^{\mathrm{T}}$, is a parameter being monitored in an iterated simulation such that the targeted value is reached by the end of the construction (Potts & Zdravković 2001). This method is particularly useful for back analysis of tunnelling operations. This approach is also widely used in industry, with a range of volume loss, to simulate standard and conservative scenarios (e.g. Dulake 2011).

Indirect approach. The proportions of unloading pressure or reduction in stiffness due to tunnel excavation are prescribed. This approach obtains the volume loss as an output of the simulation. This method is typically used to predict the volume loss when the assessors are confident with the parameters regarding the tunnelling operation.

2.4.1 Two-dimensional (2D) tunnel modelling

Five modelling techniques for tunnel excavation in 2D using a transverse plane strain model are discussed below. These modelling techniques are applicable to a range of real construction methods such as shield tunnelling and sprayed concrete lining, for predicting the surface ground response.

Load reduction method. The soil elements inside the tunnel are first removed and replaced by the equivalent pressure initially imposed by the soil inside the tunnel periphery on the surrounding soil. The tunnel excavation process is then simulated by gradually reducing the imposed pressure, based on Brown & Booker (1985). A rigid lining is activated when $V_{\mathrm{L}}^{\mathrm{T}}$ attains the targeted value. The deformation of the tunnel can then be captured. The approach is called the nodal force reduction method when the nodal forces exerted by the removed soil elements are used in the implementation, instead of pressure (Rowe et al. 1983). The method is referred to as the convergence-confinement method (Potts & Zdravković 2001), or the λ-approach (Panet & Guenot 1982), when the indirect approach is applied (e.g. reducing the pressure to a prescribed proportion of the initial value). In the indirect approach, primary and secondary linings with different properties are often incorporated in sequence (Galli et al. 2004).

Stiffness reduction method. This method is also known as the progressive softening method, or the β-method. During the excavation process, the stiffness of the soil inside the periphery of the tunnel is gradually reduced (Potts & Zdravković 2001). The lining installation is activated at a certain stage, thereby the deformation of the tunnel wall can be captured. A modified version of this method is the disk calculation method, in which the weight of the excavated soil is also removed (Karakus 2007).

Hypothetical modulus of elasticity soft lining method. Predetermined values of the elastic modulus for the lining are introduced in several steps. This allows ground deformation prior to support installation or shotcrete lining gaining full strength (Karakus & Fowell 2003).

Displacement field method. The displacement field method controls the shape of the excavated tunnel directly. While deactivating the soil elements inside the tunnel section, a prescribed displacement field is applied to the nodes of the soil at the tunnel boundary to simulate the movement of the soil owing to the tunnel excavation (Amorosi et al. 2014). The lining is usually ignored since the displacement of the tunnel is fixed at each increment. Unrealistic external reactions may be induced on the tunnel to satisfy the prescribed displacement conditions on the tunnel.

Lining shrinkage method. Nodal forces or hoop strains are applied in the tunnel lining to generate a specified $V_{\mathrm{L}}^{\mathrm{T}}$. The forces may lead to additional hoop stresses, which have no physical significance if the lining is modelled as elastic (Augarde & Burd 2001).

2.4.2 Three-dimensional (3D) tunnel modelling

The modelling techniques described in the previous section can be extended to 3D models; however, the tunnel excavation process in the longitudinal direction is an additional consideration in 3D modelling. In a 2D simulation or a 3D model assuming single-stage excavation, the soil movement induced as the tunnel heading approaches is

not modelled. A step-by-step approach can be used to simulate the sequential construction events to model face loss and movements in the longitudinal direction, although the final transverse surface settlement troughs have previously been found to be similar to those obtained from 2D modelling (Franzius et al. 2005*a*).

Step-by-step excavation (SBS) method. Tunnel construction is modelled by consecutive removal of soil elements in front of the tunnel face (by completely releasing the interacting pressure and weight), while successively installing lining elements behind the face. The SBS method often does not follow the volume loss control approach strictly since rather repetitive analysis would be needed to monitor $V_{\mathrm{L}}^{\mathrm{T}}$ for every excavation stage. Instead, the targeted $V_{\mathrm{L}}^{\mathrm{T}}$ can be achieved roughly, by trial and error, by varying the excavation length in each stage (L_{exc}), with greater L_{exc} resulting in larger $V_{\mathrm{L}}^{\mathrm{T}}$ (Franzius et al. 2005*a*). The value of L_{exc} should be selected carefully as it affects the element mesh size and the number of calculation steps required.

Despite the variety of tunnel construction modelling methods, the load reduction approach (and similar methods) has dominated previous research because its concept is more analogous to real construction and it enables prediction of stresses around the tunnel. The 3D models in Augarde & Burd (2001), which adopted the nodal force reduction method, show that employing continuum elements to model the tunnel lining is more robust than using shell elements.

2.4.3 Soil constitutive models

The typical geological conditions in London have been well described in the literature (Kovacevic et al. 1996, Withers et al. 2001, Standing & Burland 2006, Dimmock & Mair 2007, Wongsaroj et al. 2013, Avgerinos et al. 2016). Table 2.4 shows an example of the soil profile beneath St James's Park reported by Avgerinos et al. (2016), where layers of made ground, Terrace Gravel, London Clay (of multiple units) and Lambeth Group were identified. Based on data from the centrifuge tests in Grant & Taylor (1996), the greenfield tunnelling-induced surface settlement profile for gravels

Table 2.4: Example stratigraphy at St James's Park (after Avgerinos et al. 2016)

Depth (m)	Thickness (m)	Soil type
0 − 5.5	5.5	Made ground
5.5 − 8.2	2.7	Terrace Gravel
8.2 − 18.7	10.5	London Clay B2 unit
18.7 − 30.7	12	London Clay A3 unit
30.7 − 40	9.3	London Clay A2 unit
40 −	-	Lambeth Group Formation

overlying clay is wider than that occurring at a homogeneous clay site. More details of layered ground conditions have been added in numerical simulations (Tables 2.2 and 2.3). Previous researchers (e.g. Jardine et al. 1986, Chow 1994) have shown that the choice of constitutive model for the soil is very important for robust calculations of the ground response to tunnelling. There has been a growing trend of adopting advanced constitutive models for analyses of this sort (Tables 2.2 and 2.3).

2.4.3.1 Mechanical behaviour

A representative soil model should be capable of capturing the aspects of mechanical behaviour that are identified as important for predicting ground movement induced by tunnelling. These aspects are listed below.

Small strain stiffness and its non-linearity. Experimental data have confirmed that soil exhibits high stiffness at small strain, and the stress-strain relationship is non-linear (Atkinson 2000). Modelling non-linear small strain stiffness has been shown to be important in analyses for predicting tunnelling-induced ground movements (Addenbrooke et al. 1997). Mair & Taylor (1993) found that better predictions of the change in pore pressure can be obtained by using a non-linear elastic-perfectly plastic model than a similar linear elastic-perfectly plastic model. This might be due to the difference in total stress path.

Elastoplastic behaviour. The laboratory tests on reconstituted London Clay in Atkinson et al. (1990) recognised inelastic behaviour even at small strains. Elastoplastic

theory provides a framework to address the development of plastic shear strain and volumetric strain.

Anisotropy. Clay generally displays non-negligible stiffness anisotropy (Lee & Rowe 1989, Potts & Zdravković 1999, Mitaritonna et al. 2014). Transverse isotropy (or cross-anisotropy) is the most obvious form. Narrow tunnelling-induced settlement troughs were modelled with an anisotropic elastic model in Puzrin et al. (2012). Lee & Rowe (1989) found that reducing the ratio of the independent shear modulus to vertical Young's modulus improves the shape of settlement trough. Nevertheless, the results of plane strain models in Addenbrooke et al. (1997) and Franzius et al. (2005*a*) show that modelling anisotropy gives little improvement of the prediction of tunnelling-induced settlement unless an unrealistically high degree of anisotropy is assumed.

Stress history. The geological stress history can be represented by the overconsolidation ratio and the coefficient of lateral stress at rest, K_0. The stress path tests on reconstituted samples of overconsolidated London Clay conducted by Atkinson et al. (1990) show that recent stress history in the form of rotation of the stress path has a major influence on the subsequent stress-strain behaviour. At small strains following a change in the direction of the stress path, the stiffness of soil may increase by up to an order of magnitude. A constitutive model incorporating kinematic yield surfaces within a state boundary surface is able to represent the recent loading and unloading history (e.g. Stallebrass & Taylor 1997, Houlsby 1999).

2.4.3.2 Advanced constitutive models

London Clay. Examples of advanced constitutive soil models which have been used to model overconsolidated clay include:

i. Multiple yield surface kinematic hardening model by Houlsby (1999). The model can simulate small-strain non-linearity in terms of total stress. Parametric studies on tunnelling were conducted with the model and results were compared with a linear elastic-perfectly plastic model in Chow (1994). The model gives a narrower

settlement trough and presents better agreement with the field measurement recorded in Peck (1969).

ii. Subloading surface model by Wongsaroj (2005). The model is formulated in terms of effective stress and is able to capture anisotropic stiffness and response to stress reversal. It was demonstrated by Wongsaroj (2005) to produce a narrower surface settlement trough compared to the linear elastic-perfectly plastic Mohr-Coulomb model and the modified Cam Clay model.

iii. Modified two-/three-surface kinematic hardening (M2-SKH/M3-SKH) models developed by Grammatikopoulou et al. (2006) based on the bubble model (Al-Tabbaa & Muir Wood 1989) and the 3-SKH model (Stallebrass & Taylor 1997) respectively. These models capture stiffness non-linearity and the effect of recent stress history. They were compared with the non-linear elastic model taken from Addenbrooke et al. (1997) and were shown to offer narrower settlement trough profiles (Grammatikopoulou et al. 2008).

Terrace Gravel/ made ground. In the context of ground response due to tunnelling in clay, less research has been focused on the constitutive models used for the shallower layers. Examples of models employed for Terrace Gravel and made ground are:

i. Subloading surface model by Wongsaroj (2005). In Wongsaroj et al. (2007), the same constitutive model was adopted for clay, gravel and made ground with different model parameters.

ii. Non-linear elastic model with perfectly-plastic Mohr-Coulomb yield surface. A stress-dependent elastic modulus expressed as a power law was employed for the made ground in Losacco et al. (2014). The Terrace Gravel in Addenbrooke et al. (1997), Jurečič et al. (2013) and Avgerinos et al. (2016) was modelled with non-linear elasticity represented by the model J4 (Jardine et al. 1986).

iii. Linear elastic model. The made ground in Addenbrooke et al. (1997), Jurečič et al. (2013) and Avgerinos et al. (2016) was modelled as an isotropic linear elastic material.

Previous research that modelled layered ground has mostly been applied to greenfield analysis. The constitutive model used for the Terrace Gravel or the made ground is, however, potentially important when surface structures are included in the model.

2.4.4 Lateral stresses

The value of the lateral stress coefficient, K_0, of the soil profile prior to tunnel excavation has a substantial influence on the computed surface settlements. A lower K_0 profile is shown to be favourable for producing narrower and deeper surface settlement troughs (Guedes de Melo & Santos Pereira 2000, Franzius et al. 2005*a*, Avgerinos et al. 2016), even though the assumed values might differ from in situ test results that indicate relatively high K_0 values.

2.5 Finite element analysis of long-term greenfield settlement

In addition to all the considerations involved in modelling short-term greenfield response as described in the last section, long-term consolidation analysis involves extra modelling complexities associated with pore water pressure, permeability, time sequence and so on.

2.5.1 Modelling approach

Both 2D and 3D models have been utilised for predicting long-term greenfield ground response to tunnelling. 2D plane strain analysis, which simulates the ground movement in the transverse direction, has obtained good agreement with field measurements (e.g. Avgerinos et al. 2016, 2018). It is expected that 3D analysis, with step-by-step excavation, should be able to predict tunnelling-induced excess pore pressure and transient effects more realistically than a 2D model, due to the 3D nature of the tunnel heading problem. Meanwhile, Wongsaroj et al. (2013) suggested that a 2D model with initial values transferred from a 3D short-term analysis of the tunnelling process is adequate

for long-term consolidation simulation if only a monitoring plane is of interest. This is because the stress and pore pressure profiles near the monitoring plane are approximately constant in the longitudinal direction once the tunnel shield advances beyond a certain distance.

Railway tunnels are usually built sequentially in pairs. One modelling approach is to follow the construction procedure directly, where typically there is a short period between the two tunnel advances (e.g. Avgerinos et al. 2016). However, omitting the rest period between the tunnel excavations in soil with low permeability was demonstrated to have little influence on the greenfield consolidation displacements (Laver 2010).

2.5.2 Soil model

The choice of soil model influences the prediction of excess pore pressures induced by tunnelling. The numerical analyses in Urciuoli et al. (1996) show that the excess pore pressure contours after tunnelling computed using a linear elastic-perfectly plastic soil model are different from those obtained using a linear elastic soil model. The parametric studies in Avgerinos et al. (2016) demonstrate that different calibrations of model parameters with the same constitutive model significantly affect the predicted surface settlements.

The magnitude of consolidation is associated with the compressibility of the soil, and thus the soil stiffness. Soil stiffness anisotropy was found to be important in modelling long-term ground response in Wongsaroj et al. (2007). When an anisotropic soil model is used, the magnitudes of the calculated negative excess pore pressures are larger at the crown and invert than at the springlines. This results in a squatting deformation of the tunnel lining in the long term, which is consistent with field observation; whereas the trend is opposite if an isotropic soil model is used. The lateral earth pressure coefficient, K_0, prior to tunnel excavation has been shown to affect the sign of the excess pore pressures generated during tunnelling (Urciuoli et al. 1996).

2.5.3 Soil permeability

The rate of consolidation depends on the rate of water seepage, which depends on soil permeability and hydraulic gradient (Atkinson & Mair 1981). Finite element analysis was conducted in Mair (2008) and Avgerinos et al. (2016) with anisotropic soil permeability (where the horizontal permeability of the soil is greater than the vertical permeability) to predict long-term ground surface settlement. The numerical results show that the consolidation-induced settlement trough is wider than the short-term settlement trough. The results in Mair (2008) and Wongsaroj et al. (2013) also demonstrate that the consolidation-induced settlement trough in the case of anisotropic permeability is wider than that in the case of isotropic permeability, and the widening effect increases with the degree of anisotropy. More specifically, increasing the degree of anisotropy of permeability for the 5 m of clay just above the tunnel crown was shown to have a significant effect on widening the long-term trough widths and increasing the magnitude of the maximum settlements (Avgerinos et al. 2016).

2.5.4 Lining permeability

Finite element parametric studies on the relative lining-soil permeability were conducted by Wongsaroj et al. (2007, 2013) and Avgerinos et al. (2018). The results show that the long-term consolidation behaviour depends on the drainage conditions of the tunnel lining relative to the surrounding soil. Higher lining-soil permeability ratio (the extreme case being a fully permeable tunnel) leads to larger consolidation settlement because greater effective stress develops in the soil around the tunnel when excess pore pressure dissipates. The analyses in Laver et al. (2017), which adopted the same modelling approach as Wongsaroj et al. (2013) and assumed lining permeability as a proportion of the horizontal soil permeability, show that the additional settlements and horizontal strains induced by consolidation are comparable to those immediately after tunnel construction, although the rate of consolidation is not fast. In the case of a completely impermeable lining, on the other hand, there is no drainage at the tunnel and therefore seepage-induced settlement is substantially less (Avgerinos et al.

2018). Analyses from Shin et al. (2002) and Wongsaroj et al. (2013) even show soil swelling and a decrease in effective stress around the tunnel in the case of a completely impermeable lining, resulting in a reduction in the volume of surface settlement in the long term.

The assumption of finite permeability for the lining was suggested by Shin et al. (2002) to be more representative as this assumption achieves an increase in settlement and an increase in lining load with time, which could not be modelled simultaneously using either of the extreme permeability cases. The numerical results in O'Reilly et al. (1991) also indicate that a lining with low permeability provides settlement profiles closest to the field measurements.

If the lining is assumed to be permeable in the finite element model, a one-way drainage flow condition should be applied on the tunnel boundary such that water can only flow from the soil into the tunnel void, but not in the opposite direction (Potts & Zdravković 2001). This ensures that the tunnel itself does not act as a source of water.

2.5.5 Hydraulic condition

The effect of groundwater discharge was investigated by Shin et al. (2002). The numerical results show that if the water table is assumed to draw down as water flows into the permeable tunnel, then the rate of settlement, the time needed to reach steady state and the total settlement at steady state are greater than those in the scenario where the phreatic surface is maintained at its initial level.

2.6 Finite element analysis of tunnel-soil-building interaction

Previous finite element analyses for masonry building response to shallow tunnelling have mainly been focused on the impact of immediate ground movement. Some representative examples are summarised in Table 2.5. The results (e.g. Burd et al. 2000) have demonstrated the modification of settlement profiles due to the presence of a

surface structure, and the ability of finite element analysis to predict crack damage in modelled facades; features that are not taken into account in the EBA method. Different strain patterns induced in facades under hogging and sagging modes of deformation were computed in Giardina et al. (2010). The finite element results in Liu et al. (2000) and Bloodworth & Houlsby (2017) show arching effects in the lower part of the facade deforming in sagging, reducing the damage in the upper part of the facade. The arching behaviour, which is evidenced by closing cracks in the building survey recorded in Bloodworth & Houlsby (2017), is again not considered in simplified assessment methods based on beam theory.

2.6.1 Modelling approach of the building

Both 2D and 3D finite element modelling procedures have been developed to evaluate the effects of tunnelling on surface structures, in which the ground, tunnelling process and building are all included in a 'coupled' model. Masonry buildings have been represented in several different ways, characterised by different constitutive models, in this kind of coupled modelling.

2.6.1.1 Two-dimensional modelling

2D plane strain finite element analysis was conducted in Franzius et al. (2004) and Giardina et al. (2015a) with the building modelled using elastic beam elements, as a continued study of the relative stiffness approach (Potts & Addenbrooke 1997). Liu et al. (2000) and Amorosi et al. (2014) performed 2D simulations assuming plane strain conditions for the soil and plane stress conditions for the masonry structures; the former modelled a simplified facade with openings for a parametric study, and the latter simulated an aqueduct subjected to a twin-tunnel construction process for comparison with monitoring data. A discontinuous model for the masonry was used in Miliziano et al. (2002), in which bricks and mortar were modelled separately using elastic macroelements and elastoplastic interfaces. A semi-coupled modelling approach with only a facade model and a steel beam underneath was implemented in Giardina

Table 2.5: Examples of finite element analysis models incorporating soil-building interaction

		Soil			Structure			Soil-building
Reference	2/3D	Type	Element	Model	Type	Element	Model	interface
Potts & Addenbrooke (1997)	2D	London Clay	8-node plane strain quadrilateral	non-linear elastic & perfectly plastic (Mohr-Coulomb)	concrete slabs	3-node Mindlin beam	elastic	rough (tie)
Burd et al. (2000)	3D	London Clay	10-node tetrahedral	multiple surface plasticity	masonry building	6-node plane stress triangle	elastic no-tension	tie
Liu et al. (2000)	2D	London Clay	6-node plane strain triangle	multiple surface plasticity	masonry facade	6-node plane stress triangle	elastic no-tension	tie
Miliziano et al. (2002)	2D	medium to stiff clay	quadrilateral	linear elastic & perfectly plastic (Mohr-Coulomb)	masonry facade	brick: macroelement; mortar: interface	brick: linear elastic; mortar: elastic perfectly plastic, with tensile strength limit	frictional
Franzius et al. (2004)	2D	London Clay	8-node plane strain quadrilateral	non-linear elastic & perfectly plastic (Mohr-Coulomb)	multi-storey building	3-node Mindlin beam	elastic	tie
Giardina et al. (2010)	3D	soft soil	tetrahedral	linear elastic	2-unit masonry building	quadrilateral shell	elastic with linear softening in tension	frictional
Pickhaver et al. (2010)	3D	-	10-node tetrahedral	multiple surface plasticity	masonry building	2-node 6-dof equivalent beam	linear elastic	tie
Amorosi et al. (2014)	2D	clayey soil	8-node plane strain quadrilateral	linear elastic-perfectly plastic (Mohr-Coulomb)	masonry wall	4-node plane stress quadrilateral	elastic & perfectly plastic (anisotropic elasticity & strength envelope)	tie
Giardina et al. (2017)	2D	sand	quadratic plane strain	non-linear elastic power law	masonry facade	quadratic plane strain	elastic with linear softening in tension	frictional
Bloodworth & Houlsby (2017)	3D	stiff clay	tetrahedral	multiple surface plasticity	connected masonry buildings	plane stress	elastic no-tension	tie

et al. (2013). A displacement profile was imposed on the base of the steel beam to resemble the surface settlement caused by tunnelling. The facade was modelled with plane stress continuum elements and connected to the beam with a layer of non-linear interface elements. The soil and the building were modelled by quadratic plane strain elements in Giardina et al. (2017), where the 2D simulations reproduced the results of centrifuge testing with 3D building models.

2D plane strain analysis is limited to the particular building-tunnel configuration where the face of the facade is orthogonal to the tunnel longitudinal axis. It also does not allow the 3D effects associated with the soil-building interaction to be modelled.

2.6.1.2 Three-dimensional modelling

Although 3D models usually require longer computation time than 2D ones, the 3D environment enables the simulation of multi-staged tunnel excavation (Section 2.4.2), the modelling of other components of the building in directions different to the facade under consideration, and more importantly, the incorporation of the 3D nature of the soil-building interaction.

In previous studies, the roof and the floor of the masonry building are usually neglected in the building model because their stiffness is negligible with respect to the overall stiffness of the building. Burd et al. (2000) modelled a masonry building with facades and external walls using plane stress elements with openings in the facades (represented by empty spaces). The masonry was modelled as a continuous homogeneous material. In Bloodworth & Houlsby (2017), the facades and walls were also modelled with plane stress elements, but the openings in the facades were discretized using elements with reduced stiffness. Giardina et al. (2010) modelled the external facades and internal walls using shell elements, with the openings represented by empty spaces. Pickhaver et al. (2010) developed equivalent beam elements, which are structurally identical to masonry panels based on Timoshenko beam theory, to reduce the complexity of modelling the building in 3D finite element analysis. However, a separate assessment is needed in this case to analyse structural damage in the building.

2.6.1.3 Masonry constitutive model

As tunnelling-induced damage in masonry buildings is mainly due to tensile and shear stresses, a continuum constitutive model that can capture the crack, damage and plasticity characteristics is considered representative, although the computed cracking direction does not necessarily follow the material texture (Giardina et al. 2013). Homogenized material models also benefit from a smaller number of model parameters and shorter computation time compared to heterogeneous models. In this thesis, the masonry is modelled as a continuous homogenized material combining the behaviours of bricks and mortar. Some of the constitutive models used in previous analyses are described here.

The elastic no-tension model used in Burd et al. (2000) and Bloodworth & Houlsby (2017) describes tensile failure with a low tensile strength and ignores compressive failure by using an infinite compressive strength. When the major principal strain (taking tension positive) becomes tensile, cracks form along the minor principal strain direction. The material stiffness in the direction perpendicular to the crack and the tensile stress across the crack reduce to residual values. The small residual values of tensile stress and stiffness are needed for numerical stability.

A fixed crack model was adopted in Giardina et al. (2013) such that the facade behaves as a homogeneous isotropic linear elastic continuum material prior to cracking and becomes a non-linear orthotropic continuum when cracks are initiated (indicated by tensile strain). The non-linearity is approximated by reducing the shear stiffness step-wisely as strain becomes more tensile. The axes of orthotropy are assumed to be fixed upon crack initiation. Similarly to the no-tension model in Burd et al. (2000), no stiffness reduction occurs in compression.

The periodic masonry model employed in Amorosi et al. (2014) is a homogenisation of the periodic pattern of blocks and joints in masonry structures. The masonry blocks are assumed to be elastic and the joints are cohesive-frictional. In the homogenised model, the elasticity is formulated from the dimensions of the blocks and the stiffness of both blocks and joints, while the mortar joints, which are assumed to be the only

source of failure, are characterised by multi-surface perfect plasticity.

2.6.1.4 Soil-building interface

The coupling of strains from the ground to the building occurs at the soil-building interface, yet little investigation has been done on the features of the interface. There is little variation of the interface model in the literature, for example those in Table 2.5, where a tie interface was mostly used. None of the previous studies in Table 2.5 modelled any form of building foundation explicitly.

Tie. A tie interface refers to equalising the degrees of freedom for a pair of surfaces, which prevents any relative movement across the interface in both normal and tangential directions. Burd et al. (2000), Liu et al. (2000), Pickhaver et al. (2010) and Bloodworth & Houlsby (2017) used the tie elements formulated by Houlsby et al. (2000) between the building and the soil. In Franzius et al. (2004) and Amorosi et al. (2014), the building was simply 'connected' to the soil (original terminology used, without further explanation).

Although the term 'rough' was used to describe the interface in Potts & Addenbrooke (1997), the interface behaviour appears to be tied as the tunnelling-induced surface vertical displacement beneath a relatively stiff building is flat across the span of the building, with a magnitude smaller than the maximum greenfield settlement.

Frictional. A frictional interface defines the tangential behaviour of a pair of surfaces, where the two surfaces are assumed to have no relative movement when the contact shear stress is below the critical shear stress, τ_{crit}. The interface can be specified as smooth ($\tau_{\text{crit}} = 0$), frictional (or rough) ($0 < \tau_{\text{crit}} < \infty$) or fully rough ($\tau_{\text{crit}} = \infty$).

In Miliziano et al. (2002), the frictional interface was defined with the same elastic and plastic properties as the soil. Giardina et al. (2010, 2017) employed interface elements with Coulomb frictional behaviour with a friction angle of 30° in the tangential direction and zero tensile strength in the normal direction. The friction parameter of the interface model was obtained by calibrating against the horizontal displacements

measured in the equivalent centrifuge model.

The tunnelling-induced gap between the beam and the soil observed in the centrifuge testing of Farrell et al. (2014) was reproduced in the finite element analysis by Giardina et al. (2015a) using a no-tension interface, whereas a tie interface results in the beam being pulled down by the ground.

2.6.2 Effect of tunnel excavation on building

A step-by-step tunnel excavation procedure is adopted in most of the previous 3D studies, for instance, Burd et al. (2000), Giardina et al. (2010) and Pickhaver et al. (2010). Torsional behaviour of the building is accounted for in Franzius (2003) and Pickhaver et al. (2010). Comparing the results obtained by multi-staged and single-staged excavation, data in Giardina et al. (2010) indicate that over-simplification of the tunnel advance process underestimates the building damage. In the analysis with step-by-step tunnel excavation, plastic strain develops in the facade as the tunnel passes underneath, while the relevant strain pattern is not seen in the analysis where the tunnel excavation is modelled in a single stage (Giardina et al. 2010). However, it is noted that the range of tunnel volume loss considered in Giardina et al. (2010) is rather severe ($V_{\mathrm{L}}^{\mathrm{T}} = 4 - 12\%$). It is not clear whether the effect of modelling staged excavation would be as dominant for the common range of volume loss occurring in modern projects.

Alternatively, Bloodworth & Houlsby (2017) simplified the tunnel excavation process as a single stage on the basis that the study focuses on the final condition of the ground and buildings after tunnelling is completed. The computation run time was shortened significantly as a result.

2.6.3 Influence of building features

It is generally impractical to include every detail of the building in a finite element model. However, some building features directly affect the reliability of the computed results; therefore, it is important to identify the critical features and their extent of

influence before making assumptions and simplifications for finite element modelling.

Stiffness of the building. The structural stiffness is widely regarded as being important in assessing building risk (e.g. Liu et al. 2000, Franzius et al. 2004). Increasing the stiffness of the building reduces the differential settlement experienced by the building, resulting in less building damage.

Weight of the building. The self-weight of the building is significant for the additional building settlement induced by tunnelling (Burd et al. 2000). The magnitude of building settlement induced by tunnelling was demonstrated to be larger for a heavier building because of the activation of yielding in the soil (Liu et al. 2000). The building self-weight is also non-negligible for the change in stress state in the soil below the building foundation (Mroueh & Shahrour 2003). The parametric study in Franzius et al. (2004) shows that increasing building load results in an increase in mean effective stress and a decrease in K_0 in the soil at tunnel depth, eventually affecting the tunnel volume loss (with respect to the same unloading portion in the load reduction method for modelling tunnel excavation).

Initial structural damage of the building. The height of the building plays an important role in resisting tension in the hogging mode of deformation. Frischmann et al. (1994) correlated the extent of existing cracks to reduced stiffness of the building by lowering its height in the models.

Both stiffness and weight increase with the height of the building. As the height increases, larger total settlements occur due to greater weight, while lower relative deflections are associated with larger stiffness (Amorosi et al. 2014). Franzius et al. (2004) suggested that the relief from the increase in stiffness outweighs the damage caused by the increase in weight for taller buildings.

Internal walls. The inclusion of internal walls in the building model, which increases the overall structural stiffness, was shown to reduce the severity of damage to the front and rear facades (Bloodworth & Houlsby 2017). The results in Bloodworth & Houlsby

(2017) show that damage in the internal walls is likely to start at the ends where the adjoining facades connect.

Openings in the facade. The presence of openings in the facade (i) increases the bending flexibility of the facade and causes increased differential settlements, and (ii) reduces the overall shear resistance and introduces localised strain at the internal corners of the openings. Giardina et al. (2017) simulated several facades with openings, where the openings covered $20 - 40\%$ of the total facade area. The results show that shear outweighs bending in causing the total deflection of the facades, and the contribution of shear increases with the percentage of openings. Facades in hogging are more sensitive to an increase in the proportion of openings than facades in sagging (Pickhaver 2006, Giardina et al. 2015b). The pattern of openings alters the stress arching paths (Pickhaver 2006).

Eccentricity. The position of the building relative to the tunnel, together with the building length relative to the settlement tough width, influence the form of deformation along the building span. Parametric studies of different ranges of eccentricity for a single tunnel were conducted in Liu et al. (2000), Giardina et al. (2010) and Amorosi et al. (2014) in which sagging and hogging deformations were detailed at different eccentricities.

2.7 Concluding remarks

The current building damage assessment process involves a systematic scheme where buildings subject to higher risk due to tunnel excavation are evaluated with increasing detail. Previous research has demonstrated the applicability of finite element analysis for predicting short-term and long-term tunnelling-induced greenfield ground movement and immediate building response to tunnelling, with varying modelling complexity. An expeditious finite element-based procedure for practical tunnelling-induced building damage assessment purposes, however, should avoid excessively detailed in-

puts and over-conservatism.

Although direct comparison between previous studies is difficult because of the differences in the models and parameters adopted in each procedure, it can be deduced that the computed results are dependent on several key factors, including geometric features, material constitutive models, interface contact models, and tunnel excavation modelling procedures. In particular, the mechanical features captured by the soil constitutive model are important in reproducing the ground response caused by tunnelling.

The integrated prediction of building response and long-term consolidation caused by tunnelling is a more complicated problem. Although the rate of long-term settlement is often sufficiently slow for mitigation measures to be implemented when an alert level is reached, a deeper understanding of the interaction problem would provide a more comprehensive overview of the viability of the tunnelling project and the possible extent of long-term building damage. The literature related to the finite element analysis of long-term greenfield ground response caused by tunnelling, for example regarding the lining-soil permeability and the choice of constitutive models, can undoubtedly facilitate the proposed initial research on building response to long-term tunnelling-induced consolidation.

Chapter 3

Finite element modelling procedure

The major study of this thesis is based on finite element analysis of an example masonry building affected by tunnelling in central London. The set-up of the simulations determines the reliability of the research findings. Various modelling approaches were considered and assumptions were made carefully. The numerical calculations were performed using the finite element program Abaqus v2016 (Dassault Systèmes Simulia Corp., Providence, RI, USA) with some user-defined material (UMAT) subroutines.

This chapter documents the developed modelling procedures in detail. The example scenario is first specified. Consideration is then given to appropriate approaches for modelling the building, the foundation-facade interface and the soil-foundation interface. Total stress analysis (TSA) and effective stress analysis (ESA) are used to conduct simulations for the short-term and the long-term building response to tunnelling. The procedures for selecting material constitutive models and their parameters are described. In particular, respective advanced constitutive models are selected to model London Clay in TSA and ESA. The calculation procedures used for TSA and ESA are explained, together with the main assumptions made. Lastly, several result processing methods are developed and tailored to evaluate various aspects of the finite element analysis results.

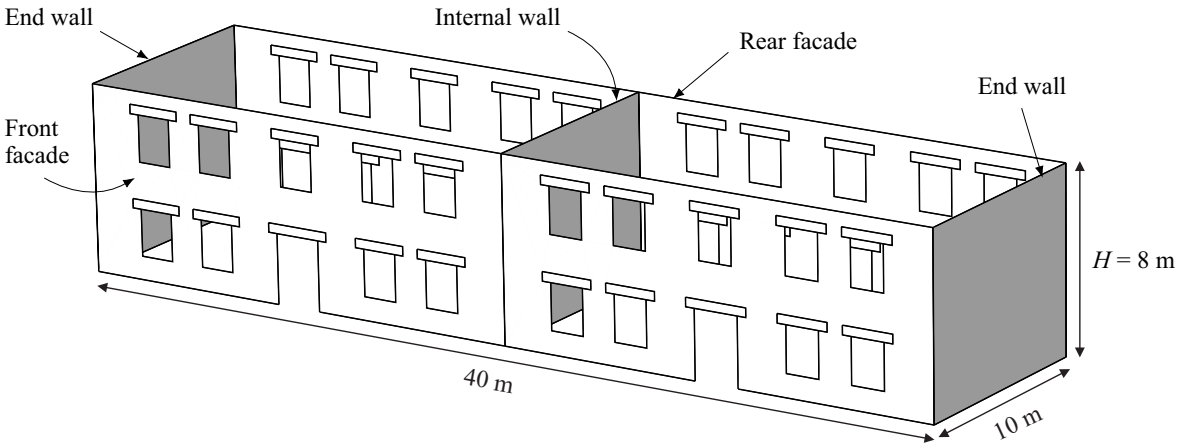


Figure 3.1: Layout and dimensions of the masonry building (above-ground height $H = 8$ m for two-storey and 12 m for three-storey)

3.1 Specification of the scenario

The study is based on a typical London situation — shallow tunnels are constructed underneath a masonry building, which is founded on a continuous strip footing. The building and the tunnels are assumed to be independent of other structures and utilities.

3.1.1 Building

The structure considered in the example scenarios is a masonry building comparable to those in central London (e.g. the Victorian buildings in Kensington, and the Moodkee Street buildings shown in Withers (2001*b*)). The dimensions of the building and the layout of the openings in the front and rear facades, as shown in Figs 3.1 and 3.2, are based on previous numerical work at Oxford (Burd et al. 2000, Wisser et al. 2005, Pickhaver et al. 2010). Lintels are included above all of the window and door openings in the facades to avoid tensile failure in the masonry due to local sagging effects. The masonry building is 40 m long and 10 m wide. The thickness of the masonry wall is assumed to be 0.215 m, which corresponds to the thickness of two standard UK bricks. Two building heights are considered: a two-storey variant ($H = 8$ m) and a three-storey variant ($H = 12$ m); the two-storey variant is depicted in Figs 3.1 and 3.2. The area of openings accounts for 20.6% and 20.0% of the gross area (above ground level) for facades of height $H = 8$ m and $H = 12$ m respectively.

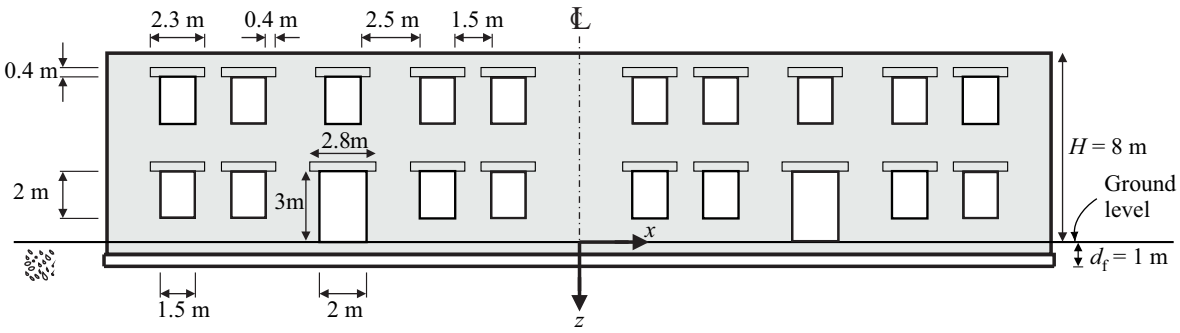


Figure 3.2: Dimensions of facade openings and lintels. Also showing coordinate axes, with the y-axis directed into the paper

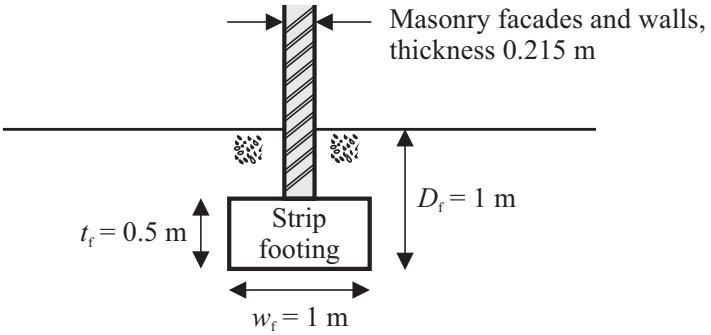


Figure 3.3: Geometrical details of masonry and foundation

3.1.2 Foundation

A continuous strip footing made of masonry of width $w_\mathrm{f} = 1$ m, thickness $t_\mathrm{f} = 0.5$ m and embedded depth $D_\mathrm{f} = 1$ m is adopted in the main study, as shown in Fig. 3.3. These dimensions are based on the foundations of the low-rise residential masonry building described by Withers (2001*b*). The building foundation is modelled explicitly to allow coupling of stress and strain from the soil to the facade and to enable possible gapping and sliding beneath the footing. The sensitivity of building damage to the dimensions and the material of the footing is studied in Section 6.3.5.1.

3.1.3 Geological conditions

The soil conditions assumed (Fig. 3.4) are representative of those in central London where, typically, a layer of Terrace Gravel overlies London Clay. It is noted that layers of alluvium and made ground usually exist above the Terrace Gravel. These superficial soils are omitted from the current model for simplicity. Moreover, major masonry

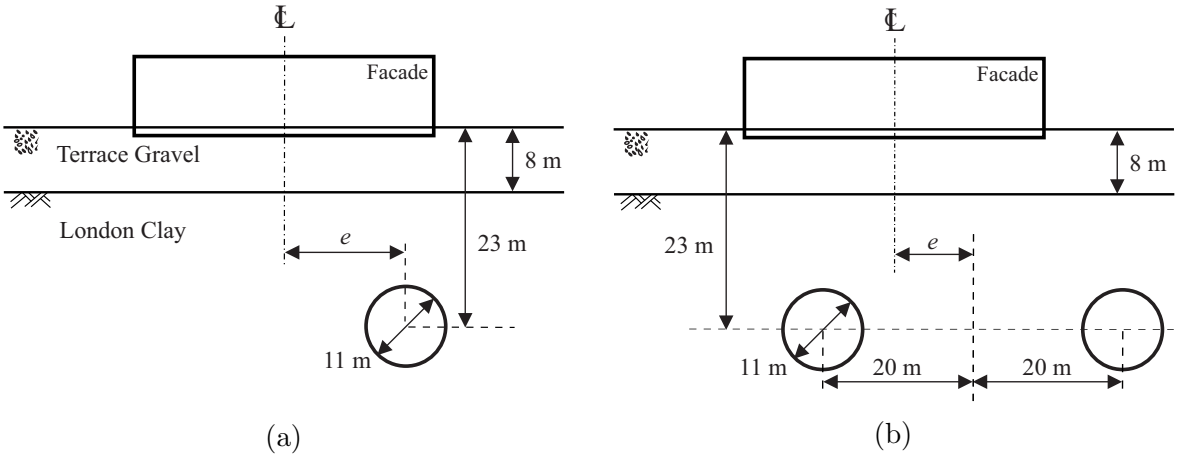


Figure 3.4: Soil configuration, tunnel dimensions and definition of eccentricity, e: (a) single-tunnel analyses; (b) twin-tunnel analyses

buildings in London often have basements and are typically founded either on the Terrace Gravel or, for deep basements, on the London Clay (e.g. Harris 2001, Viggiani & Standing 2001). In the current model, no attempt was made to represent a basement. To enable the footings to bear directly on the Terrace Gravel, the Terrace Gravel in the model is assumed to extend upwards to the ground surface. As a consequence, the thickness of the gravel layer in the model (8 m) is rather larger than that typically encountered in London. The water table is assumed to be located at 2.7 m above the surface of the London Clay (Grammatikopoulou et al. 2008). The pore water pressure distribution is assumed to be hydrostatic with depth in the steady state.

3.1.4 Tunnel configuration

Horizontal single and twin tunnels installed beneath the building are considered. The tunnels are orthogonal to the front and rear facades of the building, except in the skew tunnel case, where the horizontal tunnel is assumed to approach the building at 45°. A series of eccentric orthogonal tunnels in the range $0 \leq e \leq 30$ m are studied. The eccentricities of the tunnel to the building, e, are defined in Figs 3.4(a) and 3.4(b) for the single-tunnel case and twin-tunnel case respectively. The tunnel diameter (11 m) and depth (23 m) are intended to be representative of typical Crossrail platform tunnels (Gakis et al. 2014, Skinner et al. 2014). A volume loss of 1.5% is assumed for each tunnel, corresponding to the 'moderately conservative' volume loss adopted for the

concourse and platform tunnels in the Crossrail project (Dulake 2011).

3.2 Building modelling approach

To simulate the building introduced in Section 3.1.1, one option is to develop a model for the whole building. However, the part of the building of most concern for damage is usually the front or rear facade. Isolating a single facade for analysis, which is simpler to model and reduces the computational resources required, is therefore worth considering. Two building modelling approaches are thus developed; in both cases the masonry panels are modelled with shell elements and the footing uses continuum elements:

'3D complete building analysis'. All facades, internal and end walls are included in the model, although the floors and roof are excluded on the basis that they are unlikely to contribute significantly to the stiffness of the building or to require detailed consideration in the damage assessment process. This approach provides a great level of detail of the building being modelled, but at the expense of high geometrical complexity and long computation time.

'3D isolated facade analysis'. A single facade (the front or rear facade, together with its strip footing) is modelled in isolation. Although certain 3D effects (e.g. due to return walls and foundations) are excluded, these analyses have the advantages that they are simpler to set up and quicker to compute. Since parametric studies can be conducted relatively quickly, the isolated facade approach could potentially be an attractive option for practical assessment purposes. Despite the fact that the facade is modelled as a planar structure, it still needs to be incorporated in a 3D analysis to capture the interaction between the foundation and the ground. For comparison purposes, a small number of analyses were conducted in which the window and door openings are absent (referred to as 'plain facade' analyses).

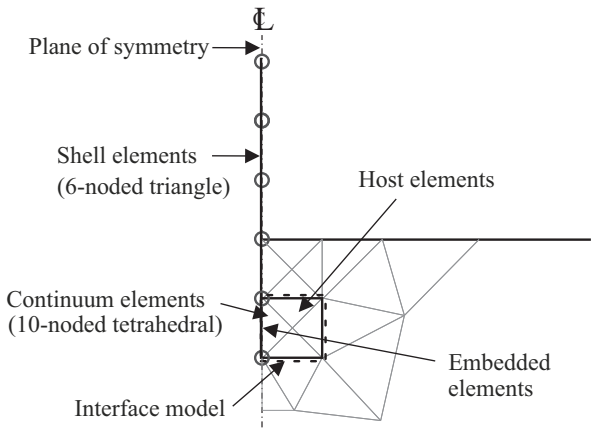


Figure 3.5: Finite element representation of the facade, the foundation and the soil-foundation-facade interfaces. The plane of symmetry along the mid-plane of the facade is exploited

Comparisons between the results of the 3D complete building analyses and the corresponding 3D isolated facade analyses provide a means of assessing the accuracy and usefulness of the isolated facade modelling approach.

3.3 Foundation-facade interface

In a real building of the type being modelled, each masonry wall is supported directly on a strip footing, as illustrated in Fig. 3.3. However, since the facade is modelled with shell elements and the footing uses continuum elements, an unrealistic concentrated load would be induced in the elements representing the footing at the point of contact if the facade shell elements were connected to a line of nodes along the top of the footing continuum elements. To avoid unrealistic stress concentrations, the facade is connected to the footing by adopting the embedded element technique, available as a built-in feature in Abaqus. In this approach, the facade mesh is extended to the base of the footing and the additional facade shell elements are attached to the host footing continuum elements using the Abaqus keyword *EMBEDDED ELEMENT. This ties the translational degrees of freedom of the embedded elements to those of the host elements. A diagram illustrating the finite element representation around the foundation is shown in Fig. 3.5, to be compared with the geometric details in Fig. 3.3.

3.4 Soil-foundation interface

The choice of soil-footing contact model is of particular importance in tunnelling-induced building damage assessment calculations, since the contact model has a key role in governing the relative movement between the foundation and the ground. In the current modelling, the interface between the (fully drained) gravel and the masonry footing is assumed to be frictional. The surface-to-surface finite-sliding formulation between two deformable bodies, available in Abaqus, is adopted. By pairing potential contact surfaces and defining contact conditions, appropriate contact elements are generated automatically by Abaqus.

Zero tensile strength and zero penetration in the normal direction (referred to as the 'hard' pressure-overclosure relationship in Abaqus) are adopted to allow for potential gapping. The shear behaviour is represented by the classical isotropic Coulomb friction model (available as a built-in model in Abaqus) with an assumed friction coefficient, μ. Sliding occurs when the shear traction reaches the shear strength of the interface.

A friction coefficient of $\mu = 0.3$, which is considered to be approximately intermediate between smooth and fully rough, is employed in the main study. The contact model is defined using Abaqus keywords *SURFACE INTERACTION and *FRICTION, and the contact model is applied to the interface using *CONTACT PAIR. The effect of the friction coefficient in the soil-footing contact model on the computed building damage is studied in Section 6.3.5.2.

3.5 Total stress and effective stress analyses

The short-term building response to tunnelling refers to the state immediately after tunnel excavation. Owing to the relatively low permeability of London Clay, the tunnel construction is assumed to take place under undrained conditions. The long-term response includes the effect of consolidation of the London Clay induced by tunnelling, and eventually fully drained conditions are approached. The Terrace Gravel is assumed to behave in a fully drained manner in both the short term and long term.

Both the short-term and long-term processes can be simulated using effective stress analysis (ESA). Although ESA has been used in previous research for predicting green-field ground response, the current tunnelling-induced building damage assessment process, which mainly focuses on the short-term behaviour, has frequently been carried out based on total stress analysis (TSA). It is therefore more consistent and reliable to expand the current research on the short-term building response to tunnelling using TSA. The modelling procedure of TSA can be designed in a straightforward manner based on the experience from literature (e.g. those in Table 2.5). The TSA approach also provides a more efficient and convenient means for parametric studies on geometrical details and contact interaction along the interfaces.

To study the effect of long-term consolidation induced by tunnelling under a building, effective stress analysis (ESA) must be used to model the development and dissipation of excess pore pressures. Elements with pore pressure degrees of freedom are assigned to the soil, and soil parameters in terms of effective stress are required. As the study of tunnel-soil-building interaction incorporating time-dependent effects is not common, the current work provides a basis for developing a framework for these calculations. It should be noted that creep is not considered in the current scope of work.

Since the primary purposes of the employment of TSA and ESA are different, two sets of calculation procedures are developed in the thesis (these are described in Sections 3.8 and 3.9). It is also noted that two different constitutive models, which are formulated using total stress and effective stress parameters respectively, are selected for the London Clay (Section 3.6.5). As the input modelling parameters in the ESA were not calibrated against those used in the TSA, the long-term building response to tunnelling is determined by comparing it with the short-term response obtained in the ESA calculations, instead of the results obtained from the TSA.

3.6 Constitutive models

An appropriate constitutive model should be able to capture desired behaviours yet be kept simple enough to balance the performance of the models and the computation time. In this section, the choice of the constitutive model for each material is explained. The adopted model parameters are also included, apart from the models implemented for the Terrace Gravel and the London Clay, for which the process of calibrating the model parameters is detailed in Chapters 4 and 5 respectively.

3.6.1 Masonry building

A key aspect to consider is the loss of strength and stiffness that occurs when tensile cracking develops in the masonry building. However, since the focus of the current work is the development of relatively straightforward computational procedures for practical risk assessment purposes, detailed considerations such as the analysis of likely geometric cracking patterns are unnecessary. A homogenised approach, which is adequate to identify strain concentration, is therefore preferred, rather than attempting to model the details of individual masonry blocks and mortar joints. It is noted that in a practical assessment exercise, the actual building damage also depends on existing conditions and cracks; anything more than a relatively simple modelling approach at this stage of assessment is therefore unlikely to be justified.

The masonry in this study is represented using the 'concrete damaged plasticity' model available as a built-in model in Abaqus. This model is based on the formulation in Lee & Fenves (1998) and has been used previously by Furtmuller & Adam (2011) for the analysis of masonry buildings. The model is designed particularly to represent cyclic degradation (via the use of a damage parameter). In the current analyses, however, the material is assumed to remain undamaged. Prior to failure, the masonry is elastic, with Young's modulus $E_{\mathrm{m}} = 3$ GPa and Poisson's ratio $\nu_{\mathrm{m}} = 0.2$ (Giardina et al. 2013). The material has an infinite compressive strength. When loaded in uniaxial tension, the material is linear elastic until a fracture stress, $f_{\mathrm{t}} = 50$ kPa, is reached. This value of f_{t} is comparable to data employed in previous studies; e.g. Furtmuller &

Adam (2011) and Giardina et al. (2013) both adopt 100 kPa as the tensile strength of masonry. The value of 50 kPa employed in the current work is intended to provide a realistic lower bound on tensile strength.

Masonry would be expected to exhibit a softening response after the onset of cracking. From a numerical perspective, however, a softening post-cracking response is undesirable because of pathological mesh-dependent behaviour and the likelihood of numerical difficulties. Accordingly, the post-failure gradient of the uniaxial tensile stress-strain response in the current model is specified to be a small positive value fE_{m}, with $f = 0.01$. The Abaqus keywords *CONCRETE DAMAGED PLASTICITY, *CONCRETE COMPRESSION HARDENING and *CONCRETE TENSION STIFFENING are used to specify this model.

The unit weight of the masonry is assumed to be 19 kN/m^3 (Giardina et al. 2013). To ensure that the overall loading on the foundation is representative of a real building, allowance is made by using an artificially increased unit weight for the masonry to account for the weight of the roof, floors, windows, internal plaster and internal fixtures and fittings. In the current analysis, the unit weight of the masonry is set to 23.75 kN/m^3, which is equivalent to an uplift of 25% on the actual unit weight, following Losacco et al. (2014).

3.6.2 Lintel

The unit weight of the lintels is set to the same value as the masonry (23.75 kN/m^3) for convenience. The lintels are assumed to be made from concrete and are modelled as a linear elastic material with a Young's modulus of 9 GPa and a Poisson's ratio of 0.2.

3.6.3 Footing

The footing is assumed to be constructed from masonry in the main study, and is represented by the same constitutive model that is employed for the masonry building. As a simplification of the construction process of the building foundation, the footing is embedded in the Terrace Gravel when the Terrace Gravel is activated in the beginning

of the simulations (see assumptions in Sections 3.8 and 3.9). For the convenience of establishing geostatic stresses in the calculations, the unit weight of the footing is set equal to that of the surrounding soil (20 kN/m^3).

Strip footings of low-rise masonry buildings might alternatively be constructed from concrete (e.g. the Moodkee Street buildings in Withers (2001*b*)) which would presumably result in a stiffer building response, or from some less stiff material such as rubble (University of the West of England 2009). The effect of the stiffness of the footing is investigated in Section 6.3.5.1. The adoption of masonry footings in the main study is thought to provide a moderately conservative approach for damage prediction.

3.6.4 Terrace Gravel

3.6.4.1 Identification of problem and selection of constitutive models

An important feature of the current analysis is the interaction between the Terrace Gravel and the building foundation. As a result of building construction, the soil surrounding the building foundation is compressed and higher shear strength is anticipated compared to other soil of the same depth. Moreover, in a typical tunnelling scenario with non-uniform settlements along the building, some regions of the soil underlying the foundation experience an increase in load, whereas other regions undergo unloading. Another essential feature of the gravel is the small-strain stiffness non-linearity.

The conventional linear elastic, perfectly plastic Mohr-Coulomb (MC) model is commonly used to represent granular soil. It is available in Abaqus as a built-in material model. However, the model does not capture the soil response related to density and stress history conditions. Abaqus allows the application of user-defined material constitutive models via subroutines called UMAT (in Abaqus/Standard) coded in Fortran. Three advanced constitutive models, namely Nor-Sand (Jefferies 1993), Severn Trent sand (Gajo & Muir Wood 1999) and extended Mohr-Coulomb (Doherty & Muir Wood 2013), were considered for a more representative model for the Terrace Gravel.

Nor-Sand (Jefferies 1993) is a rigid-plastic model which directly couples hardening with void ratio in the critical state framework (elasticity could be incorporated). The

flow rule is governed by normality. The maximum dilatancy of sand is matched by constraining yield surface hardening via a relationship derived from experiments.

Severn Trent sand (Gajo & Muir Wood 1999) is an extension of the MC model. It combines small-strain elasticity, kinematic hardening MC yield criterion and critical state. Critical state is incorporated by a stress-dependent relative density, which relates the maximum strength to the distance of the current volumetric state from the critical state at the same stress level. The flow rule is derived from the Cam Clay model to link between volumetric and deviatoric plastic strain increments.

The extended Mohr-Coulomb (EMC) model of Doherty & Muir Wood (2013) is another extension of the MC model and was originally developed to be used in shallow foundation problems. The EMC model incorporates kinematic hardening in terms of plastic distortional strain and features a degradation of soil stiffness as the soil is sheared towards failure. The EMC model employs linear elasticity.

The three advanced constitutive models considered here are regarded as being suitable for the current application. The EMC model is selected over the others because of its advantages of directness in formulation and calibration. The EMC model handles the behaviour on initial unloading as an elastic process, and provides representations of stiffness degradation as the soil is sheared towards failure. It is noted that the EMC model does not consider directly the effect of relative density of the soil, yet this is not a commonly documented parameter for Terrace Gravel.

3.6.4.2 Features of the extended Mohr-Coulomb model

The EMC model employs a hardening form of the Mohr-Coulomb (MC) yield surface in which hardening is linked to plastic deviatoric strain and mobilised friction angle. It requires a relatively small set of constitutive parameters — two for the elastic behaviour and four for the plastic response. Within the yield surface, the soil obeys isotropic linear elasticity, which is defined by the small-strain shear modulus, G_0, and Poisson's ratio, ν. The plastic and hardening behaviours are specified by a peak friction angle, ϕ_{p}, a constant volume friction angle, ϕ_{cv}, an attraction parameter, a, and a hardening

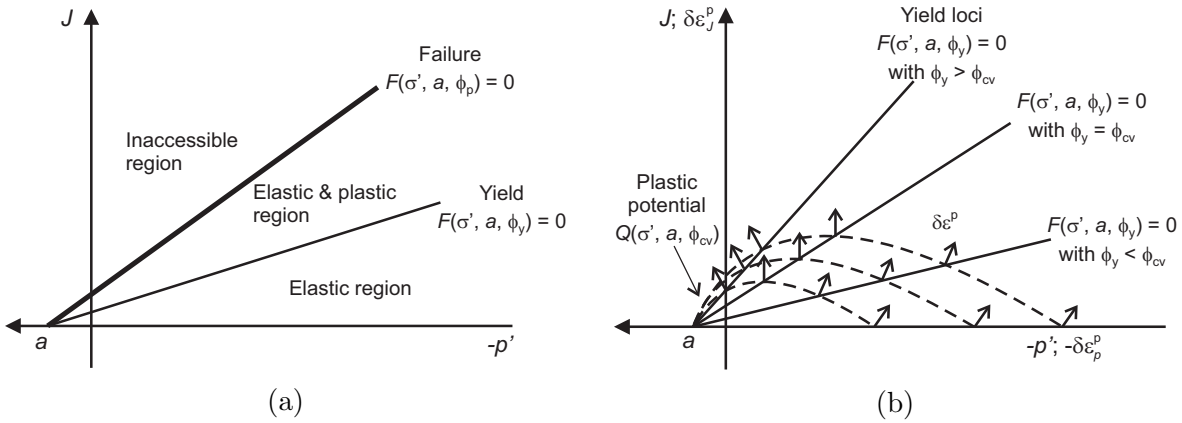


Figure 3.6: Extended Mohr-Coulomb model: (a) failure surface and yield surface; (b) plastic potential surface intersecting yield surfaces of different relative sizes of ϕ_{y} to ϕ_{cv} and the direction of plastic strain increments normal to the plastic potential (after Figs 2 and 4 in Doherty & Muir Wood (2013)). Stress invariants defined in Nomenclature

parameter, β. The flow rule is based on a variant of the original Cam Clay plastic potential.

The yield surface, F, is described by the current stress, $\boldsymbol{\sigma'}$, the mobilised friction angle, ϕ_{y}, and a. When hardening is activated, it is represented by an increasing ϕ_{y}, until the yield surface coincides with the failure surface defined by ϕ_{p} (i.e. when $\phi_{\mathrm{y}} = \phi_{\mathrm{p}}$). The rate of stiffness degradation is associated with β. The yield surface and the relationship between the peak friction angle, ϕ_{p}, and the mobilised friction angle, ϕ_{y}, are illustrated in Fig. 3.6(a). The sign convention adopted is tension positive.

The current plastic potential, Q, is expressed in terms of $\boldsymbol{\sigma'}$, ϕ_{cv} and a. The term ϕ_{cv} is referred to as the constant volume friction angle based on the representation that yielding at $\phi_{\mathrm{y}} = \phi_{\mathrm{cv}}$ indicates plastic deformation at constant volume, while yielding at $\phi_{\mathrm{y}} < \phi_{\mathrm{cv}}$ implies volumetric compression, and yielding at $\phi_{\mathrm{y}} > \phi_{\mathrm{cv}}$ results in volumetric expansion. The plastic potential surface and the implication of the value of ϕ_{y} relative to ϕ_{cv} are visualised in Fig. 3.6(b).

The details of the implementation of the UMAT subroutine and the calibration of the model parameters are given in Chapter 4. The bulk unit weight is assumed to be 20 kN/m^3 (Withers et al. 2001, Avgerinos et al. 2016) and the initial value of the coefficient of lateral stress, K_0, is set to equal $1 - \sin\phi_{\mathrm{p}}$.

3.6.5 London Clay

3.6.5.1 Identification of problem and selection of constitutive models

In the current work, different models were considered for conducting total stress analysis and effective stress analysis.

For total stress analysis. The multiple yield surface kinematic hardening model developed for overconsolidated clay by Houlsby (1999), which is formulated in terms of total stress, has been employed in previous related research (e.g. Burd et al. 2000, Bloodworth 2002, Dong et al. 2016). This model characterizes the reduction of shear stiffness in discrete steps. The parameters of individual surfaces associated with London Clay are also available in the cited literature. The typical version of this model, which consists of a series of nested von Mises yield surfaces, gives relatively fast and stable numerical convergence. For these reasons, the multiple yield surface kinematic hardening model is adopted to represent the undrained response of the London Clay in total stress analysis in the present work. The model was implemented in a UMAT by Dong (2014) and consent of use was obtained from Dr. Y. P. Dong.

For effective stress analysis. Excess pore pressure is developed in the clay around a newly constructed tunnel. Long-term consolidation or swelling develops as the soil loads or unloads (in effective stress) when the excess pore pressure dissipates in the long term. A model expressed in terms of effective stress is therefore needed. The modified Cam Clay model (Roscoe & Burland 1968), one of the earliest critical state models, captures the volumetric response associated with the extent of overconsolidation. There are a number of carefully developed advanced constitutive models extended from the conventional modified Cam Clay model. Examples include the bubble model (Al-Tabbaa & Muir Wood 1989), the 3-SKH model (Stallebrass & Taylor 1997), the M2-SKH and M3-SKH models (Grammatikopoulou et al. 2006), the subloading surface model (Wongsaroj 2005), and the MIT-E3 model (Whittle & Kavvadas 1994). All of them are capable of capturing small-strain stiffness degradation via a plasticity model.

The MIT-E3 model, which is based on a bounding surface approach, and the subloading surface model, which is built on expanding and contracting an inner surface, assume unloading soil behaviour to be purely elastic, which restricts the shear behaviour during unloading (Zytynski et al. 1978). The bubble model employs an inner kinematic yield surface within a bounding surface. This aspect of the model simulates variation in stiffness owing to recent stress history. The bubble model is therefore sometimes referred to as the 2-SKH model, which stands for the two-surface kinematic hardening model. The 3-SKH model, which is based on the 2-SKH model but with an additional yield surface to record an extra level of stress history, improves the smoothness of the stiffness-strain curve (Grammatikopoulou et al. 2006). The modified versions, which are the M2-SKH and M3-SKH models by Grammatikopoulou et al. (2006), where a new hardening modulus relationship is introduced to smooth the transition from elastic to elastoplastic behaviour, provide even better prediction of the stiffness-strain curve than obtained with the 2-SKH and 3-SKH models (Grammatikopoulou et al. 2006).

In particular, the M2-SKH (modified two-surface kinematic hardening) model has been employed in predicting tunnelling-induced ground movements in London Clay and gives satisfactory predictions of greenfield settlement both in the short term and the long term, using the Imperial College Finite Element Program (ICFEP) (Avgerinos et al. 2016). The calibration data are also available in Avgerinos et al. (2016). Based on the success in the literature, the M2-SKH model is chosen as the material model for London Clay in the effective stress analyses in this study.

3.6.5.2 Features of multiple von Mises yield surface kinematic hardening model

The multiple yield surface model takes into account small-strain non-linearity, hysteresis and dependence of stiffness on recent stress history. An outermost perfectly plastic von Mises surface is used as a failure surface. A series of nested yield surfaces of the same shape as the outermost fixed failure surface are used to represent a gradual variation of stiffness. The stiffness is highest (equal to the small-strain elastic shear

modulus, G_0) when the stress state is inside the innermost yield surface, where the response is purely elastic. As the stress state changes and activates the inner yield surfaces in turn, the stiffness reduces in steps, providing a step-wise non-linear response. Meanwhile, the inner yield surfaces translate, in the framework of the kinematic hardening theory of plasticity, and the relative position of the yield surfaces records the recent stress history. Each yield surface is described by two parameters (c'_α and g'_α) specifying the size of the yield surface and the magnitude of the stiffness reduction as the yield surface is activated.

Parameters. For consistency with previous work (e.g. Houlsby 1999, Burd et al. 2000), a total of nine inner yield surfaces are used, with a fixed outer von Mises failure surface. The non-dimensional constitutive parameters (c'_α and g'_α) defining the nine inner yield surfaces used in Burd et al. (2000) are adopted, and are listed in Table 3.1, with Surface 1 being the innermost yield surface. This set of parameters implies an evolution of normalised tangent shear modulus with shear strain as shown in Fig. 3.7.

On the basis of data in Withers (2001*b*), the undrained shear strength, s_u (in kPa), is assumed to vary with depth below the clay surface, z_c (in metres), as:

$$s_\mathrm{u} = 100 + 8z_\mathrm{c} \tag{3.1}$$

The small-strain elastic shear modulus is assumed to be $G_0 = 500s_\mathrm{u}$, also based on the data in Withers (2001*b*). The bulk modulus is taken as $K = 50G_0$, which corresponds to an undrained Poisson's ratio of 0.49. The bulk unit weight of the London Clay is assumed to be 20 kN/m^3 (Withers et al. 2001, Avgerinos et al. 2016). The initial position of the yield surfaces and failure surface is set to be concentric at the principal stress space diagonal ($\sigma_1 = \sigma_2 = \sigma_3$). The initial stress state is assumed to be at the centre of the surfaces, such that the initial geostatic stress state is established with $K_0 = 1$.

Table 3.1: Values of non-dimensional parameters adopted in the multiple yield surface kinematic hardening model (after Houlsby 1999, Burd et al. 2000)

Surface	1	2	3	4	5	6	7	8	9
c'_α	0.02	0.04	0.06	0.1	0.15	0.2	0.3	0.5	0.7
g'_α	0.9	0.75	0.5	0.3	0.2	0.15	0.1	0.05	0.025

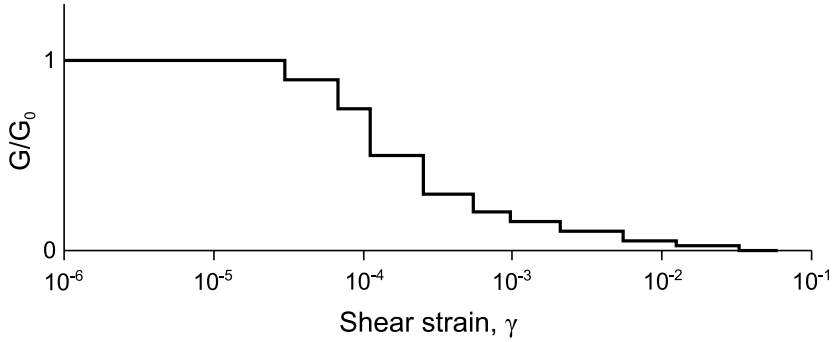


Figure 3.7: Variation of normalised tangent shear modulus with shear strain for the multiple yield surface model (after Burd et al. 2000)

3.6.5.3 Features of modified two-surface kinematic hardening model

The M2-SKH model described in Grammatikopoulou et al. (2006) is an extended version of the bubble model developed by Al-Tabbaa & Muir Wood (1989). This model is able to predict non-linear pre-failure behaviour at small strains, hardening and softening, as well as stress path-dependent stiffness.

The constitutive model is formulated in general stress space in terms of the mean effective stress, p', and the deviatoric stress tensor, $\hat{\boldsymbol{s}}$ (defined in Nomenclature). Within the outer modified Cam Clay (MCC) bounding surface (BS), there is a single inner kinematic yield surface (YS) with the same shape as the BS but smaller size. Fig. 3.8(a) presents the model in the triaxial plane; where J is the square root of the second deviatoric stress invariant, p'_0 indicates the value of the mean effective stress at the intersection of the current swelling line with the isotropic normal compression line, the parameters with the subscript a relate to the centre of the YS, and the function $g(\theta)$ defines the shape of the surface in the deviatoric plane (θ is the Lode angle, see Nomenclature). The model can be formulated with various shapes in the deviatoric plane for the yield, bounding and plastic potential surfaces, for instance, the Mohr-Coulomb hexagon and the Lade shape shown in Fig. 3.8(b).

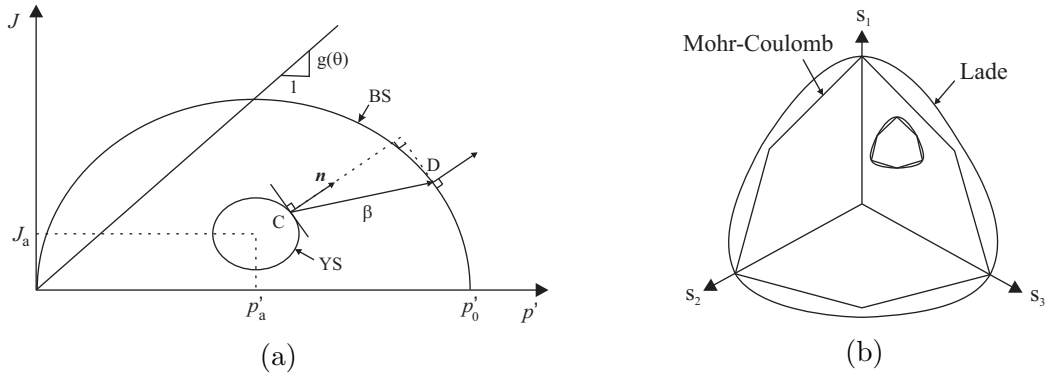


Figure 3.8: Representation of YS and BS in the M2-SKH model (a) in p'-J stress space (b) in deviatoric plane (after Grammatikopoulou et al. (2006, Fig. 1))

When the stress state is within the YS, the behaviour is elastic. It is inadmissible for any stress state to lie outside the YS. When the stress state attempts to cross the YS, elastoplastic behaviour is initiated and the YS is dragged along the stress path within the BS. In addition to the yield and plastic potential functions, the elastoplastic behaviour when the stresses lie on the YS is defined by a hardening/softening law with mapping functions for stiffness variation and a translation rule for the shift of the YS. On yielding, the YS is translated in the direction of $\hat{\boldsymbol{\beta}}$ such that the two surfaces can only intersect on a common tangent. As illustrated in Fig. 3.8(a), $\hat{\boldsymbol{\beta}}$ is the tensor connecting the current stress state on the YS (point C) to its conjugate point on the BS (point D), which is defined as the point on the BS where the direction of the outward normal is the same as at point C. Once the YS is in contact with the BS, the behaviour of model reduces to that of the BS. Provided that the BS is active, the YS remains tangential to the BS regardless of whether the BS is expanding or contracting. In this case, the elastoplastic behaviour is equivalent to the MCC model.

Following Avgerinos et al. (2016) and Grammatikopoulou et al. (2008), two units of London Clay (units B2 and A3) are modelled. It is assumed that $\gamma_{\text{bulk}} = 20$ kN/m^3 for both units, and initial $K_0 = 1 - \sin\phi'$, where $\phi' = 25°$ and $20.3°$ for units B2 and A3 respectively. During the current implementation, aspects such as the shape of surfaces in the deviatoric plane and the measure of the proximity of the YS to the BS were considered carefully. The modification of the model and the calibration of model parameters are detailed in Chapter 5.

3.6.6 Lining

Two tunnel modelling procedures are adopted in the analyses. One of them (the nodal force reduction method) involves a tunnel lining (see Section 3.9.2) while the other one (the displacement field method) does not (see Section 3.8.2). In the former approach, the tunnel lining is modelled with linear elasticity and the parameters $E = 28$ GPa, $\nu = 0.15$ and $\gamma = 24$ kN/m^3 are adopted (Addenbrooke & Potts 1996).

3.6.7 Ghost membrane

To capture the additional tunnelling-induced strains directly for data analysis, a layer of 'ghost' membrane elements is attached to the surfaces of the building facades and walls (using Abaqus keyword *TIE) immediately prior to simulating the tunnel construction process. The membrane has zero density and a very small stiffness relative to the masonry.

3.7 Element types and mesh boundary

The element types adopted for each modelling part are listed in Table 3.2 in terms of their Abaqus identifier. General stress/displacement elements are used in total stress analysis (TSA). In effective stress analysis (ESA), elements with coupled pore pressure degrees of freedom are assigned for the soil and the lining. The finite element meshes are generated using Abaqus CAE. Following Wongsaroj et al. (2007), the depth from the ground surface to the base of the London Clay is taken to be 50 m. The length and the width of the soil block is varied to minimize boundary effects. The mesh size also depends on whether any of the symmetry planes (i) about the longitudinal direction along the tunnel and (ii) about the mid-plane of the isolated facade or the complete building are exploited. The degrees of freedom on the base boundary are fixed in all directions and the vertical boundaries have roller supports. Example meshes are displayed in Chapters 6 and 7 for TSA and ESA respectively.

Table 3.2: Element types adopted in total stress analysis (TSA) and effective stress analysis (ESA). The code of element types follows Abaqus terminology

	TSA	ESA
Building/ facade	STRI65	STRI65
Footing	C3D10	C3D10
Terrace Gravel	C3D10	C3D10P
London Clay	C3D10	C3D10P
Tunnel lining	-	C3D10P
Ghost membrane	M3D6	M3D6

STRI65: 6-node triangular thin shell element with five Gauss points
C3D10: 10-node quadratic tetrahedron continuum element
C3D10P: 10-node quadratic displacement, linear pore pressure element
M3D6: 6-node triangular membrane element

3.8 Calculation procedure: total stress analysis

3.8.1 Main assumptions

Total stress analysis (TSA) is employed to simulate the short-term building response to tunnelling by assuming the London Clay to behave in an undrained manner. Various simplifications are made for the purpose of developing practical modelling procedures:

i. The Terrace Gravel and the London Clay are configured as in Fig. 3.4 at the beginning of the simulation (i.e. without any simulation of the geological history) with a prescribed value of K_0.

ii. The ground water table is assumed to be located at the surface of the London Clay throughout the calculation.

iii. The footing is embedded in the gravel from the start of the simulation as a simplification of the process of constructing a building foundation.

3.8.2 Tunnel modelling procedure

The tunnel construction process is simplified as a single-stage excavation (i.e. construction of the entire length of tunnel within the finite element model is simulated in a single analysis step) with multiple calculation increments to accommodate non-linear behaviour. Although this procedure does not allow transient 3D effects due to step-by-

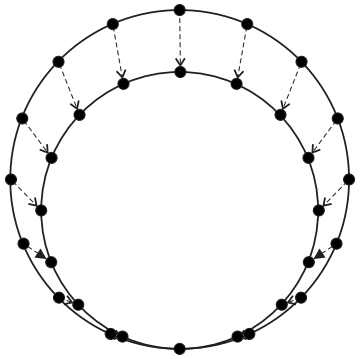


Figure 3.9: Initial and final configurations of the tunnel cross-section using the displacement field method (after Amorosi et al. 2014)

step tunnel construction to be modelled, it provides an efficient means of establishing the deformations induced in the building after the tunnel heading has passed. It also has the advantages of reducing the mesh size and exploiting the plane of symmetry (along the building if applicable) transverse to the direction of the tunnel.

The displacement field method used by Amorosi et al. (2014) is chosen to model the tunnel volume loss in TSA for computational efficiency. It is a direct approach for achieving the desired volume loss by prescribing nodal displacements as boundary conditions at the nodes around the tunnel perimeter. The prescribed displacements consist of radial shrinkage combined with a rigid vertical offset, such that the invert of the tunnel remains at its initial position (Fig. 3.9). The final configuration of the tunnel is assumed to remain circular and the new radius, r_1, is determined from the desired volume loss, $V_{\mathrm{L}}^{\mathrm{T}}$, as

$$r_1 = r_0\sqrt{1 - V_{\mathrm{L}}^{\mathrm{T}}} \tag{3.2}$$

where r_0 is the initial tunnel radius. The difference $r_0 - r_1$ is equivalent to the magnitude of the rigid vertical downward movement.

This procedure introduces a fictitious vertical force on the tunnel boundary; it cannot therefore be used reliably to compute soil deformations local to the tunnel. It is considered, however, that this procedure is acceptable for a study focused on the short-term effect of ground movements on buildings with shallow foundations under undrained conditions, on the basis that the soil-foundation interaction occurs some distance from the tunnel perimeter. Provided realistic greenfield settlement profiles

are obtained, the actual conditions in the neighbourhood of the tunnel are regarded as being of secondary importance for the building-focused analyses undertaken here.

Construction of twin tunnels is modelled as a simultaneous event. It is acknowledged that, in practice, twin tunnels are likely to be advanced using a sequence of alternate drives, such that the soil movements induced by the second tunnel may be influenced by the presence of the first tunnel (Addenbrooke & Potts 2001). Tunnel-tunnel interaction during sequential construction was not considered in the current work.

3.8.3 Simulation steps

The geostatic step is conducted using Abaqus keywords *GEOSTATIC under *STEP, and the following static load steps are simulated using the keywords *STATIC under *STEP. All calculation steps are conducted using the automatic incrementation procedures provided in Abaqus, except for Step 1 which is completed in one increment.

1. Geostatic step. The shell elements modelling the building and the 'ghost' membrane elements (Section 3.6.7) are deactivated using Abaqus keyword *MODEL CHANGE, REMOVE. Geostatic stresses are initialised throughout the soil and the footing by applying gravity, density and the prescribed K_0 values.

2. Building step. The building (or facade) is reactivated by adding the stiffness of the shell elements at the beginning of the step, then applying the building self-weight (using Abaqus keyword *MODEL CHANGE, ADD).

3. Membrane step. The layer of ghost membrane elements attached to the building shell elements is reactivated.

4. Tunnel removal step. The soil elements within the tunnel periphery are deactivated and the nodes at the tunnel periphery remain fixed at their current positions using Abaqus keyword *BOUNDARY, FIXED.

5. Tunnel shrinkage step. The movement of the tunnel corresponding to the desired tunnel volume loss is imposed by applying prescribed displacements to the nodes at the tunnel periphery.

For analyses in greenfield conditions (i.e. with the building absent), the building foundation is substituted with the Terrace Gravel and Steps 2 and 3 are skipped.

3.9 Calculation procedure: effective stress analysis

3.9.1 Main assumptions

More detailed and complex calculation procedures are adopted for the study of the effect of consolidation on building damage using effective stress analysis (ESA). The soil is assumed to behave in an undrained manner during the tunnel construction process, whereas drainage is assumed for the long-term analysis.

Pore pressure degree of freedom. The elements used in ESA have a degree of freedom for pore pressure at the vertex nodes. Fixed pore pressure or flow conditions are defined when appropriate. The pore pressure at the soil boundaries is prescribed with a hydrostatic distribution below the water table, and zero above the water table. The simulation of undrained conditions during the tunnel construction and lining installation processes is facilitated by assigning relatively small step time and temporarily applying a no-flow condition to all boundaries of the whole model. If the lining is assumed to be permeable, zero pore pressure and a drainage-only flow boundary condition are applied at the lining inner surface after the tunnel is built. The water table is assumed to remain at the prescribed level without any drawdown.

Permeability and initial void ratio. The permeability and initial void ratio of the Terrace Gravel are assumed to be 10^{-8} m/s and 0.3 respectively (Geotechdata.info 2013). For the London Clay, the anisotropic permeability model described in Avgerinos et al. (2016) is used and the initial void ratio is derived from the calibration of the M2-SKH model. The data are specified in Section 5.4. The effect of the permeability of the tunnel lining is studied in Chapter 7.

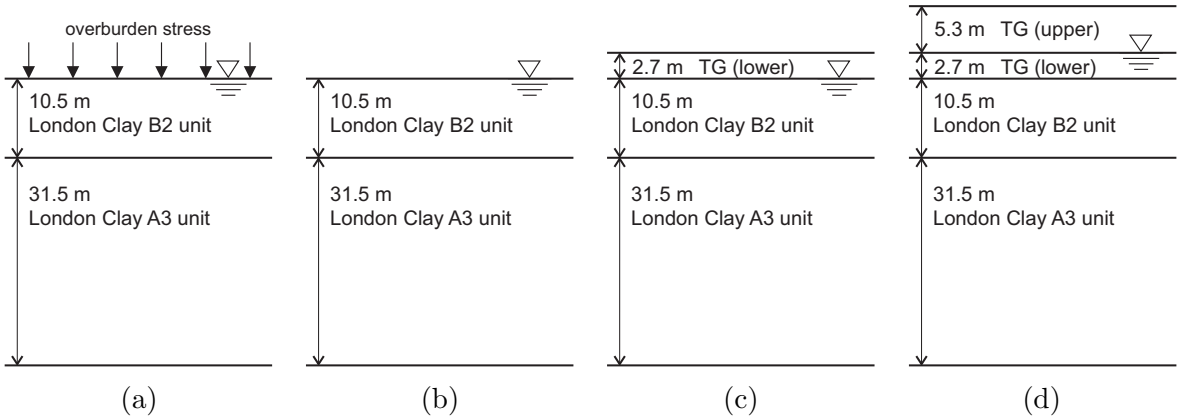


Figure 3.10: Simulation of the process of geological stress history: (a) historical deposits represented by overburden stress; (b) erosion of overburden material by removing the overburden stress; (c) deposition of the lower layer of Terrace Gravel; (d) deposition of the upper layer of Terrace Gravel and raising of water table; this is the soil configuration when the tunnel is constructed (TG stands for Terrace Gravel)

Geological configuration. The soil configuration in Avgerinos et al. (2016) includes a layer of made ground overlying the Terrace Gravel (Table 2.4). The two soil layers differentiate the deposition of soil on the London Clay in order, and the final water level is defined at the surface of the Terrace Gravel. The Terrace Gravel in the current study, which extends to the ground surface, is therefore divided into lower and upper layers, such that the thickness of the lower layer is equivalent to the thickness of the Terrace Gravel in Avgerinos et al. (2016). The division of the London Clay also follows Avgerinos et al. (2016) in which the upper 10.5 m is categorised as unit B2 and the remainder is represented by the properties of unit A3. The soil configuration adopted in the current analysis is shown in Fig. 3.10(d). The water level is consistent with that in Avgerinos et al. (2016). All soils are assumed to be fully saturated.

Geological stress history. The process of geological stress history based on Grammatikopoulou et al. (2008) is illustrated schematically in Fig. 3.10. Simulation of this process establishes an appropriate stress history and stress state in the soil constitutive models and determines the K_0 profile (see next paragraph) when the tunnel is constructed.

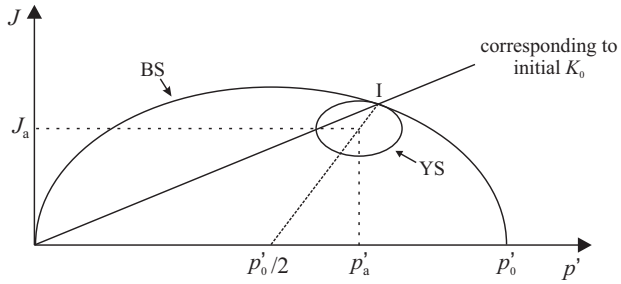


Figure 3.11: Initial stress conditions in the M2-SKH model at the start of the simulation

Coefficient of lateral stress, K_0. The K_0 in the soil when the tunnel is constructed, which has a significant influence on the shape of the tunnelling-induced settlement trough, is determined by simulation of the geological stress history, rather than being directly specified (Grammatikopoulou et al. 2008, Avgerinos et al. 2016). Although the initial K_0 value is assumed to be $1-\sin\phi'$, the effect of this assumption is considered to be insignificant as the values of K_0 at different levels in the model develop throughout the geological history simulation process.

Initialisation of the M2-SKH model. Initial conditions are required for the M2-SKH model employed for the London Clay. The initial stress state at the start of the simulation is assumed to be on the bounding surface (BS) with the initial K_0 value (Point I on Fig. 3.11), owing to the overburden stress (Fig. 3.10(a)). The initial size of the bounding surface (in terms of p'_0) is determined from the overburden stress and the soil self-weight. The centre of the yield surface (YS) is located by the geometrical relationship of the surfaces (Fig. 3.11). The yield surface is then relocated and the bounding surface is resized upon the simulation of the geological stress history.

Construction process. The construction process for the building foundation is simplified. The footing is embedded in the upper layer of Terrace Gravel when the deposition is modelled. The process of tunnel construction is described in next section.

3.9.2 Tunnel modelling procedure

Excess pore pressures develop in the soil during tunnel construction. The dissipation of the excess pore pressure causes consolidation (or swelling) to occur. Realistic modelling

of the tunnel construction process is essential for ensuring realistic development of excess pore pressure. The displacement field method, where reaction forces are developed to keep the tunnel in shape and in place, was hence considered not suitable. Instead, the nodal force reduction method with the volume loss control approach is adopted (e.g. Grammatikopoulou et al. 2008). In Abaqus, this method is implemented by, firstly, removing the soil elements inside the tunnel periphery using the keyword *MODEL CHANGE, REMOVE. This essentially removes the stiffness of the soil elements to be excavated and substitutes the stresses being carried by the excavated elements with equivalent nodal forces. These nodal forces are then removed incrementally during the step. The unloading occurs linearly over the prescribed step time. Secondly, the tunnel cross-sectional area during the unloading increments ($A_{\text{unloading}}$) is monitored to compute the volume loss. It is noted that the tunnel nodes might have displaced during the simulation of geological stress history, resulting in a tunnel area (A_{history}) different from the one computed with the original diameter (A_{original}). Therefore, the volume loss caused by tunnelling, V_{L}^{T}, is defined as follows.

$$V_{\text{L}}^{\text{T}} = \frac{A_{\text{unloading}} - A_{\text{history}}}{A_{\text{original}}} \tag{3.3}$$

Finally, once the desired volume loss has been reached, the tunnel lining is installed by activating the lining elements. The lining is modelled as a continuous concrete ring to represent a stiff tunnel upon construction. The tunnel nodal forces remaining from the unloading process are then removed completely, introducing stresses and displacements to the lining. Despite that fact that the volume loss control approach is used to obtain the desired volume loss, the computed volume loss is not exact unless very small increments are used during unloading.

When a building exists on the ground surface, its weight modifies the stress state of the soil around the tunnel. The soil response to the removal of the elements in the tunnel becomes slightly different from that in the greenfield conditions. The study of the effect of soil-building interaction can be calibrated against the greenfield analysis based on either (i) the tunnel volume loss, or (ii) the unloading proportion of the nodal

forces. In the current work, the tunnel volume loss evaluated in a plane well away from the building is used to determine the completion of tunnel excavation in the building analysis, by targeting the same desired tunnel volume loss as in the greenfield analysis. As a consequence, the percentage of unloading of nodal forces in the analysis with the building is expected to be different from the one in the greenfield analysis.

Although more sophistication is introduced in modelling the tunnel excavation process in ESA, the current project is not intended to model a complete 3D tunnelling process such as the one in Kasper & Meschke (2004). Tunnel construction is still modelled as a single process, similar to TSA, which avoids additional complexities including excavation and lining installation sequence, excavation length, and face pressure. In the twin-tunnel case, the construction of both tunnels is assumed as a simultaneous event (except for the verification case of Jubilee Line Extension twin tunnels in Section 5.4.) Tunnel-tunnel interaction during sequential construction is not considered in the main study. It is acknowledged that some transient effects of tunnel construction are neglected by these simplifications. However, they are not considered to the critical factors for investigating the long-term consolidation response.

3.9.3 Simulation steps

The geological stress history (Steps 1 to 4) and building construction (Steps 5 to 6) are simulated in steady state using the Abaqus keywords *SOILS under *STEP. The tunnelling process (Steps 7 to 9) is modelled with transient analysis using Abaqus keywords *SOILS, CONSOLIDATION. The short-term tunnelling-induced building response is captured immediately after Step 9. The long-term response is evaluated after Step 11.

1. Geostatic and overburden step, drained. The continuum elements modelling the tunnel lining, the continuum elements for the Terrace Gravel, the shell elements for the building, and the 'ghost' membrane elements attached on the building are deactivated. Geostatic stresses are initialised throughout the London Clay by establishing gravity and applying overburden stress (Fig. 3.10(a)). Fixed pore pressure boundary conditions corresponding to a hydrostatic distribution

are applied on the two side boundaries of the London Clay.

2. Erosion step, drained steady state. The overburden stress is removed by resetting the load using Abaqus keyword *DSLOAD, OP=NEW (Fig. 3.10(b)).

3. Deposition (lower Terrace Gravel) step, drained steady state. The lower layer of the Terrace Gravel is activated (Fig. 3.10(c)).

4. Deposition (upper Terrace Gravel) and raising of water table step, drained steady state. The upper layer of the Terrace Gravel and the footing are activated. Zero pore pressure is prescribed at the surface of the lower layer of the Terrace Gravel (Fig. 3.10(d)). New hydrostatic pore pressure boundary conditions, which correspond to the water level being located at the surface of the lower layer of the Terrace Gravel, are applied on the two side boundaries of the Terrace Gravel and the London Clay, and on the base boundary.

5. Building step, drained steady state. The building (or facade) is activated.

6. Membrane step, drained steady state. The layer of ghost membrane elements attached to the building shell elements is activated.

7. Tunnel excavation step, undrained transient state (small step time). No-flow condition is applied to all boundaries. The soil elements inside the tunnel periphery are deactivated. To prepare for continuing the simulation with the desired volume loss, the Abaqus keyword *RESTART, WRITE, FREQUENCY=1 is used.

8. Lining step, undrained transient state (small step time). The simulation is restarted from Step 7 at increment x, where x corresponds to the increment closest to the targeted tunnel volume loss, using the keyword *RESTART, READ, STEP=7, INC=x, END STEP. The lining elements are activated with the nodes at the tunnel periphery temporarily fixed using the keyword *BOUNDARY, FIXED.

9. Lining stress step, undrained transient state (small step time). The displacement

boundary conditions at the tunnel periphery are removed such that movements and stresses develop in the lining.

10. Resumption of hydraulic condition step, drained transient state (small step time). The hydraulic boundary conditions deactivated in Step 7 are restored. The default condition of the lining inner surface is no-flow in Abaqus, which fulfils the assumption of a completely impermeable lining. If permeable lining is assumed, zero pore water pressure and a drainage-only flow boundary condition are applied to the lining nodes at the inner tunnel periphery. The drainage-only flow is employed using Abaqus keyword *SFLOW with flow type QD, which prohibits flow from the tunnel to the soil when the surface pore pressures are negative, but permits flow into the tunnel void when the surface pore pressures are positive.

11T-17T. Consolidation step, drained transient state. Sevens steps of transient calculations corresponding to 1, 5, 10, 15, 30, 60 and 100 years after tunnel construction are conducted (using Abaqus keyword *SOILS, CONSOLIDATION).

OR

11S. Consolidation step, drained steady state. Steady state analysis is declared by the keyword *SOILS, instead of *SOILS, CONSOLIDATION.

For greenfield analysis, where the building is absent, the building foundation is substituted with Terrace Gravel and Steps 5 & 6 are skipped. The time-scale of consolidation obtained from the greenfield transient analysis (Steps 11T to 17T) can be used to estimate the time needed for consolidation to reach steady state, although transient consolidation analysis with the building present could not be conducted due to convergence problems (more detail deferred to Section 7.3).

3.10 Result processing

When applying the conventional elastic beam assessment (EBA) method, damage categories are commonly assumed to correlate with the magnitude of the maximum tensile

strain estimated to occur in the building (e.g. Mair et al. 1996, Burland 2001). Consistent with this approach, a strain-based damage correlation is employed in the present work, though certain issues require careful consideration as described below.

Firstly, the construction of the building in the finite element analysis induces initial strains in the facades, walls and foundations. In the current study, these initial strains are typically of the order of 10 $\mu\varepsilon$ (microstrain), rising to about 100 $\mu\varepsilon$ around the openings. Since the building construction process adopted in the model is highly simplified, the computed initial strains do not provide a precise representation of the strains actually present in a real building after construction. Moreover, additional post-construction building strains are likely to occur as a consequence of further differential settlements and seasonal effects. It is impractical to include these pre-existing strains directly within a tunnel-soil-building model and so, consistent with the EBA approach, assessments of tunnelling-induced damage are based on the *additional* tensile strains developed in the building facades due to tunnel construction. Since a non-linear constitutive model is employed for the masonry, the strains induced in the building during the simulated construction process will have some influence on the subsequent behaviour, but this influence is not considered in the simulations described in the thesis.

Secondly, when openings for windows and doors exist in the building facades, the computed strains are affected by stress singularities that occur at any internal corners (e.g. Hills & Dini 2011). In practical terms, this means that the maximum value of the computed tensile strain is liable to increase without limit as the mesh is refined around the corners of the openings. Any damage correlation based on the maximum value of the computed tensile strains, $\varepsilon^{\mathrm{t}}_{\mathrm{max}}$, may therefore suffer from undesirable mesh-dependent effects.

A further consideration is that it may not always be appropriate to categorise the damage of a building using a single strain value. A single metric, for example, does not indicate whether the damage is localised or more widely distributed.

As a result, the following means are developed to evaluate the results obtained from finite element analysis. The strain and displacement data relate to the net values

induced by the tunnelling process, while only the contact traction plots show the values obtained before and after tunnelling.

3.10.1 Displacement and strain profile

The values of vertical displacement, horizontal displacement and horizontal strain are extracted at the level of the base of the footing ($z = 1$ m in Fig. 3.2) along the centreline of the footing (on the plane of symmetry in Fig. 3.5). Strains are tension positive.

3.10.2 Contact traction profile

The normal and shear tractions are extracted as nodal contact variables associated with the integration points of the continuum elements of the footing. The nodal data at the interface are extracted along the centreline of the base of the footing. Normal tractions are compression positive; shear tractions are positive when applied to the foundation in the positive x-direction.

3.10.3 Tensile strain field

The computed strains within the 'ghost' elements (Section 3.6.7) provide a direct indication of the tunnelling-induced strains. The tensile strain field (contour plot) provides very detailed information about the magnitude and distribution of computed strain.

It is noted that for the 3D complete building analyses, the facades and walls may experience some out-of-plane bending. The ghost elements are specified to deform with the central plane of the shell elements using Abaqus keyword *TIE, NO THICKNESS. Any strain gradients in the shell elements caused by out-of-plane bending are therefore excluded from the subsequent data processing.

3.10.4 Characteristic strain

In practice, a single metric could be useful for screening a large number of affected buildings. The highly mesh-dependent value of maximum tensile strain, $\varepsilon^{\mathrm{t}}_{\mathrm{max}}$, induced

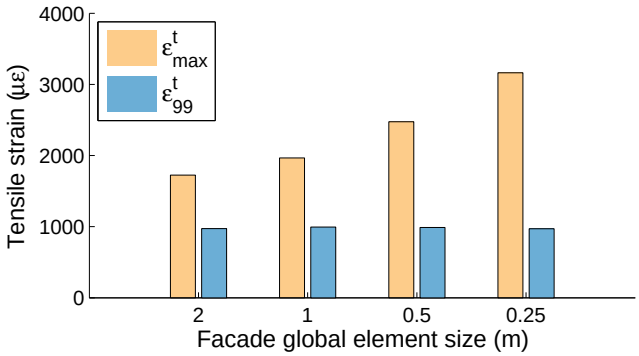


Figure 3.12: Maximum and characteristic tensile strains computed in a facade with openings subject to tunnelling, with varying global element size of the facade mesh. The global element size represents the approximate distances between seeds on all feature edges during the meshing procedure. The facade global element size is 0.5 m in the main calculations

around the internal corners in a facade with openings is addressed via a 'characteristic strain' approach. In this procedure, the severity of the tensile strains in the facade is quantified in terms of a characteristic value of tensile strain that is not exceeded in an area ηA_{facade}, where A_{facade} is the total area of facade being assessed and η is a characteristic proportion. Here the characteristic proportion is arbitrarily chosen to be $\eta = 0.99$ and the corresponding characteristic tensile strain is denoted by $\varepsilon^{\text{t}}_{99}$.

A mesh sensitivity test was conducted with the model TSA-F08O-T1e00 (model specification see Section 6.1) by varying the global element size of the facade mesh. The values of $\varepsilon^{\text{t}}_{\text{max}}$ and $\varepsilon^{\text{t}}_{99}$ computed in these facades are shown in Fig. 3.12. As expected, the value of $\varepsilon^{\text{t}}_{\text{max}}$ increases without convergence as the mesh refines. The $\varepsilon^{\text{t}}_{99}$, which is shown to be insensitive to the element size used for the facade, therefore provides a more reliable means to interpret the results from the finite element analysis of this sort (provided that the mesh is refined to a certain level for accuracy).

3.10.5 Damage bar chart

The damage bar chart is proposed to provide information which is more comprehensive than the characteristic strain and more concise than the strain field. The damage bar chart (which has previously been employed by Truong-Hong & Laefer (2013)) characterises the proportion of the facade area experiencing a particular category of damage. This is done by classifying the area of the facade element corresponded to

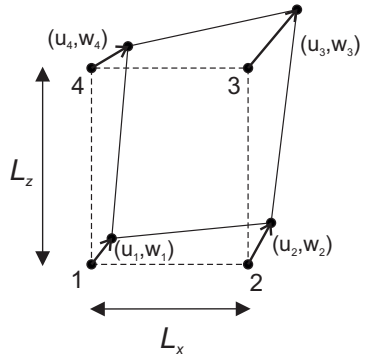


Figure 3.13: A quadrilateral finite element with nodal displacements at the corners, representative of an opening of the facade for quantification of opening distortion

every integration point into the damage category using the tensile strain computed at the integration point. The bar chart indicates whether the high strains, which signify significant damage, are localised or more widely distributed.

3.10.6 Facade opening distortion

Although damage assessment of masonry buildings is usually focused on tensile cracking in the facades and walls, loss of serviceability can also occur to windows (e.g. distortion of the frames could lead to cracks developing in the glazing) and to doors (which may become stuck or otherwise inoperable if significant distortions develop in the frames). Since the sensitivity of doors and windows to tunnelling-induced deformation depends on the nature of the construction, no attempt is made here to suggest serviceability limits for practical assessment purposes. It is, however, straightforward to quantify the distortions that develop in the openings in the facade from the finite element results. This is achieved by treating each opening as a quadrilateral finite element with bilinear interpolation of the nodal displacements at the corners (Fig 3.13), then applying the usual strain-displacement matrix to evaluate the engineering shear strain, γ_{xz}, at the centroid of the opening using the following equation.

$$\gamma_{xz} = \frac{1}{L_z}\left(\frac{u_3+u_4}{2} - \frac{u_1+u_2}{2}\right) + \frac{1}{L_x}\left(\frac{w_2+w_3}{2} - \frac{w_1+w_4}{2}\right) \tag{3.4}$$

where L_x and L_z are the dimensions indicated in Fig. 3.13.

Chapter 4

Extended Mohr-Coulomb (EMC) model for Terrace Gravel

The extended Mohr-Coulomb (EMC) model developed by Doherty & Muir Wood (2013) is selected to represent Terrace Gravel in the current study. The features of the EMC model have been described in Section 3.6.4. The EMC model is implemented in Abaqus via a user-defined material model (UMAT), coded in Fortran. The current implementation is based mainly on the numerical integration scheme described in Sloan et al. (2001) and attempts are made to improve the robustness of the algorithms. This chapter first explores the challenges encountered during implementation. The implemented EMC model is validated through three types of simulations conducted in Doherty & Muir Wood (2013). The model is calibrated to represent the Terrace Gravel in central London with reference to the small-strain stiffness variation used in Jurečič et al. (2013), which was used to characterise the Terrace Gravel found at St James's Park in London.

4.1 Overview of the model

The EMC model uses a Mohr-Coulomb (MC) yield surface, F, described in terms of the current effective stress, $\boldsymbol{\sigma}'$ (in the form of stress invariants p', J and θ, defined in Nomenclature), the mobilised friction angle, ϕ_{y}, and the attraction parameter, a

(Doherty & Muir Wood 2013, Equations 4 and 5). The sign convention adopted in Doherty & Muir Wood (2013) and in the current thesis is tension positive. The equation for F is

$$F(\boldsymbol{\sigma}', a, \phi_{\mathrm{y}}) = (p' - a)\sin\phi_{\mathrm{y}} + JK(\theta, \phi_{\mathrm{y}}) = 0 \tag{4.1}$$

where

$$K(\theta, \phi_{\mathrm{y}}) = \cos\theta - \frac{\sin\theta \sin\phi_{\mathrm{y}}}{\sqrt{3}} \tag{4.2}$$

The current plastic potential, Q, is expressed in terms of $\boldsymbol{\sigma}'$, the constant volume friction angle, ϕ_{cv}, and a (Doherty & Muir Wood 2013, Equation 11):

$$Q(\boldsymbol{\sigma}', a, \phi_{\mathrm{cv}}) = JK(\theta, \phi_{\mathrm{cv}}) - \ln\left(\frac{p' - a}{p'_{\mathrm{r}}}\right)(p' - a)\sin\phi_{\mathrm{cv}} \tag{4.3}$$

where p'_{r} is an undetermined constant. The yield surface and the plastic potential are illustrated in Figs 3.6(a) and 3.6(b).

When hardening is activated, it is represented by an increasing ϕ_{y} (with the limit of the peak friction angle, ϕ_{p}), and fulfils the consistency condition

$$dF = \left(\frac{\partial F}{\partial \boldsymbol{\sigma}'}\right)^{\mathrm{T}} d\boldsymbol{\sigma}' + \frac{\partial F}{\partial \phi_{\mathrm{y}}} d\phi_{\mathrm{y}} = 0 \tag{4.4}$$

where the equation corresponds to $\boldsymbol{\sigma}'$ in the Voigt form. The rate of change of ϕ_{y} with respect to the plastic distortional strain, $\varepsilon_J^{\mathrm{p}}$ (ε_J defined in Nomenclature), is expressed in terms of ϕ_{p}, ϕ_{y} and the hardening parameter β:

$$\frac{\partial \phi_{\mathrm{y}}}{\partial \varepsilon_J^{\mathrm{p}}} = \frac{(\phi_{\mathrm{p}} - \phi_{\mathrm{y}})^2}{\beta \phi_{\mathrm{p}}} \tag{4.5}$$

Since the MC yield surface in principal stress space has non-differentiable singularities at corners and edges, it can be difficult to determine the direction of plastic flow and reach convergence, especially with a non-associated flow rule. Instead of smoothing the yield surface, the gradient of the yield function is rounded when the magnitude of Lode angle is larger than a threshold value, θ_{t}, and the precise form of the MC yield

surface is retained (Appendix 2 in Doherty & Muir Wood (2013)). The gradient of the plastic potential is also rounded in a similar manner.

4.2 Implementation

The model was implemented as a UMAT, using an explicit modified Euler integration scheme with adaptive sub-stepping and error control (Sloan et al. 2001). Modifications to this algorithm were made when numerical difficulties were encountered. Details of the algorithm are described in Sloan et al. (2001) and the elastoplastic equations are presented in Doherty & Muir Wood (2013); therefore the details are not repeated in this thesis. This section focuses on considerations encountered during the implementation that are not discussed in Doherty & Muir Wood (2013) or Sloan et al. (2001). In the UMAT implementation, the Voigt form of stress and strain is adopted.

4.2.1 Consistency in presentation

Table 4.1 provides a mapping between the key parameters and variables used in Sloan et al. (2001) and Doherty & Muir Wood (2013). This chapter mainly follows the notation in Doherty & Muir Wood (2013), except the stiffness matrix is denoted by $\boldsymbol{D}$ and the elastic stiffness matrix by $\boldsymbol{D}^{\mathrm{e}}$. The mobilised friction angle, ϕ_{y}, is the hardening parameter of this model. Although β is named as a hardening parameter in Doherty & Muir Wood (2013), it is in fact a model input constant that determines the rate of hardening.

4.2.2 Overview of the integration scheme

The value of the EMC yield function, F (Equation 4.1), is used to identify the type of stress-strain behaviour. The stress state lies on the yield surface when $F = 0$. In numerical computation, however, the computed value of F is unlikely to be precisely zero even though the stress state is close to the yield surface. A small positive tolerance, FTOL, is therefore used to approximate the yield condition such that the stress state

Table 4.1: Symbols used in Sloan et al. (2001) and Doherty & Muir Wood (2013)

Parameters	Integration scheme	Soil model
	Sloan et al. (2001)	Doherty & Muir Wood (2013)
Hardening parameter	H	ϕ_{y}
Hardening modulus	A	H
Change of hardening parameter	$\dot{H}$	$\delta\phi_{\mathrm{y}}$
Plastic strain multiplier	$\dot{\lambda}$	Λ
Plastic potential	g	Q
Elastic stiffness matrix	$\boldsymbol{D}_{\mathrm{e}}$	$[D]$

is considered to lie on the yield surface when $|F| \leq \mathrm{FTOL}$. Moreover, a yield condition inequality independent of the magnitude of stress is useful for consistency. A dimensionless form of F is obtained by normalising Equation 4.1 by the magnitude of mean stress, $|p'|$. The adopted value of FTOL is 1×10^{-9} in the current implementation.

The role of the UMAT is to compute from the inputs (i.e. the initial stress state, $\boldsymbol{\sigma}'_0$, initial hardening parameter which is the mobilised friction angle, $\phi_{\mathrm{y},0}$, and total strain increment, $\Delta\boldsymbol{\varepsilon}$) to the outputs (i.e. the updated stress state, $\boldsymbol{\sigma}'_{\mathrm{end}}$, updated hardening parameter, $\phi_{\mathrm{y,end}}$, and constitutive matrix, $\boldsymbol{D}_{\mathrm{end}}$). The hardening parameter is defined in the UMAT as a solution-dependent state variable (referred to as STATEV in Abaqus) to be saved and loaded throughout the calculation.

The numerical integration scheme incorporated in the UMAT for the EMC model is summarised in Fig. 4.1. The incremental elastic trial stress, $\Delta\boldsymbol{\sigma}'^{\mathrm{e}}_{\mathrm{tr}} = \boldsymbol{D}^{\mathrm{e}}\Delta\boldsymbol{\varepsilon}$, where the elastic constitutive matrix $\boldsymbol{D}^{\mathrm{e}}$ is constant because linear elasticity is adopted in the EMC model, is first computed. The initial yield function, F_0, and the trial yield function, F_{tr}, (and, if applicable, the angle between the normal to the yield surface and the elastic trial stress) are calculated to determine the stress-strain behaviours. The possible cases corresponding to a particular $\Delta\boldsymbol{\sigma}'^{\mathrm{e}}_{\mathrm{tr}}$ are illustrated schematically in Fig. 4.2.

In all cases shown in Fig. 4.2, the strain increment can be described by the sum of an elastic and a plastic proportion, i.e. $\Delta\boldsymbol{\varepsilon} = \Delta\boldsymbol{\varepsilon}^{\mathrm{e}} + \Delta\boldsymbol{\varepsilon}^{\mathrm{p}}$ ($\Delta\boldsymbol{\varepsilon}^{\mathrm{e}}$ or $\Delta\boldsymbol{\varepsilon}^{\mathrm{p}}$ can be zero). The incremental elastic stress associated with $\Delta\boldsymbol{\varepsilon}^{\mathrm{e}}$ is updated by simple calculation using

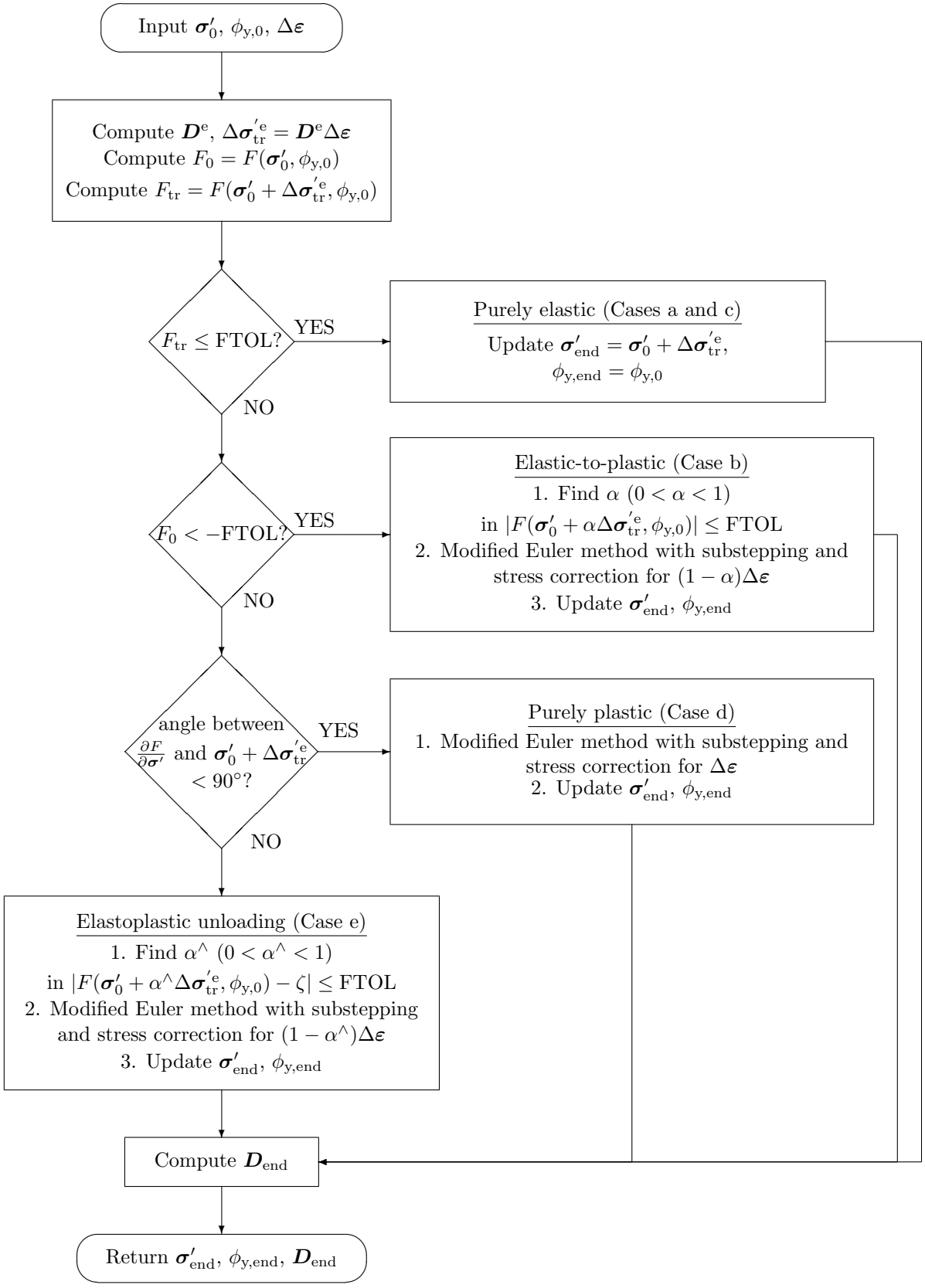


Figure 4.1: Stress update algorithm adopted in the UMAT for the EMC model

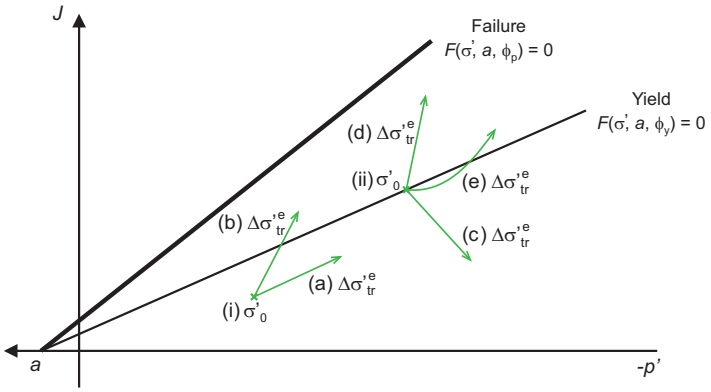


Figure 4.2: Schematic representation of possible cases of an elastic trial stress with respect to the current yield surface: (i) initial stress within yield surface; (a) purely elastic; (b) elastic-to-plastic; (ii) initial stress on yield surface (c) purely elastic; (d) purely plastic; (e) elastoplastic unloading

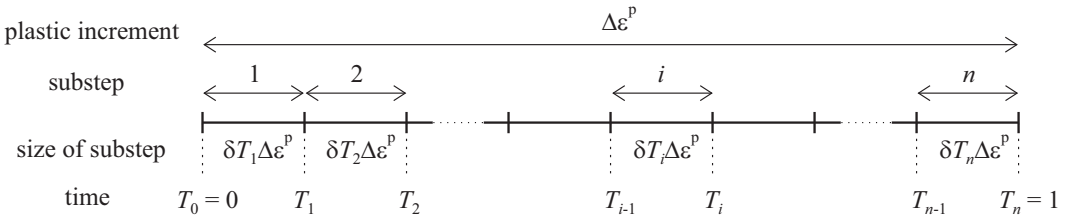


Figure 4.3: Nomenclature of substepping of the plastic strain increment employed in the EMC model implementation

Hooke's law since linear elasticity is adopted in the model, and ϕ_{y} remains unchanged. The changes in stress and hardening parameter corresponding to $\Delta\boldsymbol{\varepsilon}^{\mathrm{p}}$ are determined by integrating the constitutive relations numerically.

In the current implementation, substepping is implemented to divide the plastic strain increment into smaller increments called 'substeps' (represented by $\delta T_i \Delta\boldsymbol{\varepsilon}^{\mathrm{p}}$ at substep i), as illustrated in Fig. 4.3, to achieve an accurate integral. The plastic strain increment is associated with a pseudo time T and numerical integration takes place from $T = 0$ to $T = 1$. The stress increment at each substep is computed using the explicit modified Euler method, where the reliability is assessed by comparing the relative error of the explicit modified Euler method and the forward Euler method, R, to a tolerance, STOL. If $R >$ STOL, then the substep is repeated with a reduced size (bounded by $\delta T_{\min} \Delta\boldsymbol{\varepsilon}^{\mathrm{p}}$). For each accepted substep i, if the updated stress state does not satisfy the yield condition (i.e. $|F(\boldsymbol{\sigma}'_i, \phi_{\mathrm{y},i})| >$ FTOL), a stress and hardening parameter correction procedure takes place before the next substep.

4.2.3 Challenges and modifications

4.2.3.1 Yield surface intersection

To identify the purely elastic section of the strain increment in the elastoplastic case (Case b in Fig. 4.2), the yield surface intersection is determined by finding $\Delta\boldsymbol{\varepsilon}^{\mathrm{e}} = \alpha\Delta\boldsymbol{\varepsilon}$ (where $0 < \alpha < 1$), such that $|F(\boldsymbol{\sigma}'_0 + \alpha\boldsymbol{D}^{\mathrm{e}}\Delta\boldsymbol{\varepsilon}, \phi_{\mathrm{y},0})| \leq \mathrm{FTOL}$. Since linear elasticity is adopted in the model, this is equivalent to finding α in $|F(\boldsymbol{\sigma}'_0 + \alpha\Delta\boldsymbol{\sigma}'^{\mathrm{e}}_{\mathrm{tr}}, \phi_{\mathrm{y},0})| \leq \mathrm{FTOL}$.

In Sloan et al. (2001), the 'Pegasus intersection scheme' is adopted to obtain α. The Pegasus scheme is also known as the regula falsi (or false position) method. This method usually serves well for continuous functions but sometimes fails to converge at a useful rate. In Sloan et al. (2001), a maximum number of iterations is set to avoid excessive computation. However, the program in Sloan et al. (2001) is suggested to stop and exit if a converged α is not found after the maximum number of iterations is reached.

Alternative solutions are developed to achieve a more robust approach. It is recognised that the adopted yield function of the EMC model is continuous, but sometimes small oscillations occur because of the trigonometric functions and numerical round-off error. Singularities exist at the corners of the hexagonal yield surface in the deviatoric plane (at Lode angle $\theta = \pm 30^{\circ}$) and at the apex. An example of oscillation near the corner is illustrated in Fig. 4.4, which shows $F(\boldsymbol{\sigma}'_0 + \alpha\Delta\boldsymbol{\sigma}'^{\mathrm{e}}_{\mathrm{tr}}, \phi_{\mathrm{y},0})$ for $0 \leq \alpha \leq 1$ extracted from a Gauss point. When convergence is not achieved after the maximum number of iterations, the regula falsi method cannot deduce how close the current guess of α is from the real root. In the current implementation, the bisection method is adopted as a stable root-finding algorithm (to replace the regula falsi method), with initial guesses of $\alpha = 0$ and 1, to ensure that α is close to the real root with certain confidence. For example, after 15 iterations of bisection, the interval is reduced by $2^{15} = 32768$ times. In the case of slow convergence and the maximum number of iterations has reached, the final guess of α from the bisection method is returned as a root to continue the program.

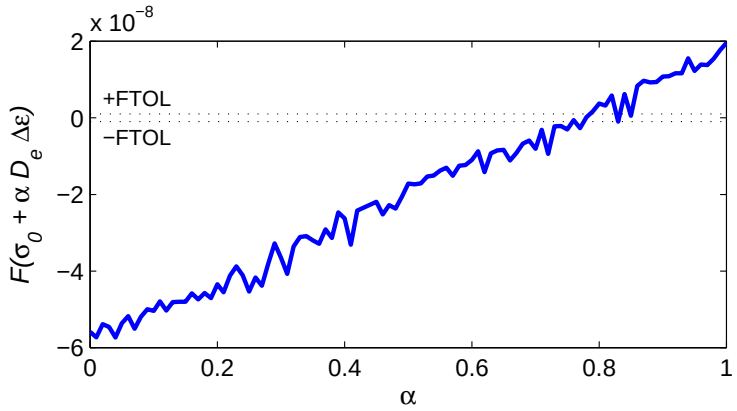
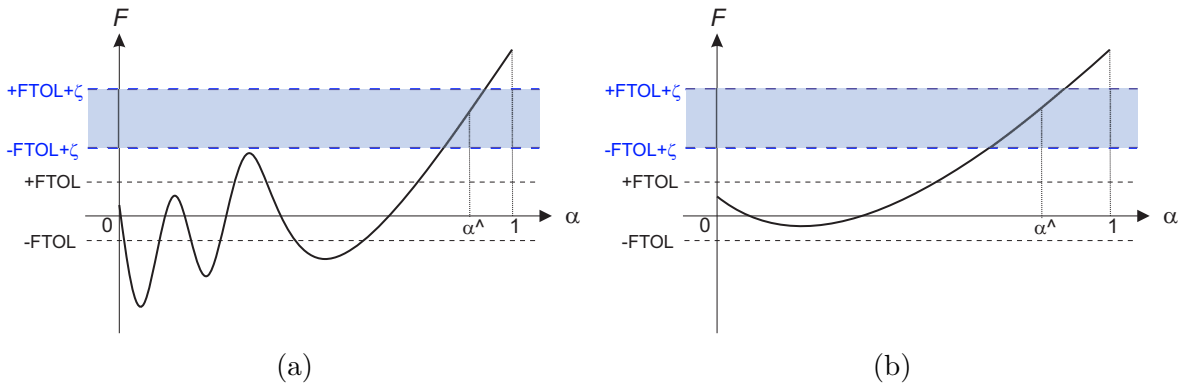


Figure 4.4: An example of the oscillating behaviour of the yield function, F, of the EMC model with α from 0 to 1

4.2.3.2 Elastoplastic unloading

The possible case of plastic-to-elastic-to-plastic transition for a stress state initially on the yield surface (Case e in Fig. 4.2) is termed 'elastoplastic unloading' in Sloan et al. (2001). The stress state, initially $|F(\boldsymbol{\sigma}'_0, \phi_{\mathrm{y},0})| \leq \mathrm{FTOL}$, is subject to a stress increment consisting of an elastic part passing inside the yield surface and then an elastoplastic part where its elastic trial stress lies outside the yield surface. The algorithm in Sloan et al. (2001) first identifies this case by the angle between the yield surface gradient and the elastic trial stress being greater than a right angle. Then, the method in Sloan et al. (2001) attempts to reduce it to a simple elastic-to-plastic transition by bracketing the second crossing of the yield surface. The bracket is represented by a stress state inside the yield surface with an α^{e} ($0 < \alpha^{\mathrm{e}} < 1$) such that $F(\boldsymbol{\sigma}'_0 + \alpha^{\mathrm{e}}\Delta\boldsymbol{\sigma}'^{\mathrm{e}}_{\mathrm{tr}}, \phi_{\mathrm{y},0}) < -\mathrm{FTOL}$ and the elastic trial stress where $F(\boldsymbol{\sigma}'_0 + \Delta\boldsymbol{\sigma}'^{\mathrm{e}}_{\mathrm{tr}}, \phi_{\mathrm{y},0}) > \mathrm{FTOL}$. The yield surface intersection, α ($\alpha^{\mathrm{e}} < \alpha < 1$), is then obtained using a root-finding algorithm. However, bracketing the crossing may not work when there are multiple roots (e.g. as a result of oscillations of the yield function near the corners and the apex) or where there is no elastic portion (e.g. the stress state only passes inside the region of ±FTOL before the elastic trial stress lies outside the yield surface).

A modification is developed based on the presumption that the strain increment is small enough to ignore an even smaller increment for unloading and any significant unloading should have been captured in the case of 'purely elastic'. Instead of detecting



(a) (b)

Figure 4.5: Illustration of the suggested method in addressing special scenarios in elastoplastic unloading: (a) multiple roots (e.g. oscillations); (b) no elastic portion

the crossing at α^{e}, a root-finding algorithm is applied to a function offset by ζ (where $\zeta = 10^{-8}$ in the current implementation) from the current yield surface, i.e. to find $\alpha^{\wedge}$ ($0 < \alpha^{\wedge} < 1$) satisfying $|F(\boldsymbol{\sigma}_0 + \alpha^{\wedge}\Delta\boldsymbol{\sigma}'^{\mathrm{e}}_{\mathrm{tr}}, \phi_{\mathrm{y}}) - \zeta| \leq \mathrm{FTOL}$, and the portion of the strain increment beyond $\alpha^{\wedge}$ is treated as plastic. Fig. 4.5 illustrates the suggested method in the two special cases symbolically, with $\alpha^{\wedge}$ being any point intersecting the yield function inside the blue shade. In the case of multiple roots (Fig. 4.5(a)), insignificant oscillations of the value of F are ignored using this method; and a root can be sought when there is no elastic portion (Fig. 4.5(b)). In both cases, the offset from the yield surface, ζ, is eliminated in the stress correction process during numerical integration.

4.2.3.3 Numerical integration at non-differentiable singularities

To retain the soil behaviour described by the Mohr-Coulomb (MC) model, the EMC model uses the precise form of the MC yield function. There are non-differentiable singularities of the MC yield surface at Lode angles $\theta = \pm 30°$ in the deviatoric plane and at the apex. The EMC model in Doherty & Muir Wood (2013) addresses the first case by rounding the gradient of yield function and the gradient of the plastic potential using the approximation formulated in Sloan & Booker (1986) when the Lode angle $|\theta| > \theta_{\mathrm{t}}$, where θ_{t} is a constant indicating the threshold of rounding ($\theta_{\mathrm{t}} = 25°$ in Doherty & Muir Wood (2013)). However, no special treatment is mentioned for the apex of the yield surface. As a consequence, when the stress state is at the apex and there is a plastic strain increment, the integration scheme using the modified explicit

Euler method, which requires derivatives, cannot advance.

A solution to this issue is developed based on the concept that the modified explicit Euler method can proceed if the stress state is moved away from the singularity. When the numerical integration starts at the apex, a small portion of the substep, $\chi\delta T_i\Delta\varepsilon^{\mathrm{p}}$ $(0 < \chi < 1)$, is assumed to be elastic and the remaining of the substep then continues with the modified explicit Euler scheme with stress correction procedure. In the current implementation, $\chi = 0.1$ is adopted.

Separate attempts were made to consider transition of gradients while approaching the apex. The hyperbolic rounding of the yield surface described in Abbo (1997) was incorporated and tested; however, the computation time significantly increased. Therefore, hyperbolic rounding was not adopted in the current implementation.

4.2.3.4 Stress and hardening parameter correction

At the end of accepted substep i, if the updated stress and hardening state deviates from the yield surface (i.e. $|F(\boldsymbol{\sigma}'_i, \phi_{\mathrm{y},i})| >$ FTOL), it is corrected back to the yield surface (Sloan et al. 2001). Sloan's approach is based on iterative multi-variable ($\boldsymbol{\sigma}'$ and ϕ_{y}) Newton's method. Within an iteration, if the corrected state is not closer to the yield surface than the uncorrected one, a second attempt at using Newton's method but assuming constant ϕ_{y} is conducted instead. If no solution is found after the maximum number of iterations, the program stops in Sloan et al. (2001). The second attempt with Newton's method in the above approach is suggested to solve the non-convergence problem near the singularity of the yield surface. However, two convergence issues were still observed in the current EMC model — slow convergence (the sign of F alternates but the magnitude of F reduces at a slow rate) and overshooting corrected values (the sign of F remains positive but with no converging pattern on its magnitude). The latter behaviour was observed to occur for tensile stresses and stresses near the apex of the yield surface; rotation of principal axes is deduced as a result of the stress correction.

Methods are developed to extend the original correction scheme after the maximum number of iterations is reached, to deal with the above cases. The first case is addressed

by applying a multi-variable root-finding algorithm with the uncorrected stress and hardening state and the last estimate of corrected state that is located on the opposite side of the yield surface. This assumes, if there are two states (denoted by subscripts a and b) where $F(\boldsymbol{\sigma}'_{\mathrm{a}}, \phi_{\mathrm{y,a}}) < -\mathrm{FTOL}$ and $F(\boldsymbol{\sigma}'_{\mathrm{b}}, \phi_{\mathrm{y,b}}) > \mathrm{FTOL}$, then there exists an η $(0 < \eta < 1)$ such that $|F\big(\boldsymbol{\sigma}'_{\mathrm{a}} + \eta(\boldsymbol{\sigma}'_{\mathrm{b}} - \boldsymbol{\sigma}'_{\mathrm{a}}), \phi_{\mathrm{y,a}} + \eta(\phi_{\mathrm{y,b}} - \phi_{\mathrm{y,a}})\big)| \leq \mathrm{FTOL}$. For the second scenario which is observed near the apex, as a last resort, the stress is corrected to the apex and ϕ_{y} remains unchanged.

4.2.3.5 Numerical integration at the minimum size of substep

It is possible that even when the size of a substep reduces to the prescribed minimum value, $\delta T_{\min}$, the integrated stresses and hardening parameter will still fail the relative error check. According to the scheme in Sloan et al. (2001), the program will then enter an infinite while-loop and will not advance. In the current algorithm, once the time step reduces to $\delta T_{\min}$, the integrated stresses and hardening parameter are accepted without other conditions and the calculation proceeds to the stress correction procedure. The value of $\delta T_{\min}$ is taken as 1×10^{-5} in the current implementation.

4.2.3.6 Constitutive matrix

The tangent constitutive matrix (denoted by DDSDDE in Abaqus and $\boldsymbol{D}_{\mathrm{end}}$ in Fig. 4.1) is required in the UMAT to be returned to Abaqus. When the material behaves elastically, $\boldsymbol{D}_{\mathrm{end}}$ is equal to the elastic constitutive matrix, $\boldsymbol{D}^{\mathrm{e}}$. When the yield surface is active, the elastoplastic constitutive matrix, $\boldsymbol{D}^{\mathrm{ep}}$, is used. Since the apex in this model is on the hydrostatic axis, $\boldsymbol{D}^{\mathrm{ep}}$ corresponding to the stress at the apex is singular with respect to any direction of the general stress space (Clausen et al. 2007). Therefore $\boldsymbol{D}_{\mathrm{end}} = \boldsymbol{0}$ when the updated stress $\boldsymbol{\sigma}'_{\mathrm{end}}$ is at the apex.

$$\boldsymbol{D}_{\mathrm{end}} = \begin{cases} \boldsymbol{D}^{\mathrm{e}} & \text{when elastic} \\ \boldsymbol{D}^{\mathrm{ep}} = \boldsymbol{D}^{\mathrm{e}} - \dfrac{\boldsymbol{D}^{\mathrm{e}} \frac{\partial Q}{\partial \boldsymbol{\sigma}'} \frac{\partial F}{\partial \boldsymbol{\sigma}'}^{\mathrm{T}} \boldsymbol{D}^{\mathrm{e}}}{\frac{\partial F}{\partial \boldsymbol{\sigma}'}^{\mathrm{T}} \boldsymbol{D}^{\mathrm{e}} \frac{\partial Q}{\partial \boldsymbol{\sigma}'} + H} & \text{when yield, except } \boldsymbol{\sigma}'_{\mathrm{end}} \text{ is at apex} \\ \boldsymbol{0} & \text{when } \boldsymbol{\sigma}'_{\mathrm{end}} \text{ is at apex} \end{cases} \tag{4.6}$$

4.2.4 Additional considerations

4.2.4.1 Error check for each substep

According to Sloan et al. (2001), the relative error between the modified Euler increment and the forward Euler increment (which is computed as part of the modified Euler increment), R, is compared with a tolerance STOL to decide whether the substep solution can be accepted. The relative error is also used to determine the ratio of the size of the next substep to the current one, $q = q(R, \text{STOL}) = \delta T_{i+1}/\delta T_i$ (Sloan et al. 2001, Equations 25 and 27). However, a stress correction procedure follows when the accepted stress state deviates from the yield surface. In this situation, the corrected state and R are no longer related. Moreover, there is no guarantee on the claimed relation in Sloan et al. (2001) between successive local truncation relative errors, $R_{i+1} \approx q^2 R_i$. It is also noted that the stated error bound of the Euler method $O(\delta T^2)$ refers to local truncation absolute error, which has no implication on the successive local truncation relative error up to the current stress state.

4.2.4.2 Initialisation of the size of the yield surface

The size of the yield surface relates to the mobilised friction angle, ϕ_y. The initial size of the yield surface, denoted by ϕ_y^0, is prescribed in the model as an initial condition. If the initial stress $\boldsymbol{\sigma}'_0$ is intended to lie on the yield surface at the start of a simulation, the initial mobilised friction angle, $\phi_{\text{y},0}$, can be determined through the relationship $F(\boldsymbol{\sigma}'_0, \phi_{\text{y},0}) = 0$. However, to establish a more realistic stiffness variation at small strain, ϕ_y^0 is suggested to be set greater than $\phi_{\text{y},0}$ by an arbitrary factor, f, such that $\phi_\text{y}^0 = f\phi_{\text{y},0}$ (Doherty & Muir Wood 2013), as illustrated in Fig. 4.6. A value $f = 1.05 - 1.10$ is recommended in Doherty & Muir Wood (2013). An additional constraint $\phi_\text{y}^0 \leq \phi_\text{p}$ is imposed in the current implementation to ensure that the initial size of the yield surface is bounded by the failure surface, which is represented by ϕ_p.

4.2.4.3 Typographical errors in Doherty & Muir Wood (2013)

There are some typographical errors in the original publication as described below.

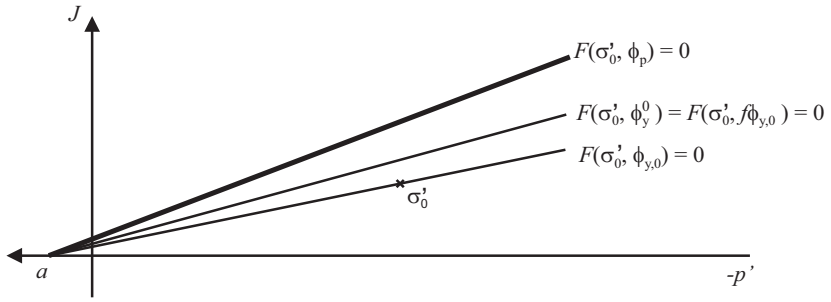


Figure 4.6: Illustration of the yield surfaces corresponding to the initial size, ϕ_{y}^{0}, and the initial mobilised friction angle, $\phi_{\mathrm{y},0}$, when the initial stress $\boldsymbol{\sigma}_0'$ is intended to lie on the yield surface at the start of a simulation

Firstly, the power index in Equation 20 in Doherty & Muir Wood (2013) is missing. The correct equation for Lode angle is

$$\theta = \frac{1}{3}\sin^{-1}\left(\frac{-3\sqrt{3}J_3}{2J^3}\right) \tag{4.7}$$

where J_3 is the third invariant of the deviatoric stress tensor.

Secondly, there is an error in the fraction in the first term of Equation 26c in Doherty & Muir Wood (2013). The equations, in Voigt form, should be corrected as

$$\left\{\frac{\delta J_3}{\delta \boldsymbol{\sigma}}\right\} = \frac{1}{J^2}\begin{Bmatrix} s_y s_z - \tau_{yz}^2 \\ s_x s_z - \tau_{zx}^2 \\ s_x s_y - \tau_{xy}^2 \\ 2(\tau_{yz}\tau_{zx} - s_z\tau_{xy}) \\ 2(\tau_{zx}\tau_{xy} - s_x\tau_{yz}) \\ 2(\tau_{xy}\tau_{yz} - s_y\tau_{zx}) \end{Bmatrix} + \frac{1}{3}\begin{Bmatrix} 1 \\ 1 \\ 1 \\ 0 \\ 0 \\ 0 \end{Bmatrix} \tag{4.8}$$

Separately, the terms related to C_3 and $\{\frac{\delta J_3}{\delta \boldsymbol{\sigma}}\}$ in Doherty & Muir Wood (2013) and here are not the direct results obtained from partial differentiation. The paper does not mention that the terms (e.g. in Equations 25, 26c and 32 of Doherty & Muir Wood (2013)) are grouped intentionally so that J always divides quantities of similar magnitude and hence the loss of numerical accuracy is minimised as J approaches zero. The same strategy is used in Abbo (1997).

Thirdly, there is an error in Equation 41 in Doherty & Muir Wood (2013). The

correct version is

$$\left\{\frac{\delta Q}{\delta \theta}\right\} = -J\left(\sin\theta + \frac{\cos\theta \sin\phi_{\mathrm{cv}}}{\sqrt{3}}\right) \tag{4.9}$$

4.3 Validation

Three sets of simulations described in Doherty & Muir Wood (2013) were repeated to validate the UMAT implementation of the EMC model, as described below.

4.3.1 Reduction to elastic, perfectly plastic Mohr-Coulomb

The EMC model can be reduced to the elastic, perfectly plastic Mohr-Coulomb (MC) model with zero dilation angle by setting $\phi_{\mathrm{y}} = \phi_{\mathrm{cv}} = \phi_{\mathrm{p}}$. This enables a comparison between the implemented UMAT, the built-in MC model in Abaqus and the implementation by Doherty & Muir Wood (2013), via the load-displacement response of a footing loading problem as described in Doherty & Muir Wood (2013). A circular footing with radius of 0.378 m, thickness of 1.1 m and embedment of 1 m is modelled as a linear elastic material using eight-noded axisymmetric elements with reduced integration (Abaqus code CAX8R) in the current work. The mesh is shown in Fig. 4.7 (comparable to the mesh in Doherty & Muir Wood (2013, Fig. 7)). An additional 0.1 m above the ground surface is added to the intended footing thickness of 1 m to enhance stability, following the mesh shown in Doherty & Muir Wood (2013) however the magnitude of the additional thickness is not stated. The model parameters for the elastic footing and the EMC model for the soil are shown in Table 4.2. The same elastic parameters and the MC parameters $\phi = 32°$, $\psi = 0.1°$ (minimum dilation angle allowed in Abaqus) and $c' = a\tan\phi_{\mathrm{y}} \approx 2.5$ kPa are used in the Abaqus built-in MC model. The interface between the base of the footing and the soil is modelled with a rough surface, while the interface along the side of the footing is assumed frictionless.

Fig. 4.8 shows the load-displacement response of the footing. In general, there is a good agreement among the models, particularly at small displacement. The data extracted from Doherty & Muir Wood (2013) is intermediate between the two current

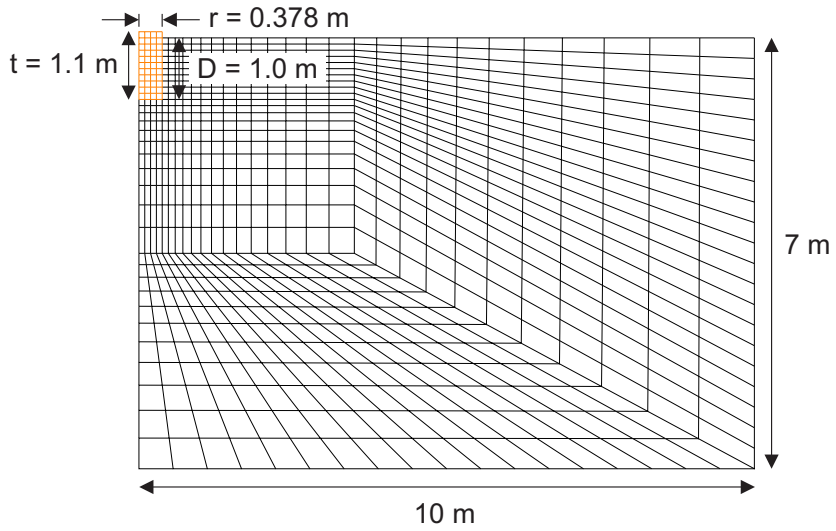


Figure 4.7: Dimensions and mesh adopted in the footing loading problem for the analysis of reducing the EMC model to elastic, perfectly plastic Mohr-Columb model. The footing is highlighted in orange. (This mesh is also used for Footing 4 in Section 4.3.3)

Table 4.2: EMC model parameters for the soil and linear elastic model parameters for the footing in the elastic, perfectly plastic Mohr-Coulumb analysis

Parameter		Value	
		Soil	Footing
Young's modulus	E	80 MPa	30 GPa
Poisson's ratio	ν	0.2	0.2
Unit weight	γ	18 kN/m^3	24 kN/m^3
Lateral stress coefficient	K_0	0.43	-
Peak friction angle	ϕ_{p}	32°	-
Constant volume friction angle	ϕ_{cv}	32°	-
Attraction	a	4 kPa	-
Hardening parameter	β	n/a	-
Initial mobilised friction angle	$\phi_{\mathrm{y},0}$	32°	-
Initial size of yield surface	ϕ_{y}^0	32°	-

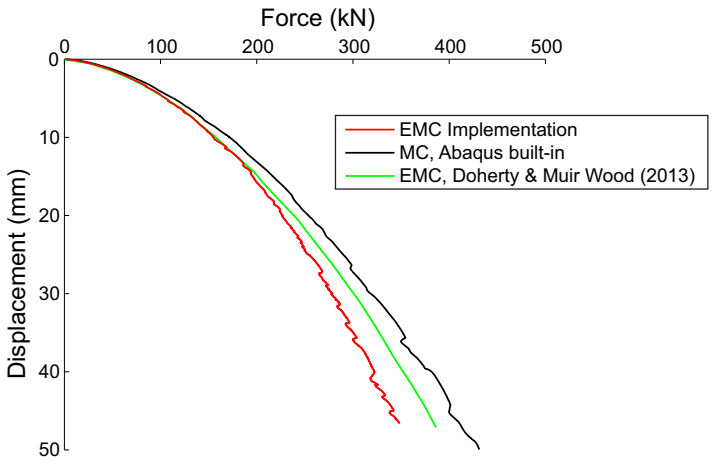


Figure 4.8: Performance of the implemented EMC model, the Abaqus built-in model and the EMC model in Doherty & Muir Wood (2013) in the footing loading problem. Each model is set to behave as an elastic, perfectly plastic Mohr-Coulomb material with zero dilation.

simulations. The EMC model and the Abaqus built-in MC model adopt different plastic potential functions and different rounding approaches. In the Abaqus built-in MC model the flow potential is represented by a hyperbolic function in the meridional stress plane and the smooth elliptic function proposed by Menétrey & Willam (1995) in the deviatoric stress plane, while the plastic potential of the EMC model is derived from the original Cam Clay plastic potential and the gradients of the yield surface and plastic potential are only rounded for Lode angles close to $\pm 30°$ using the technique in Sloan & Booker (1986). Considering this, the discrepancy of the perfectly plastic behaviours is reasonable. The difference in the current implementation of the EMC model and the one in Doherty & Muir Wood (2013) might be due to the differences in the implementation technique as described in Section 4.2.

4.3.2 Triaxial test simulations

Consolidated drained triaxial compression tests are conducted for two soil profiles (denoted by Test 1 and Test 2) described in Doherty & Muir Wood (2013, Table 3). The results are compared with the numerical data from Doherty & Muir Wood (2013, Figs 10-12).

In the current work, these simulations are modelled with one 8-node linear hexahedral element (Abaqus code C3D8), with one vertex being fixed and the three planes

Table 4.3: Loading and EMC model parameters used in the triaxial test simulations

Parameter		Value	
		Test 1	Test 2
Initial axial stress	σ'_{a}	100 kPa	300 kPa
Initial radial stress	σ'_{r}	50 kPa	150 kPa
Initial shear modulus	G_0	125 MPa	208 MPa
Poisson's ratio	ν	0.2	
Peak friction angle	ϕ_{p}	32°	
Constant volume friction angle	ϕ_{cv}	36°	
Attraction	a	2.2 kPa	0 kPa
Hardening parameter	β	0.0015	
Initial mobilised friction angle	$\phi_{\mathrm{y},0}$	18.9°	19.5°
Initial size of yield surface*	ϕ_{y}^0	18.9°/20.0°	19.5°/20.7°

* Two values of ϕ_{y}^0 correspond to $f = 1$ and $f = 1.06$ with respect to $\phi_{\mathrm{y}}^0 = f\phi_{\mathrm{y},0}$

connecting the fixed vertex being supported by roller boundary conditions. The initial loading conditions and model parameters for Test 1 and Test 2 are listed in Table 4.3. The initial mobilised friction angles are $\phi_{\mathrm{y},0} = 18.9°$ and 19.5° for Test 1 and Test 2 respectively, which correspond to the initial stress state lying on the initial yield surface. The initial size of yield surface is set to equal to the initial mobilised friction angle (i.e. $f = 1$ in $\phi_{\mathrm{y}}^0 = f\phi_{\mathrm{y},0}$). To demonstrate the significance of the arbitrary increase in the initial size of yield surface in elastic-elastoplastic transition in this case, another set of simulations with $f = 1.06$ in $\phi_{\mathrm{y}}^0 = f\phi_{\mathrm{y},0}$ is conducted, following Doherty & Muir Wood (2013). That is, $\phi_{\mathrm{y}}^0 = 20.0°$ in Test 1 and $\phi_{\mathrm{y}}^0 = 20.7°$ in Test 2. The values of attraction, a, are obtained by back calculation from $F(\boldsymbol{\sigma}'_0, \phi_{\mathrm{y},0}) = 0$.

The measurement of strain can sometimes be unclear. The stress path of a triaxial compression test (path (1)+(2)) is illustrated in Fig. 4.9 and two reference points of zero strain are considered to be possible: (i) strain is measured after isotropic confining stress is applied in all directions; (ii) strain is reset after both the initial radial and axial stresses are established. Back-analysis reveals that procedure (ii) was the one adopted in Doherty & Muir Wood (2013). Therefore, the current plots refer to the same strain reference point (ii). Owing to elasticity, path (3) and path (1)+(2) in Fig. 4.9 result in the same stress state at (ii). In the current simulation, therefore, the initial axial and radial stresses, σ'_{a} and σ'_{r}, are established in a single geostatic step. The subsequent

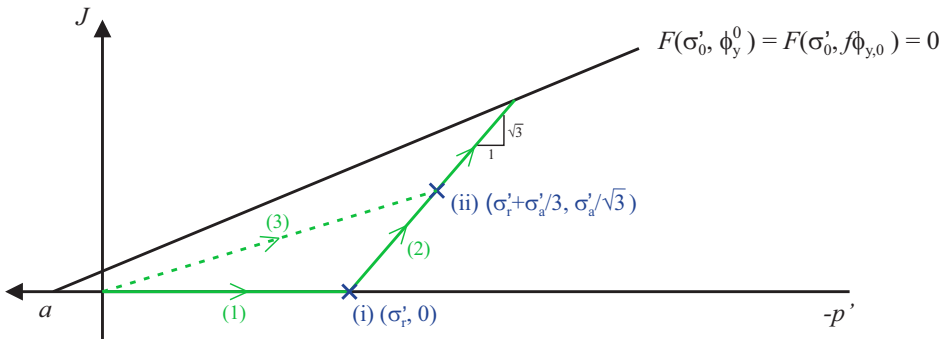


Figure 4.9: Stress path of triaxial test in $p' - J$ plane: (i) after isotropic confining stress is applied; (ii) after both the initial radial stress and initial axial stress are established

axial loading is applied by prescribing displacement boundary conditions.

Figs 4.10, 4.11 and 4.12 compare the results obtained from the current EMC implementation with the corresponding results from Doherty & Muir Wood (2013, Figs. 10, 11 and 12). Fig. 4.10 exhibits a nearly identical hardening response in terms of the ratio of $\phi_{\mathrm{y}}/\phi_{\mathrm{p}}$ against the distortional strain, ε_J, between the two implementations. Fig. 4.11 shows the degradation of secant shear modulus, G_{sec}, with ε_J and the response with different values of the initial size of yield surface, demonstrating that the arbitrary increase in ϕ_{y}^0 facilitates a realistic representation of small-strain stiffness degradation. For clarity, the secant shear modulus, G_{sec}, is obtained using the following equations.

$$G_{\mathrm{sec}} = \frac{q}{3\varepsilon_q} = \frac{J}{\varepsilon_J} = \frac{\sigma'_{\mathrm{a}} - \sigma'_{\mathrm{r}}}{2(\varepsilon_{\mathrm{a}} - \varepsilon_{\mathrm{r}})} \tag{4.10}$$

Fig. 4.11(a) indicates well matching small-strain behaviours between the two implementations for both values of ϕ_{y}^0 in Test 1. However, for Test 2, the computed results (blue line in Fig. 4.11(b)) appear to have shifted to the right compared to the published data (green line in Fig. 4.11(b)). It is suspected that there might be a misprint in the magnitude of the ε_J-axis in Fig. 11(b) of Doherty & Muir Wood (2013). Since the value of ε_J corresponding to the trigger of hardening (denoted by $\varepsilon_{J,\mathrm{t}}$) under triaxial conditions can be calculated using Mohr's circle and Hooke's law, $\varepsilon_{J,\mathrm{t}}$ of Test 2 should not be smaller than that of Test 1 (see Appendix A at the end of this chapter). A potential factor of 10 is applied to the ε_J values of Doherty & Muir Wood (2013, Fig. 11(b)) in the current Fig. 4.11(b) (indicated as 'factored' with magenta lines in Fig. 4.11(b)),

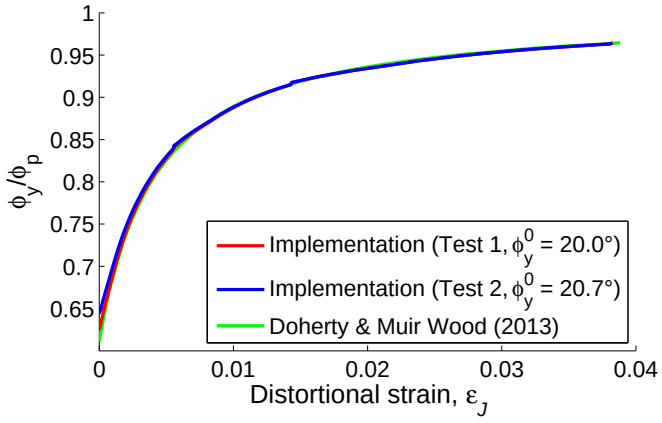


Figure 4.10: Comparison of the EMC model implementation in triaxial test simulations: normalised mobilised friction angle varying with distortional strain

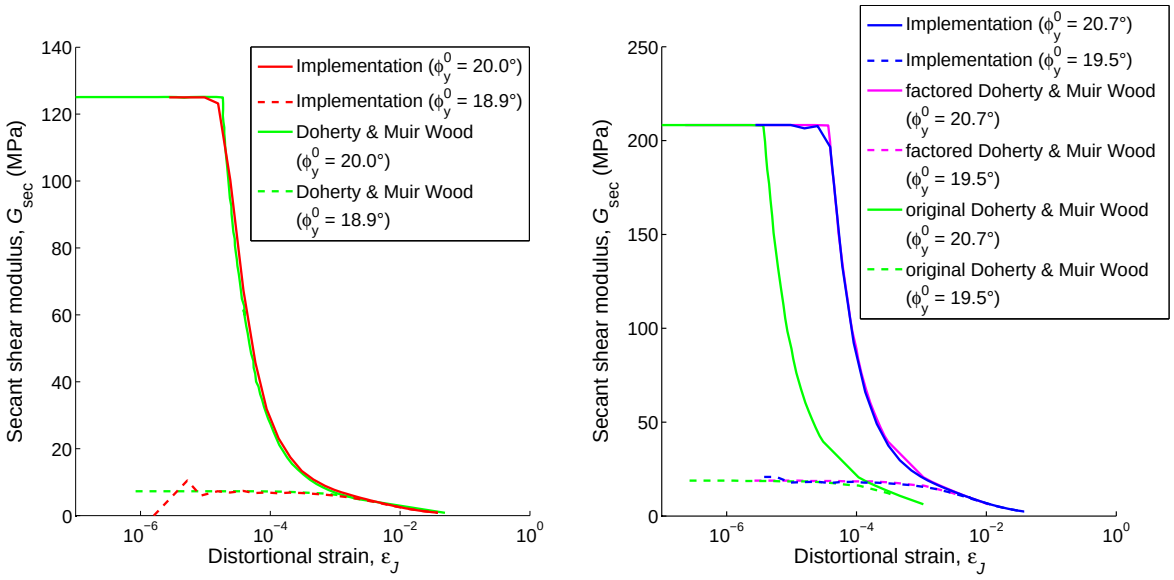
resulting in a more reasonable agreement and more consistent comparison with other figures that also involve the ε_J-axis.

Fig. 4.12(a) shows the distortional stress-strain response and the response with different ϕ_y^0 values. There is a close match between the two implementations (the values on the ε_J-axis are not factored). Fig. 4.12(b) displays the volumetric response (the values on the ε_J-axis are not factored). It is noted that the new implementation leads to greater contraction than that indicated in the results of Doherty & Muir Wood (2013).

It is clear from Fig. 4.11 that the stiffness variation at small strain is dependent on the factor f in $\phi_y^0 = f\phi_{y,0}$, but Fig. 4.12(a) supports the conclusion that the overall stress-strain response is insensitive to f. In general, the good agreement of the EMC response in the triaxial tests with the data in Doherty & Muir Wood (2013) provides confidence in the new implementation.

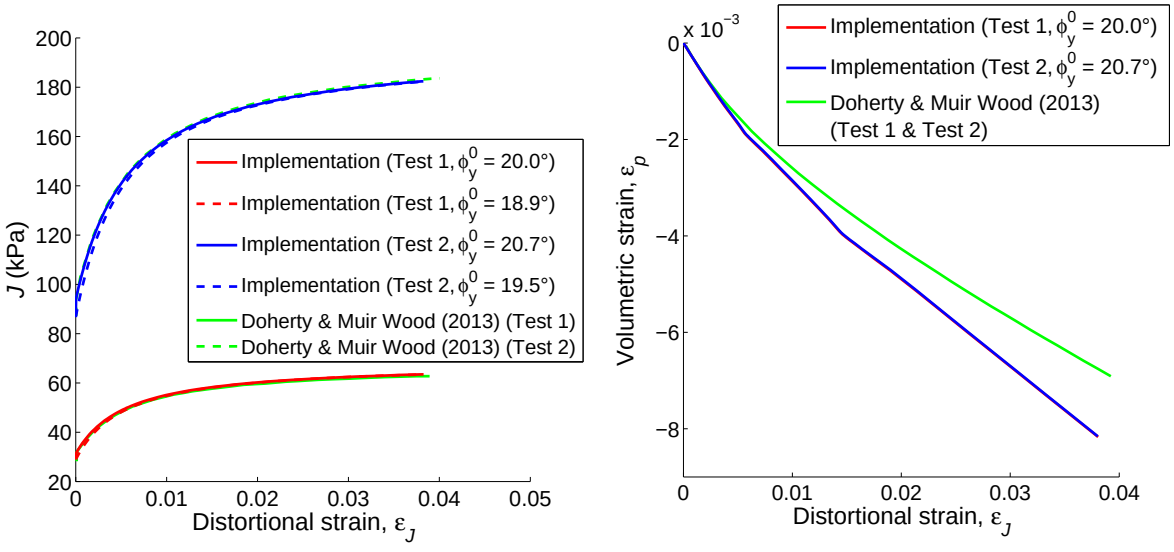
4.3.3 Footing test simulations

Further footing loading analyses are conducted with the addition of soil hardening features, for two soil profiles and four footing configurations. The four square footings with dimensions described in Doherty & Muir Wood (2013, Table 2) are modelled as circular footings with equivalent bearing areas, following Doherty & Muir Wood (2013). The modelled footing configurations are listed in Table 4.4 (the thickness is



(a) (b)

Figure 4.11: Comparison of the EMC model implementation in triaxial test simulations, showing secant shear modulus against distortional strain with different ϕ_y^0 values: (a) Test 1 ($\phi_{y,0} = 18.9°$); (b) Test 2 ($\phi_{y,0} = 19.5°$). 'factored' refers to the extracted data from Doherty & Muir Wood (2013) with the ε_J values multiplied by a factor of 10



(a) (b)

Figure 4.12: Comparison of the EMC model implementation in triaxial test simulations: (a) distortional stress-strain response with different ϕ_y^0 values; (b) volumetric response

Table 4.4: Footing geometrical details in the footing test simulations

Footing	Embedment depth, D: m	Thickness, t: m	Equivalent radius, r: m
1	1.0	1.1	0.846
2	1.0	1.1	0.564
3	0.5	0.6	0.564
4	1.0	1.1	0.378

Table 4.5: EMC model parameters for the soil in the footing test simulations

Parameter		Value	
		Soil profile 1	Soil profile 2
Initial shear modulus	G	$G = (\frac{\lambda z+\beta_1}{\beta_2})^m G_0^{\text{ref}}$	
	λ	7.74	
	β_1	1.43 m	
	β_2	101.43 m	
	G_0^{ref}	170 MPa	160 MPa
	m	0.5	0.25
Poisson's ratio	ν	0.2	
Peak friction angle	ϕ_{p}	32°	
Constant volume friction angle	ϕ_{cv}	36°	
Attraction	a	4 kPa	
Hardening parameter	β	0.0015	
Initial size of yield surface	ϕ_{y}^0	$1.10\phi_{\text{y},0}$	

again increased by 0.1 m). The soil model parameters for profiles 1 and 2 are shown in Table 4.5. The simulation set-up is the same as in Section 4.3.1, except $f = 1.10$ in $\phi_{\text{y}}^0 = f\phi_{\text{y},0}$ (Doherty & Muir Wood 2013). The mesh for Footing 4 is shown in Fig. 4.7.

Fig. 4.13 shows the load-settlement response for the four footings and two soil profiles, plotted along with the results shown in Doherty & Muir Wood (2013, Fig. 13). The current implementation displays a less stiff behaviour than that in Doherty & Muir Wood (2013). Nevertheless, the trend of the load-displacement response is consistent between the two implementations, and the effect of altering the soil profile is coherent within the same implementation. Fig. 4.14 shows contours of the mobilised friction angle, ϕ_{y}, for Footing 2 with soil profile 1 at different stages of loading. The pattern and magnitude of the variation of ϕ_{y} are very similar to those in Doherty & Muir Wood (2013, Fig. 14) (not shown here). The mobilised friction angle of the soil near the footing, especially around the corner, increases towards the peak friction an-

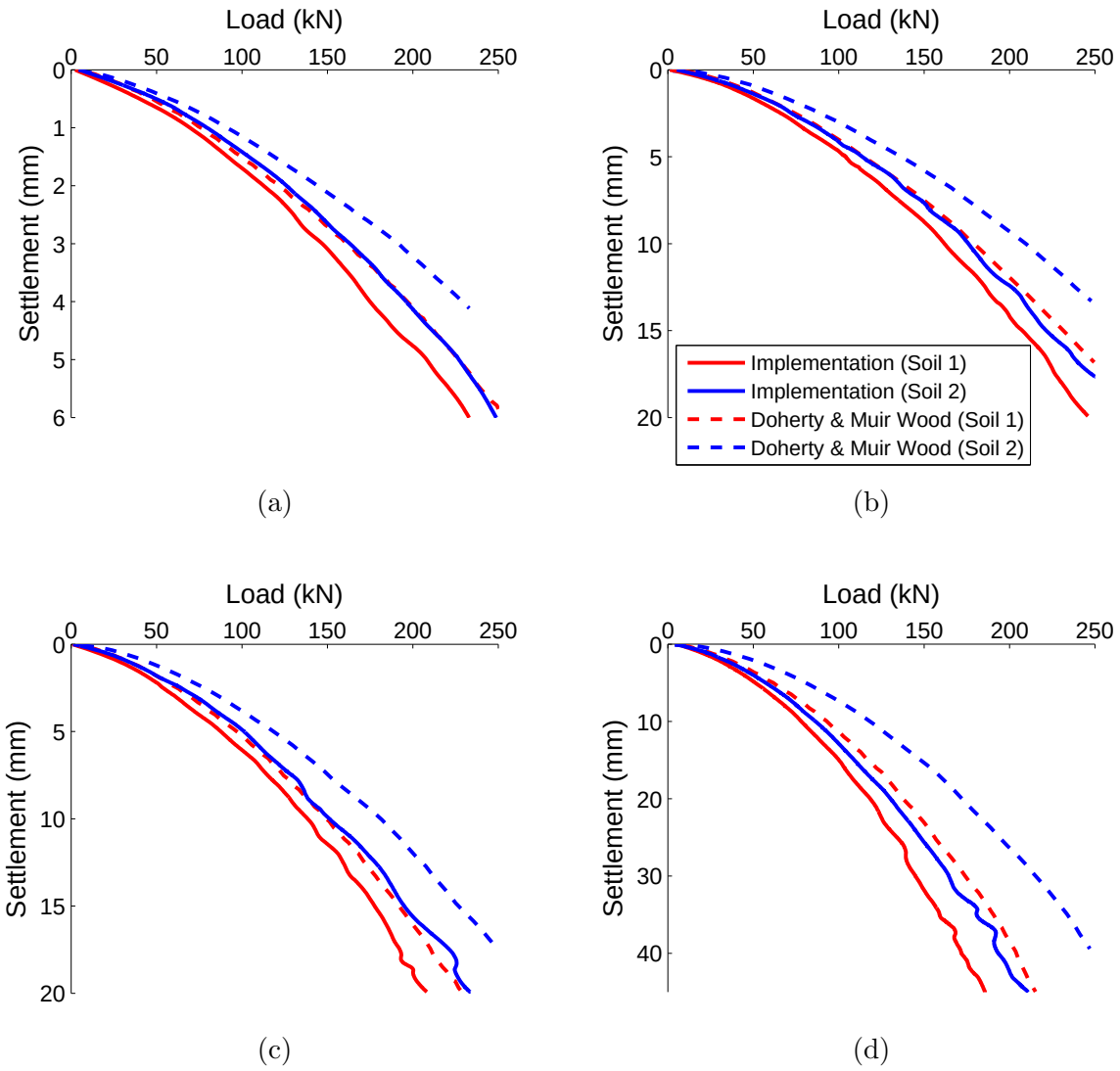


Figure 4.13: Comparison of the EMC model implementations in load-settlement response from the footing test simulations: (a) Footing 1; (b) Footing 2; (c) Footing 3; (d) Footing 4

gle as the load increases. The figure also demonstrates one of the main features of the EMC model where the mobilised friction angle, also implying the soil stiffness, varies with the level of loading, not only with the depth.

Overall, the results of the shallow foundation analyses shown in Figs. 4.13 and 4.14 are comparable to those in Doherty & Muir Wood (2013, Figs. 13 and 14), indicating that a robust implementation of the EMC model has been achieved. It is noted that the greater settlement of the implemented EMC model observed in Fig. 4.13 is consistent with the greater volumetric compression response shown in Fig. 4.12(b).

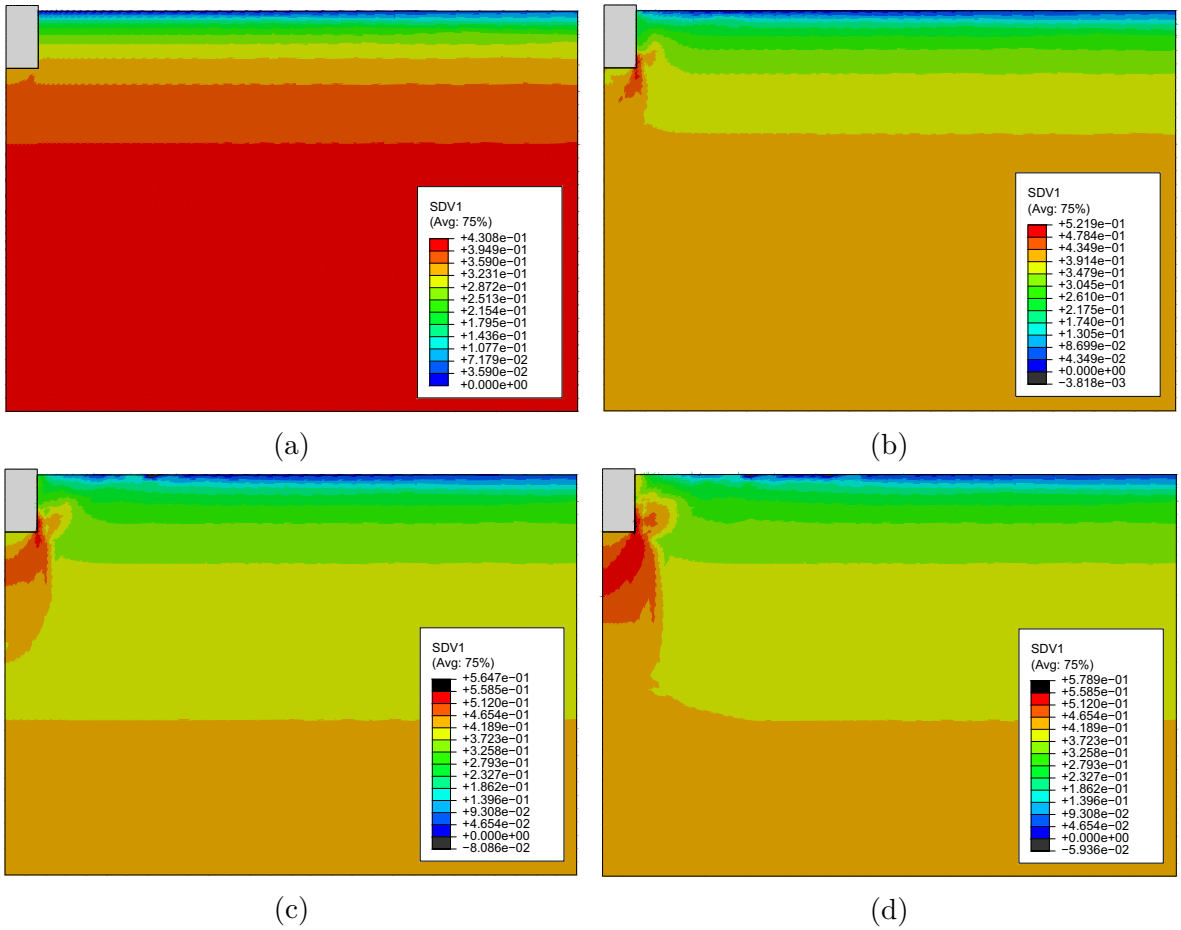


Figure 4.14: Contours of ϕ_y for Footing 2, soil profile 1, at different stages of loading: (a) footing self-weight only; (b) load $\approx$ 50 kN; (c) load $\approx$ 100 kN; (d) load $\approx$ 200 kN. The legend SDV1 refers to ϕ_y in units of radian (Note $\phi_p = 32° = 0.5585$ rad). The magnitude of load is not exact as displacement-controlled loading is applied

4.4 Calibration to the Terrace Gravel

Past literature has documented some soil properties of Terrace Gravel. In particular, the Terrace Gravel at St James's Park in central London is modelled in Addenbrooke et al. (1997) and Jurečič et al. (2013) using the non-linear elastic model J4 and a non-associated perfectly plastic Mohr-Coulomb model (this combination is denoted here by J4-MC). Since the J4-MC model presents a clearly defined stiffness degradation curve and operates with model parameters similar to those of the EMC model (Jurečič et al. 2013, Tables 4 and 5 and Appendix), the EMC model is calibrated against the J4-MC model to represent the Terrace Gravel in central London in the current work.

The EMC model parameters to be calibrated are G_0, ν, ϕ_p, ϕ_{cv}, a and β, and ϕ_y^0 needs to be initialised. The calibrated parameters for the EMC model are listed in

Table 4.6: Calibrated parameters used in the extended Mohr-Coulomb model for Terrace Gravel in central London

Parameter		Value
Elastic shear modulus	G_0	$3G_0/p'_0 = 2621$
Poisson's ratio	ν	0.2
Peak friction angle	ϕ_{p}	35°
Constant volume friction angle	ϕ_{cv}	35°
Attraction	a	4 kPa
Hardening parameter	β	0.00015
Initial size of yield surface	ϕ_{y}^0	$1.06\phi_{\mathrm{y},0}$

Table 4.6. The values of ν and ϕ_{p} are taken directly from the Poisson's ratio and the angle of shearing resistance in Jurečič et al. (2013). Critical state shearing is assumed at failure so that $\phi_{\mathrm{cv}} = \phi_{\mathrm{p}}$. Although the Terrace Gravel is recorded to have zero cohesion, a small value of attraction ($a = 4$ kPa) is adopted for numerical stability, following Doherty & Muir Wood (2013).

The shear stiffness profile of the Terrace Gravel is given in terms of normalised tangent shear modulus, $3G/p'$, against distortional strain, ε_J, with a minimum value of $G = 2000$ kPa in Jurečič et al. (2013) (ε_J is denoted as deviatoric strain, ε_{d}, in Jurečič et al. (2013)). The initial normalised stiffness $3G_0/p'$ of the J4-MC model is obtained by substituting the lower bound of the given range of ε_J of the non-linear elastic model (Jurečič et al. 2013, Appendix), such that $3G_0/p' \approx 2621$. In the current implementation of the EMC model, the dependence of soil stiffness on stress level is approximated by specifying a variation of initial shear modulus with depth. This is based on the geostatic mean effective stress, p'_0 (when the building is absent) such that $3G_0/p'_0 = 2621$ and is subject to a minimum of $G_0 = 2000$ kPa. Hence, the initial shear modulus of the EMC model is obtained by,

$$G_0 = \frac{2621}{3} p'_0 \quad \text{with} \quad p'_0 = \frac{(1 + 2K_0)\gamma' z}{3} \quad \text{and} \quad \min(G_0) = 2000 \text{ kPa} \tag{4.11}$$

A bulk unit weight of $\gamma_{\mathrm{bulk}} = 20$ kN/m^3, based on the values suggested in Withers et al. (2001) and Avgerinos et al. (2016), and an initial lateral earth pressure coefficient of $K_0 = 1 - \sin\phi_{\mathrm{p}} = 0.426$ are adopted in the model.

The initial stress in the gravel at the geostatic state is assumed to be on the initial mobilised yield surface due to its self-weight and the prescribed K_0 value. A multiplying factor $f = 1.06$ is applied to the initial size of the yield surface, $\phi_{\mathrm{y}}^0 = f\phi_{\mathrm{y},0}$, where the same value of f is used in the triaxial compression test simulations in Section 4.3.2.

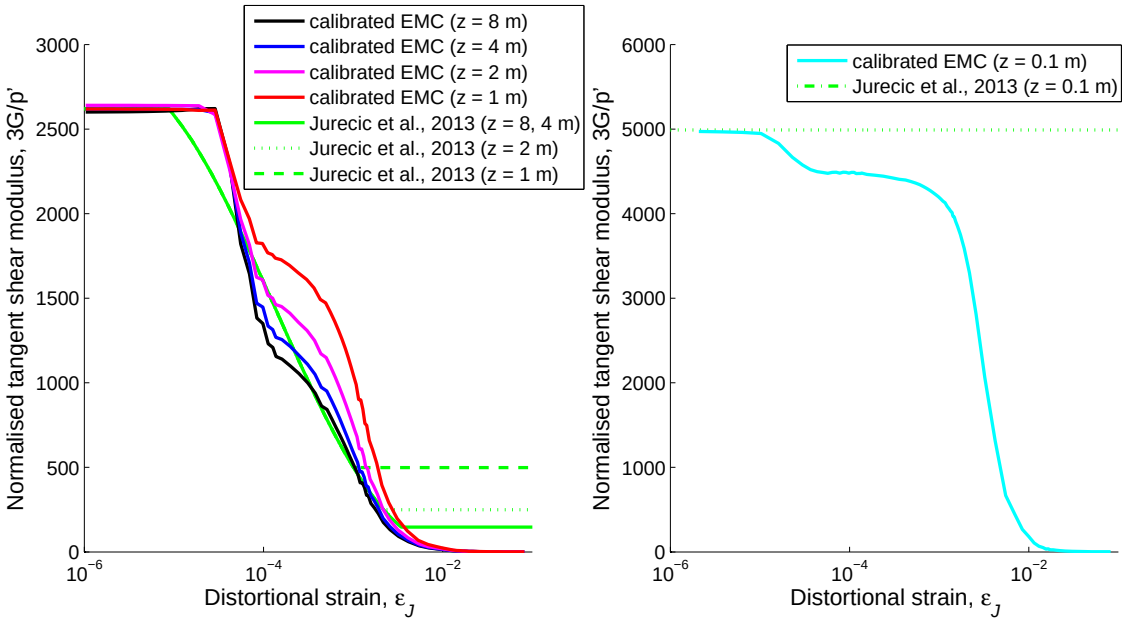
The hardening parameter β is determined by fitting with the stiffness variation data available in Jurečič et al. (2013). A single value of β is chosen based on a series of drained triaxial compression simulations with different confining stresses corresponding to various depths. The selected value $\beta = 0.00015$ is obtained by best-fit-by-eye. The resulting variation of normalised tangent shear modulus, $3G/p'$, with distortional strain, ε_J, from the EMC model is plotted in Fig. 4.15 (note that this plot differs from the secant modulus plots presented in Fig. 4.11). Fig. 4.15(b) shows the significance of the hardening behaviour represented by the EMC model compared to the constant pre-failure stiffness of the J4-MC model when the minimum value of G_0 is imposed in both models, especially at shallow depth (e.g. $z = 0.1$ m in Fig. 4.15(b)). For clarity, the normalised tangent shear modulus, $3G/p'$, is computed using the equation below (in discrete notation):

$$3G/p'_0 = \frac{\Delta q}{\Delta \varepsilon_q}\frac{1}{p'_0} = \frac{\Delta \sigma'_{\mathrm{a}} - \Delta \sigma'_{\mathrm{r}}}{\frac{2}{3}(\Delta \varepsilon_{\mathrm{a}} - \Delta \varepsilon_{\mathrm{r}})}\frac{1}{p'_0} \tag{4.12}$$

It is noted that there is a mismatch of stiffness in the relatively large strain regime, as the non-linear elastic (J4) model used in Jurečič et al. (2013) assumes $3G/p'$ to be constant beyond the specified range of ε_J (Potts & Zdravković 1999). However, this non-linear elastic model is used with a perfectly plastic model in Jurečič et al. (2013), resulting in zero tangent shear modulus once the material yields. It is consistent with the EMC model, as shown in Fig. 4.15, where the EMC model possesses low stiffness at relatively large ε_J values associated with the yielding behaviour of the material.

4.5 Limitations

There are some potential limitations of the EMC model as follows.



(a) (b)

Figure 4.15: Variation of normalised tangent shear modulus with distortional strain for the calibrated EMC model, compared with the pre-failure stiffness of the model used in Jurečič et al. (2013): (a) at depths $z = 8$, 4, 2, and 1 m; (b) at depth $z = 0.1$ m

1. As shown in Fig. 4.15, there is a sharp degradation of stiffness at a strain level around $\varepsilon_J = 4 \times 10^{-4}$, due to the transition from the linear elastic model to the hardening model.

2. The strain level corresponding to the activation of hardening behaviour can be increased by enlarging the initial size of yield surface, but cannot be reduced to a smaller magnitude. This is because the initiation of hardening is linked to the mobilised friction angle, which cannot be smaller than the value implied by the geostatic stresses. The calculation of ε_J corresponding to the beginning of hardening is described in Appendix A at the end of this chapter.

3. In the current work, the dependence of initial stiffness on stress level is simplified by considering the geostatic stress only. This simplification ignores the effect of the building weight on the soil stiffness.

Appendix

A. ε_J corresponding to the beginning of hardening

The value of distortional strain corresponding to the start of hardening in a stiffness degradation curve of the EMC model can be calculated using the properties of the MC model, Mohr's circle and Hooke's law in principal stress space.

Distortional strain ε_J can be expressed in terms of principal strains. In this section, the sign convention is compression positive, subscript 1 refers to the major principal axis and 3 to the minor principal axis and $\sigma_1 \geq \sigma_2 \geq \sigma_3$. In the triaxial compression conditions, the total and incremental values of stress and strain for the intermediate principal axis equal to those for the minor axis ($\Delta\sigma_2 = \Delta\sigma_3$ and $\Delta\varepsilon_2 = \Delta\varepsilon_3$). Therefore,

$$\varepsilon_J = \sqrt{3}\Delta\varepsilon_q = \sqrt{3}\big(\frac{2}{3}(\Delta\varepsilon_1 - \Delta\varepsilon_3)\big) \tag{4.13}$$

Following Hooke's law, for the elastic regime before hardening is triggered,

$$\Delta\varepsilon_1 - \Delta\varepsilon_3 = \frac{1+\nu}{E_0}(\Delta\sigma_1 - \Delta\sigma_3) = \frac{1+\nu}{E_0}(\Delta q) \tag{4.14}$$

and thus from Equations 4.13 and 4.14,

$$\varepsilon_J = \sqrt{3}\Delta\varepsilon_q = \frac{2\sqrt{3}(1+\nu)}{3E_0}(\Delta q) = \frac{\sqrt{3}}{3G_0}(\Delta q) \tag{4.15}$$

From the MC yield surface, where a is attraction, also the x-intercept of the yield surface in τ-σ space,

$$\sin\phi = \frac{(\sigma_1 - \sigma_3)/2}{(\sigma_1 + \sigma_3)/2 + a} \tag{4.16}$$

Assuming $a = 0$ for approximation purpose, Equation 4.16 becomes

$$\sin\phi = \frac{(\sigma_1 - \sigma_3)}{(\sigma_1 + \sigma_3)} = \frac{q}{3p - \sigma_3} \tag{4.17}$$

Hardening is triggered once the stress state touches the yield surface. The start of

yielding is denoted by a subscript h. Given the stress path of the triaxial compression test, where p_0 is the mean stress after the isotropic confining stress is applied in all directions (i.e. $p_0 = \sigma_3$), Equation 4.17 can be rewritten as

$$\sin\phi_{\mathrm{h}} = \frac{q_{\mathrm{h}}}{3p_{\mathrm{h}} - \sigma_{3,\mathrm{h}}}, \text{ where } p_{\mathrm{h}} = p_0 + \frac{q_{\mathrm{h}}}{3} = \sigma_3 + \frac{q_{\mathrm{h}}}{3} \tag{4.18}$$

Substitute Equation 4.15 into Equation 4.18,

$$\sin\phi_{\mathrm{h}} = \frac{q_{\mathrm{h}}}{3p_{\mathrm{h}} - \sigma_{3,\mathrm{h}}} = \frac{3G_0\varepsilon_{J,\mathrm{h}}}{\sqrt{3}} \frac{1}{3(\sigma_3 + \sqrt{3}\varepsilon_{J,\mathrm{h}}G_0) - \sigma_3} \tag{4.19}$$

Finally, by rearranging the equation, $\varepsilon_{J,h}$ is obtained,

$$\varepsilon_{J,\mathrm{h}} = \frac{(2\sigma_3)\sin\phi}{\sqrt{3}(1-\sin\phi)G_0} \tag{4.20}$$

If $a = 0$ for Test 1 and Test 2 in Section 4.3.2, $\varepsilon_{J,\mathrm{h}}$ of Test 1 $= 2.40 \times 10^{-4}$ and $\varepsilon_{J,\mathrm{h}}$ of Test 2 $= 4.55 \times 10^{-4}$. It is noted that this $\varepsilon_{J,\mathrm{h}}$ is measured after the initial radial stress is applied (at reference point (i) in Fig. 4.9). Subtracting the strain induced by the initial axial stress, which is calculated from Equation 4.15, the trigger strain $\varepsilon_{J,\mathrm{t}}$ (measured after the initial stresses are established, at reference point (ii) in Fig. 4.9) can be approximated as 9.06×10^{-6} for Test 1 and 3.86×10^{-5} for Test 2. Comparing with the trigger strain in Fig. 4.11, there is a slight difference in Test 1 because a positive a value is used in Test 1, while the trigger strain matches well with the implemented UMAT data (and the 'factored' data) in Test 2 where $a = 0$ is used.

Chapter 5

Implementation of the M2-SKH model for London Clay

The M2-SKH model developed by Grammatikopoulou et al. (2006) is selected to represent London Clay and its general features have been discussed in Section 3.6.5. The M2-SKH model is implemented as a UMAT in Abaqus in the current work. Some modifications are made to the M2-SKH model in the current implementation. The stress update algorithm is customised for the non-linear two-surface model, based on the scheme in Sloan et al. (2001). The calibration procedure for two sets of model parameters is described, with discussion of the correlation between the hardening parameter, the K_0 profile and the overburden stress assumed in the geological stress history. The implemented model is validated using the greenfield settlement profile at St James's Park induced by the construction of the Jubilee Line Extension tunnels. Through comparing the computed ground settlements at different time periods with the field measurements, respective sets of model parameters are identified for the prediction of the immediate and longer-term tunnelling-induced ground responses.

The implementation of the M2-SKH model in a UMAT is based mainly on the elastoplastic formulation described in Grammatikopoulou et al. (2006); the development and the equations of the model are not repeated here unless they are relevant to the current decisions and modifications.

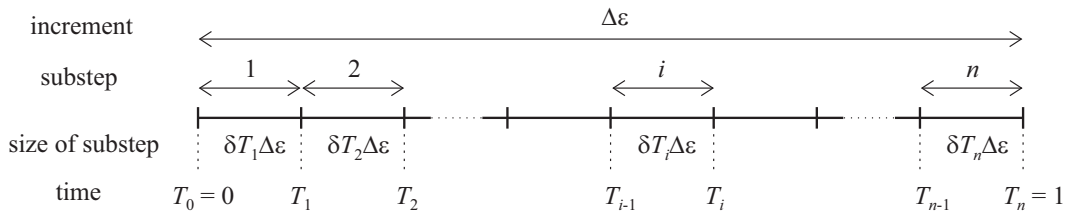


Figure 5.1: Nomenclature of substepping of the strain increment employed in the M2-SKH model implementation

5.0.1 Nomenclature of substepping in implementation

As both the elastic and elastoplastic stress-strain relationships of the M2-SKH model are non-linear, a substepping algorithm is employed for the whole strain increment, $\Delta\boldsymbol{\varepsilon}$, in the current implementation. The nomenclature of the substepping used for the implementation of this model is shown in Fig. 5.1. The integration of $\Delta\boldsymbol{\varepsilon}$ is associated with a pseudo time T_i, where $0 \leq T_i \leq 1$; starting at $T_0 = 0$ and ending at $T_n = 1$. The size of a substep i is denoted as $\delta T_i \Delta\boldsymbol{\varepsilon}$ and time $T_i = T_{i-1} + \delta T_i$.

5.1 Overview of the model

5.1.1 MCC model

The adopted MCC surface assumes the isotropic normal compression line and the elastic part of the isotropic swelling line to be straight in $\ln v - \ln p'$ space (Equations 5.1 and 5.2), where v is the specific volume and p' is the mean effective stress. Their slopes are λ^* and κ^* respectively. v_1^* and v_κ^* are the intercepts taken at $p' = 1$ kPa of the lines.

$$\ln v = v_1^* - \lambda^* \ln p' \tag{5.1}$$

$$\ln v = v_\kappa^* - \kappa^* \ln p' \tag{5.2}$$

5.1.2 Elastic behaviour

The model assumes isotropic elastic behaviour. The elastic bulk modulus, K^{e}, is

$$K^e = \frac{p'}{\kappa^*} \tag{5.3}$$

The elastic shear modulus, G_0, is represented by a stress-dependent relation suggested by Viggiani & Atkinson (1995):

$$\frac{G_0}{p_\mathrm{r}} = A\left(\frac{p'}{p_\mathrm{r}}\right)^n {R_0}^m \tag{5.4}$$

where A, n, m are material parameters, p_r is a reference mean stress taken to be 1 kPa, and $R_0 = p'_0/p'$ is the overconsolidation ratio.

5.1.3 Yield, bounding and plastic potential surfaces

Bounding and yield surfaces. The bounding surface (BS) and yield surface (YS) functions are formulated in general stress space as described below and illustrated in Fig. 3.8. The subscript b relates to the BS, y to the YS, and a to the centre of the YS. The deviatoric stresses ($\hat{\boldsymbol{s}}$, $\hat{\boldsymbol{s}}_\mathrm{a}$) are in the tensor form (see Nomenclature) and the symbol : refers to tensorial contraction. The BS and YS are given by

$$F_\mathrm{b} = \left(p' - \frac{p'_0}{2}\right)^2 + \frac{1}{2}\frac{\hat{\boldsymbol{s}} : \hat{\boldsymbol{s}}}{g^2(\theta_\mathrm{b})} - \frac{{p'_0}^2}{4} = 0 \tag{5.5}$$

$$F_\mathrm{y} = (p' - {p_\mathrm{a}}')^2 + \frac{1}{2}\frac{(\hat{\boldsymbol{s}} - \hat{\boldsymbol{s}_\mathrm{a}}) : (\hat{\boldsymbol{s}} - \hat{\boldsymbol{s}}_\mathrm{a})}{g^2(\theta_\mathrm{y})} - R^2\frac{{p'_0}^2}{4} = 0 \tag{5.6}$$

where p'_0 is the value of the mean effective stress at the intersection of the current swelling line with the isotropic normal compression line, $g(\theta)$ defines the shape of the surface in the deviatoric plane, θ is the Lode angle, and R is the ratio of the size of the YS to that of the BS. θ_b represents the Lode angle for the BS and is expressed as $\theta_\mathrm{b} = \theta(\hat{\boldsymbol{s}})$, while θ_y is the Lode angle with respect to the YS and is defined as $\theta_\mathrm{y} = \theta(\hat{\boldsymbol{s}} - \hat{\boldsymbol{s}}_\mathrm{a})$ (see Nomenclature).

The shape in the deviatoric plane, $g(\theta)$, can be a Mohr-Coulomb hexagon or any other convex surface, such as from the family of continuous surfaces proposed by van

Eekelen (1980) (Grammatikopoulou et al. 2006):

$$g(\theta) = \frac{\sin\phi'}{\cos\theta + \frac{\sin\theta\sin\phi'}{\sqrt{3}}} \quad \text{for Mohr-Coulomb hexagon} \tag{5.7}$$

$$g(\theta) = \frac{X}{(1 + Y\sin 3\theta)^Z} \quad \text{for van Eekelen surface} \tag{5.8}$$

where ϕ' is the angle of shearing resistance. X, Y and Z are material constants and $X = \sin(\phi'_{\theta=0})$ where $\phi'_{\theta=0}$ is the angle of shearing resistance associated with Lode angle $\theta = 0$ (pure shear).

Plastic potential surfaces. The plastic potential surfaces associated with the BS and the YS, denoted by P_b and P_y, are given by Equations 5.5 and 5.6 with the functions $g(\theta_\mathrm{b})$ and $g(\theta_\mathrm{y})$ replaced by $g_\mathrm{p}(\theta_\mathrm{b})$ and $g_\mathrm{p}(\theta_\mathrm{y})$ respectively. The function $g_\mathrm{p}(\theta)$ defines the shape of the plastic potential surface in the deviatoric plane and is assumed to be in the family of surfaces proposed by van Eekelen (1980):

$$g_\mathrm{p}(\theta) = \frac{X_\mathrm{p}}{(1 + Y_\mathrm{p}\sin 3\theta)^{Z_\mathrm{p}}} \tag{5.9}$$

where Y_p and Z_p are material constants and X_p varies to satisfy the condition that the current plastic potential surface passes through the current stress state.

Current implementation. For numerical implementation, smooth continuous surfaces are often preferred for reasons of numerical convergence. The current implementation therefore employs the family of surfaces from van Eekelen (1980) for both $g(\theta)$ and $g_\mathrm{p}(\theta)$ (Equations 5.8 and 5.9).

5.1.4 Measure of proximity of the YS to the BS

The hardening modulus of the M2-SKH model (referred as A in Grammatikopoulou et al. (2006, Equation 14) but denoted here as H for consistency with the nomenclature employed in this thesis (Table 4.1)) is the sum of two components, $H = H_0 + H_1$. In the original formulation of the M2-SKH model, the second component of the hardening

modulus, H_1, is expressed in Equation 19 in Grammatikopoulou et al. (2006) as

$$H_1 = \frac{4}{\lambda^* - \kappa^*}\alpha\left(\frac{b^*}{b^*_{\max} - b^*}\right)\left(\frac{p'_0}{2}\right)^3 R^2 \tag{5.10}$$

where α is a model parameter controlling the rate of decay of stiffness with strain (a lower value of α indicates a faster decay), b^* is the measure of the proximity of the YS to the BS, and $b^*_{\max}$ is the maximum value of b^*.

The term $\frac{b^*}{b^*_{\max}-b^*}$ was introduced by Grammatikopoulou et al. (2006) to give a smooth transition for the value of H_1 from infinity when the YS is initiated, to zero when the YS is in contact with the BS (such that the hardening modulus, H, starts from an infinite positive value upon initiation of yielding and reduces to the value of H_0 when the BS governs the elastoplastic response). The values of b^* and $b^*_{\max}$ are computed throughout the stress update and $b^*_{\max}$ is reset to the current value of b^* every time the YS is newly engaged.

The measure b^* is defined as the product of the tensors $\hat{\boldsymbol{\beta}}$ and $\hat{\boldsymbol{n}}$ (see Fig. 5.2(a)), as written in Grammatikopoulou et al. (2006, Equation 20),

$$b^* = (p' - p'_{\mathrm{a}})\left[\frac{p' - p'_{\mathrm{a}}}{R} - \left(p' - \frac{p'_0}{2}\right)\right] + \frac{1}{2}\left[\left(\frac{\partial F_{\mathrm{y}}}{\partial \hat{\boldsymbol{s}}}\right) : \left(\frac{\hat{\boldsymbol{s}} - \hat{\boldsymbol{s}}_a}{R} - \hat{\boldsymbol{s}}\right)\right] \tag{5.11}$$

and in Grammatikopoulou et al. (2006, Equation 8),

$$\hat{\boldsymbol{\beta}} = \frac{\hat{\boldsymbol{\sigma}}' - \hat{\boldsymbol{\sigma}}'_{\mathrm{a}}}{R} - \left(\hat{\boldsymbol{\sigma}}' - \frac{\hat{\boldsymbol{\sigma}}'_0}{2}\right) \tag{5.12}$$

where $\hat{\boldsymbol{\sigma}}'_0/2$ represents the centre of the BS. From Equations 5.11 and 5.12, the $\hat{\boldsymbol{n}}$ implied can be obtained by back calculation as

$$\hat{\boldsymbol{n}} = \frac{1}{2}\frac{\partial F_{\mathrm{y}}}{\partial \hat{\boldsymbol{\sigma}}'} \tag{5.13}$$

which is an outward normal tensor of the YS at the current stress state. It is noted that the tensor $\hat{\boldsymbol{n}}$ is not a unit tensor. Nevertheless, the magnitude of $\hat{\boldsymbol{n}}$ does not affect the

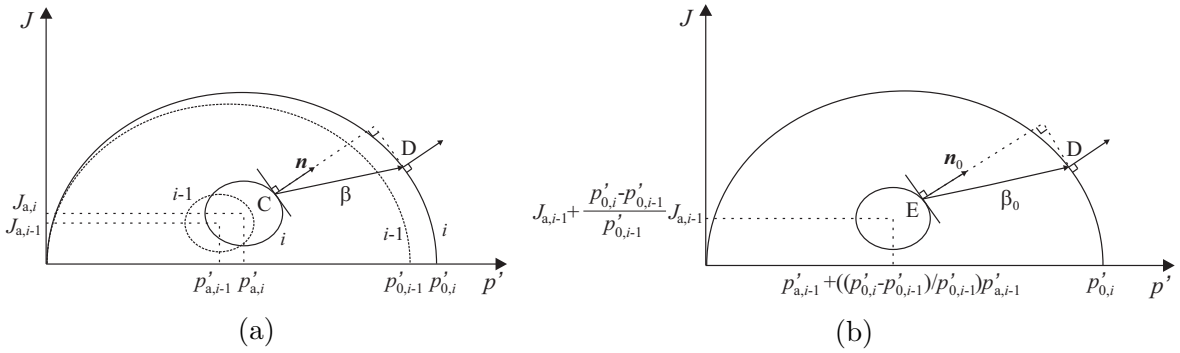


Figure 5.2: Representation of the model in $p' - J$ space: (a) at the end of substeps $i-1$ and i; (b) configuration of surfaces for calculation of value of b_0^* (after Grammatikopoulou et al. (2006, Fig. 3))

search for the conjugate stress state on the BS (point D in Fig. 5.2(a)) corresponding to the current stress state (point C in Fig. 5.2(a)) as point D can be located using the geometrical relationship in terms of $\hat{\boldsymbol{\beta}}$.

Ambiguity relating to the use of $\hat{\boldsymbol{n}}$ arises when it comes to the calculation of $b^*_{\max}$ subsequent to the initialisation of its value. The value of $b^*_{\max}$ is computed incrementally using Equation 5.14 (Grammatikopoulou et al. 2006, Equation 21),

$$b^*_{\max,i} = \frac{b^*_0}{b^*_{i-1}/b^*_{\max,i-1}} \tag{5.14}$$

which means the ratio $b^*_0/b^*_{\max}$ at the end of substep i is equal to the ratio $b^*/b^*_{\max}$ at the end of substep $i-1$. The value of b^*_0 is defined as the product of the tensor $\hat{\boldsymbol{\beta}}_0$, which connects point E to point D, and the tensor $\hat{\boldsymbol{n}}_0$, which is the outward normal of the YS at point E (Fig. 5.2(b)). Point E is the stress state lying on the YS at the end of substep $i-1$ scaled by the ratio of the change in the size of the BS in substep i, and has the same outward normal direction as point D (Fig. 5.2). This gives

$$\hat{\boldsymbol{\beta}}_0 = \hat{\boldsymbol{\beta}}_i + \hat{\boldsymbol{\sigma}}'_{\mathrm{a},i} - \hat{\boldsymbol{\sigma}}'_{\mathrm{a},i-1}\left(1 + \frac{p'_{0,i} - p'_{0,i-1}}{p'_{0,i-1}}\right) \tag{5.15}$$

Grammatikopoulou et al. (2006) stated that the stress states C, D and E had the same outward normal and $\hat{\boldsymbol{n}}_0 = \hat{\boldsymbol{n}}$, which is not necessarily true. As noted in Equation 5.13, the tensor $\hat{\boldsymbol{n}}$ is not a unit tensor. Although the points C, D and E are defined as

the stress states with the same *direction* of outward normal, the magnitudes of the outward normal depend on their corresponding surfaces and stress states. Therefore, the equality $\hat{\boldsymbol{n}}_0 = \hat{\boldsymbol{n}}$ used in Grammatikopoulou et al. (2006) may not be valid and the use of $\hat{\boldsymbol{n}}_0 = \hat{\boldsymbol{n}}$ in the calculation of b_0^* may not guarantee that $b_{\max}^*$ computed from Equation 5.14 is in the same magnitude scale as b^* calculated from Equation 5.11. As a consequence, the $b_{\max}^*$ in Equation 5.10 may not represent the maximum value of b^*.

The formulation can be improved by replacing the outward normal tensors with the outward normal unit tensors. Alternatively, the measure of the proximity of the YS to the BS can be redefined using the magnitude of the tensor connecting the stress states. Replacing Equation 5.10, the second component of the hardening modulus, H_1, is now expressed as

$$H_1 = \frac{4}{\lambda^* - \kappa^*}\alpha\left(\frac{\|\hat{\boldsymbol{\beta}}\|}{\|\hat{\boldsymbol{\beta}}\|_{\max} - \|\hat{\boldsymbol{\beta}}\|}\right)\left(\frac{p_0'}{2}\right)^3 R^2 \tag{5.16}$$

where

$$\|\hat{\boldsymbol{\beta}}\|_{\max,i} = \|\hat{\boldsymbol{\beta}}\|_i \quad \text{on initiation of the YS, and} \tag{5.17}$$

$$\|\hat{\boldsymbol{\beta}}\|_{\max,i} = \frac{\|\hat{\boldsymbol{\beta}}_0\|}{\|\hat{\boldsymbol{\beta}}\|_{i-1}/\|\hat{\boldsymbol{\beta}}\|_{\max,i-1}} \quad \text{for subsequent substeps} \tag{5.18}$$

and $\|\hat{\boldsymbol{\beta}}\|$ is the magnitude of $\hat{\boldsymbol{\beta}}$. The tensors $\hat{\boldsymbol{\beta}}$ and $\hat{\boldsymbol{\beta}}_0$ are calculated with Equations 5.12 and 5.15. This approach, which was adopted in the formulation of the bounding surface model (Ottosen & Ristinmaa 2005), is straightforward in its quantification of the distance between two stress points and has the computational benefit of involving fewer operations, yet retains a smooth transition of the value of H_1 as intended. In the current implementation, the proximity of the YS to the BS is measured with $\|\hat{\boldsymbol{\beta}}\|$ and H_1 is computed using Equation 5.16.

5.2 Implementation

The M2-SKH model with the aforementioned modifications is implemented as a material constitutive model in Abaqus via a UMAT subroutine. The tensor variables

are represented by column vectors in the UMAT. The operations also change accordingly (e.g. $\hat{\boldsymbol{s}} : \hat{\boldsymbol{s}}$ for $\hat{\boldsymbol{s}}$ in tensor form becomes $\boldsymbol{s}^{\mathrm{T}}\boldsymbol{s}$ for $\boldsymbol{s}$ in vector form). Note that the order of components of the column vectors passed to and from the UMAT is $\{a_{xx}, a_{yy}, a_{zz}, a_{xy}, a_{xz}, a_{yz}\}^{\mathrm{T}}$ for variable $\boldsymbol{a}$, which is different from the typical Voigt ordering $\{a_{xx}, a_{yy}, a_{zz}, a_{xy}, a_{yz}, a_{zx}\}^{\mathrm{T}}$. For every increment, at each integration point, the UMAT reads the current stress state, state variables and strain increment and then updates the new stress state, state variables and constitutive matrix.

5.2.1 Model parameters

The current implementation of the M2-SKH model requires 13 parameters, as defined below. The number of model parameters can vary depending on the elastic model and the shape of the surfaces in the deviatoric plane.

λ^*: slope of the normal compression line (NCL) in $\ln v - \ln p'$ space (Equation 5.1)

κ^*: slope of the elastic part of the swelling line in $\ln v - \ln p'$ space (Equation 5.2)

X, Y, Z: parameters defining the shape of the yield and bounding surfaces in the deviatoric plane (Equation 5.8)

Y_{p}, Z_{p}: parameters defining the shape of the plastic potential surfaces in the deviatoric plane (Equation 5.9)

R: ratio of the size of the kinematic yield surface to that of the bounding surface (Equation 5.6)

α: parameter controlling the rate of stiffness degradation with strain (Equation 5.16)

n, m, A: parameters for the elastic shear modulus (Equation 5.4)

e_0: initial void ratio (or use v_1^*, the specific volume of NCL at $p' = 1$ kPa)

The initial void ratio, e_0, is required as an input for using pore pressure elements in Abaqus. e_0 can be determined by the initial specific volume, v_0, by $e_0 = v_0 - 1$, in which v_0 is obtained using Equation 5.1 with v_1^*, λ^*, and initial mean effective stress.

5.2.2 State variables

STATE_i is defined in the model to represent an array of 12 variables at the end of substep i as follows.

$p'_{0,i}$: size of the BS at the end of substep i

$\{\sigma'_{\text{a},xx,i}, \sigma'_{\text{a},yy,i}, \sigma'_{\text{a},zz,i}, \tau_{\text{a},xy,i}, \tau_{\text{a},xz,i}, \tau_{\text{a},yz,i}\}$: centre of the YS at the end of substep i

$\|\boldsymbol{\beta}\|_i$: proximity of the YS to the BS at the end of substep i

$\|\boldsymbol{\beta}\|_{\max,i}$: maximum value of $\|\boldsymbol{\beta}\|$ at the end of substep i

Fy_on: Boolean value indicating whether the YS is active

Fb_on: Boolean value indicating whether the BS is active

Fy_engage: Boolean value indicating whether the YS is newly engaged

In the implementation of the UMAT, the solution-dependent state variable array (referred to as STATEV in Abaqus) comprises STATE_{i-1} and STATE_i.

5.2.3 Stress update algorithm

The overall stress update process for a given strain increment, $\Delta\boldsymbol{\varepsilon}$, is summarised in Fig. 5.3. The substepping algorithm is applied for the whole $\Delta\boldsymbol{\varepsilon}$ (Fig. 5.1). The model is first assumed to behave elastically, and then proceeds through three stress update algorithms, from 'elastic update routine' to 'YS update routine' and finally 'BS update routine'. The stress update algorithm is designed in this way such that, regardless of whether the stress point lies on the YS or the BS at time T_0, the possibility of the given $\Delta\boldsymbol{\varepsilon}$ leading to an unloading stress path is considered. If a stress point lying on the YS continues yielding, the output values from 'elastic update routine', with the subscript elas, are equal to the input values; and it is similar if a stress point continues yielding on the BS in 'elastic update routine' and 'YS update routine'. When $T_n = 1$ is attained within any of the update routines, the stress state and the state variables at $T_n = 1$ are carried to the remaining routines and output directly.

Within each of the 'update routine' algorithms, the explicit Runge-Kutta-Dormand-Prince (RK) integration scheme described in Sloan et al. (2001) is adopted. Stress

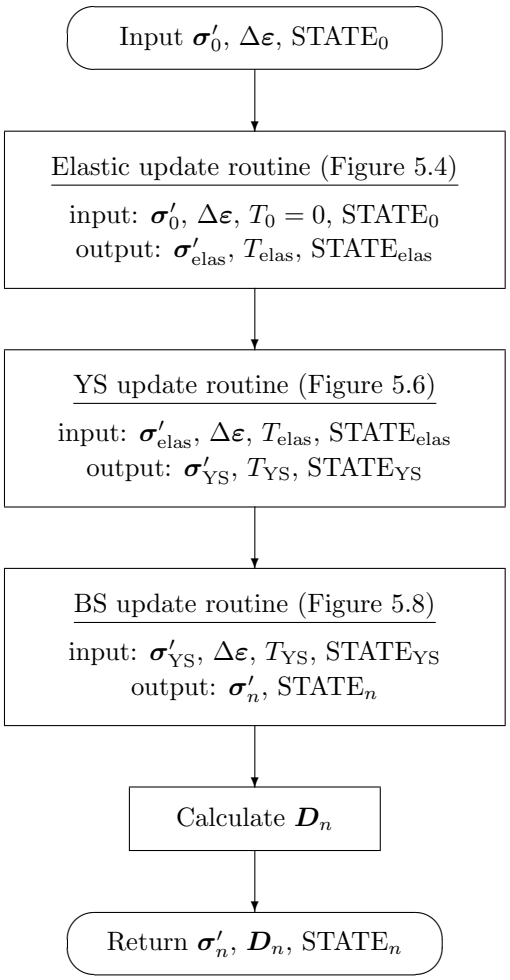


Figure 5.3: Overview of the stress update algorithm. STATE$_0$ corresponds to the initial conditions of the simulation or the values at the end of the last increment

correction accommodated to the current model is applied within 'YS update routine' and 'BS update routine' (see Sections 5.2.3.2 and 5.2.3.3). The acceptance of the RK integration over a substep is associated with the relative error (denoted as R in the flowcharts) with respect to the tolerance constant (denoted as STOL). The ratio of R to STOL also controls the size of the subsequent or repeating substep, noting that δT has a predefined minimum value, δT_{min}, to limit the maximum possible number of substeps. In the current implementation, STOL $= 1 \times 10^{-10}$ and $\delta T_{\text{min}} = 1 \times 10^{-4}$.

Numerical representation of the yield and bounding functions. The values of the yield and bounding functions corresponding to the YS and the BS, F_{y} and F_{b}, are used to identify the type of stress-strain behaviour. As expected in numerical computation, the values of F_{y} and F_{b} are unlikely to be precisely zero. The yield and bounding

surface conditions are therefore implemented with a small positive tolerance, FTOL, such that the conditions become $|F_{\mathrm{y}}| \leq \mathrm{FTOL}$ and $|F_{\mathrm{b}}| \leq \mathrm{FTOL}$. For convenience of presentation, in the following sections, the yield and bounding cases are still written with respect to zero, e.g. $F_{\mathrm{y}} = 0$, $F_{\mathrm{b}} < 0$.

It is beneficial to express the yield and bounding conditions in a dimensionless form such that the judgement of yielding is made independent of the magnitude of stress. The equations of the yield and bounding functions (Equations 5.6 and 5.5) are normalised by $p_0'^2$ and a dimensionless small positive number is assigned for FTOL (e.g. 1×10^{-8}). The normalised form of the functions is only used to determine whether the yield and bounding conditions are fulfilled.

The Boolean parameters, Fy_on, Fb_on and Fy_engage in STATE_i, indicate the activation of the surfaces in the analysis. They are also used in the program to direct the computation to the specific set of equations associated with the activated surfaces.

5.2.3.1 Elastic stress update routine

The stress-strain behaviour of the substep is first assumed to be elastic. The flowchart of the 'elastic update routine' algorithm is displayed in Fig. 5.4.

RK integration. The explicit Runge-Kutta-Dormand-Prince (RK) scheme is applied to compute the value of $\delta\boldsymbol{\sigma}'$ corresponding to $\delta T_i \Delta\boldsymbol{\varepsilon}$ with error control based on the procedures detailed in Sloan et al. (2001), with p_0' being constant (equal to the initial value, $p_{0,0}'$). In the case of substep $\delta T_i = \delta T_{\min}$, the outcome from the RK integration is accepted unconditionally and proceeds forward. If $\delta T_i = \delta T_{\min}$ and $F_{\mathrm{y},i} > 0$, the stress update will continue in 'YS update routine' and the discrepancy of $F_{\mathrm{y},i} > 0$ will be addressed by stress correction there, as described in Section 5.2.3.2.

Possible outcomes. Since every invocation of the UMAT begins with 'elastic update routine', the outcome of a successful RK integration over the first substep (i.e. $F_{\mathrm{y},1}, F_{\mathrm{b},1}$) is considered carefully. All the possible cases of the initial stress state and the stress paths of the first substep are illustrated in Fig. 5.5, described in Table 5.1 and addressed

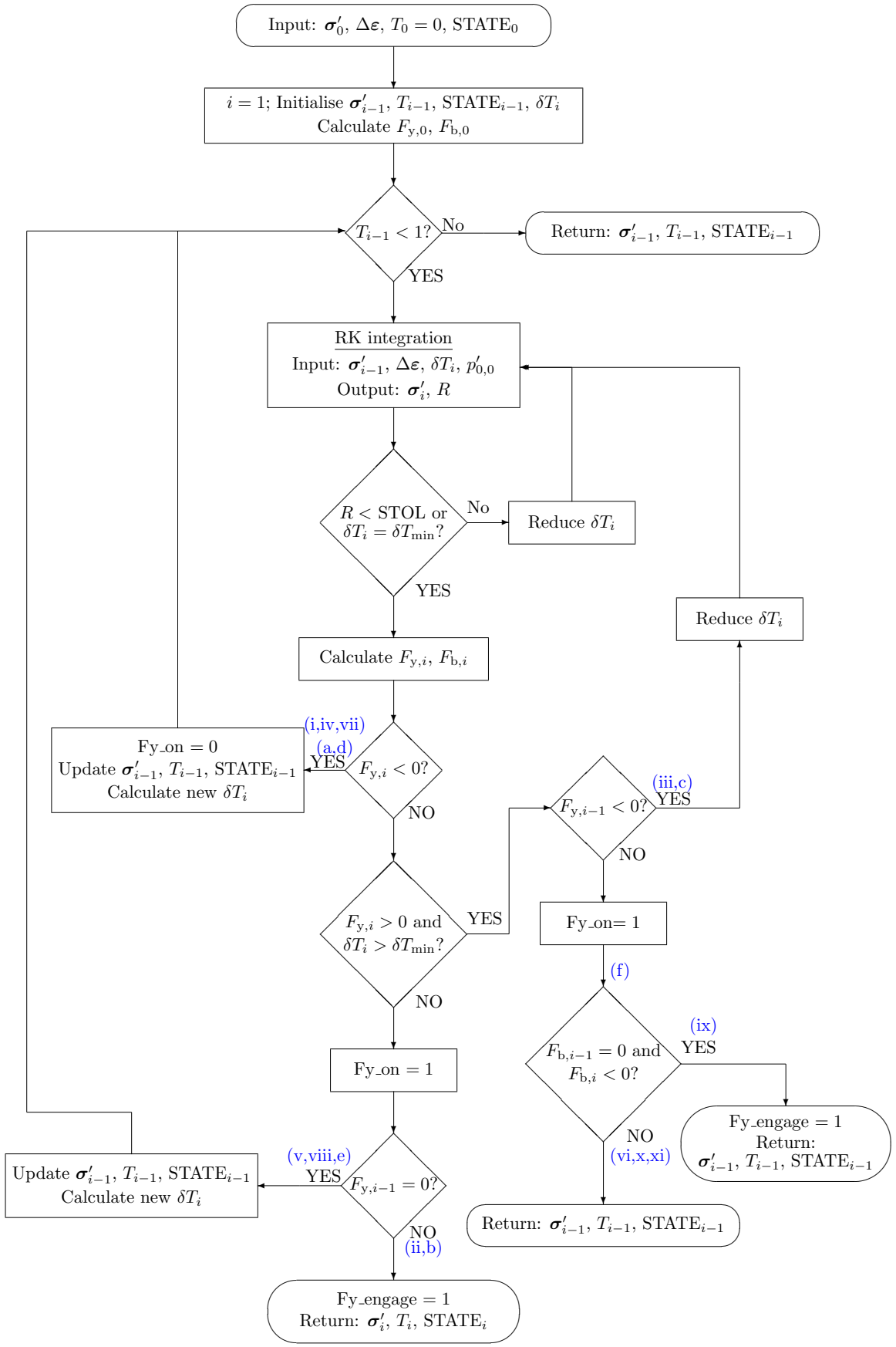


Figure 5.4: Flowchart of the elastic update routine. The roman numerals refer to the cases in Table 5.1 and Fig. 5.5. The letters refer to the cases in Table 5.2

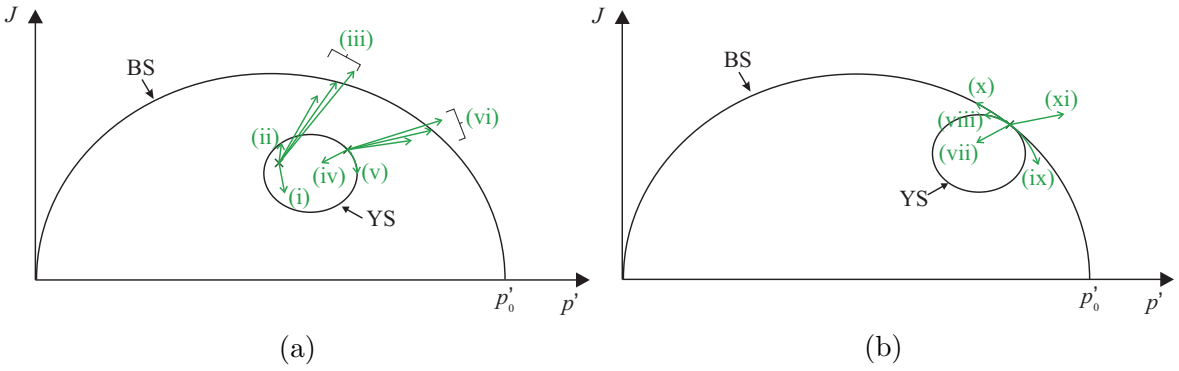


Figure 5.5: Schematic representation of possible cases of the first substep in the elastic update routine: (a) initial stress within yield surface or on yield surface; (b) initial stress on bounding surface. The roman numerals refer to the cases in Table 5.1

Table 5.1: Possible outcomes of the first substep in the elastic update routine. The roman numerals refer to the cases in Fig. 5.5. The letters in the bracket refer to the cases in Table 5.2

Case	$F_{y,0}$	$F_{b,0}$	$F_{\mathrm{y},1}$	$F_{\mathrm{b},1}$	Representation of behaviour and flow
(i)	< 0	< 0	< 0	< 0	Elas $\rightarrow$ Elas, continue with (a, b, c)
(ii)	< 0	< 0	$= 0$	< 0	Elas $\rightarrow$ YS, return with $i = 1$
(iii)	< 0	< 0	> 0	any	Elas $\rightarrow$ YS, repeat with reduced δT_i, until (ii)
(iv)	$= 0$	< 0	< 0	< 0	YS $\rightarrow$ Elas, continue with (a, b, c)
(v)	$= 0$	< 0	$= 0$	< 0	YS $\rightarrow$ unknown, continue with (d, e, f)
(vi)	$= 0$	< 0	> 0	any	YS $\rightarrow$ YS, return with $i = 0$
(vii)	$= 0$	$= 0$	< 0	< 0	BS $\rightarrow$ Elas, continue with (a, b, c)
(viii)	$= 0$	$= 0$	$= 0$	< 0	BS $\rightarrow$ unknown, continue with (d, e, f)
(ix)	$= 0$	$= 0$	> 0	< 0	BS $\rightarrow$ YS, return with $i = 0$
(x)	$= 0$	$= 0$	> 0	$= 0$	BS $\rightarrow$ unknown (YS/BS), return with $i = 0$
(xi)	$= 0$	$= 0$	> 0	> 0	BS $\rightarrow$ BS, return with $i = 0$

in Fig. 5.4. Elastic behaviour is assumed on the YS/BS for the cases (v, viii) since it is uncertain whether elastic unloading or further YS yielding will follow. For cases in which the subsequent substep stays in the 'elastic update routine', the possible outcomes are summarised in Table 5.2. The algorithm continues with the elastic update routine if $F_{\mathrm{y},i} < 0$, or if $F_{\mathrm{y},i} > 0$ it repeats the substep with a smaller size until an intersection with the YS is found. The stress state exits from 'elastic update routine' when $T_{i-1} = 1$ or $F_{\mathrm{y},i} = 0$ (or when $\delta T_i = \delta T_{\min}$ and $F_{\mathrm{y},i} > 0$).

5.2.3.2 Yield surface stress update routine

The flowchart of the 'YS update routine' algorithm is shown in Fig. 5.6. For $T_{\mathrm{elas}} \neq 1$, the YS remains active and the elastoplastic behaviour depends on the proximity of the

Table 5.2: Possible outcomes of the subsequent substeps in the elastic update routine

Case	$F_{\mathrm{y},i-1}$	$F_{\mathrm{y},i}$	Representation of behaviour and flow
(a)	< 0	< 0	continue Elas
(b)	< 0	$= 0$	return with i
(c)	< 0	> 0	repeat with reduced δT_i, until (b)
(d)	$= 0$	< 0	continue Elas
(e)	$= 0$	$= 0$	continue Elas, until (d) or (f)
(f)	$= 0$	> 0	return with $i - 1$

YS to the BS. The YS moves within the BS until $T_i = 1$, unless the BS is activated. It is noted that $F_{\mathrm{y},i} = 0$ is required at the end of each substep i.

RK integration. The Runge-Kutta-Dormand-Prince (RK) scheme detailed in Sloan et al. (2001) is applied to compute the values of $\delta\boldsymbol{\sigma}'$, $\delta p'_0$ and $\delta\boldsymbol{\sigma}'_{\mathrm{a}}$ corresponding to a substep $\delta T_i \Delta\boldsymbol{\varepsilon}$. In the computation of the hardening modulus, the value of $\|\boldsymbol{\beta}\|_{\max,i}$ is computed using STATE_{i-1} (Equation 5.18). The values of $p'_{0,i}$, $\boldsymbol{\sigma}'_{\mathrm{a},i}$, $\|\boldsymbol{\beta}\|_i$ and $\|\boldsymbol{\beta}\|_{\max,i}$ obtained in the RK integration are stored in STATE_i. After a successful substep, $\boldsymbol{\sigma}'_i$ and STATE_i are checked for the necessity of stress correction (see next paragraph). The values of the BS function, $F_{\mathrm{b},i-1}$ and $F_{\mathrm{b},i}$, determine the flow of the next substep. If $\delta T_i = \delta T_{\min}$ and $F_{\mathrm{b},i} > 0$, the stress update will continue in the 'BS update routine' and the discrepancy of $F_{\mathrm{b},i} > 0$ will be addressed by stress correction there.

Stress correction on YS. Immediately after an accepted RK integration of a substep i, if significant yield surface drift has occurred (i.e. $F_{\mathrm{y},i} \neq 0$), then the stress and the hardening parameters are corrected to ensure that the stress point lies on the YS. The iterative stress correction scheme employed is based on that in Sloan et al. (2001), with modification to account for the parameter specifying the centre of the YS, $\boldsymbol{\sigma}'_{\mathrm{a}}$.

The behaviour of F_{y} in the neighbourhood of the uncorrected $F_{\mathrm{y},i}$ can be approximated as a first order Taylor series derived from Equation 5.6.

$$F_{\mathrm{y}} = F_{\mathrm{y},i} + \left(\frac{\partial F_{\mathrm{y}}}{\partial \boldsymbol{\sigma}'}\right)^T \delta^{\mathrm{c}}\boldsymbol{\sigma}' + \frac{\partial F_{\mathrm{y}}}{\partial p'_0}\delta^{\mathrm{c}} p'_0 + \left(\frac{\partial F_{\mathrm{y}}}{\partial \boldsymbol{\sigma}'_{\mathrm{a}}}\right)^T \delta^{\mathrm{c}}\boldsymbol{\sigma}'_{\mathrm{a}} \tag{5.19}$$

where $\delta^{\mathrm{c}}\boldsymbol{\sigma}'$, $\delta^{\mathrm{c}} p'_0$ and $\delta^{\mathrm{c}}\boldsymbol{\sigma}'_{\mathrm{a}}$ represent small corrections of the variables. Equation 5.19

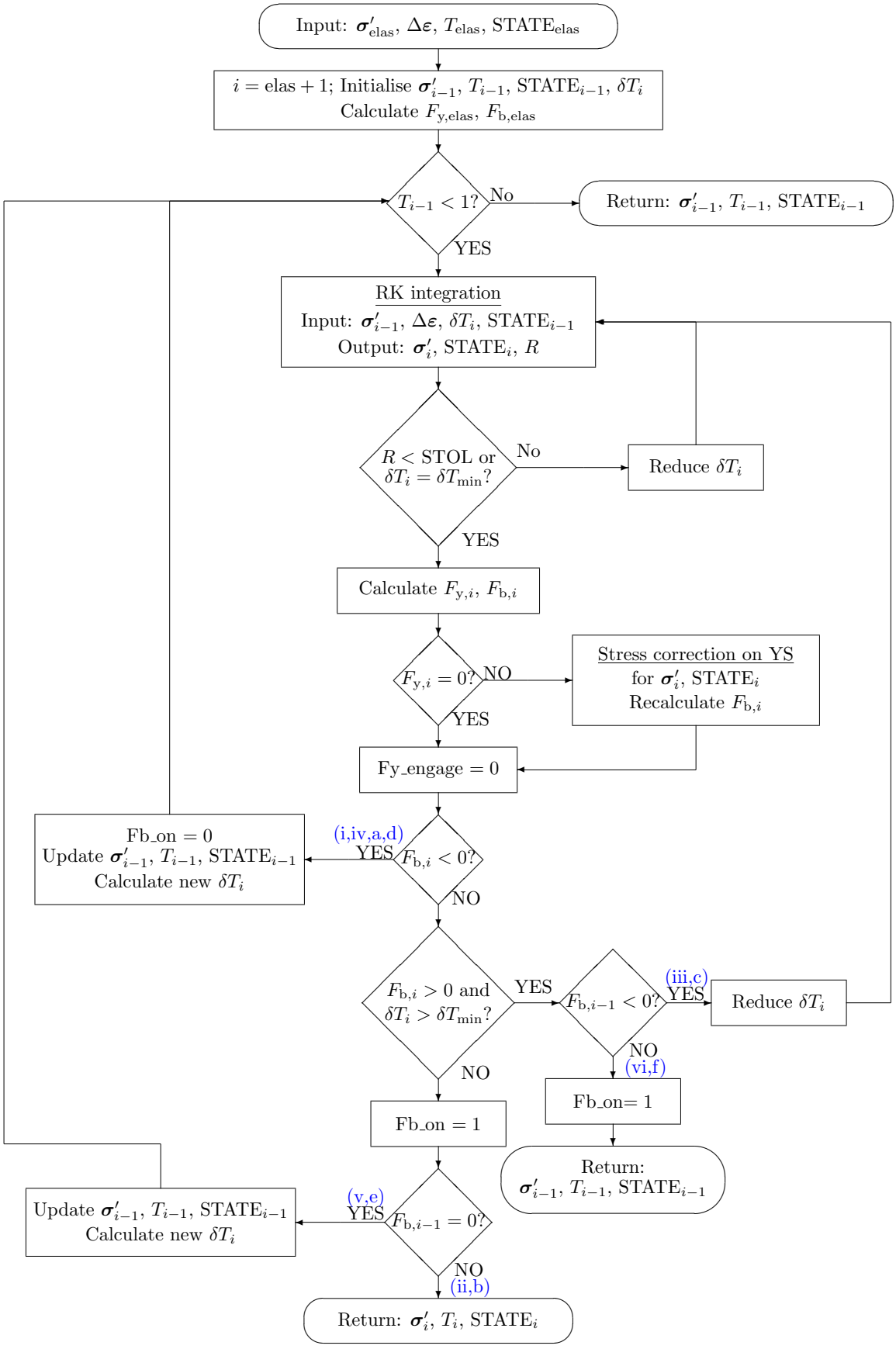


Figure 5.6: Flowchart of the yield surface update routine. The roman numerals refer to the cases in Table 5.3 and Fig. 5.7. The letters refer to the cases in Table 5.4

has one more term compared to the scheme described by Equation 15 in Sloan et al. (2001). In the following, Method (a) is consistent with Sloan et al. (2001) while Method (b) addresses the correction for $\boldsymbol{\sigma}'_{\mathrm{a}}$.

Method (a) – correct by adjusting $\boldsymbol{\sigma}'$ and p'_0

For $\delta^{\mathrm{c}}\boldsymbol{\sigma}'_{\mathrm{a}} = 0$, the last term of Equation 5.19 is eliminated. To conserve the total strain increment,

$$\delta^{\mathrm{c}}\boldsymbol{\sigma}' = \boldsymbol{D}^{\mathrm{e}}(\delta^{\mathrm{c}}\boldsymbol{\varepsilon} - \delta^{\mathrm{c}}\boldsymbol{\varepsilon}^{\mathrm{p}}) = -\boldsymbol{D}^{\mathrm{e}}\delta^{\mathrm{c}}\boldsymbol{\varepsilon}^{\mathrm{p}} = -\delta^{\mathrm{c}}\mu\boldsymbol{D}^{\mathrm{e}}\frac{\partial P_{\mathrm{y}}}{\partial \boldsymbol{\sigma}'} \tag{5.20}$$

where $\delta^{\mathrm{c}}\boldsymbol{\varepsilon}^{\mathrm{p}}$ is the correction of plastic strain increment. Also, according to the flow rule adopted (after Equation 7 in Grammatikopoulou et al. (2006)),

$$\delta^{\mathrm{c}}p'_0 = \delta^{\mathrm{c}}\mu\frac{p'_0}{\lambda^* - \kappa^*}\left(\frac{\partial P_{\mathrm{y}}}{\partial p'}\right) \tag{5.21}$$

Substituting these two equations into Equation 5.19 with $F_{\mathrm{y}} = 0$ gives

$$-F_{\mathrm{y},i} = -\delta^{\mathrm{c}}\mu\left[\left(\frac{\partial F_{\mathrm{y}}}{\partial \boldsymbol{\sigma}'}\right)^T\boldsymbol{D}^{\mathrm{e}}\frac{\partial P_{\mathrm{y}}}{\partial \boldsymbol{\sigma}'} - \frac{p'_0}{\lambda^* - \kappa^*}\frac{\partial F_{\mathrm{y}}}{\partial p'_0}\frac{\partial P_{\mathrm{y}}}{\partial p'}\right] \tag{5.22}$$

and rearranging the equation gives the value of $\delta^{\mathrm{c}}\mu$ and hence $\delta^{\mathrm{c}}\boldsymbol{\sigma}'$ and $\delta^{\mathrm{c}}p'_0$ can be obtained from Equations 5.20 and 5.21.

Method (b) – correct by adjusting $\boldsymbol{\sigma}'_{\mathrm{a}}$

For $\delta^{\mathrm{c}}\boldsymbol{\sigma}' = 0$ and $\delta^{\mathrm{c}}p'_0 = 0$, only the last term on the right side of Equation 5.19 remains. The translation of the centre of the YS within the BS derived from the consistency condition (after Equation 9 in Grammatikopoulou et al. (2006)) is

$$\delta^{\mathrm{c}}\boldsymbol{\sigma}'_{\mathrm{a}} = \frac{\delta^{\mathrm{c}}p'_0}{p'_0}\boldsymbol{\sigma}'_{\mathrm{a}} + \delta^{\mathrm{c}}S\boldsymbol{\beta} = \delta^{\mathrm{c}}S\boldsymbol{\beta} \tag{5.23}$$

Substituting into Equation 5.19 with $F_{\mathrm{y}} = 0$ gives

$$-F_{\mathrm{y},i} = \delta^{\mathrm{c}}S\left(\frac{\partial F_{\mathrm{y}}}{\partial \boldsymbol{\sigma}'_{\mathrm{a}}}\right)^T\boldsymbol{\beta} \tag{5.24}$$

and rearranging the equation gives the value of $\delta^{\mathrm{c}}S$ and hence $\delta^{\mathrm{c}}\boldsymbol{\sigma}'_{\mathrm{a}}$ can be computed from Equation 5.23.

In the current implementation, the principal correction approach employs both Methods (a) and (b) on a '50:50' basis, i.e. $\delta^{\mathrm{c}}\boldsymbol{\sigma}'$ and $\delta^{\mathrm{c}}p'_0$ are calculated by replacing $F_{\mathrm{y},i}$ with $F_{\mathrm{y},i}/2$ in Equation 5.22; and similarly, $\delta^{\mathrm{c}}\boldsymbol{\sigma}'_{\mathrm{a}}$ is obtained using $F_{\mathrm{y},i}/2$ in Equation 5.24. This scheme is applied repeatedly until the corrected $F_{\mathrm{y},i} = 0$.

Nevertheless, if non-convergent behaviour is observed during any iteration of the principal approach, the change computed from the principal approach is discarded and a subsidiary approach is employed. Following Sloan et al. (2001) and as described in Section 4.2.3.4, the subsidiary approach neglects any changes to p'_0 and $\boldsymbol{\sigma}'_{\mathrm{a}}$. This gives a small correction $\delta^{\mathrm{c}}\boldsymbol{\sigma}'$ in which

$$\delta^{\mathrm{c}}\boldsymbol{\sigma}' = -F_{\mathrm{y},i}\left(\frac{\partial F_{\mathrm{y}}}{\partial \boldsymbol{\sigma}'}\right) \Bigg/ \left[\left(\frac{\partial F_{\mathrm{y}}}{\partial \boldsymbol{\sigma}'}\right)^{T}\left(\frac{\partial F_{\mathrm{y}}}{\partial \boldsymbol{\sigma}'}\right)\right] \tag{5.25}$$

In the case of no satisfactory stress state being found using the principal and subsidiary approaches after a certain number of iterations, a third approach involving multi-variable root-finding is adopted as a last resort in the current implementation. Bisection is applied with the uncorrected stress and hardening state and the last estimate of corrected state that is located on the opposite side of the yield surface.

It is noted again that the normalised value of $F_{\mathrm{y},i}$ is only used in checking whether the stress state is on the YS and the 'real' value of $F_{\mathrm{y},i}$ is used in other parts of calculations, for instance Equations 5.22, 5.24 and 5.25.

Possible outcomes and subsequent substeps. After ensuring $F_{\mathrm{y},i} = 0$ at T_i, $F_{b,i}$ is recalculated, STATE_i is updated and the next action can be determined. The possible cases after the first substep in the 'YS update routine' are summarised in Fig. 5.7 and Table 5.3. For cases where the subsequent substep continues in the 'YS update routine', the numerical integration advances with an updated T_{i-1} and δT_i, and the possible outcomes are listed in Table 5.4. The algorithm continues with the YS update routine if $F_{b,i} < 0$, or if $F_{b,i} > 0$ it repeats with a smaller substep size to seek an

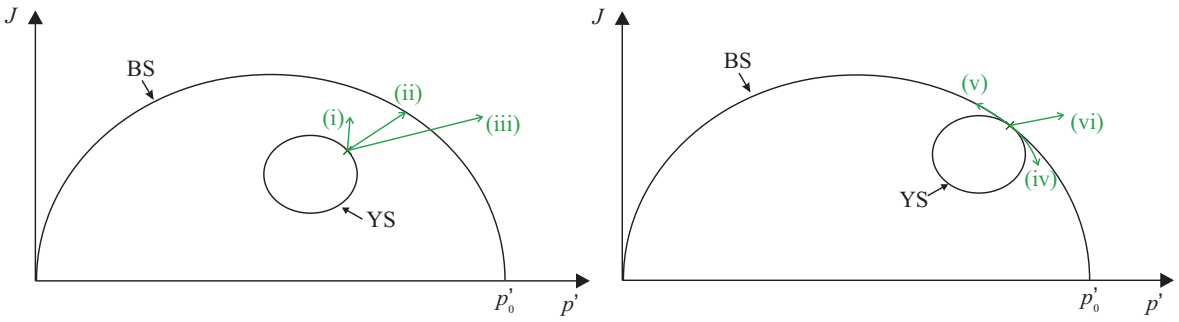


Figure 5.7: Schematic representation of possible cases of the first substep in the YS update routine: (a) initial stress on yield surface; (b) initial stress on bounding surface. The roman numerals refer to the cases in Table 5.3

Table 5.3: Possible outcomes of the first substep in the YS update routine. The letters in the bracket refers to the cases in Table 5.4

Case	$F_{\text{b, elas}}$	$F_{\text{b, elas+1}}$	Representation of behaviour and flow
(i)	< 0	< 0	YS $\rightarrow$ YS, continue with (a, b, c)
(ii)	< 0	$= 0$	YS $\rightarrow$ BS, return with $i = \text{elas} + 1$
(iii)	< 0	> 0	YS $\rightarrow$ BS, repeat with reduced δT_i, until (ii)
(iv)	$= 0$	< 0	BS $\rightarrow$ YS, continue with (a, b, c)
(v)	$= 0$	$= 0$	BS $\rightarrow$ unknown, continue with (d, e, f)
(vi)	$= 0$	> 0	BS $\rightarrow$ BS, return $i = \text{elas}$

intersection with the BS. The stress state exits from 'YS update routine' when $T_i = 1$ or $F_{b,i} = 0$ (or when $\delta T_i = \delta T_{\text{min}}$ and $F_{\text{b},i} > 0$).

5.2.3.3 Bounding surface stress update routine

When the BS is activated, the constitutive model reduces to the MCC model. The YS translates according to the movement of the stress point and the change of size of the BS (Equation 13 in Grammatikopoulou et al. (2006)). The 'BS update routine' in

Table 5.4: Possible outcomes of the subsequent substeps in the YS update routine

Case	$F_{\text{b},i-1}$	$F_{\text{b},i}$	Outcome of the subsequent substep
(a)	< 0	< 0	continue YS
(b)	< 0	$= 0$	return with i
(c)	< 0	> 0	repeat with reduced δT_i, until (b)
(d)	$= 0$	< 0	continue YS
(e)	$= 0$	$= 0$	continue YS, until (d) or (f)
(f)	$= 0$	> 0	return with $i - 1$

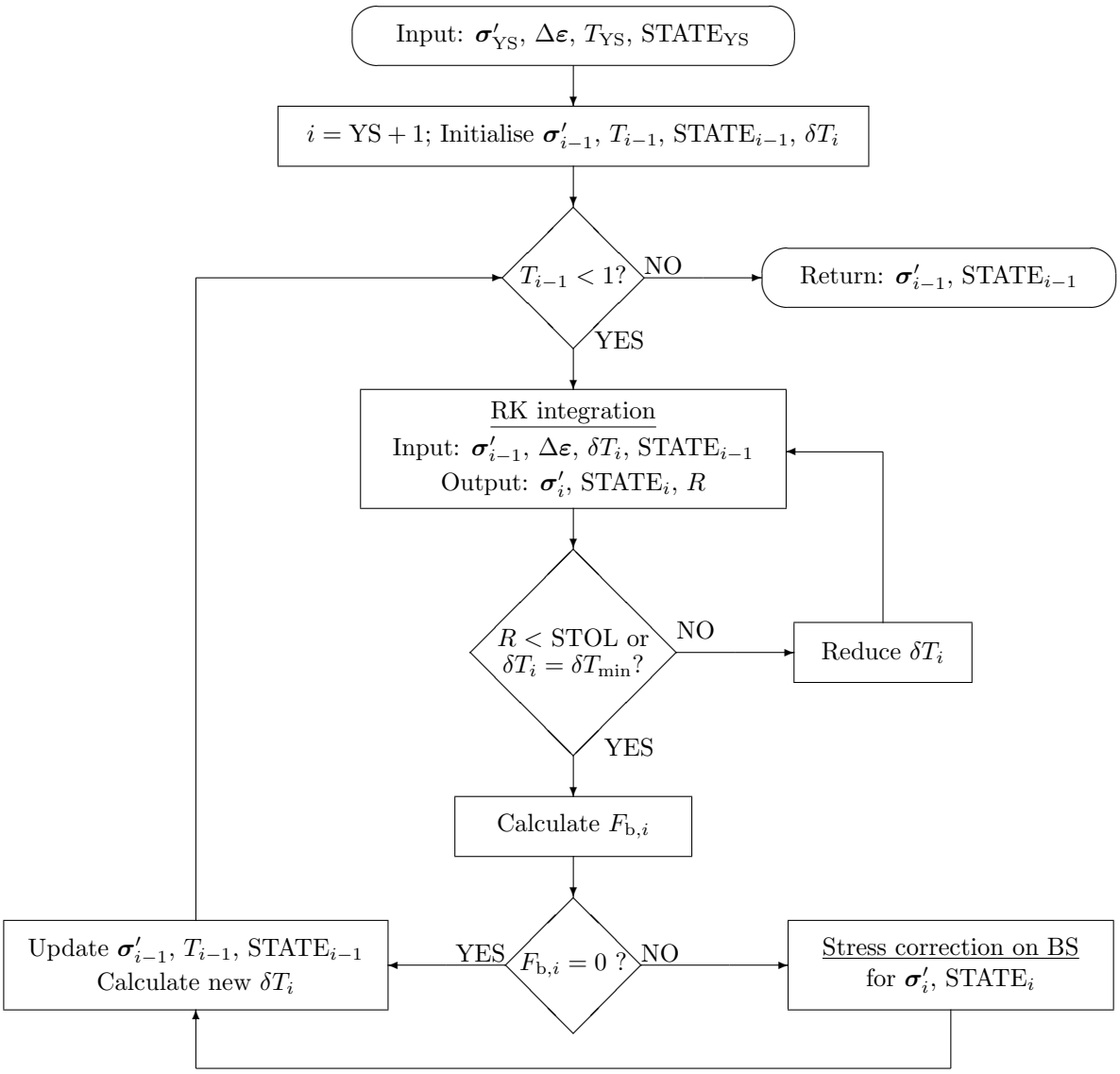


Figure 5.8: Flowchart of the bounding surface update routine

Fig. 5.8 therefore represents a basic stress update scheme using one surface, with stress correction. The yield and bounding conditions $F_{\mathrm{y},i} = 0$ and $F_{\mathrm{b},i} = 0$ are required at the end of substep i.

The update of STATE becomes simpler as $\|\boldsymbol{\beta}\|$ and $\|\boldsymbol{\beta}_{\max}\|$ are zero when the YS and the BS are in contact. The same stress correction scheme as in the 'YS update routine' is used but the principal approach is reduced solely to Method (a).

5.2.3.4 Constitutive matrix

The tangent constitutive matrix (denoted by DDSDDE in Abaqus and $\boldsymbol{D}_n$ in Fig. 5.3) is required in the UMAT to be returned to Abaqus. $\boldsymbol{D}_n$ is computed as follows.

$$\boldsymbol{D}_n = \begin{cases} \boldsymbol{D}^{\mathrm{e}} & \text{when elastic} \\ \boldsymbol{D}^{\mathrm{ep}}_{\mathrm{y}} = \boldsymbol{D}^{\mathrm{e}} - \dfrac{\boldsymbol{D}^{\mathrm{e}} \frac{\partial P_{\mathrm{y}}}{\partial \boldsymbol{\sigma}'} \left(\frac{\partial F_{\mathrm{y}}}{\partial \boldsymbol{\sigma}'}\right)^{\mathrm{T}} \boldsymbol{D}^{\mathrm{e}}}{\left(\frac{\partial F_{\mathrm{y}}}{\partial \boldsymbol{\sigma}'}\right)^{\mathrm{T}} \boldsymbol{D}^{\mathrm{e}} \frac{\partial P_{\mathrm{y}}}{\partial \boldsymbol{\sigma}'} + H} & \text{when only YS is active} \\ \boldsymbol{D}^{\mathrm{ep}}_{\mathrm{b}} = \boldsymbol{D}^{\mathrm{e}} - \dfrac{\boldsymbol{D}^{\mathrm{e}} \frac{\partial P_{\mathrm{b}}}{\partial \boldsymbol{\sigma}'} \left(\frac{\partial F_{\mathrm{b}}}{\partial \boldsymbol{\sigma}'}\right)^{\mathrm{T}} \boldsymbol{D}^{\mathrm{e}}}{\left(\frac{\partial F_{\mathrm{b}}}{\partial \boldsymbol{\sigma}'}\right)^{\mathrm{T}} \boldsymbol{D}^{\mathrm{e}} \frac{\partial P_{\mathrm{b}}}{\partial \boldsymbol{\sigma}'} + H} & \text{when BS is active} \end{cases} \tag{5.26}$$

5.3 Calibration

Avgerinos et al. (2016) present a detailed study of employing the M2-SKH model to represent London Clay, with different calibrations against laboratory tests on intact samples of London Clay, in the context of predicting greenfield ground movements resulting from the excavation of the Jubilee Line Extension tunnels. Four sets of model parameters are named by a combination of 'high' or 'low' depending on the inferred value of the elastic stiffness from undrained triaxial tests, and 'triaxial' or 'both' indicating whether only triaxial test data or both triaxial and oedometer test data were used for calibration. The calibration is detailed in Avgerinos (2014). The finite element results in Avgerinos et al. (2016) show that using the 'low triaxial' parameters in the M2-SKH model provides excellent agreement with field measurements for the short-term surface and subsurface settlements induced by the construction of tunnel, and the 'high both' calibration performs the best among the four calibrations in predicting the long-term tunnelling-induced soil movements. This implies that it is difficult to find a unique set of parameters to calibrate the M2-SKH model for the purpose of both short-term and long-term predictions. The current work focuses on the 'low triaxial' and 'high both' calibrations.

The original aim was to adopt the same model parameters from Avgerinos et al. (2016, Table 3) and conduct the same simulations to validate the current implementation of the M2-SKH model. However, some discrepancies between the two formulations

are noted:

i. The parameters adopted in Avgerinos et al. (2016) indicate that the MCC model is formulated in $v - \ln p'$ space, instead of $\ln v - \ln p'$ space as used in Grammatikopoulou et al. (2006) and employed in the current model (Section 5.1.1).

ii. The measurement of the proximity of the YS to the BS is expressed in terms of different functions, as explained in Section 5.1.4.

iii. The shape of the yield and bounding surfaces in the deviatoric plane employed in Avgerinos et al. (2016) is a Mohr-Coulomb hexagon, while only the smooth van Eekelen surfaces are implemented in the current model (Section 5.1.3).

Therefore, the model parameters provided in Avgerinos et al. (2016, Table 3) could not be adopted directly; instead they are used indirectly to calibrate the current model. London Clay is classified into several geological units according to their properties. Two units are considered in Avgerinos et al. (2016), with unit B2 overlying unit A3. Table 5.5 is an extract of the model parameters corresponding to the 'low triaxial' and 'high both' calibrations for units B2 and A3 from Avgerinos et al. (2016, Table 3) where

v_1: specific volume at 1 kPa in $v - \ln p'$ space

λ: slope of the normal compression line in $v - \ln p'$ space

κ: slope of swelling lines in $v - \ln p'$ space

n, m, A: parameters for calculating the elastic shear modulus

ϕ': angle of internal shearing resistance defining the Mohr-Coulomb hexagon in the deviatoric plane

R: ratio of the yield surface size to that of the bounding surface

α: coefficient of the hardening modulus

Section 5.2.1 describes all the model parameters needed for the current implementation. The same two London Clay units (B2 and A3) are considered in the current model. Considering that n, m, A and R have the same meaning in both implementations, their values in Table 5.5 are adopted directly. This leaves the parameters λ^*, κ^*, X, Y, Z, Y_p, Z_p, α and e_0 for further calibration for each London Clay unit.

Table 5.5: Extract of the model parameters adopted in Avgerinos et al. (2016)

Model parameters	'low triaxial' (London Clay unit B2/ unit A3)	'high both' (London Clay unit B2/ unit A3)
v_1	2.5/2.75	2.5/2.75
λ	0.12/0.15	0.12/0.15
κ	0.06/0.063	0.06/0.063
n	0.87	0.87
m	0.28	0.28
A	250/180	550/470*
ϕ'	25°/20.3°	25°/20.3°
R	0.01/0.005	0.016/0.005
α	0.8	2.5

*obtained from Avgerinos (2014).

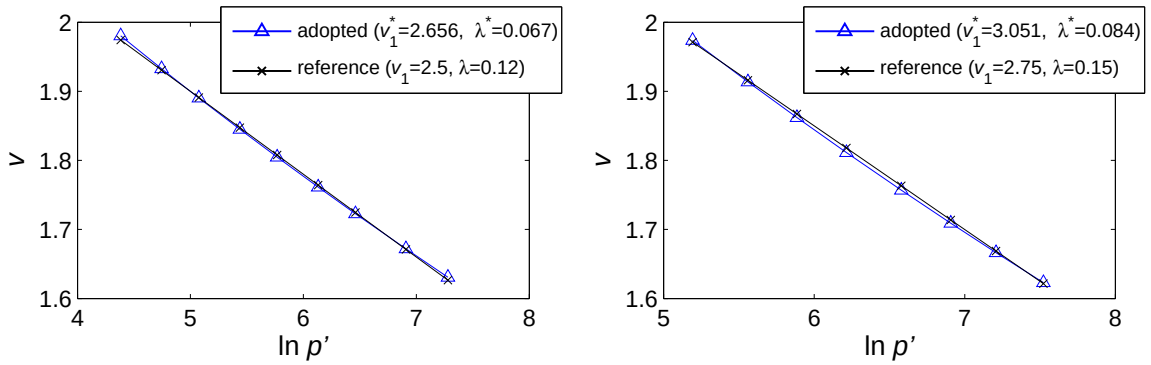
5.3.1 Normal consolidation and swelling lines

The normal consolidation line in $\ln v - \ln p'$ space is defined by the slope, λ^*, and the specific volume at $p' = 1$ kPa, v_1^*. The values of λ^* and v_1^* are obtained by least squares fitting a curve in $v - \ln p'$ space to the linear normal consolidation line obtained using the λ and v_1 adopted by Avgerinos et al. (2016). Only the likely range of p' in the current problem (Section 3.9.3) is considered in the fitting process. The maximum p' value is taken at the base of each clay unit under the overburden pressure of the geological history, and the minimum p' encountered in each unit is approximated to be at the surface of each unit after establishment of the geological stress history. Equation 5.1 is rearranged to compute v in $\ln v - \ln p'$ space for the calibration as

$$v = \exp\left(\ln\left(\frac{v_1^*}{p'^{\lambda^*}}\right)\right) = \frac{v_1^*}{p'^{\lambda^*}} \tag{5.27}$$

Fig. 5.9 shows the implemented model with the adopted parameters in $v - \ln p'$ space and the reference normal consolidation line employed in Avgerinos et al. (2016) for the two units of London Clay. The values of v_1^* and λ^* adopted are 2.656 and 0.067 for unit B2, and 3.051 and 0.084 for unit A3.

It is noted that v_1^* is not a model input parameter in the current formulation of the M2-SKH model. The calibrated value of v_1^* is converted to the initial void ratio (as a function of depth), e_0, as an initial condition that needs to be prescribed for pore



(a) (b)

Figure 5.9: The curve in $v - \ln p'$ space of the current implementation with the adopted parameters, which is fitted with the reference normal consolidation line adopted in Avgerinos et al. (2016): (a) unit B2; (b) unit A3. The unit of p' is kPa

pressure elements in Abaqus (Section 5.2.1).

The slope of the elastic swelling ling, κ^*, is associated with the bulk modulus, K, which is defined by

$$K = -V\frac{dP}{dV} = -v\frac{dp'}{dv} \tag{5.28}$$

where P is pressure and V is volume. Differentiating the swelling line in $\ln v - \ln p'$ space (Equation 5.2) gives

$$\frac{1}{v}dv = -\frac{\kappa^*}{p'}dp' \tag{5.29}$$

Rearranging the equation becomes

$$\frac{p'}{\kappa^*} = -v\frac{dp'}{dv} = K \tag{5.30}$$

which is the definition of elastic bulk modulus used in Equation 5.3. Whereas the swelling line in $v - \ln p'$ space is expressed as

$$v = v_\kappa - \kappa \ln p' \tag{5.31}$$

Differentiating Equation 5.31,

$$dv = -\frac{\kappa}{p'}dp' \tag{5.32}$$

Rearranging Equation 5.32 and multiplying both sides with v gives

$$v\frac{p'}{\kappa} = -v\frac{dp'}{dv} = K \tag{5.33}$$

Comparing the bulk modulus K obtained from the two formulations in Equations 5.30 and 5.33, $\kappa^* = \kappa/v$. As the specific volume v is stress dependent, the value of κ^* is approximated by $\kappa/\bar{v}$, where $\bar{v}$ is the mean value of v corresponding to the same maximum and minimum values of p' considered while calibrating λ^*. The value of κ^* is computed as 0.034 and 0.036 for unit B2 and unit A3 respectively.

5.3.2 Shape of yield and bounding surfaces in deviatoric plane

The model used in Avgerinos et al. (2016) employs a Mohr-Coulomb (MC) hexagon for the yield and bounding surfaces in the deviatoric plane. The function $g(\theta)$ in this case is given by Equation 5.7, with ϕ' being the model parameter in each clay unit ($\phi' = 25°$ and 20.3° for units B2 and A3 respectively). As explained in Section 5.1.3, the family of van Eekelen surfaces represented by Equation 5.8 is implemented in the current work. The calibration of the model parameters X, Y and Z is based on triaxial test data, as detailed below.

Calibrating against triaxial compression and extension test data.
With reference to the experimental results of the undrained triaxial tests in Hight et al. (2007, Fig. 18), the values of ϕ' used in Avgerinos et al. (2016) for units B2 and A3 are the post-rupture angles of shearing resistance obtained from triaxial compression tests, ϕ'_{TXC}, for unit B2(a) (which is a sub-unit of unit B2) and unit A3. The same values are used in the current calibration (i.e. $\phi'_{\mathrm{TXC}} = 25°$ and 20.3° for units B2 and A3 respectively). Moreover, the post-rupture angles of shearing resistance obtained from triaxial extension tests, ϕ'_{TXE}, are 16° for unit B2(a) and 17° for unit A3 (Hight et al. 2007). These ϕ'_{TXE} values are used for units B2 and A3 in this calibration.

An attempt was made to capture the experimental response in both triaxial compression and triaxial extension conditions by fitting a van Eekelen curve that coincides

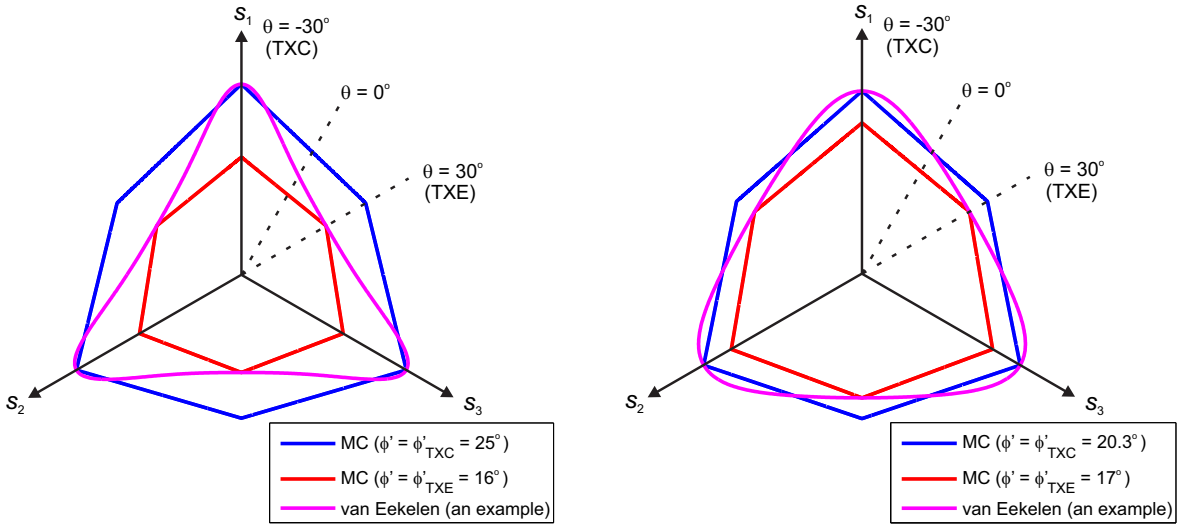


Figure 5.10: Shape of the bounding surfaces in the deviatoric plane using a general van Eekelen equation, calibrated against the angle of shearing resistance from triaxial compression and triaxial extension tests: (a) unit B2; (b) unit A3. An example of the van Eekelen shape with $Z = 0.25$ is displayed

with the MC hexagon of $\phi' = \phi'_{\mathrm{TXC}}$ at the triaxial compression condition ($\theta = -30°$) and also with the MC hexagon of $\phi' = \phi'_{\mathrm{TXE}}$ at the triaxial extension condition ($\theta = 30°$). Fig. 5.10 displays an example of such a fitted van Eekelen curve and the MC hexagons in the deviatoric plane. The example van Eekelen shape is obtained by setting $Z = 0.25$ and solving for X and Y by satisfying the two triaxial conditions. Nevertheless, the curves acquired for unit B2 with various values of Z are found to be concave (Fig. 5.10(a)) since the difference between ϕ'_{TXC} and ϕ'_{TXE} is too large. Convexity of yield surface is highly desirable for numerical stability (van Eekelen 1980).

Calibrating against triaxial compression with Lade shape.

The difficulty with the above approach could be overcome by reducing the difference between ϕ'_{TXC} and ϕ'_{TXE} of unit B2, for example by increasing the assumed ϕ'_{TXE}. Consistent with the assumption inherent in Avgerinos et al. (2016) where only a single angle of shearing resistance is used, the soil behaviour in triaxial extension is assumed to have the same angle of shearing resistance as in triaxial compression, i.e. $\phi'_{\mathrm{TXE}} = \phi'_{\mathrm{TXC}}$. The MC hexagon representing $\phi' = \phi'_{\mathrm{TXC}}$ (25° for unit B2 and 20.3° for unit A3) is shown by the blue line in Fig. 5.11.

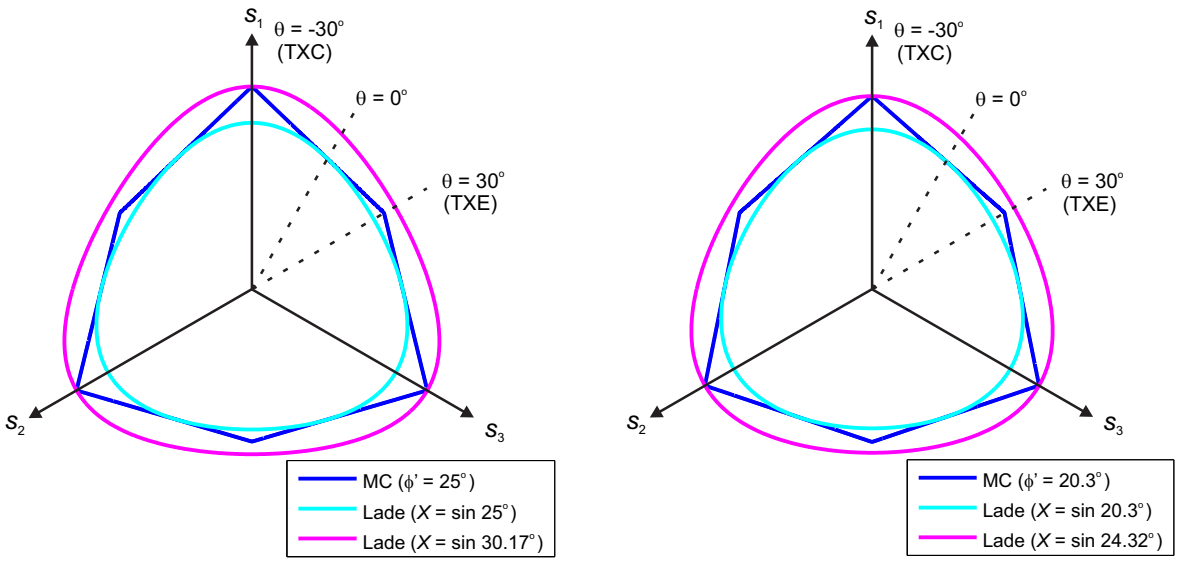


Figure 5.11: Shape of the bounding surfaces in the deviatoric plane with a van Eekelen equation taking Lade shape, calibrated against the angle of shearing resistance in triaxial compression: (a) unit B2; (b) unit A3

The Lade surface (Lade & Duncan 1975) is one of the best-known shapes for smoothing the corners of the MC hexagon. The predicted performance of an embankment resulting from using Lade as the deviatoric shape of the yield and bounding surfaces in the bubble model was shown to be intermediate between those employing a MC hexagon and a circle in Grammatikopoulou et al. (2007). The Lade shape can be expressed in the van Eekelen formulation (Equation 5.8) by setting Y to be $4X/(3\sqrt{3})$ and Z to be 0.25 (van Eekelen 1980). X is defined as $\sin\phi'_{\theta=0}$ (Grammatikopoulou et al. 2006), as $g(\theta) = X$ when $\theta = 0$. If $\phi'_{\theta=0}$ is set to ϕ'_{TXC} (the cyan line in Fig. 5.11), then the Lade shape touches the MC hexagon at $\theta = 0$ and underestimates both the compression and extension strengths implied by the MC hexagon. Alternatively, $\phi'_{\theta=0}$ can be recalculated for X such that the Lade curve coincides with the MC hexagon at the triaxial compression condition, as illustrated by the magenta line in Fig. 5.11. One drawback of this is the overestimation of the strength in triaxial extension.

Calibrating against triaxial compression with Matsuoka-Nakai-like shape. The Matsuoka-Nakai shape captures both the triaxial compression and extension conditions of a MC hexagon (Matsuoka & Nakai 1974). While this may not necessarily

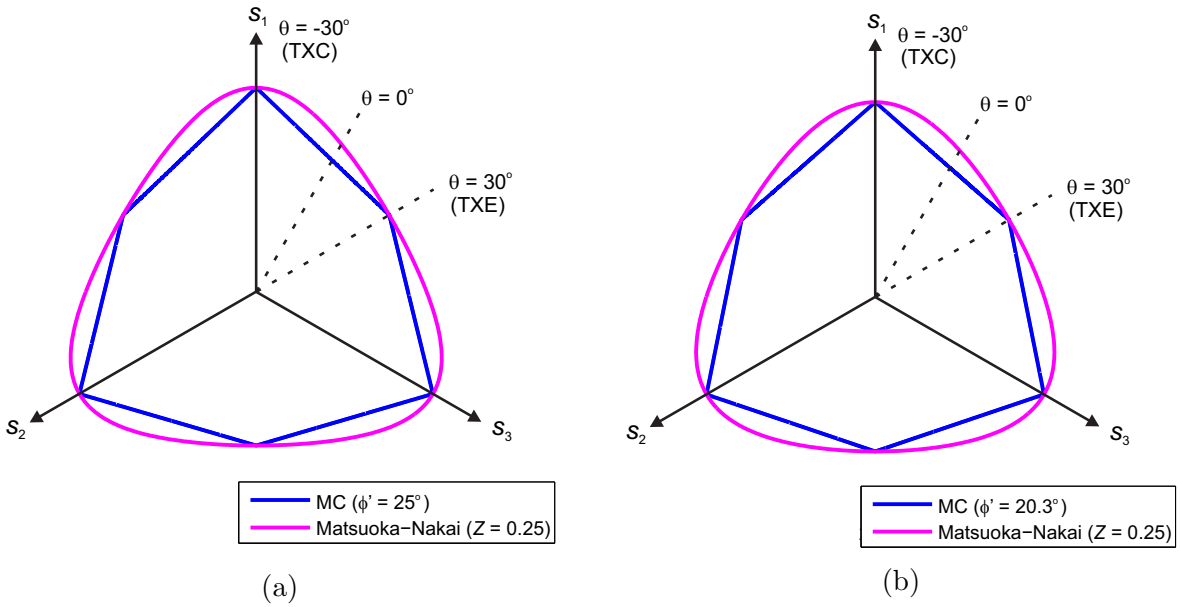


Figure 5.12: Shape of the bounding surfaces in the deviatoric plane with a van Eekelen equation taking Matsuoka-Nakai shape, calibrated against the angle of shearing resistance in triaxial compression: (a) unit B2; (b) unit A3

make the use of the Matsuoka-Nakai shape more correct, it achieves the intentions of smoothing and fulfilling both of the triaxial conditions represented by a MC hexagon.

A Matsuoka-Nakai-like shape expressed in the van Eekelen equation is produced by assuming a value for Z and then solving for X and Y using the conditions that the curve coincides with the MC hexagon at $\theta = 30°$ and $\theta = -30°$. A range of Z values is feasible, and $Z = 0.25$ is adopted with the advantage that the curve remains convex for higher values of ϕ' (van Eekelen 1980). This gives the following values of X and Y: for unit B2, $X = 0.474422$, $Y = 0.513347$ and for unit A3, $X = 0.392934$, $Y = 0.433874$. The corresponding deviatoric shapes are illustrated in magenta in Fig. 5.12.

Current implementation. The Matsuoka-Nakai shape presented in Fig. 5.12, which provides a smooth curve that matches the triaxial conditions represented by the MC hexagon used in Avgerinos et al. (2016), is employed in the current implementation.

5.3.3 Shape of plastic potential surface in deviatoric plane

Following Grammatikopoulou et al. (2008), the plastic potential is assumed to have a circular shape in the deviatoric place. The difference in the deviatoric shape from the

one adopted for the yield and bounding surfaces results in a non-associated flow rule. The circular shape is described by fixing $Y_\mathrm{p} = 0$ and $Z_\mathrm{p} = 1$ in Equation 5.9, giving $g_\mathrm{p}(\theta) = X_\mathrm{p}$ which is independent of θ.

The value of X_p is required whenever the derivative of the plastic potential, $\partial P/\partial \boldsymbol{\sigma}'$ or $\partial P/\partial \boldsymbol{s}$, needs to be determined. On yielding, the current stress state satisfies $F_\mathrm{b} = 0$ or $F_\mathrm{y} = 0$ (Equations 5.5 or 5.6) and there exists a plastic potential surface $P = 0$ of either

$$P_\mathrm{b} = \left(p' - \frac{p'_0}{2}\right)^2 + \frac{1}{2}\frac{\boldsymbol{s}^\mathrm{T}\boldsymbol{s}}{X_\mathrm{p}^2} - \frac{{p'_0}^2}{4} + k_\mathrm{b} = 0 \text{ , or} \tag{5.34}$$

$$P_\mathrm{y} = (p' - {p_\mathrm{a}}')^2 + \frac{1}{2}\frac{(\boldsymbol{s} - \boldsymbol{s}_\mathrm{a})^\mathrm{T}(\boldsymbol{s} - \boldsymbol{s}_\mathrm{a})}{X_\mathrm{p}^2} - R^2\frac{{p'_0}^2}{4} + k_\mathrm{y} = 0 \tag{5.35}$$

depending on which surface is active, and k_b and k_y are undetermined constants. By comparing the terms in Equation 5.5 with 5.34 and Equation 5.6 with 5.35, one trivial option for X_p is $g(\theta_\mathrm{b})$ or $g(\theta_\mathrm{y})$ respectively. It is noted that only the current value of $g(\theta_\mathrm{b})$ or $g(\theta_\mathrm{y})$ is involved, and X_p is independent of the stress state and the Lode angle.

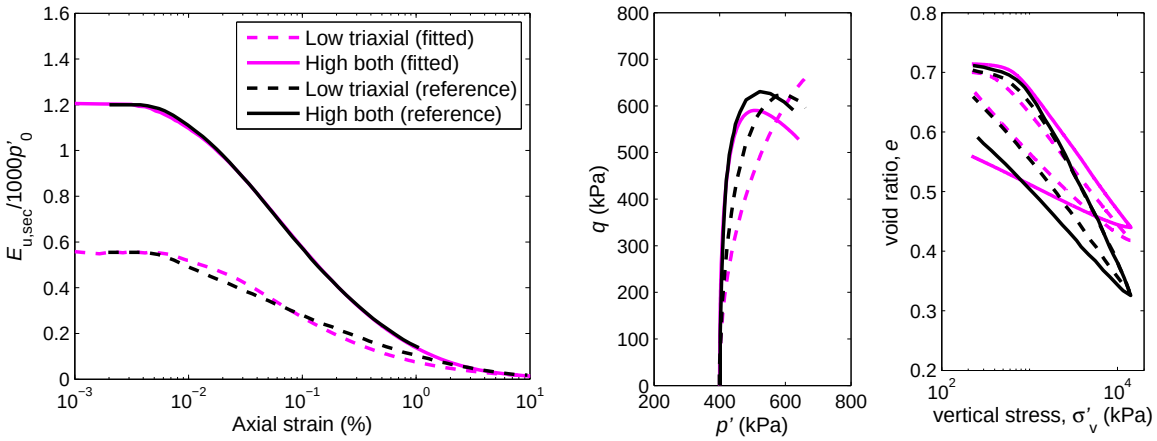
5.3.4 Hardening parameter

The parameter α is the coefficient of the hardening modulus H_1 (Equation 5.16) and it controls the rate of stiffness degradation. As described in Avgerinos (2014), α was the last model parameter to be calibrated, through a trial-and-error process. The α for the 'low triaxial' calibration was obtained by fitting the undrained triaxial compression test with the 'lower' elastic stiffness test data, while that for the 'high both' calibration was first determined from fitting the triaxial test with the 'higher' elastic stiffness test data and then adjusted to be consistent with the oedometer test data.

The aim of the current calibration is to match the calibration in Avgerinos (2014). The values of α for both the 'low triaxial' and 'high both' calibrations are determined based on the triaxial test simulation results and checked with the oedometer results, via best fit by eye. Simulations of the undrained triaxial compression test and the oedometer test for units B2 and A3 are conducted with the current M2-SKH model

Table 5.6: Yield stress ratios adopted for the undrained triaxial compression test and odeometer test simulations (after Avgerinos (2014))

	low triaxial		high both	
	unit B2	unit A3	unit B2	unit A3
triaxial	5.5	9.4	5.2	8.0
oedometer	9.8	6.8	9.2	5.8



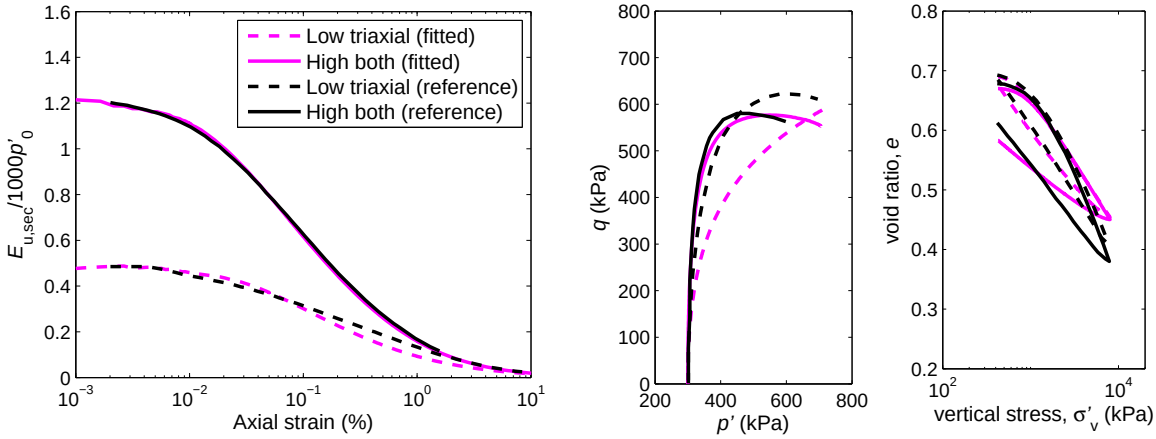
(a) (b) (c)

Figure 5.13: Simulated element test results for the calibration of α against data in Avgerinos (2014) for unit B2: (a) stiffness response from triaxial test; (b) stress path of triaxial test; (c) void ratio-effective stress response from oedometer test. In the plot, 'fitted' denotes the results of the current model and 'reference' denotes the data in Avgerinos (2014)

using a 3D unit cubic element (element type C3D20RP in Abaqus). The values of yield stress ratio, YSR, which defines the initial size of the BS relative to the initial stress state in Avgerinos (2014) (YSR $= p'_0/p' =$ overconsolidation ratio), adopted for the individual simulation are listed in Table 5.6. The simulated element test results and the corresponding data from Avgerinos (2014) are shown in Figs 5.13 and 5.14 for unit B2 and unit A3 respectively. For 'low triaxial', α is 0.4 for unit B2 and 0.5 for unit A3. For 'high both', the best-fit α is taken as 2.6 for unit B2 and 3.0 for unit A3.

5.3.5 Correlations between the hardening parameter, K_0 profile and overburden stress

Before validating the implemented M2-SKH model with predictions of tunnelling-induced ground movements, plane strain simulations of the geological stress history



(a) (b) (c)

Figure 5.14: Simulated element test results for the calibration of α against data in Avgerinos (2014) for unit A3: (a) stiffness response from triaxial test; (b) stress path of triaxial test; (c) void ratio-effective stress response from oedometer test. In the plot, 'fitted' denotes the results of the current model and 'reference' denotes the data in Avgerinos (2014)

at St James's Park are conducted using the ground details shown in Fig. 5.18 and the calculation steps 1 to 4 described in Section 3.9.3. The lateral stress coefficient, K_0, over the depth of the soil after the geological stress history, prior to tunnel construction, is obtained. The K_0 profile is important in modelling the ground response to tunnelling as a lower K_0 profile has been found to be favourable for producing narrower surface settlement troughs, which are closer to the shape measured in the field (Franzius et al. 2005*a*). However, values of K_0 estimated for London Clay tend to be relatively high (e.g. 0.8 to 2 in Withers et al. (2001), 1 to 4 in Hight et al. (2007)). A careful balance is therefore needed between a high K_0 profile (representative of real conditions) and a low K_0 profile (required for realistic settlement trough prediction).

Avgerinos et al. (2016) show that the K_0 profile at the end of the geological stress history in the simulation is sensitive to the value of the hardening parameter α. As some features of the M2-SKH model are modified during the implementation, it is expected that the computed K_0 profile will differ from that in Avgerinos et al. (2016). Moreover, during the simulation of the geological history process, an initial K_0 value of $1 - \sin\phi'$ was assumed and an initial overburden stress of 1835 kPa, representing approximately 180 m of eroded overlying deposits, was applied in Avgerinos et al. (2016). These two assumptions, which bear some degree of uncertainty, also affect the

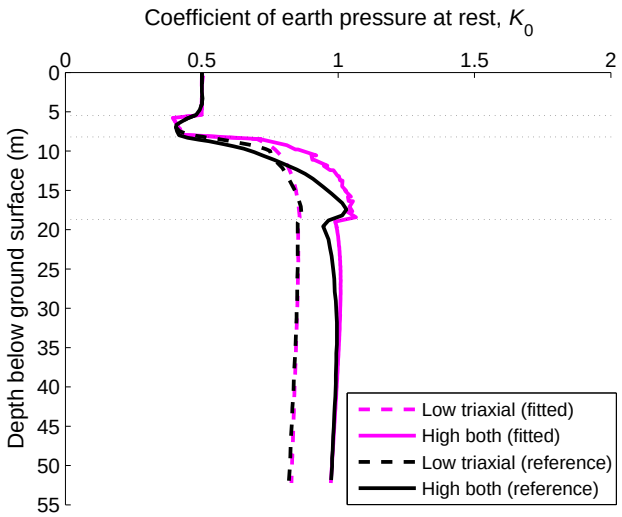


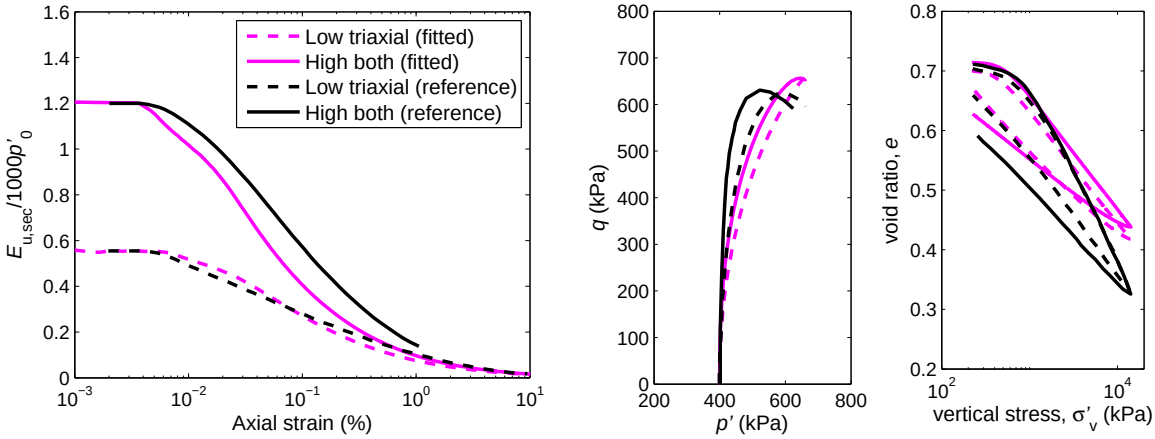
Figure 5.15: K_0 profiles at the end of geological stress history obtained from the recalibrated overburden stress and model parameters. In the plot, 'fitted' denotes the results of the current model and 'reference' denotes the data in Avgerinos et al. (2016)

computed K_0 profile at the end of the geological history.

Due to the significance of K_0 for the tunnelling-induced settlement, the aforementioned assumptions are adjusted to match the simulated K_0 profile with the one in Avgerinos et al. (2016, Fig. 6). The adopted approach keeps the initial value of K_0 as $1 - \sin\phi'$ ($\phi' = 25°$ for unit B2 and $\phi' = 20.3°$ for unit A3) and adjusts the assumed overburden stress based on the K_0 profile at the end of the geological stress history, first using the 'low triaxial' parameters. The best-fit K_0 profile for 'low triaxial', which is determined by eye (Fig. 5.15), corresponds to an overburden stress of 1300 kPa. Then, to impose consistency with this assumed overburden stress and match the K_0 profile, the hardening parameter α of 'high both' is recalibrated against the K_0 profile with the new overburden stress. The new values of α are 0.7 for unit B2 and 1.5 for unit A3, and the fitted K_0 profile for 'high both' is also shown in Fig. 5.15. The responses of the triaxial compression test and odeometer test simulations using the new α in 'high both' are indicated in Figs 5.16 and 5.17. The performance of the stiffness degradation using the adjusted 'high both' parameters appears to be reasonable.

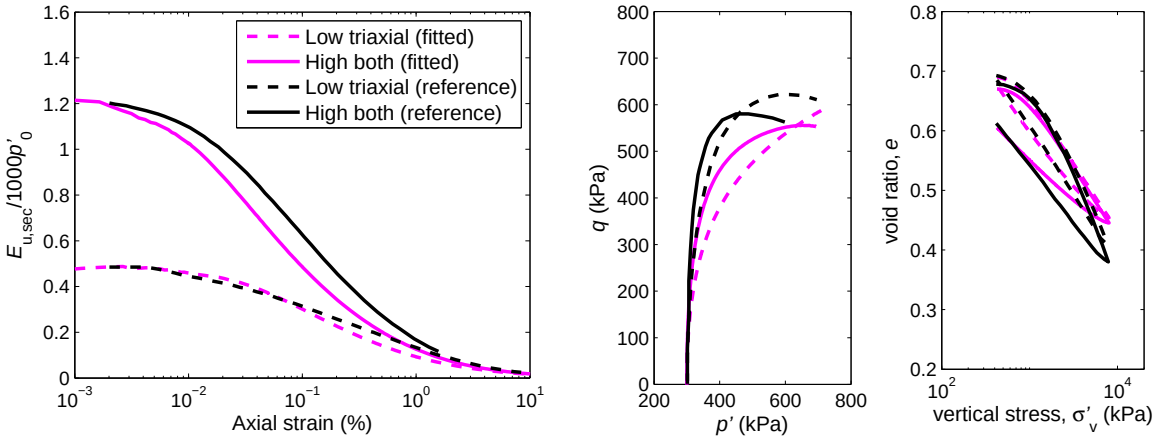
5.3.6 Summary of the adopted parameters

The calibrated parameters for the current M2-SKH model are summarised in Table 5.7.



(a) (b) (c)

Figure 5.16: Simulated element test results after the adjustment of α for the 'high both' calibration for unit B2: (a) stiffness response from triaxial test; (b) stress path of triaxial test; (c) void ratio-effective stress response from oedometer test. The response using the 'low triaxial' calibration is also plotted. In the plot, 'fitted' denotes the results of the current model and 'reference' denotes the data in Avgerinos (2014)



(a) (b) (c)

Figure 5.17: Simulated element test results after the adjustment of α for the 'high both' calibration for unit A3: (a) stiffness response from triaxial test; (b) stress path of triaxial test; (c) void ratio-effective stress response from oedometer test. The response using the 'low triaxial' calibration is also plotted. In the plot, 'fitted' denotes the results of the current model and 'reference' denotes the data in Avgerinos (2014)

Table 5.7: Adopted M2-SKH model parameters

Model parameters	'low triaxial' (London Clay unit B2/A3)	'high both' (London Clay unit B2/A3)
λ^*	0.067/0.084	0.067/0.084
κ^*	0.034/0.036	0.034/0.036
X	0.474422/0.392934	0.474422/0.392934
Y	0.513347/0.433874	0.513347/0.433874
Z	0.25	0.25
Y_{p}	0	0
Z_{p}	1	1
R	0.01/0.005	0.016/0.005
α	0.4/0.5	0.7/1.5‡
n	0.87	0.87
m	0.28	0.28
A	250/180	550/470
$v_1^{\dagger}$	2.656/3.051	2.656/3.051

† employed in the form of initial void ratio

‡ based on the adjusted overburden stress of 1300 kPa

5.4 Validation with greenfield response induced by tunnelling modelled in plane strain

The implementation and calibration of the M2-SKH model are validated by modelling the greenfield ground movements at St James's Park during excavation of the Jubilee Line Extension tunnels and comparing the data with the numerical results and field measurements in Avgerinos et al. (2016). The simulations are based on Avgerinos et al. (2016) and Grammatikopoulou et al. (2008) and the modelling procedures are summarised below.

The geometrical details of the ground and the tunnels are shown in Fig. 5.18. The assumed soil profile consists of made ground, Terrace Gravel and London Clay unit B2 and unit A3; with London Clay unit A3 extending to a far depth. The westbound (WB) tunnel is excavated prior to the eastbound (EB) tunnel. The volume losses of the WB and EB tunnels are 3.3% and 2.9% respectively. The tunnels are supported with concrete tunnel linings with an assumed thickness of 500 mm.

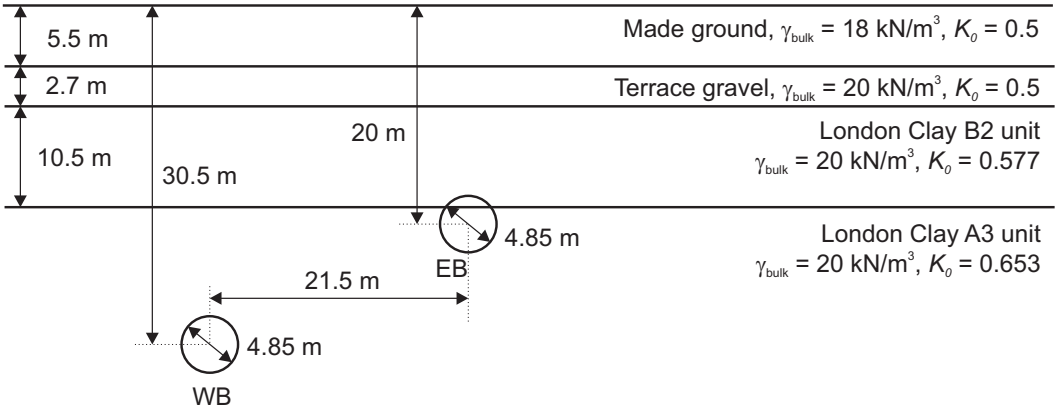


Figure 5.18: Geometrical details of ground and tunnels at St James's Park (after Avgerinos et al. 2016)

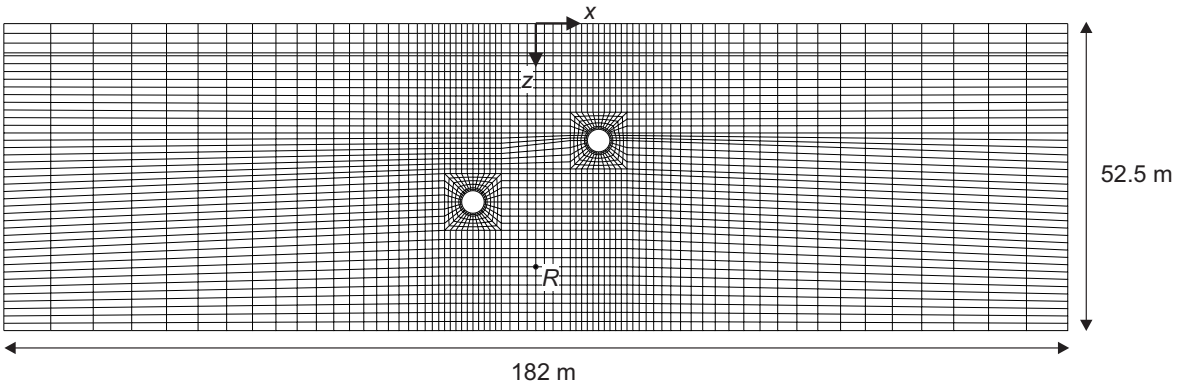


Figure 5.19: Mesh employed for plane strain simulation of the Jubilee Line Extension tunnels. Also shows the coordinate axes, and the reference point R at the depth of 40 m

Mesh. The problem is modelled in plane strain and the mesh is shown in Fig. 5.19. The mesh size follows that used in Avgerinos et al. (2016). The soil and the tunnel lining are modelled with Abaqus element types CPE8RP and CPE8R respectively.

Boundary condition. The bottom of the mesh is fixed in both vertical and horizontal directions and the vertical boundaries have roller supports. The initial water table is located at the surface of the London Clay. The pore pressure is set to be hydrostatic at the boundaries. Zero pore water pressure and a drainage-only flow boundary condition are applied at the tunnel periphery. A no-flow condition is temporarily applied to the boundaries over the whole model during the undrained calculation steps.

Constitutive model. The assumed bulk unit weight, γ_{bulk}, and initial K_0 value of the soil are shown in Fig. 5.18. The soil is assumed to be fully saturated ($S_{\text{sat}} = 1$).

γ_{bulk} needs to be converted to dry density, ρ_{dry}, for coupled pore fluid flow and stress analysis in terms of total pore pressure in Abaqus, as follows.

$$\rho_{\text{dry}} = \left(\gamma_{\text{bulk}} - \frac{S_{\text{sat}} e}{1+e}\gamma_{\text{w}}\right)/g \tag{5.36}$$

where e is the void ratio, γ_{w} is the unit weight of water and g is the gravitational acceleration.

The made ground is modelled as a linear elastic material with Young's modulus $E = 5000$ kPa and Poisson's ratio $\nu = 0.3$ (Avgerinos et al. 2016). The Terrace Gravel is represented by a linear elastic, perfectly plastic Mohr-Coulomb model. Based on Addenbrooke et al. (1997), the model parameters for the Terrace Gravel are taken as $E = 6000z$ kPa, $\nu = 0.2$, angle of friction $\phi' = 35°$, angle of dilation $\psi = 17.5°$ and cohesion $c' = 0.1$ kPa (for numerical stability). In the current simulation, $\nu = 0.28$ is adopted for the Terrace Gravel to obtain a K_0 profile matching that in Avgerinos et al. (2016). The London Clay unit B2 and unit A3 employ the M2-SKH model with the parameters listed in Table 5.7. Separate calculations are conducted using the 'low triaxial' and 'high both' calibrations. The concrete tunnel lining adopts a linear elastic model with $E = 28 \times 10^6$ kPa, $\nu = 0.15$ and $\gamma = 24$ kN/m^3 (Addenbrooke et al. 1997).

Permeability and initial void ratio. The permeability and initial void ratio of both the made ground and the Terrace Gravel are assumed to be 10^{-8} m/s and 0.3 respectively (Geotechdata.info 2013). For the London Clay, the anisotropic permeability model described in Avgerinos et al. (2016) is used. The vertical permeability, k_{v}, is assumed to be linear with depth in $\log k_{\text{v}} - z$ space. The value of k_{v} at the top of unit B2 is 2.3×10^{-10} m/s and decreases with depth to 2.5×10^{-11} m/s at the bottom of unit A3. The horizontal permeability is $k_{\text{h}} = 2k_{\text{v}}$. In addition, the upper 5 m of unit A3 has a constant $k_{\text{v}} = 3 \times 10^{-10}$ m/s and $k_{\text{h}} = 25k_{\text{v}}$ to account for the high permeability encountered in this region. The initial void ratio of the London Clay is calculated from the calibrated v_{I}^* as described in Section 5.2.1. Its magnitude decreases with depth from 0.6413 to 0.6352 for unit B2 and from 0.6514 to 0.6293 for unit A3.

Calculation sequence. The development of geological stress history is first modelled as described in Steps 1 to 4 of Section 3.9.3. Next, the excavation of the WB tunnel is simulated using the nodal force reduction method with the volume loss control approach (Section 3.9.2) under undrained conditions. The tunnel lining is activated when the target volume loss is reached. A consolidation period of eight months is then simulated before the excavation of the EB tunnel is modelled with the same technique. Finally, the long-term consolidation is simulated and data are collected at one year, 10 years and 15 years after the construction of both tunnels.

5.4.1 Short-term ground response

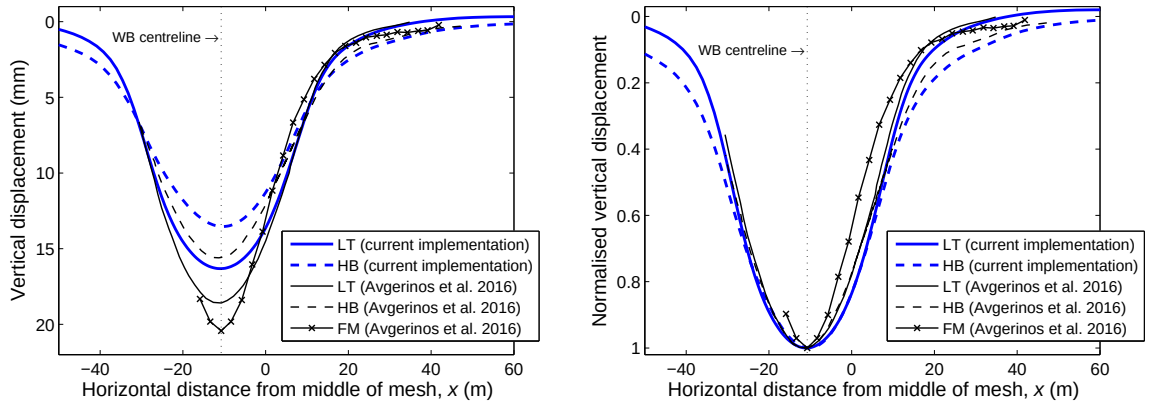
The results of the simulations can be categorised into three time scales. The analysis after the installation of the lining of the WB tunnel specifies the short-term response to tunnelling (denoted as 'after WB').

Owing to the nature of the nodal force reduction method, it can only provide an approximation to the desired volume loss, $\widetilde{V}_{\mathrm{L}}^{\mathrm{T}}$. The actual volume loss, $V_{\mathrm{L}}^{\mathrm{T}}$, is determined by back calculation. The value of $V_{\mathrm{L}}^{\mathrm{T}}$ and the corresponding percentage of unloading for the WB tunnel are listed in Table 5.8, with reference to those presented in Avgerinos et al. (2016). The percentage of unloading with the current implementation is comparable to that of Avgerinos et al. (2016) for each set of model parameters.

Fig. 5.20(a) plots the net surface vertical displacement profiles induced by the excavation of the WB tunnel obtained from the current implementation, the numerical results in Avgerinos et al. (2016) and the field measurements shown in Avgerinos et al. (2016). Although there is some discrepancy in the magnitudes of the settlement between the current analyses and the ones in Avgerinos et al. (2016), the differences in magnitude between the 'low triaxial' and 'high both' calibrations in the individual implementations are similar. Moreover, the normalised vertical displacement profiles shown in Fig. 5.20(b) confirm that the shapes of the settlement troughs from the two implementations are in close agreement. Yet the field measurement features a noticeably narrower profile. Consistent with Avgerinos et al. (2016), the results obtained

Table 5.8: Actual values of tunnel volume loss, $V_{\mathrm{L}}^{\mathrm{T}}$, and percentage of unloading for WB tunnel. Target $\widetilde{V}_{\mathrm{L}}^{\mathrm{T}} = 3.3\%$

	Current results		Avgerinos et al. (2016)	
	$V_{\mathrm{L}}^{\mathrm{T}}$ (%)	Unloading (%)	$V_{\mathrm{L}}^{\mathrm{T}}$ (%)	Unloading (%)
Low triaxial	3.36	12.4	3.39	13.5
High both	3.37	31.4	3.37	37.0



(a) (b)

Figure 5.20: Surface vertical displacement profiles induced by WB tunnel: (a) computed magnitude; (b) normalised by maximum settlement. LT: low triaxial, HB: high both, FM: field measurement

with the 'low triaxial' calibration provide a narrower and deeper vertical displacement profile after the construction of the WB tunnel than using the 'high both' parameters. Hence, the 'low triaxial' calibration is considered to be more suitable for predicting the short-term ground response.

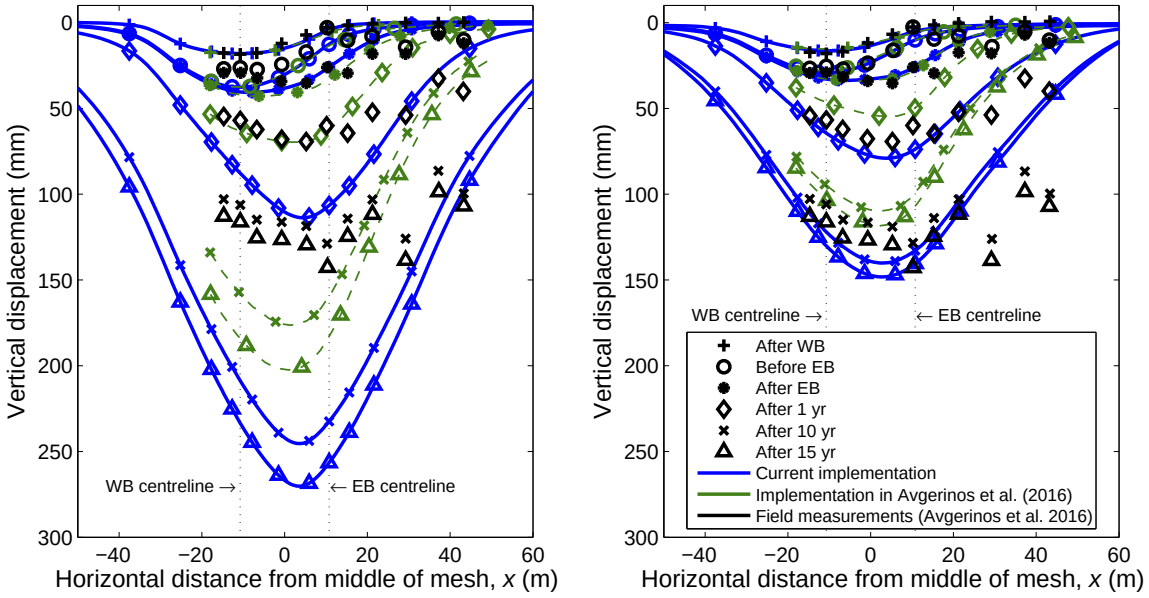
5.4.2 Medium-term ground response

The medium-term corresponds to the cases after the eight-month consolidation period between the two tunnel constructions (denoted as 'before EB') and immediately after the installation of the lining of the EB tunnel (denoted as 'after EB'). Table 5.9 shows the actual volume loss and the percentage of unloading for the EB tunnel.

The relative vertical movements at 5 m below ground level at various time points are plotted in Fig. 5.21. These movements are relative to the reference point (point R in Fig. 5.19) which represents the base of a borehole at a depth of 40 m between

Table 5.9: Actual values of tunnel volume loss, $V_{\mathrm{L}}^{\mathrm{T}}$, and percentage of unloading for EB tunnel. Target $\widetilde{V}_{\mathrm{L}}^{\mathrm{T}} = 2.9\%$

	Current results	
	$V_{\mathrm{L}}^{\mathrm{T}}$ (%)	Unloading (%)
Low triaxial	2.90	15.7
High both	2.94	42.4



(a) (b)

Figure 5.21: Vertical displacement profiles at 5 m below ground level relative to the reference point R (Fig. 5.19) at various time points, compared to the simulation results and field measurements in Avgerinos et al. (2016): (a) low triaxial; (b) high both

the two tunnels. The simulation results and field measurements from Avgerinos et al. (2016) are also plotted in Fig. 5.21. There is excellent agreement in the magnitude and shape of the computed medium-term ground movements (at 'before EB' and 'after EB') between the current implementation and that of Avgerinos et al. (2016), especially for the 'high both' calibration (Fig. 5.21(b)). It is noted that after the construction of the EB tunnel, the location of the maximum settlement shifts to be between the two tunnel centrelines, indicating the effect of tunnel-tunnel interaction. The comparison between the finite element analyses and the field measurements for the medium-term ground response is also close, although the measured settlement troughs are slightly wider.

5.4.3 Long-term ground response

The consolidation after the two tunnel constructions is referred to as the long-term ground response. Fig. 5.21 also shows the profiles of vertical movements one year, 10 years and 15 years after the construction of both tunnels (denoted as 'after 1 yr', 'after 10 yr' and 'after 15 yr'). These time points are approximated from the dates recorded in Nyren et al. (2001), Avgerinos (2014) and Avgerinos et al. (2016).

The calculation using the 'low triaxial' calibration in Avgerinos et al. (2016) is shown to overpredict the long-term ground movement and compute relatively narrow long-term settlement troughs. The current analysis unfortunately amplifies the overprediction of the long-term consolidation measured in the field when the 'low triaxial' parameters are used (Fig. 5.21(a)).

Alternatively, Avgerinos et al. (2016) demonstrate that the analysis employing the 'high both' parameters gives better predictions in terms of the magnitude and the shape of the settlement troughs between the two tunnels. Consistently, the current implementation using the 'high both' calibration displays significant improvements in the prediction of the magnitude of the settlement and the development of the trough width for the long-term ground response, as shown in Fig. 5.21(b).

Although the current analysis using the 'high both' parameters slightly overpredicts the maximum settlement, in comparison to the underprediction in Avgerinos et al. (2016), the computed long-term settlement trough widths from the current implementation are wider and more like the field measurements (Fig. 5.21(b)). This improvement is particularly noticeable for the result at 'after 1 yr'. For the longer durations 'after 10 yr' and 'after 15 yr', the settlement troughs measured in the field widen and extend considerably towards the east, which cannot be simulated in either analysis. The current analysis, however, provides reasonable settlement profiles up to around 15 m eastwards from the centreline of the EB tunnel. The performance of the current implementation using the 'high both' parameters is thus considered to be satisfactory for the prediction of long-term ground response.

Chapter 6

Total stress analysis of building response to tunnelling

The total stress analysis (TSA) method, which provides efficient calculations for problems assuming undrained conditions, is employed for analysing short-term building response to tunnelling. The 3D isolated facade analysis approach is exploited to investigate the tunnel-soil-building interaction, and to conduct a series of parametric studies. The assumptions of the conventional EBA method are evaluated with reference to the finite element results. Some 3D complete building calculations are also conducted.

The finite element models and the detailed calculation procedures for TSA are described in Chapter 3 and Section 3.8. The principal analyses use the multiple von Mises yield surface kinematic hardening model for the London Clay, the extended Mohr-Coulomb (EMC) model for the Terrace Gravel, a non-linear constitutive model for the masonry, and a frictional contact model for the soil-foundation interface. The displacement field method is employed to model the tunnel excavation process. The finite element data are processed using the methods described in Section 3.10.

6.1 Calculations and example meshes

On the basis of the scenario described in Section 3.1, a series of greenfield, isolated facade and complete building analyses are developed to investigate the influence of

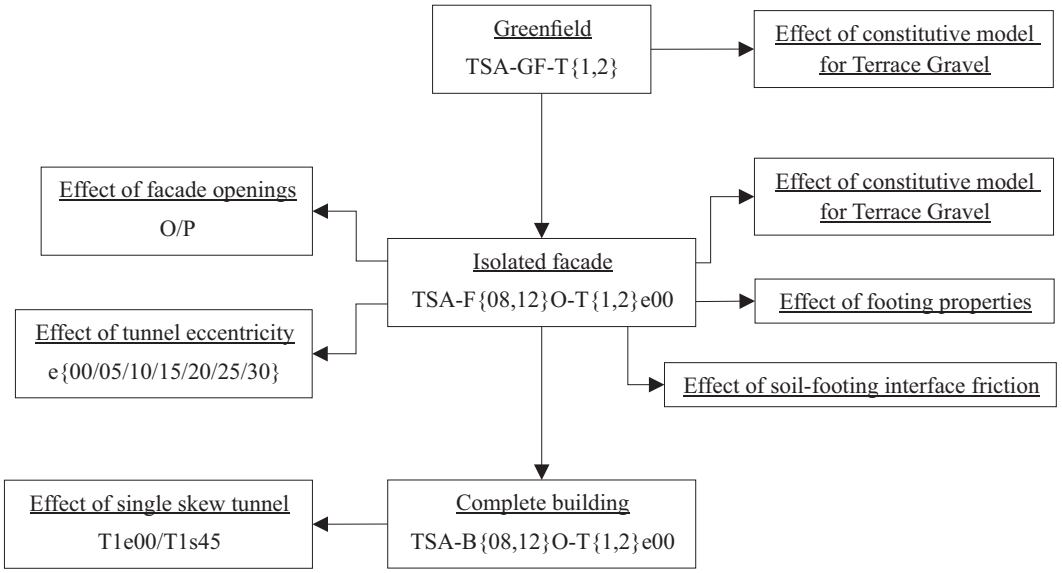


Figure 6.1: Structure of the study of the short-term effect of tunnelling in total stress analysis

various features using the TSA. The outline of the study is summarised in Fig. 6.1.

Each configuration is assigned a unique code (see Table 6.1) to characterise the geometric setting and a separate mesh is generated. The model code consists of three parts. Firstly, all the simulations in this chapter starts with 'TSA' to indicate that the modelling procedures and constitutive models developed for total stress analysis are employed. The second part of the code describes the building modelling approach ('F' for 3D isolated facade approach, 'B' for 3D complete building approach), building height ('08' for $H = 8$ m, '12' for $H = 12$ m) and presence of openings ('O' for facade with openings or 'P' for plain facade). When the simulation is conducted under greenfield conditions (i.e. without the building), this part is substituted by 'GF'. The third part defines the tunnel case ('T1' for single tunnel, 'T2' for twin tunnels) followed by its eccentricity to the facade ('e__', where __ indicates the value of eccentricity). The eccentricity is defined differently for the single-tunnel and twin-tunnel cases as illustrated in Fig. 3.4. The skew tunnel case (only applicable for the complete building analysis) is denoted by 's__', where __ indicates the angle between the tunnel alignment and the building centreline. For instance, 'TSA-F08P-T2e05' refers to a total stress analysis using the isolated facade analysis approach modelling a plain facade of height 8 m in the case of twin tunnels with an eccentricity of 5 m and 'TSA-B12O-T1e00' represents the total stress analysis using the complete building analysis approach modelling a

Table 6.1: Code representation to characterise the geometrical setting

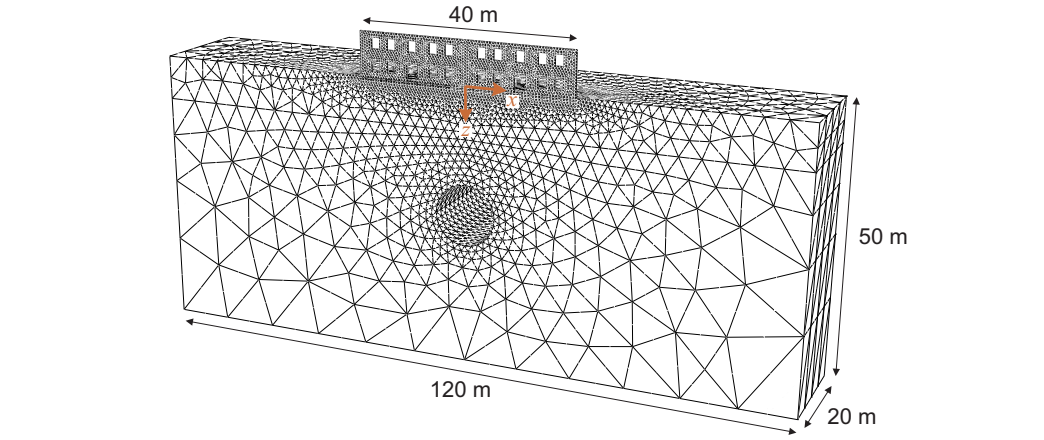
Parameter	Code components
Total stress analysis	TSA
Greenfield analysis	GF
Coupled analysis – building configuration	
Isolated facade/ completed building	F/B
Building height	08/12
Facade with openings/ plain facade	O/P
Tunnel configuration	
Single-tunnel/ twin-tunnel	T1/T2
Eccentricity	e00/e05/e10/e15/e20/e25/e30
Skew angle	s45

building of height 12 m where the front and rear facades are with openings in the case of single orthogonal tunnel with zero eccentricity.

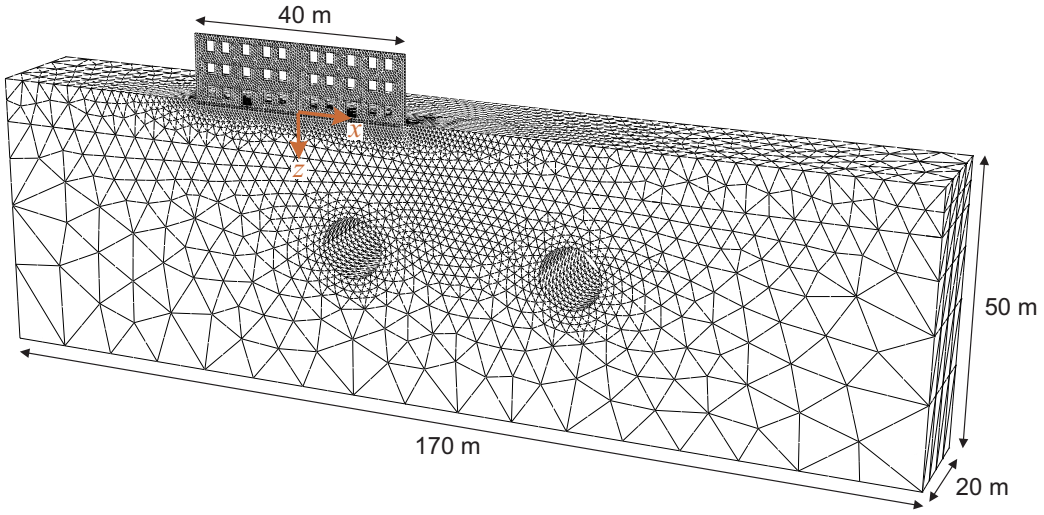
Data on the numbers of elements employed in the building and soil meshes are given in Table 6.2. The element types adopted are indicated in Table 3.2. The meshes for the models 'TSA-F08O-T1e00', 'TSA-F12O-T2e30', 'TSA-F08P-T1e10', 'TSA-B08O-T1e00', 'TSA-B12O-T2e00', 'TSA-B08O-T1e00s45' are shown in Figs 6.2 and 6.3 as examples. Symmetry about the mid-plane of the facade is exploited in the isolated facade analysis and symmetry about the vertical plane passing through the tunnel centre is applied in the complete building analysis for orthogonal tunnel. The mesh details of the facade and footing used in 3D isolated facade analysis and the mesh of the building and foundation adopted in 3D complete building analysis are shown in Fig. 6.4. Note that the result plots for models TSA-F{08,12}-T{1,2}e00 are not perfectly symmetric about $x = 0$ owing to asymmetry of the meshes.

6.2 Short-term greenfield analysis

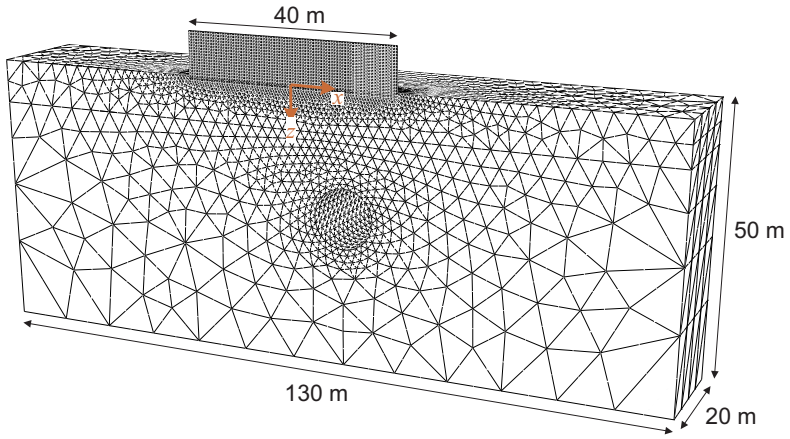
The greenfield analysis provides an important reference for interpreting the soil-building interaction in the later calculations. The finite element modelling is considered to be realistic if the trough width parameter of the computed greenfield settlement is



(a)



(b)



(c)

Figure 6.2: Example mesh employed for 3D isolated facade analyses, also showing coordinate axes (elements internal to the tunnels have been removed for clarity): (a) model TSA-F08O-T1e00; (b) model TSA-F12O-T2e30; (c) TSA-F08P-T1e10

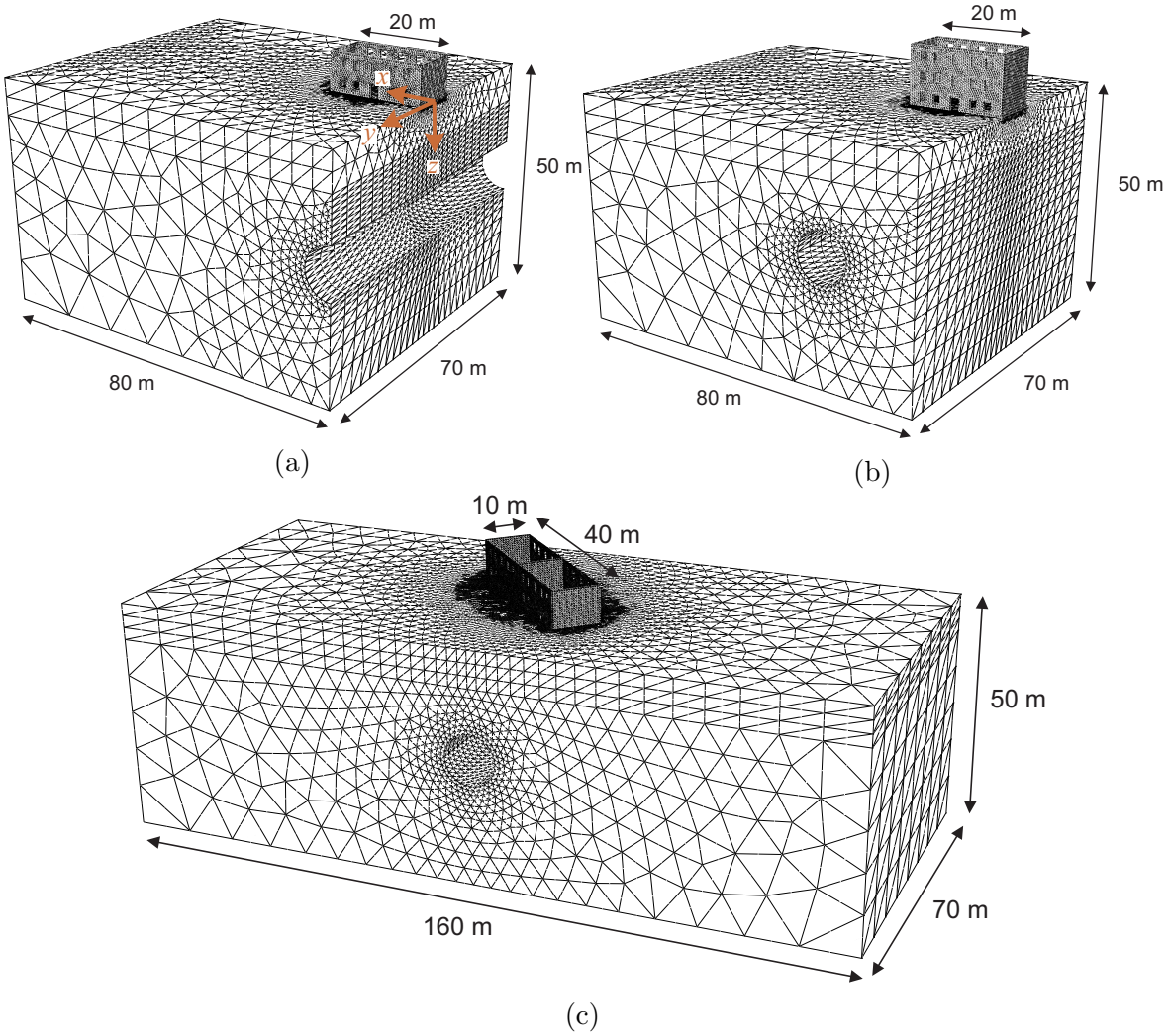


Figure 6.3: Example mesh employed for 3D complete building analyses (elements internal to the tunnels have been removed for clarity). The origin of the coordinate system is at the centre of the building on the level of ground surface: (a) model TSA-B08O-T1e00; (b) model TSA-B12O-T2e00; (c) model TSA-B08O-T1e00s45

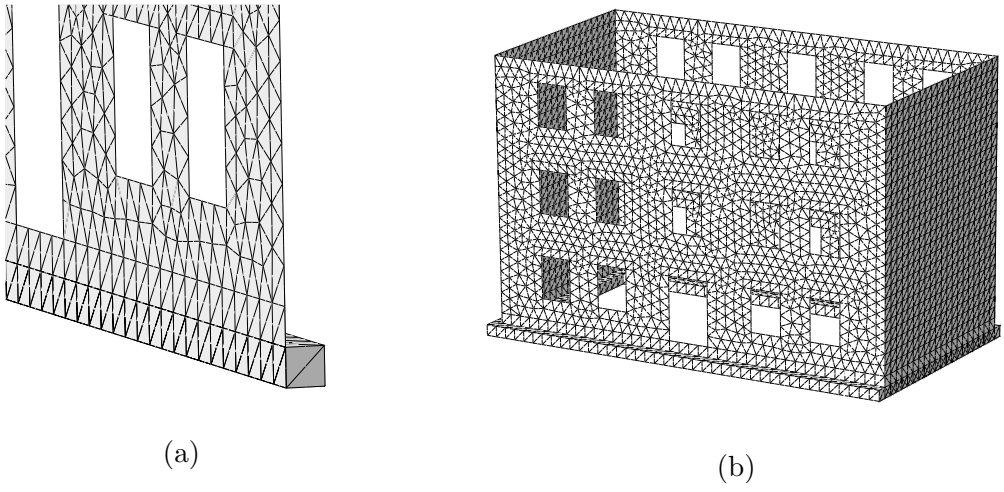


Figure 6.4: Mesh details of the building modelled: (a) facade and foundation in 3D isolated facade analysis; (b) building and foundation in 3D complete building analysis

Table 6.2: Numbers of elements employed in the finite element models

Building meshes

Analysis type	Building height	Part	Number of elements
Isolated facade	8 m	facade	2764
	12 m	facade	4096
	-	footing	955
Complete building	8 m	facades & walls	4212
(orthogonal)	12 m	facades & walls	6172
	-	footing	2616
Complete building	8 m	facades & walls	7736
(skew)	-	footing	5216

Soil meshes

		Number of elements	
Analysis type	Tunnel case	Gravel	Clay
Isolated facade	single	26465 – 27902 *	17203 – 19728 *
	twin	28391 – 30030 *	37802 – 38837 *
Complete building	single	31317	20410
(orthogonal)	twin	31317	39838
Complete building	single	51095	43127
(skew)			

* The range covers models with tunnel eccentricities $0 \leqslant e \leqslant 30$ m.

comparable with that of the typical Gaussian curve obtained from field measurements under greenfield conditions. The results of the greenfield analysis are obtained from model TSA-GF-T1 for the single-tunnel case and model TSA-GF-T2 for the twin-tunnel case.

6.2.1 Displacement and horizontal strain profiles

Greenfield settlement profiles, computed at the level of the base of the foundation ($z = 1$ m) in the absence of a building, are plotted in Fig. 6.5, together with the Gaussian curves in the form of Equation 2.1. The volume of settlement trough can be obtained by integrating Equation 2.1. Dividing the volume of the settlement trough by the theoretical volume of the tunnel gives the settlement volume loss, $V_{\mathrm{L}}^{\mathrm{S}}$, (at the

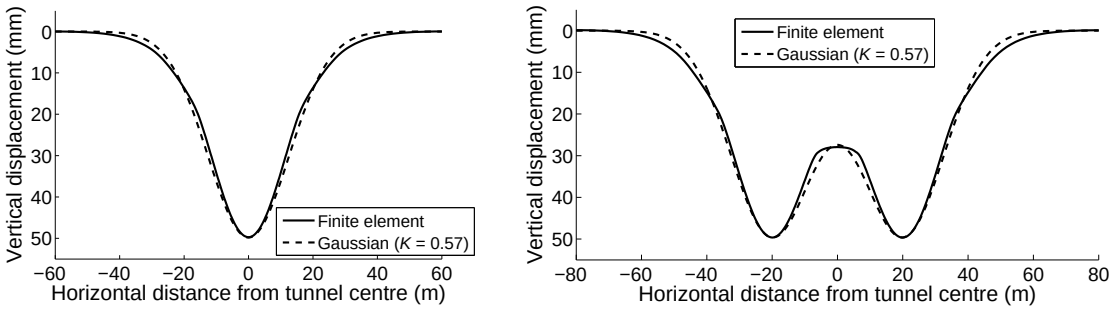


Figure 6.5: Greenfield vertical displacements at foundation base level induced by tunnelling obtained from finite element analysis, compared with the fitted Gaussian curve: (a) single tunnel; (b) twin tunnels

level of z_o).

$$V_L^S = \frac{4\sqrt{2}}{\sqrt{\pi}} \frac{iS_{v,max}}{D^2} \tag{6.1}$$

where D is the tunnel diameter. By rearranging Equations 2.1 and 6.1, the trough width parameter, K, for the corresponding Gaussian curve is calculated by

$$K = \frac{\sqrt{\pi}}{4\sqrt{2}} \frac{D^2 V_L^S}{z_o S_{v,max}} \tag{6.2}$$

The Gaussian curves are fitted to the computed profiles by matching the maximum vertical displacement, $S_{v,max}$, and V_L^S. Note that V_L^S may be different from the tunnel volume loss, V_L^T, if the soil is not incompressible.

The trough width parameter, K, determined in this way is 0.57 in the single-tunnel case. This value may be compared with the data in O'Reilly & New (1982) where $K = 0.2$ for granular materials and $K = 0.7$ for soft silty clay. Moreover, the point of inflection of the Gaussian curve in the single-tunnel case is located at $i = Kz_o = (0.57)(22) \approx 12.5$ m away from the tunnel centre and that computed from the finite element analysis is also at around 12.5 m (obtained by numerical differentiation of the displacement profile). The plausible value of K and the good agreement of the shapes of the computed greenfield ground settlement profiles with the empirical Gaussian settlement curves shown in Fig. 6.5 are attributed to the adopted modelling procedure. Superposition of Gaussian curves is employed for the twin-tunnel case Fig. 6.5(b).

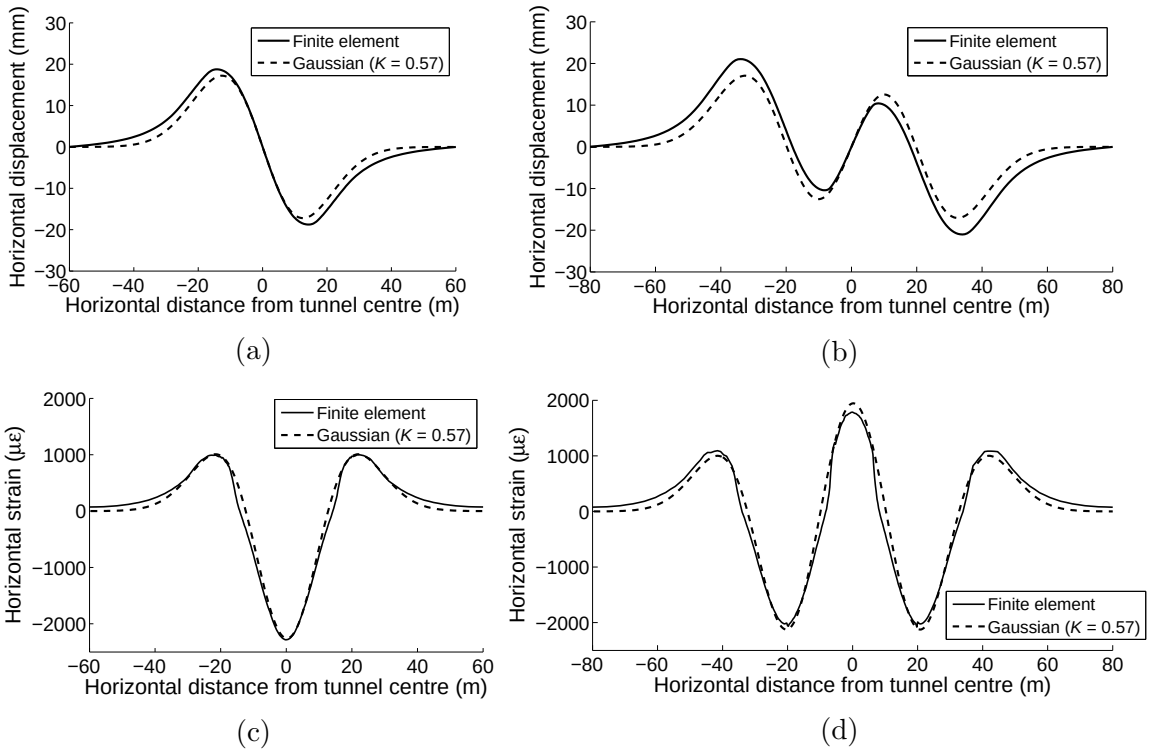


Figure 6.6: Greenfield horizontal displacements and horizontal strains at foundation base level induced by tunnelling obtained from finite element analysis, compared with the fitted Gaussian curve: (a) horizontal displacement, single tunnel; (b) horizontal displacement, twin tunnels; (c) horizontal strain, single tunnel; (d) horizontal strain, twin tunnels

The horizontal displacement and horizontal strain at the level of the base of the expected foundation are plotted in Fig. 6.6. The horizontal strain from the finite element data are extracted directly from Abaqus at the nodes of the relevant elements (rather than being computed directly from the nodal displacement). In the empirical method adopted in O'Reilly & New (1982), the horizontal displacement, S_{h}, is expressed in Equation 2.3. Differentiating Equation 2.3 gives the horizontal strain, ε_{h}, related to the assumed greenfield settlement trough. Fig. 6.6 shows that the horizontal displacement and horizontal strain obtained from the finite element analysis and the empirical method are similar. It is noted that the horizontal strain induced in the soil can be as high as 2200 $\mu\varepsilon$ (microstrain) locally.

Although a ground volume loss, $V_{\mathrm{L}}^{\mathrm{T}}$, of 1.5% is prescribed at the tunnel perimeter, the volume of the settlement trough, $V_{\mathrm{L}}^{\mathrm{S}}$, at foundation level is found to be 1.65% for the single tunnel and 1.64% for each of the twin tunnels. An investigation of the mismatch between the volume losses at the tunnel and at the shallower depth indicated that,

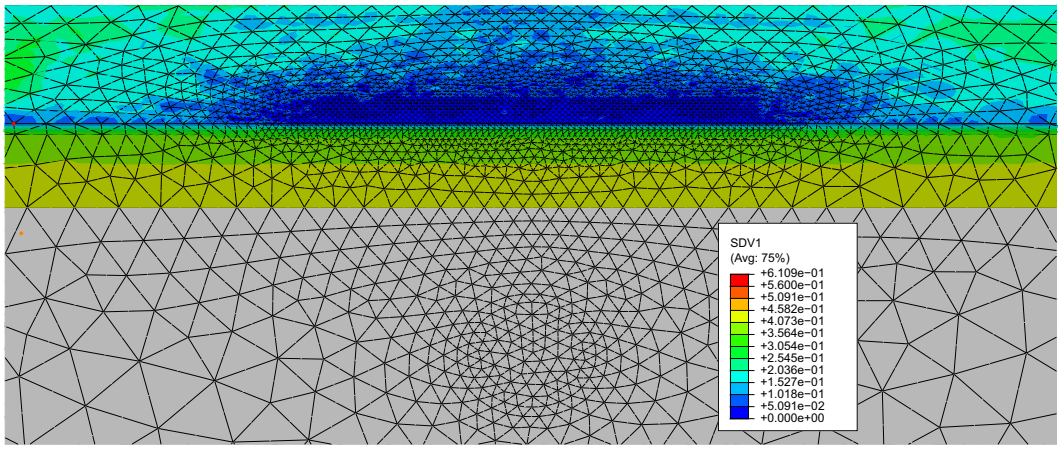
although dilational volumetric strains occur in the gravel in peripheral regions, these are more than offset by compressive volumetric strains in the gravel directly above the tunnel (see later in Fig. 6.9). A discussion of the compressive-dilational behaviour that occurs around tunnels in drained soil is given in Marshall et al. (2012).

Fig. 6.7 illustrates the variation of the mobilised friction angle, ϕ_y, which is also the hardening parameter, in the EMC model employed for the Terrace Gravel before and after tunnelling. It is noted that after the geostatic stresses are established, ϕ_y is the same at the same depth. The unphysical variation of the contours on the ground surface plane shown in Fig. 6.7(a) is due to the extrapolation of ϕ_y values within the elements of uneven sizes. After the single tunnel is excavated (Fig. 6.7(b)), ϕ_y slightly increases directly above the tunnel crown, but does not vary around the settlement inflection point. It increases significantly beyond the inflection point until ϕ_y recovers outside the influence zone (beyond $x = \pm 42$ m as displayed in the figure). The variation is consistent with the horizontal strain profile in Fig. 6.6 and the tensile strain causes greater ϕ_y than the compressive one because of the nature of lower tensile strength in the EMC model. In Fig. 6.7(c), similar soil behaviour induced by twin tunnels is exhibited. The increase in ϕ_y is superposed in the middle of the two tunnels.

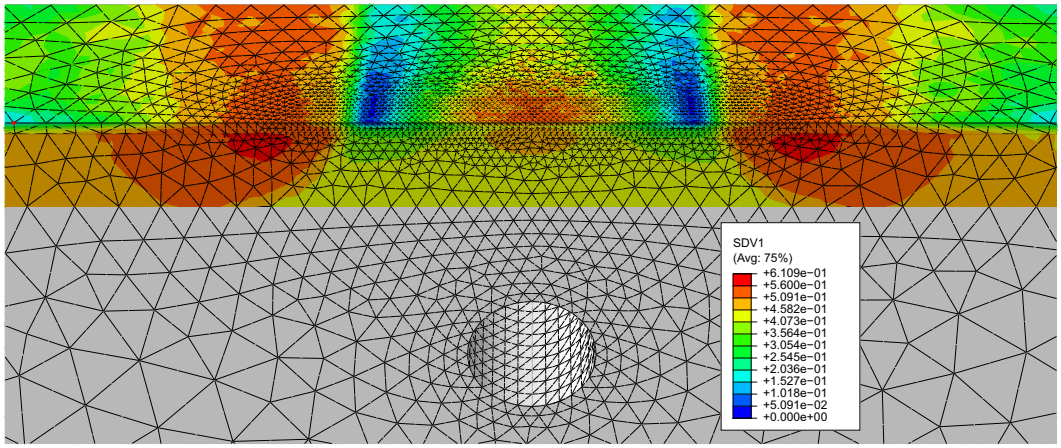
6.2.2 Effect of constitutive model for the Terrace Gravel

Results when the EMC model is employed for the Terrace Gravel are compared with those obtained using an alternative model. The aims of this investigation are (i) understanding the effect of constitutive model for the Terrace Gravel in this problem; (ii) evaluating the need for advanced models that account for small-strain stiffness variation in Terrace Gravel. This comparison is made based on the premise that the two models are calibrated against the same set of field and laboratory data (i.e. Addenbrooke et al. 1997, Jurečič et al. 2013).

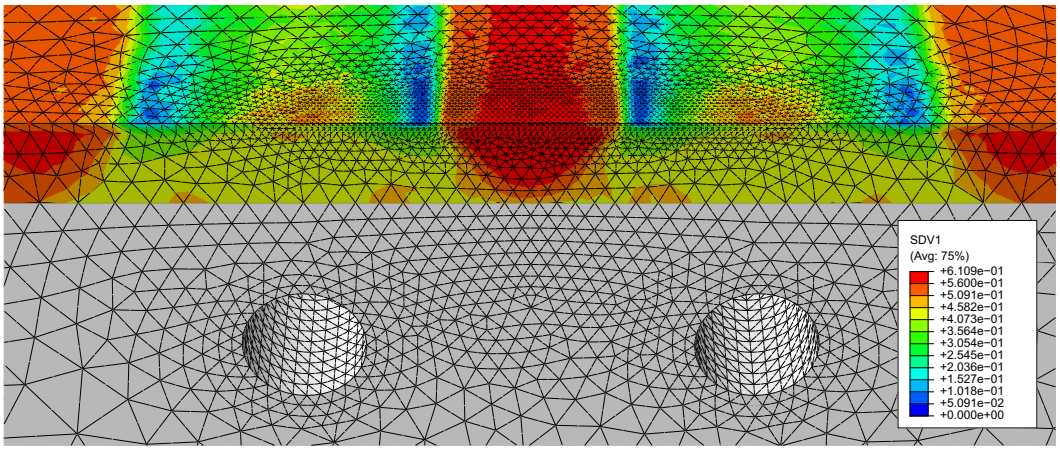
For this study, the Abaqus built-in linear elastic, perfectly plastic, non-associated Mohr-Coulomb (MC) model is selected based on its common acceptance and wide availability. The same unit weight, γ, of 20 kN/m^3 and lateral stress coefficient, K_0, of



(a)



(b)



(c)

Figure 6.7: Contours of ϕ_y of the EMC model for the Terrace Gravel in greenfield analyses at different stages: (a) after the geostatic stresses are established; (b) after the single tunnel is excavated; (c) after the twin tunnels are excavated. The figure displays the undeformed mesh with x-coordinates from -42 m to +42 m. (Note the legend is in radian; $\phi_p = 35^\circ = 0.6109$ rad)

Table 6.3: Calibrated parameters used in the linear elastic, perfectly plastic, non-associated Mohr-Coulomb model for the Terrace Gravel

Parameter		Value
Young's modulus	E	$4.8 + 12z$ MPa
Poisson's ratio	ν	0.2
Friction angle	ϕ	35°
Dilation angle	ψ	17.5°
Cohesion	c	0.1 kPa

$1 - \sin\phi = 0.426$ as when the EMC model is employed are used. The MC parameters used in Jurečič et al. (2013, Table 4) ($\phi = 35°$, $\psi = 17.5°$, $c = 0.1$ kPa) are adopted; a small value of cohesion is included for numerical stability. The stiffness parameter of the linear elastic model is obtained based on the values of initial shear modulus, G_0, adopted in the EMC model (Equation 4.11), which is determined from the non-linear stiffness parameters given in Jurečič et al. (2013, Appendix). To account for a reduction in shear modulus due to the development of small-strain, the shear modulus $G = 0.5G_0$ is adopted in the linear elastic model. Note that in Abaqus/Standard, the elastic properties of the built-in model need to be defined by the Young's modulus, E, and the Poisson's ratio, ν. The value of $\nu = 0.2$ is adopted from Jurečič et al. (2013, Table 4), and G and ν are then converted to E by Hooke's law. The calibrated parameters adopted in the linear elastic, perfectly plastic MC model for the Terrace Gravel are listed in Table 6.3. A separate set of TSA-GF-T1 and TSA-GF-T2 simulations is conducted using the calibrated MC model. A further study involving the building is included in Section 6.3.3.

Fig. 6.8 shows the greenfield settlements and the fitted Gaussian curves (trough width parameter $K = 0.54$) when the MC model is employed. The shape and the magnitude of the vertical displacement are similar to those when the EMC model is used (Fig. 6.5). The K values fitted with both gravel models are similar and within the suggested range. This suggests that, provided the constitutive model for clay described in Section 3.6.5.2 and the tunnel excavation simulation method in Section 3.8 are employed, the influence of the stiffness non-linearity of the gravel constitutive model on greenfield settlement curve may not be significant.

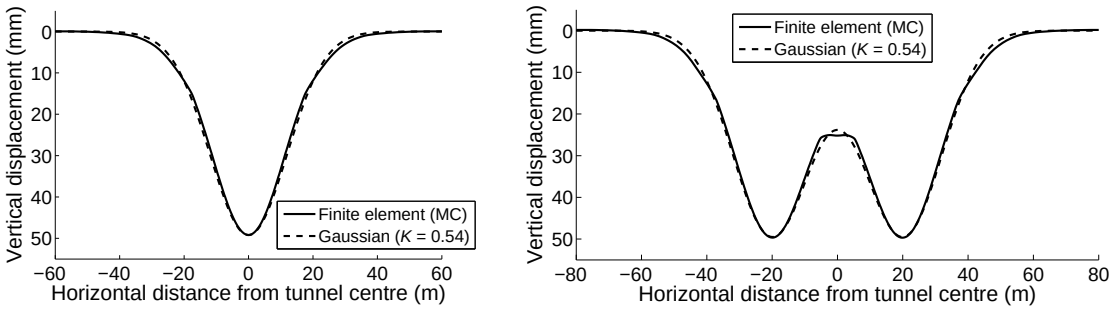


Figure 6.8: Greenfield vertical displacements at foundation base level induced by tunnelling fitted with Gaussian curves when the MC model is used: (a) single tunnel; (b) twin tunnels

The model behaviour for greenfield analyses is further investigated by comparing the volume loss, where $V_{\mathrm{L}}^{\mathrm{T}} = 1.50\%$ is specified at the tunnel perimeter using the displacement field method. Table 6.4 shows the volume loss calculated from the area of settlement trough, $V_{\mathrm{L}}^{\mathrm{S}}$, along the surface of the clay ($z = 8$ m) and of the gravel at the expected foundation level ($z = 1$ m). The $V_{\mathrm{L}}^{\mathrm{S}}$ at $z = 8$ m using both models is close to the $V_{\mathrm{L}}^{\mathrm{T}}$; this is consistent with the intended undrained behaviour of the clay. However, there is a higher $V_{\mathrm{L}}^{\mathrm{S}}$ at $z = 1$ m, especially when the EMC model is used. Fig. 6.9 shows the horizontal, vertical and volumetric strains along the surface of the clay and along the foundation level of the gravel when each of the two soil models is employed. These strains indicate that, although dilational volumetric strains occur in the gravel beyond the tunnel springlines, these are more than offset by compressive volumetric strains (which are dominated by horizontal strain) in the gravel directly above the tunnel. This observation is more noticeable when the EMC model is employed. The difference in the amount of dilation and contraction may be because the EMC model assumes $\phi_{\mathrm{cv}} = \phi_{\mathrm{p}}$ in the current implementation while the MC model is prescribed with a positive dilation angle.

The similar results from the EMC and the MC models in the greenfield analyses suggest that both models are calibrated in a coherent manner. This establishes a basis for comparison between the two models when building is present in the interaction problem in Section 6.3.3.

Table 6.4: Settlement volume loss, V_L^S, calculated at different depths when the EMC model and the MC model are used respectively. The prescribed V_L^T is 1.50%. The volume loss for the twin-tunnel case is the averaged value for each tunnel.

Soil model	Level measured	Single-tunnel	Twin-tunnel
EMC	$z = 1$ m	1.65%	1.64%
	$z = 8$ m	1.52%	1.52%
MC	$z = 1$ m	1.54%	1.55%
	$z = 8$ m	1.52%	1.52%

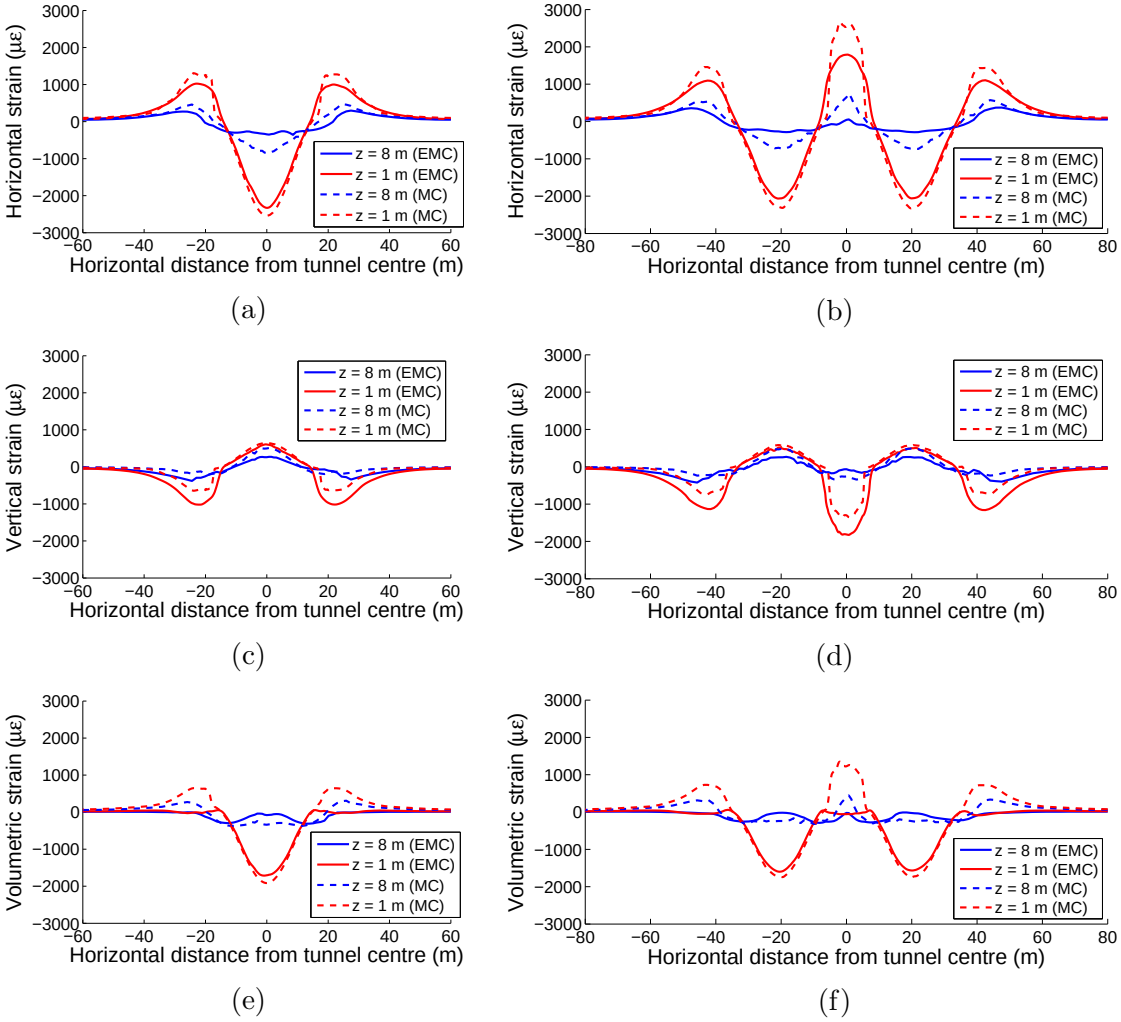


Figure 6.9: Greenfield strain profiles along the clay surface ($z = 8$ m) and the foundation level ($z = 1$ m) when the EMC model and the MC model are used for the Terrace gravel. (a) horizontal strain, single tunnel; (b) horizontal strain, twin tunnels; (c) vertical strain, single tunnel; (d) vertical strain, twin tunnels; (e) volumetric strain, single tunnel; (f) volumetric strain, twin tunnels

6.3 Short-term isolated facade analysis

The 3D isolated facade analysis approach assumes the front facade and its strip footing to be independent of other walls and connections. This simplifies the problem and facilitates analysis of the mechanisms occurring around the soil-footing interface and in the facade. As this modelling approach is relatively fast to set up and compute, extensive parametric studies are conducted to explore the importance of various aspects of the problem. The reliability concerning the simplification of the geometric features of the building in the 3D isolated facade analysis approach is verified with the 3D complete building analysis approach in Section 6.4.

6.3.1 Soil-building interaction

Isolated facade analyses with a facade with openings of height $H = 8$ m and 12 m for single tunnel and twin tunnels with zero tunnel eccentricity (models TSA-F{08,12}O-T{1,2}e00) are conducted and the features of soil-building interaction are examined.

The computed settlement profiles of both the building and the ground at the level of the base of the footing are plotted in Fig. 6.10. These data indicate the expected behaviour that (i) the facades do not conform to the greenfield displacements, and (ii) the $H = 12$ m facade responds in a stiffer way than the $H = 8$ m facade. The mode of deformation of the facade can be interpreted from the sign of the curvature of the settlement profile and located by the point of inflection. In the single-tunnel case, the mid-span of the facade deforms in sagging and the two ends experience hogging (Fig. 6.10(a)); while in the twin-tunnel case, hogging is observed in the mid-span of the facade and sagging occurs at the two ends (Fig. 6.10(b)). In both cases the points of inflection are at around 10 m from the facade centre, which is different from the value determined from the greenfield analysis ($i = 12.5$ m).

The computed horizontal displacements and horizontal strains at the base of the footing, and in the soil adjacent to the base of the footing, are shown in Fig. 6.11. For both the single-tunnel (Fig. 6.11(a)) and twin-tunnel (Fig. 6.11(b)) cases, the horizontal displacements of the footing are substantially lower in magnitude than (and typically in

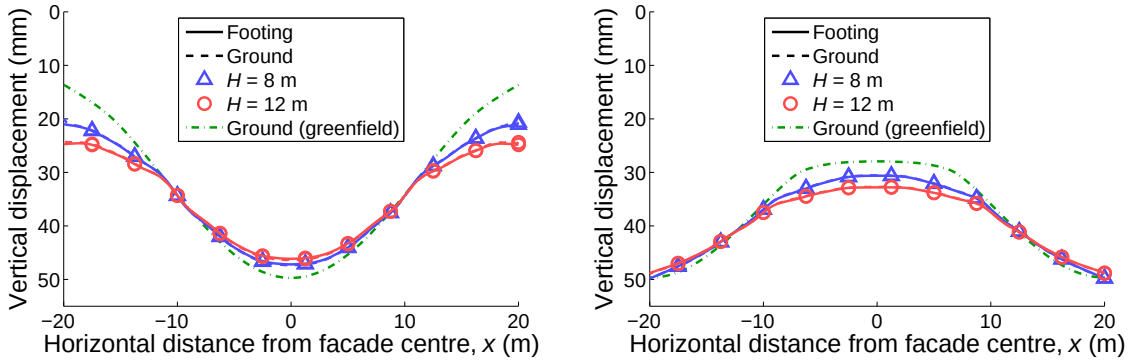


Figure 6.10: Vertical displacements at foundation base level for facades with openings of height $H = 8$ m and $H = 12$ m induced by tunnelling with $e = 0$, compared with greenfield vertical displacements: (a) single tunnel; (b) twin tunnels

the opposite direction to) those occurring in the adjacent soil, and inevitably those in the greenfield conditions. Significant sliding clearly occurs at the soil-footing interface.

The horizontal strains developed in the footing and in the adjacent soil are shown in Figs 6.11(c) and (d). The strains induced in the footing are again significantly lower in magnitude than those in the soil as the building is more rigid than the nearby soil; they are also substantially less than the computed greenfield horizontal strains. This is a significant result and is consistent with a range of previous field monitoring data from London (e.g. Burland et al. 2004, Dimmock & Mair 2008) in which the observed horizontal strains at foundation level in masonry buildings affected by tunnel-induced settlements are relatively small, compared with the estimated greenfield horizontal strains. Moreover, the nature of the soil-foundation interaction observed in the finite element results is at odds with the procedure typically employed in the elastic beam assessment (EBA) method (Boscardin & Cording 1989) in which the greenfield horizontal strains estimated to occur in the soil are combined additively with the strains developed in the building by structural (bending and shear) action. A more detailed discussion on the EBA method is included in Section 6.3.6.

The computed normal and shear tractions developed on the base of the footing are shown in Fig. 6.12. The construction of the tunnel(s) causes the normal tractions to be redistributed, towards the edges of the facade for the single-tunnel case (Fig. 6.12(a)) and towards the centre of the facade for the twin-tunnel case (Fig. 6.12(b)). Consis-

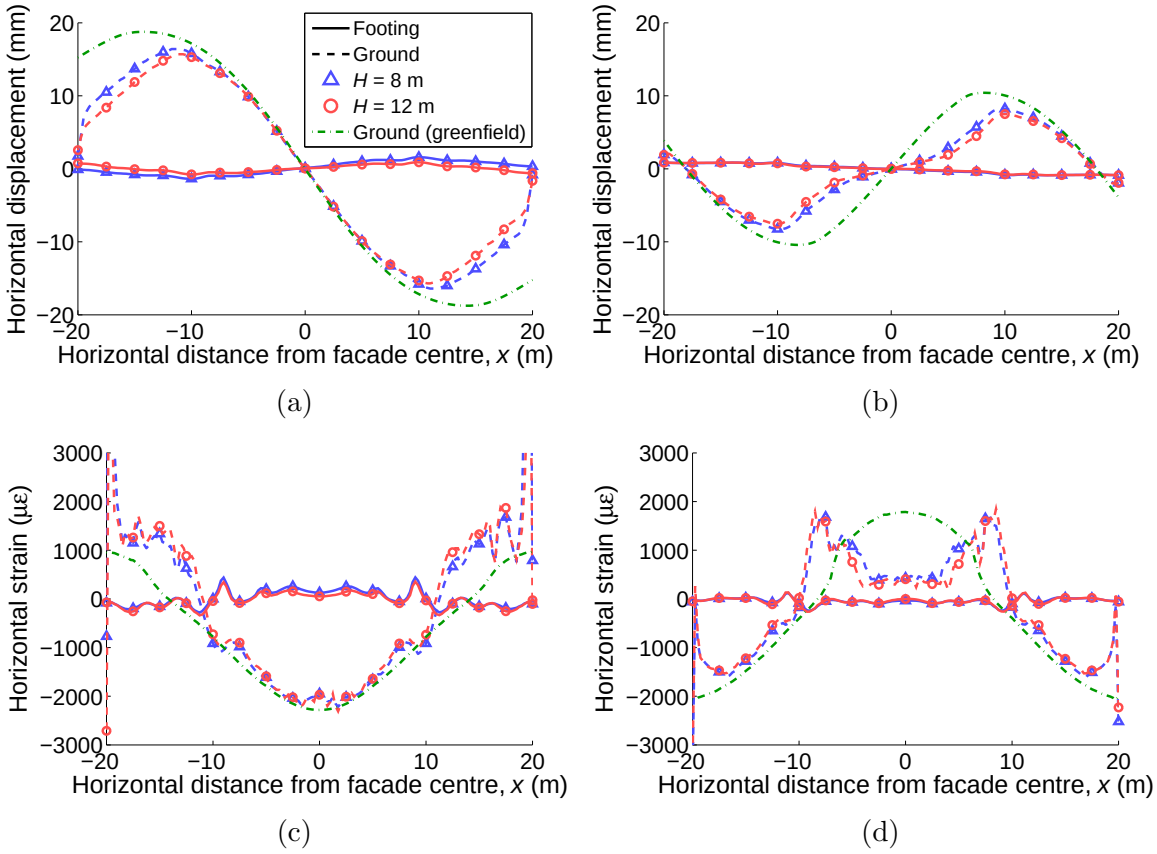


Figure 6.11: Horizontal displacements and horizontal strains at foundation base level induced by tunnelling with $e = 0$: (a) horizontal displacement, single tunnel; (b) horizontal displacement, twin tunnels; (c) horizontal strain, single tunnel; (d) horizontal strain, twin tunnels

tent with these redistributed normal tractions, additional settlements develop, which, in both the single- and twin-tunnel cases, act to reduce the differential settlements induced in the building (Fig. 6.10). Also, inward limiting friction (with the frictional coefficient, $\mu = 0.3$) is mobilised over most of footing (Figs 6.12(c) and (d)) except in relatively small zones near the facade midpoint. These observations further emphasise the need for a realistic representation of the interaction between the foundation and the ground to achieve reliable estimates of the deformations induced in the building.

An investigation of the influence of building weight and building stiffness on the stresses in the Terrace Gravel is carried out in terms of the mobilised friction angle (also the hardening parameter), ϕ_y, in the EMC model, as exhibited in Fig. 6.13 (note that the facade is not displayed for clarity). Comparing Fig. 6.7(a), which is after the geological stresses of the soil are established, with Fig. 6.13(a), which is after the

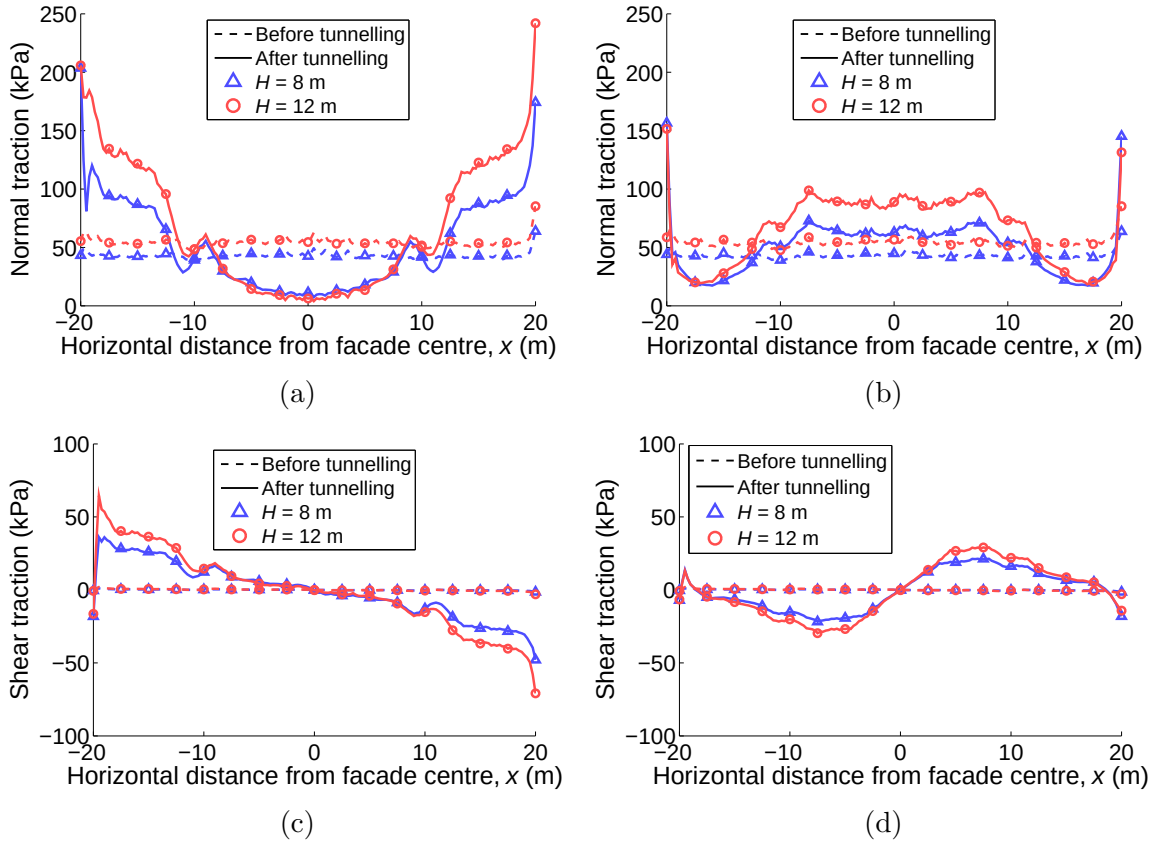
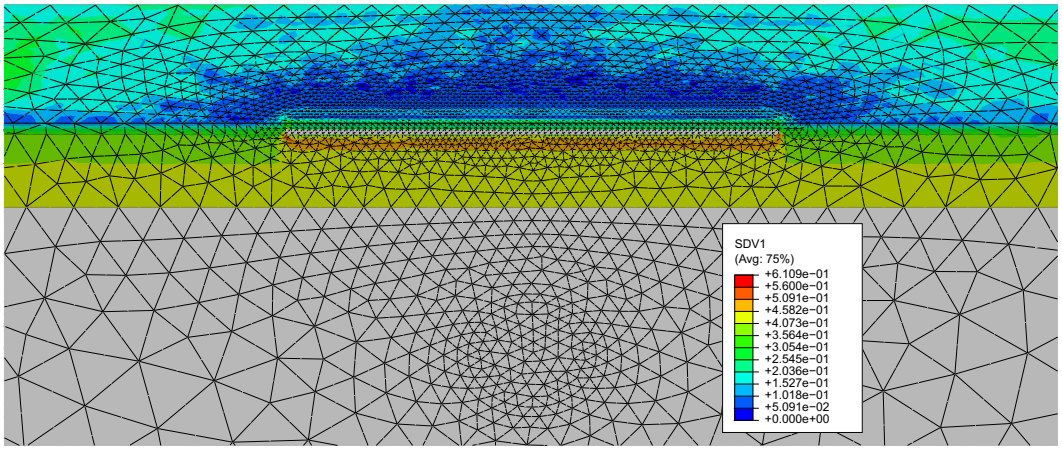


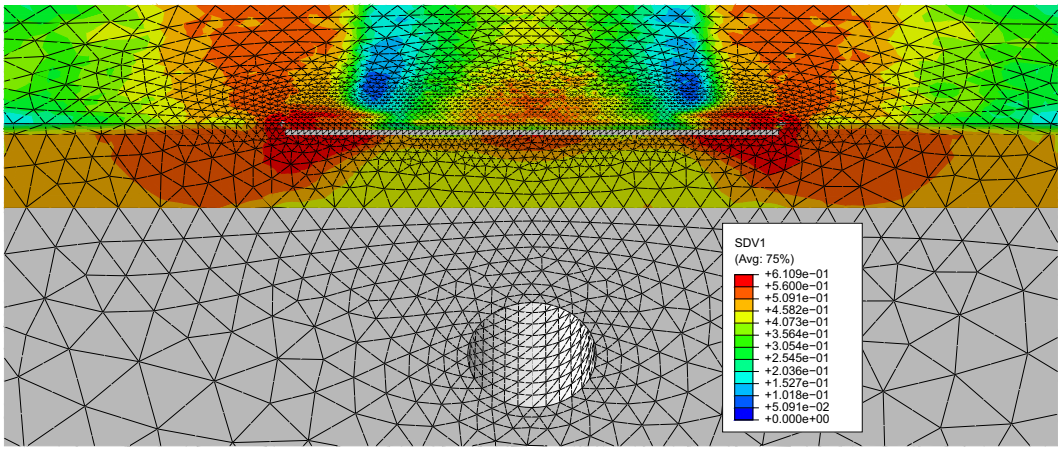
Figure 6.12: Contact tractions on foundation base, before and after tunnelling with $e = 0$: (a) normal traction, single tunnel; (b) normal traction, twin tunnels; (c) shear traction, single tunnel; (d) shear traction, twin tunnels. Normal tractions are compression positive; shear tractions are positive when applied to the foundation in the positive x-direction

building stiffness and weight ($H = 8$ m) is applied, there is an increase in ϕ_y in the soil just underneath the footing. It indicates that the building self-weight induces a significant localised effect on the soil mobilisation, resulting in hardening.

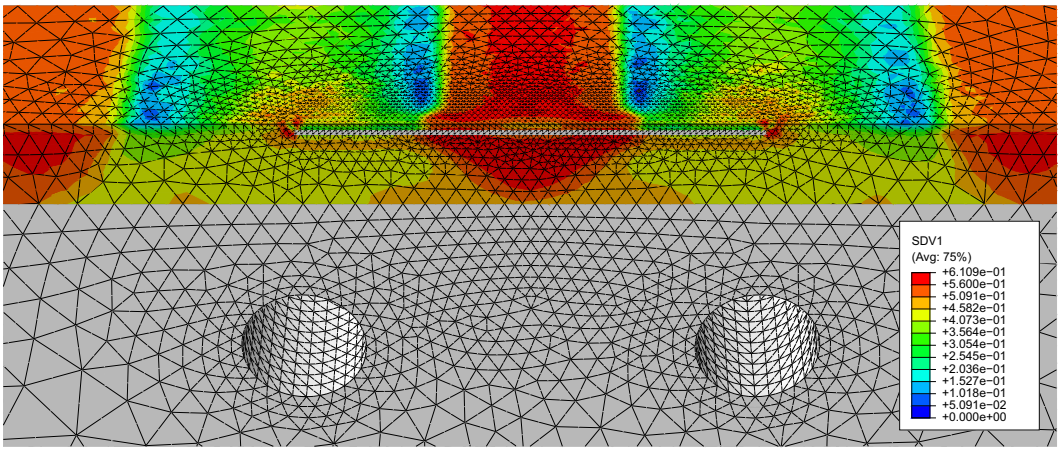
Figs 6.13(b) and 6.13(c) show the contours of ϕ_y after tunnel construction, in the single-tunnel and twin-tunnel cases respectively. Comparing with the state prior to tunnelling with the effect of building weight (Fig. 6.13(a)) and also after tunnelling in the greenfield conditions (Figs 6.7(b) and 6.7(c)), tunnelling with the presence of the building (Figs 6.13(b) and 6.13(c)) results in additional increase in ϕ_y in the EMC model for the gravel surrounding the two ends of the footing. This again indicates the effect of tunnel-soil-building interaction on the soil.



(a)



(b)



(c)

Figure 6.13: Contours of ϕ_y of the EMC model for the Terrace Gravel in isolated facade analyses ($H = 8$ m) at different stages: (a) after the building is activated; (b) after the single tunnel is excavated; (c) after the twin tunnels are excavated. The facade is not shown in the figure for clarity. The figure displays the undeformed mesh with x-coordinates from -42 m to +42 m. (Note the legend is in radian; $\phi_p = 35° = 0.6109$ rad; same scale as in Fig. 6.7)

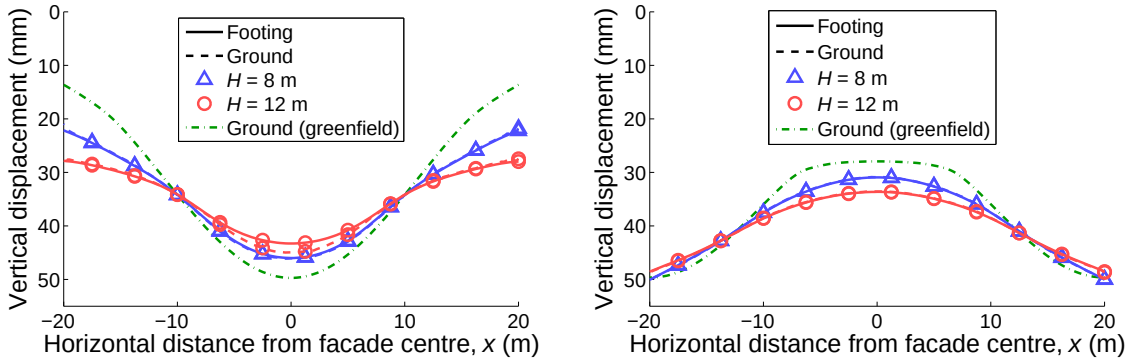


Figure 6.14: Vertical displacements at foundation base level for plain facades induced by tunnelling with $e = 0$, compared with greenfield vertical displacements: (a) single tunnel; (b) twin tunnels

6.3.2 Importance of facade openings

A key focus of this research is on the estimation of the likely extent of building damage induced by tunnelling, quantified in terms of tensile strain. Openings such as windows and doors are common features of a building facade. The influence of the openings on the development of tensile strain and the importance of modelling the facade openings are investigated. For comparison purposes, the calculations in which openings and lintels are absent in the facade (termed 'plain facade') are conducted (models TSA-F{08,12}P-T{1,2}e00).

Fig. 6.14 shows the computed vertical displacements for the plain facades, to be compared with those for the facades with openings in Fig. 6.10. As expected, the plain facades behave in a stiffer manner compared with the facades with openings. This is because the presence of openings reduces the overall building stiffness. Fig. 6.14(a) shows that a gap opens up between the foundation and the underlying soil at the centre of the plain facade with $H = 12$ m, for the single-tunnel case. This type of gapping behaviour has also been observed in centrifuge model tests (Farrell et al. 2014).

The computed major principal (tensile) strains induced in the facade (obtained from the ghost elements) for single tunnel and twin tunnels with zero eccentricity are contoured in Figs 6.15 and 6.16 for $H = 8$ m and $H = 12$ m respectively. Generally, relatively high strains are observed along the bottom of the facade for the single-tunnel

case in which the building deforms in sagging dominantly, and concentrates along the top of the facade in the twin-tunnel case where mainly hogging occurs. The data in Figs 6.15(a) and 6.16(a) (plain facade, single tunnel) indicate a rather complex pattern in which concentrations of strain occur at about 7 m from the centre of the facade. In Figs 6.15(b) and 6.16(b) (plain facade, twin tunnels) the strain gradients are more uniform around the mid-span of the facade, and more obviously consistent with beam action. The strain distributions for the facades with openings (Figs 6.15(c) and (d) and Figs 6.16(c) and (d)), however, indicate a fundamentally different pattern. Whereas the strains in the plain facade correspond broadly to beam action (although additional local effects are seen in Figs 6.15(a) and 6.16(a)), the facade with openings exhibits a more complex, frame-like action with significant concentrations of strain occurring around the windows and doors. These observations indicate the importance of accounting for openings when determining the distribution and magnitude of the tensile strains developed in a facade.

Also shown in Figs 6.15 and 6.16 are the values of maximum tensile strain computed from the finite element analysis, $\varepsilon^{\mathrm{t}}_{\mathrm{max}}$, and the characteristic strain, $\varepsilon^{\mathrm{t}}_{99}$. For facades with openings, the value of $\varepsilon^{\mathrm{t}}_{\mathrm{max}}$ is likely to be computed around an internal corner of the openings, which is affected by stress singularity and the computed strain is highly mesh-dependent. The $\varepsilon^{\mathrm{t}}_{99}$ has shown to be mesh-independent and thus provides a more reliable measure (Section 3.10.4). Fig. 6.17 shows the cumulative distribution curve of the major principal strains in the plain facade and the facade with openings ($H = 8$ m, single tunnel). The $\varepsilon^{\mathrm{t}}_{99}$ is demonstrated to remove the extreme values computed in the facade with openings but not significantly affect the result of the plain facade.

In all cases shown in Figs 6.15 and 6.16, the $\varepsilon^{\mathrm{t}}_{99}$ values are larger when the openings are incorporated in the facade than the plain facade. This is due to (i) the facade with openings being less stiff than the plain facade, resulting in greater differential settlements, and (ii) the occurrence of strain localisation around the openings.

The tensile strain data for the facade with openings are categorised based on the damage categories proposed by Boscardin & Cording (1989) in Fig. 6.18 using a stacked

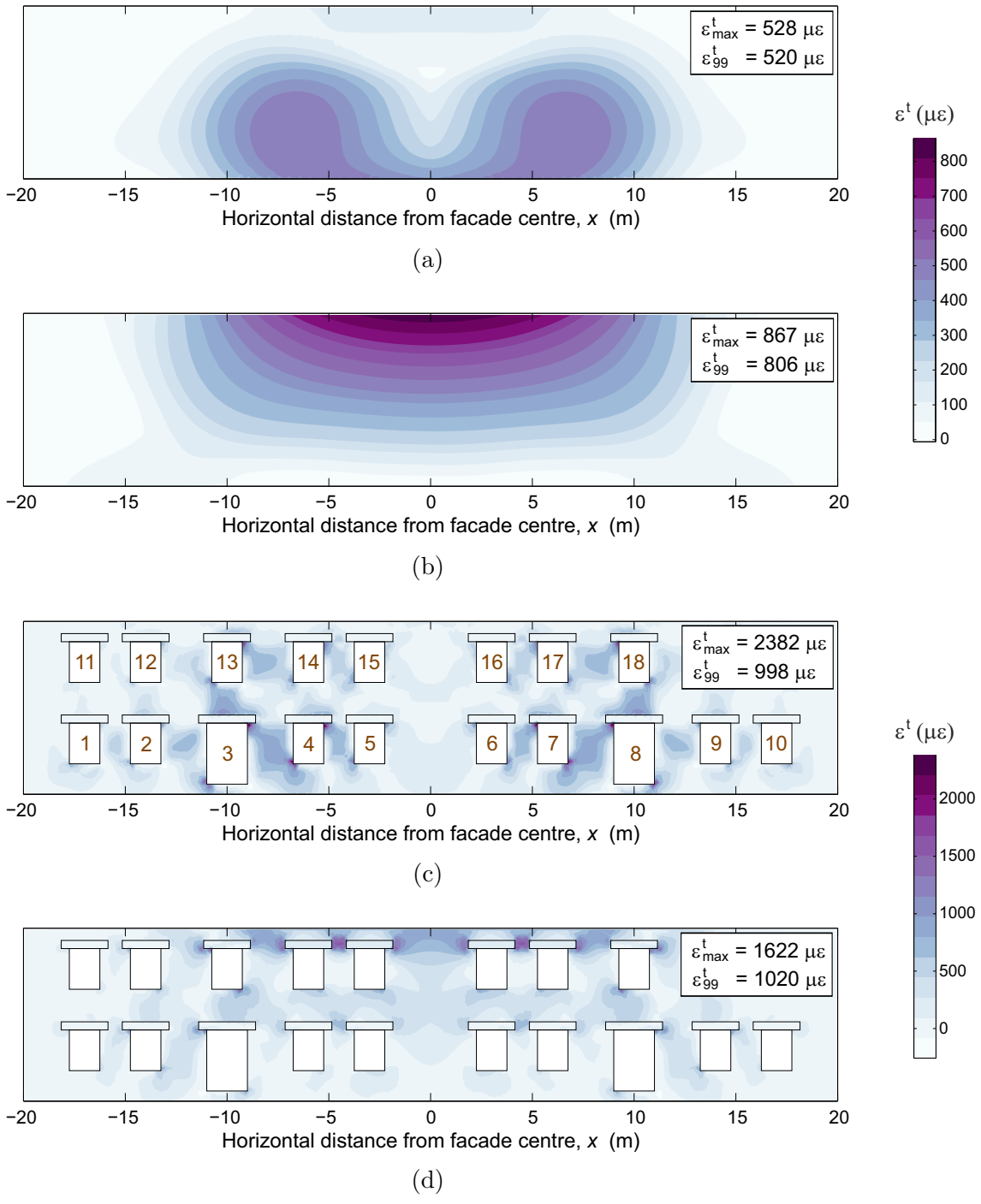


Figure 6.15: Major principal strains ε^t, maximum tensile strain ε^t_{max} and characteristic strain ε^t_{99} in facades of height $H = 8$ m induced by tunnelling with $e = 0$: (a) plain facade, single tunnel; (b) plain facade, twin tunnels; (c) facade with openings, single tunnel. Also showing opening numbers; (d) facade with openings, twin tunnels

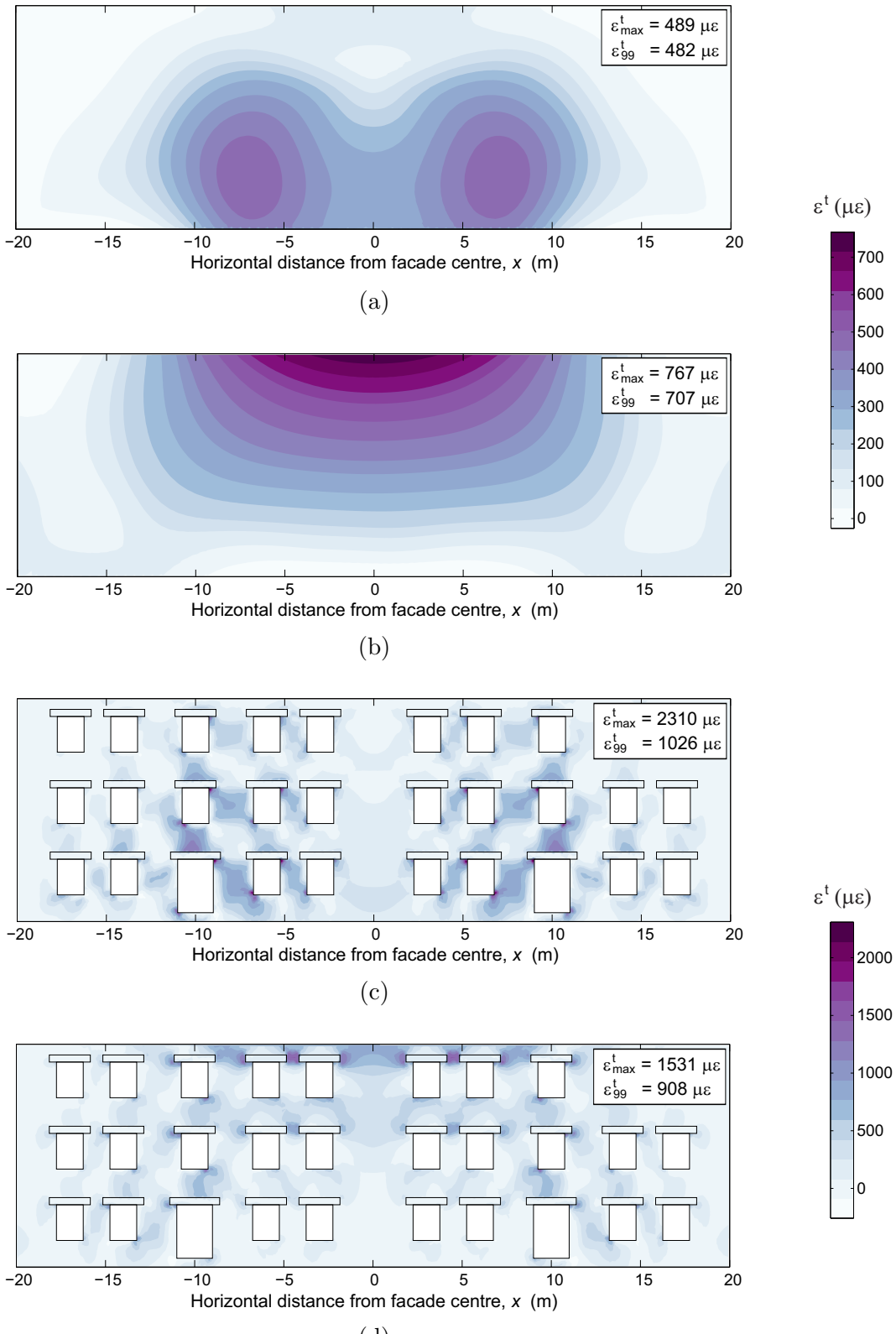


Figure 6.16: Major principal strains ε^t, maximum tensile strain ε^t_{max} and characteristic strain ε^t_{99} in facades of height $H = 12$ m induced by tunnelling with $e = 0$: (a) plain facade, single tunnel; (b) plain facade, twin tunnels; (c) facade with openings, single tunnel; (d) facade with openings, twin tunnels

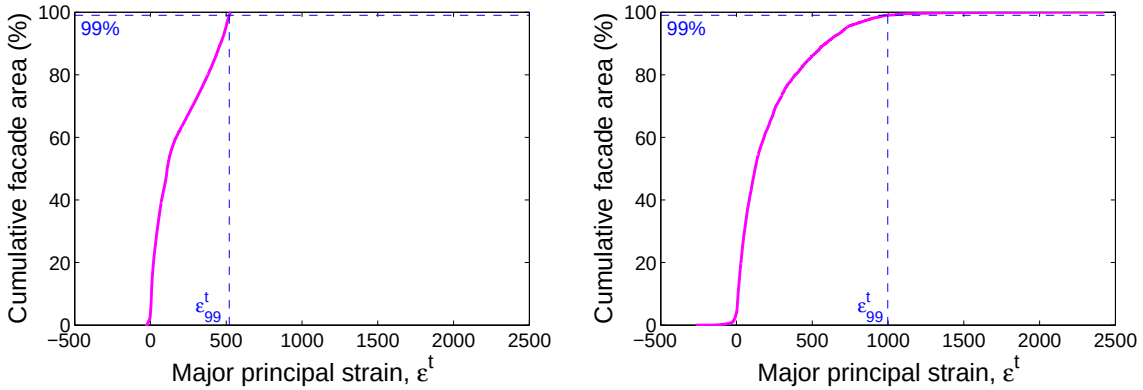


Figure 6.17: Cumulative distribution of major principal strains in facades of $H = 8$ m in the single-tunnel case, showing the meaning of ε^t_{99}: (a) plain facade; (b) facade with openings

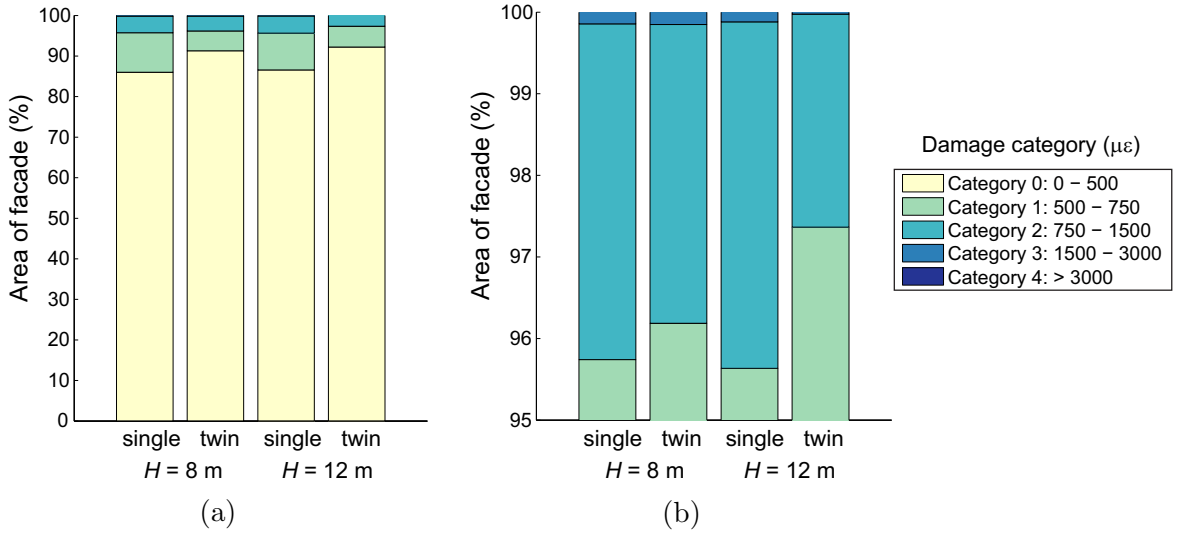


Figure 6.18: Building damage bar charts for isolated facades of height $H = 8$ m and 12 m for single and twin tunnels with $e = 0$: (a) complete range of cumulative facade area; (b) detail showing range between 95% and 100%

bar chart. This form of data presentation provides details of the proportion of the facade area that is affected by different levels of damage. For the current calculations, around 85% of the area of each facade is classified with negligible damage (Category 0). A small proportion of the facade area (less than 0.5%) is shown to suffer from Category 3 damage (Fig. 6.18(b)). However, considering the numerical properties of the strain concentration at the corners of the openings, the ε^t_{99} values determined from the analyses, which indicate Category 2 damage, probably provide a more realistic metric of the likely highest level of damage.

The distortion of the openings can be quantified approximately by assuming each

Table 6.5: Shear strains in window and door openings, facade height $H = 8$ m, single tunnel with $e = 0$. Opening numbers refer to Fig. 6.15(c)

Opening	11	12	13	14	15	16	17	18	19	20
γ ($\mu\varepsilon$)	422	1265	2934	1998	1070	1069	2001	2923	1253	419
Opening	1	2	3	4	5	6	7	8	9	10
γ ($\mu\varepsilon$)	1173	2176	3234	3026	1530	1521	3026	3232	2164	1173

opening in the facade as a quadrilateral finite element. The shear strains developed in each opening of the facade of $H = 8$ m in the single-tunnel case are shown in Table 6.5. The opening numbers refer to Fig. 6.15(c). The shear strains in several of the openings, particularly the two doors (opening number 3 and 8), are significantly larger than those in the adjacent masonry. This is to be expected, because the openings in the facade have zero stiffness assigned to them in the model. The overall shearing distortion of the facade is therefore accommodated, with a low penalty, by distortion of the openings.

6.3.3 Effect of constitutive model for the Terrace Gravel

The influence of the constitutive model used for the Terrace Gravel on the results of building damage assessments is explored. Separate simulations of the models TSA-F{08,12}O-T{1,2}e00 are conducted using the MC model specified in Section 6.2.2.

There is no significant difference in the displacement profiles of the footing and the adjacent soil between the results computed using the EMC model and the MC model (plot is not shown here). Fig. 6.19 shows the characteristic strain, $\varepsilon_{99}^{\mathrm{t}}$, computed using the EMC model and the MC model. The $\varepsilon_{99}^{\mathrm{t}}$ are similar in the single-tunnel case, while in the twin-tunnel case, the $\varepsilon_{99}^{\mathrm{t}}$ is marginally greater when the MC model is used than when the EMC model is employed. Furthermore, the choice between the two constitutive models for the Terrace Gravel appears to only have a small difference on the effect of building height to the building damage, as indicated in Table 6.6.

The current results show that, for the purpose of building damage assessments, the employment of the EMC model for the Terrace Gravel does not make a major differentiation from using the Abaqus built-in MC model. This suggests that the calibrated MC model, which incorporates a reduction in shear modulus to account for the

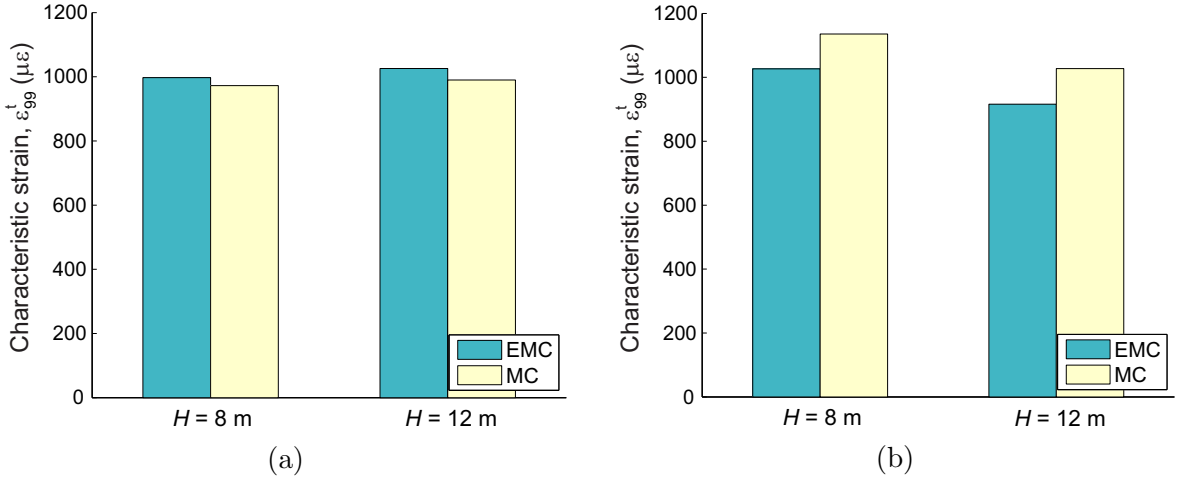


Figure 6.19: Characteristic strain ε_{99}^{t} induced on the facade (H = 8 m and 12 m) when the EMC model and the MC model are employed respectively: (a) single tunnel; (b) twin tunnels

Table 6.6: Characteristic strain ε_{99}^{t} (in microstrain) induced in the facade (H = 8 m and 12 m) and its percentage change with respect to the increase in building height when the EMC model and the MC model are employed respectively

		Building height		
	Soil model	$H = 8$ m	$H = 12$ m	Percentage change
Single tunnel				
	EMC	997	1026	+2.9%
	MC	973	990	+1.75%
Twin tunnel				
	EMC	1026	916	-10.7%
	MC	1136	1027	-9.60%

likely development of small strains (Section 6.2.2), may be adequately representative of the Terrace Gravel in the current calculations, and can be considered as a possible simplification of constitutive model in building damage assessments.

6.3.4 Effect of tunnel eccentricity

Simulations are conducted via varying the tunnel eccentricity, e, in 5 m increments for $0 \leq e \leq 30$ m. Twenty-four models TSA-F{08, 12}O-T{1, 2}e{05, 10, 15, 20, 25, 30} are created for this study. Note that the definitions of eccentricity are different in the two tunnel configurations (Fig. 3.4). An additional set of simulations with plain facades (models TSA-F{08, 12}P-T{1, 2}e{05, 10, 15, 20, 25, 30}) is included for comparison.

Fig. 6.20 plots the settlement profiles at the base of the footing of the facade with

openings of height $H = 8$ m and $H = 12$ m, and the corresponding greenfield vertical displacements. At zero eccentricity, the dominant mode of deformation of the facade is sagging in the single-tunnel case and hogging in the twin-tunnel case. As e increases gradually, the effect of the dominant deformation mode reduces. For larger values of e (around $e = 20$ m in single-tunnel case and $e = 15$ m in twin-tunnel case), the dominant mode of deformation changes in these cases. In the single-tunnel case, most parts of the facade are situated beyond the point of inflection of the settlement curve so the facade deforms predominantly in hogging, whereas in the twin-tunnel case, the facade is located above one of the tunnels and deforms in sagging predominantly.

Fig. 6.21 shows the $\varepsilon_{99}^{\mathrm{t}}$ computed in the facade with openings for different values of e. The data show that for both the single- and twin-tunnel cases, the $\varepsilon_{99}^{\mathrm{t}}$ is maximal at $e = 0$. The other local maximum of $\varepsilon_{99}^{\mathrm{t}}$ (at $e = 25$ m in the single-tunnel case and $e = 20$ m in the twin-tunnel case) occurs after the dominant mode of deformation has changed (i.e. to hogging in the single-tunnel case, and to sagging in the twin-tunnel case). The results suggest that, for building damage assessments in practice, extra attention should be paid not only to the buildings closest to the tunnel alignment, but also to those located beyond the inflection points. The data also show that the shorter building ($H = 8$ m) generally suffers from greater damage than the taller one ($H = 12$ m) as the taller building behaves in a stiffer manner.

Also presented in Fig. 6.21 is the comparison of the $\varepsilon_{99}^{\mathrm{t}}$ computed from the facade with openings to those from the plain facade. The $\varepsilon_{99}^{\mathrm{t}}$ of the facade with openings is always greater than that of the plain facade at the same e, owing to the reduced building stiffness and the strain concentrations around the openings. These effects are more significant when the dominant deformation mode of the facade is sagging (around $0 \leq e \leq 15$ m in the single-tunnel case and 15 m $\leq e \leq 30$ m in the twin-tunnel case).

6.3.5 Soil-foundation interaction sensitivity study

Building foundation details have often been excluded in previous finite element models for damage assessment purposes. One reason for this could be uncertainties in

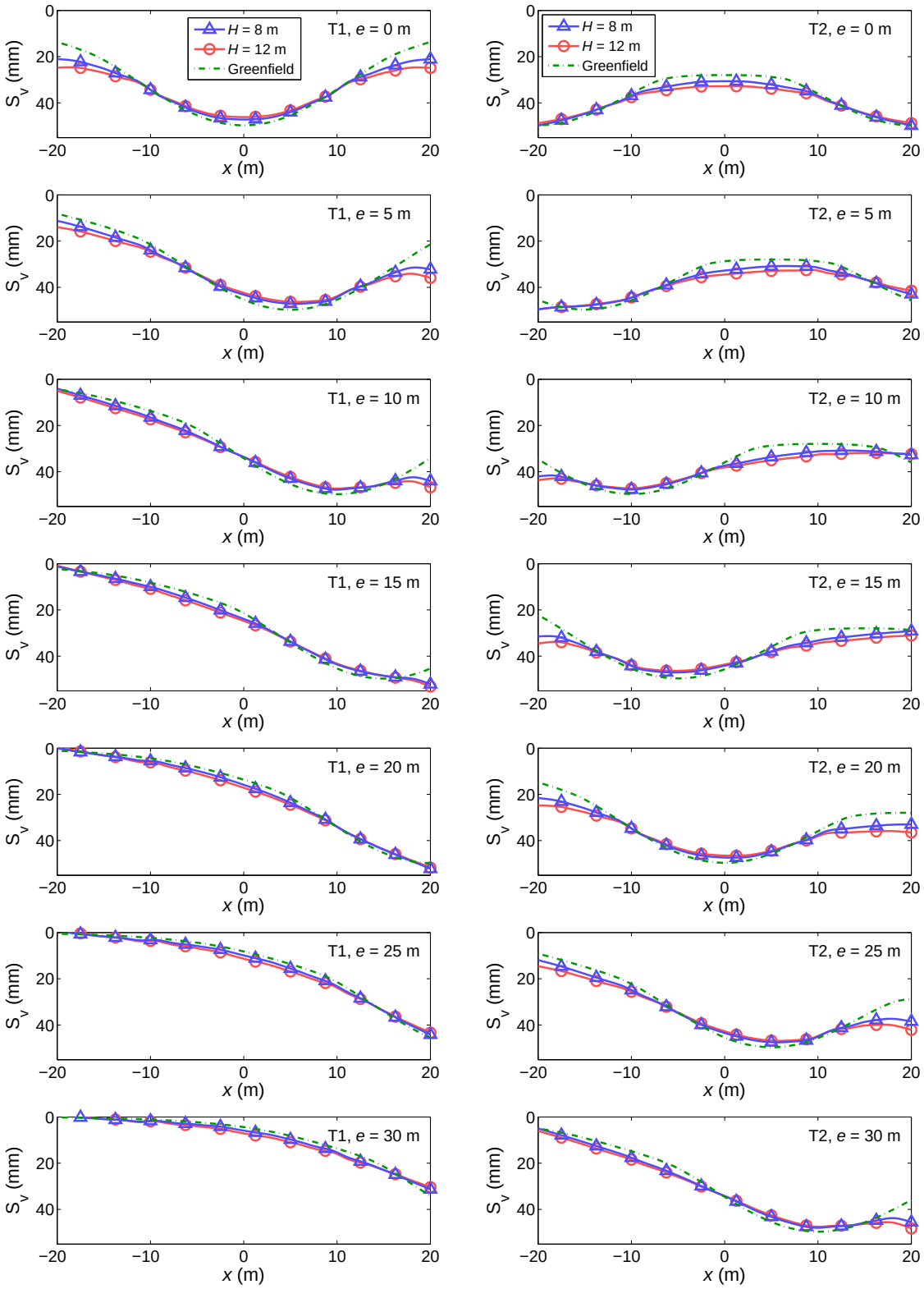
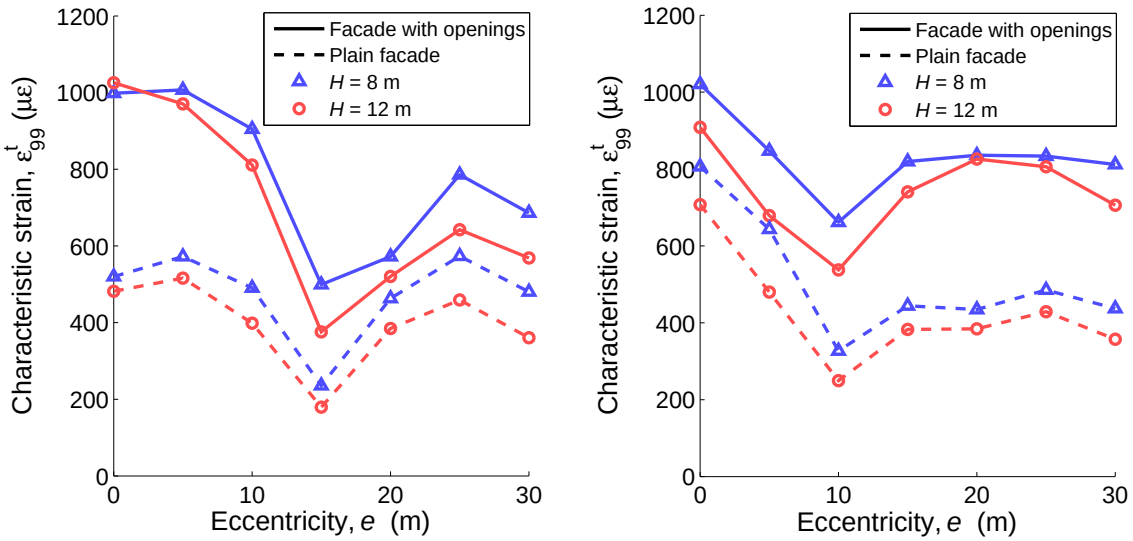


Figure 6.20: Vertical displacement, S_v, at the base of the footing of facade with openings of height $H = 8$ m and $H = 12$ m, plotting against the horizontal distance from facade centre, x, at different values of tunnel eccentricity, e: (a) single tunnel; (b) twin tunnels. Also showing the greenfield profile at the corresponding position



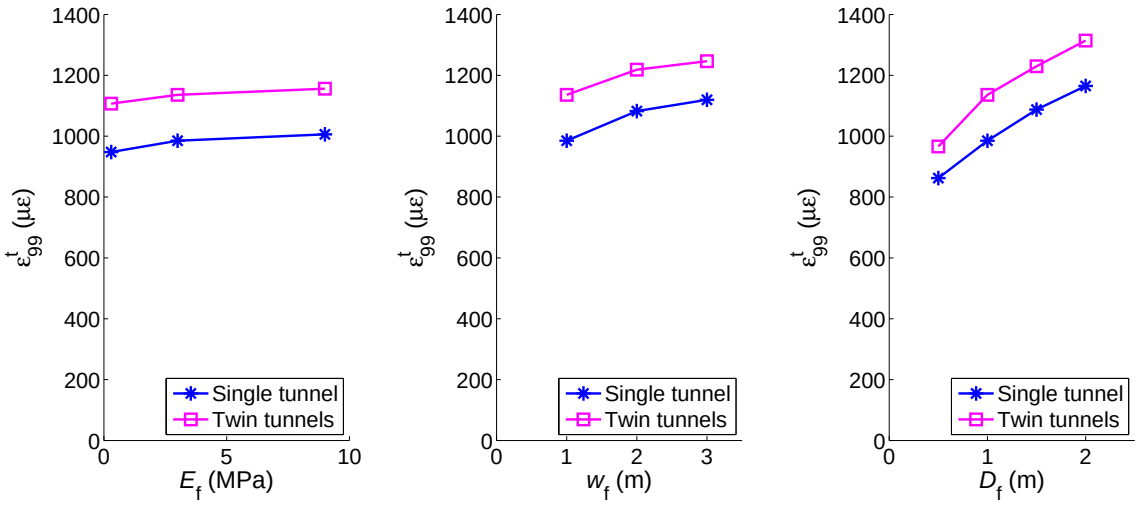
(a) (b)

Figure 6.21: Variation with eccentricity of characteristic strain $\varepsilon^{\mathrm{t}}_{99}$ for facades with openings and plain facades of height $H = 8$ m and 12 m: (a) single tunnel; (b) twin tunnels

the form, material and condition of the foundation (e.g. Viggiani & Standing 2001), particularly for historical buildings. Although it may be possible to deduce the foundation geometry and material from architectural history documents and survey data, engineering judgement is inevitably needed to determine the appropriate foundation details, and to assess the likely condition of the foundation. This section investigates the significance of footing properties and the role of soil-foundation interaction models in 3D finite element analysis of tunnelling-induced damage to a masonry building.

6.3.5.1 Footing properties

The sensitivity study on footing properties is based on a facade with openings of height $H = 8$ m in single-tunnel and twin-tunnel cases with zero eccentricity (models TSA-F08O-T{1,2}e00). The structural characteristics of the strip footing are likely to vary between buildings. In the principal calculation, the building facade is founded on a continuous strip footing with width $w_{\mathrm{f}} = 1$ m, thickness $t_{\mathrm{f}} = 0.5$ m and embedment depth $D_{\mathrm{f}} = 1$ m (Fig. 3.3) and the footing is assumed to be made of masonry. Exploratory calculations are conducted with alternative values of the elastic modulus of the material E_{f}, the width w_{f} and the embedment depth D_{f} respectively.



(a) (b) (c)

Figure 6.22: Characteristic strain, ε_{99}^{t}, induced in facade with openings of $H = 8$ m by tunnelling with $e = 0$, varying with different footing properties: (a) footing stiffness, E_f; (b) footing width, w_f; (c) footing embedment, D_f

Effect of footing stiffness.

In practice, it is likely that considerable uncertainties concerning the detailed composition and properties of the foundation exist. Three typical footing construction materials, namely rubble, masonry and concrete, are considered and modelled as a homogeneous material. To provide a preliminary understanding of the sensitivity of the computed results to the material used to construct the footing, in this exercise (Section 6.3.5.1 only), the three footing materials are represented by a linear elastic model with the Young's modulus, E_f, of 0.3 MPa, 3 MPa and 9 MPa respectively and a Poisson's ratio of 0.2.

Computed values of ε_{99}^{t} for the facade with openings are plotted in Fig. 6.22(a). The value of ε_{99}^{t} is seen to be insensitive to the value of the stiffness of the footing employed in the analysis.

Effect of footing width.

Analyses are conducted with different values of footing width, w_f, of 1 m, 2 m and 3 m (footing stiffness $E_f = 3$ MPa). Fig. 6.22(b) indicates that ε_{99}^{t} increases marginally with increasing w_f. It seems plausible that increasing the width of the footing tends to mobilize a larger volume of soil beneath the foundation, thereby increasing the effective

stiffness of the ground. As a consequence, the building is forced to follow the greenfield settlement more closely for a larger footing width, resulting in an increase in damage.

Effect of footing embedment depth.

Analyses are conducted with values of footing embedment depth, D_{f}, of 0.5 m, 1 m, 1.5 m and 2 m (footing stiffness $E_{\mathrm{f}} = 3$ MPa and footing width $w_{\mathrm{f}} = 1$ m). The results, shown in Fig. 6.22(c), indicate that increasing the value of D_{f} has a significant effect on increasing $\varepsilon^{\mathrm{t}}_{99}$. This effect is attributable to two mechanisms: (i) increasing footing embedment reduces the distance between the foundation and the tunnel, and (ii) increasing the embedment of the footing increases the effective stiffness of the ground, with a consequential increase in damage to the facade, which is similar to the mechanism occurred with an increased footing width.

6.3.5.2 Frictional soil-foundation interface

The tangential frictional contact with a friction coefficient, μ, of 0.3 and zero normal tensile strength is assumed as the interaction model at the soil-footing interface in the main scenario (Section 3.4). In practice, the frictional characteristics of the soil-footing interface are unlikely to be known with any certainty. A sensitivity study is therefore conducted to investigate the influence of this particular feature of the model on the outcome of the damage assessment. A range of interface behaviours from completely smooth to fully rough are represented by $\mu = [0, 0.3, 0.6, \infty]$. The interface model with $\mu = [0, 0.3, 0.6]$ is defined in Abaqus as described in Section 3.4. The fully rough interface ($\mu = \infty$) is defined using *FRICTION, ROUGH without a numerical value. The study is built based on the principal models TSA-F{08,12}O-T{1,2}e00.

Tractions at the soil-footing interface.

The normal tractions (compression positive) on the footing base for the facade of height $H = 8$ m and $H = 12$ m before and after tunnelling for smooth ($\mu = 0$) and rough ($\mu = \infty$) interfaces are plotted in Fig. 6.23. Construction of the tunnel causes the normal tractions at the base of the footing to redistribute, towards the edges of the

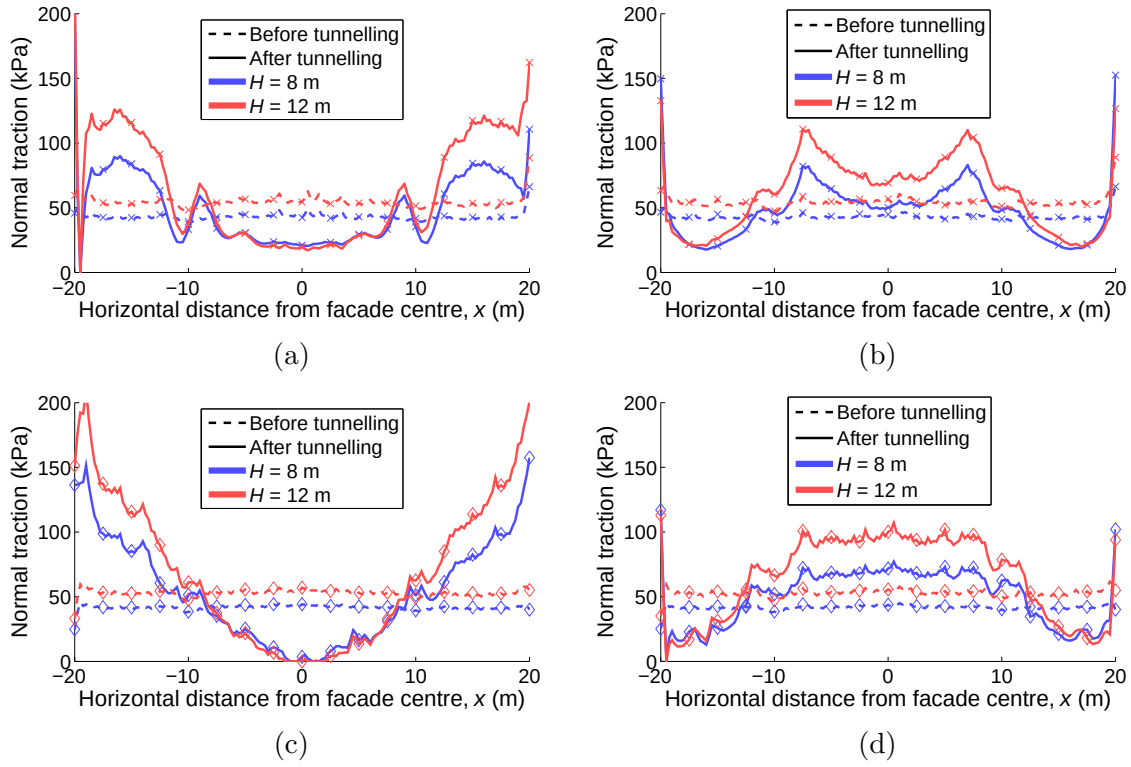


Figure 6.23: Normal traction on foundation base for facade with openings of height $H = 8$ m and $H = 12$ m, before and after tunnelling: (a) $\mu = 0$, single tunnel; (b) $\mu = 0$, twin tunnels; (c) $\mu = \infty$, single tunnel; (d) $\mu = \infty$, twin tunnels

facade in the single-tunnel case, and towards the centre of the facade in the twin-tunnel case. As the friction coefficient increases, the extent of normal traction redistribution becomes greater. Fig. 6.24 shows the shear tractions on the footing base after tunnelling corresponding for smooth ($\mu = 0$) and rough ($\mu = \infty$) interfaces. As expected, for a smooth interface ($\mu = 0$), the shear tractions at the soil-footing interface are zero. For a rough interface ($\mu = \infty$) and also for intermediate values of μ (not shown in the figure), the shear tractions typically act towards the tunnel location.

Displacement profiles.

Fig. 6.25 shows the vertical displacement profiles of the base of the footing, and of the adjacent soil, for $\mu = [0, 0.3, 0.6, \infty]$. For the single-tunnel case, as shown in Figs 6.25(a) and (c) for $H = 8$ m and $H = 12$ m respectively, as the friction coefficient increases, the displacement profile flattens, causing the differential settlement to reduce. This effect is a combined consequence of the normal traction redistribution and the beneficial inward-acting shear tractions that develop at the base of the footing as a result of

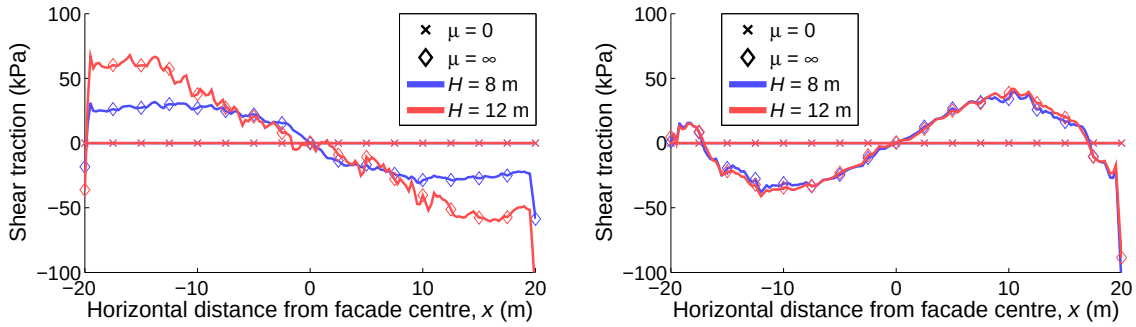


Figure 6.24: Shear traction on foundation base for facade with openings of height $H = 8$ m and $H = 12$ m after tunnelling for $\mu = [0, \infty]$: (a) single tunnel; (b) twin tunnels

the tunnel-induced ground movements. This effect is less noticeable in the vertical displacements in the twin-tunnel case, as shown in Figs 6.25(b) and (d).

The horizontal displacements of the footing and the adjacent ground at the soil-footing interface for $\mu = [0, 0.3, 0.6, \infty]$ are plotted in Fig. 6.26. As the problem is symmetric about $x = 0$, only the profiles corresponding to the right half of the span are shown. For both tunnel configurations, the friction coefficient has a significant effect on the horizontal displacement profile. In greenfield conditions, the soil moves towards the tunnel centre(s) in both tunnel cases. When the building is present with a smooth soil-footing interface ($\mu = 0$), for which the shear tractions at the interface are zero (Fig. 6.24), the soil has a horizontal displacement profile that is close to the greenfield case. The horizontal displacements of the base of the footing, however, are smaller in magnitude and opposite in direction to those in the adjacent soil due to the beam action of the building. Significant sliding therefore occurs at the soil-footing interface in both tunnel cases.

As the friction coefficient increases, as expected, the relative horizontal movements between the footing and the ground reduce. At $\mu = 0.6$, for example, in the single-tunnel case, sliding displacements at the soil-footing interface near the ends of the facade ($x \approx 15$ to 20 m) become relatively small. Similar behaviour is observed at the mid-span of the facade ($x \approx 0$ to 5 m) for the twin-tunnel case. This suggests that the regions where the building deforms in hogging are more sensitive to the frictional effects than the sagging regions. Moreover, for larger values of the friction coefficient

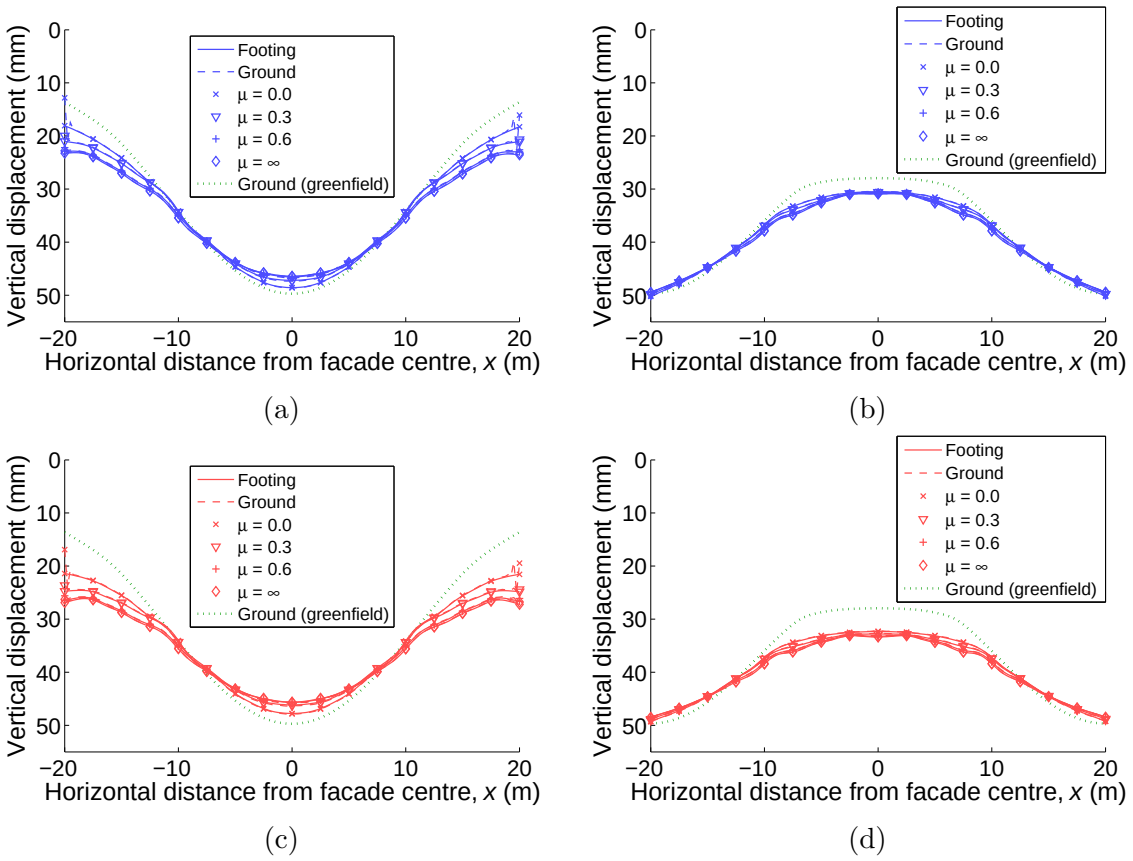


Figure 6.25: Vertical displacements at foundation base induced by tunnelling with various friction coefficients, compared with greenfield vertical displacements: (a) facade height $H = 8$ m, single tunnel; (b) facade height $H = 8$ m, twin tunnels; (c) facade height $H = 12$ m, single tunnel; (d) facade height $H = 12$ m, twin tunnels

(e.g. $\mu = 0.6$), the footing gradually moves in the same direction as the soil. In these cases, the base of the footing is compressed under sagging and extended under hogging — which is different from the conventionally assumed beam behaviour. For a fully rough interface ($\mu = \infty$), the two surfaces essentially stick together, and the horizontal displacements are substantially smaller in magnitude than those in the greenfield case.

Horizontal strains at the soil-footing interface.

The horizontal strains of the footing base and of the adjacent ground at the soil-footing interface for $\mu = [0, 0.3, 0.6, \infty]$ are shown in Fig. 6.27. In the single-tunnel case, with $\mu = 0$ (i.e. smooth interface), significant tensile strains up to $800\mu\varepsilon$ develop in the footing, which are associated with the sagging beam action of the building. The strains in the soil beneath the footing are predominantly compressive. As the friction coefficient increases and the strength of the interaction between the footing and the

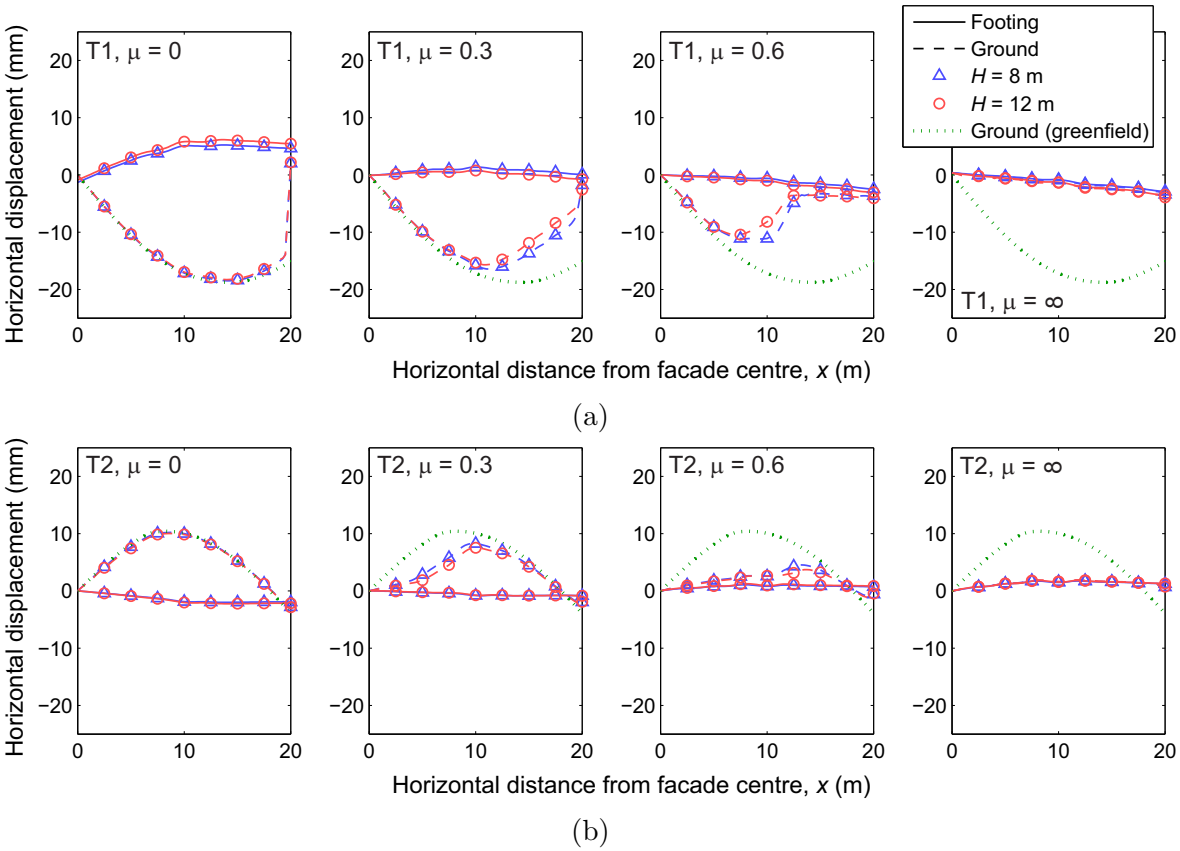


Figure 6.26: Horizontal displacements at foundation base level induced by tunnelling for various friction coefficients, $\mu = [0, 0.3, 0.6, \infty]$ from left to right: (a) single tunnel; (b) twin tunnels (Note that only the profile corresponding $0 \leq x \leq 20$ m of the facade span is shown)

soil increases, the tensile strains induced in the footing reduce. Eventually for a fully rough interface, the horizontal strains in the footing become compressive in the order of $200\mu\varepsilon$. These strains in the footing may be compared to the greenfield horizontal strains which vary between about $1000\mu\varepsilon$ tensile and $2200\mu\varepsilon$ compressive. In the twin-tunnel case, the general pattern is similar but in the opposite direction. For a smooth interface, the strains in the footing base are mainly compressive, which is consistent with the hogging deformation mode of the building, while the horizontal strains of the soil beneath the mid-span of the footing are tensile. As the friction coefficient increases, the influence of the soil causes the strains in the footing to become more tensile.

In both tunnel scenarios, it appears that for $\mu = 0.3$ (as adopted in the principal calculations), the influence of the horizontal strains in the soil combined with the beam action of the building via shear at the soil-footing interface cause the horizontal strains at the base of the footing to be approximately zero.

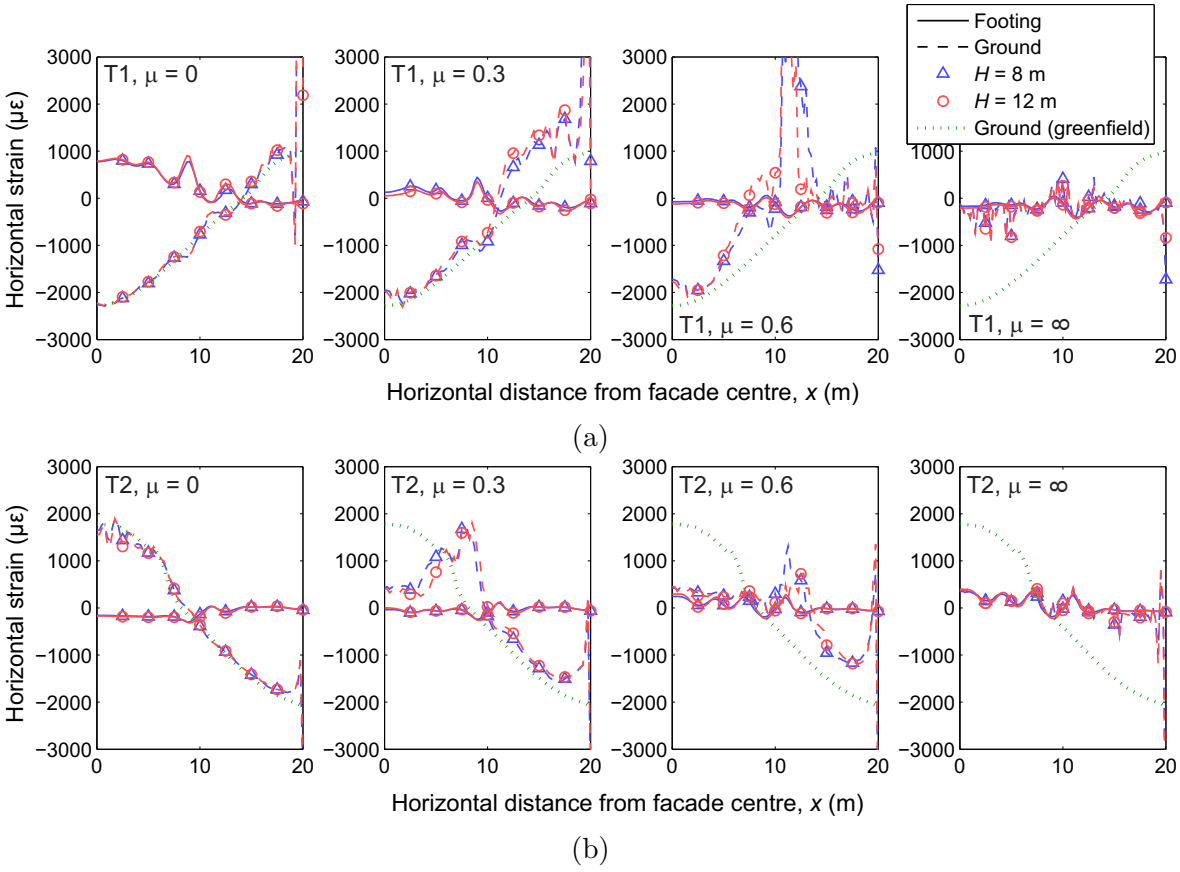


Figure 6.27: Horizontal strains at foundation base level induced by tunnelling for various friction coefficients, $\mu = [0, 0.3, 0.6, \infty]$ from left to right: (a) single tunnel; (b) twin tunnels (Note that only the profile corresponding $0 \leq x \leq 20$ m of the facade span is shown)

Tensile strains in the facade.

Figs 6.28 and 6.29 show the contour plots of the major principal strains (tension positive) induced in the 8 m high facade due to tunnelling for the single- and twin-tunnel cases respectively. Strain concentrations around the openings and the lintels are clearly visible, and it is apparent that the value of the friction coefficient at the soil-footing interface has a considerable influence on the facade strain field. Particularly in the twin-tunnel case (Fig. 6.29), when $\mu = 0$, high strain concentrates at the top of the facade and, regardless of the shear bands, there is an approximately uniform gradient of strain variation over the facade height. This roughly corresponds to the beam action with a neutral axis located at the bottom of the beam. However, as the friction coefficient increases, the facade becomes increasingly coupled to the ground. In this case, relatively high strains develop in the bottom part of the facade and the neutral axis appears to shift to a lower position.

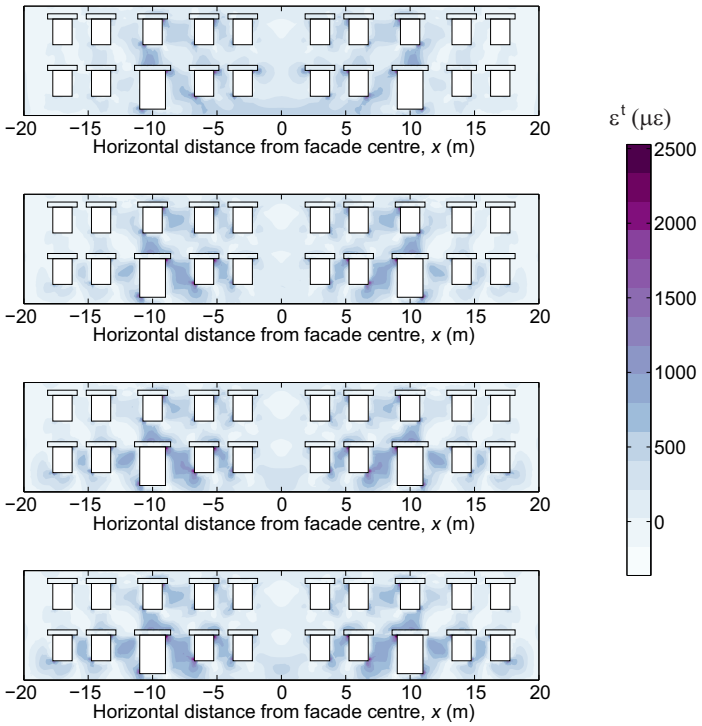


Figure 6.28: Major principal strains ε^{t} in facades of height $H = 8$ m induced by single tunnel with various friction coefficients in the contact model adopted for the soil-footing interface. From top to bottom: $\mu = [0, 0.3, 0.6, \infty]$

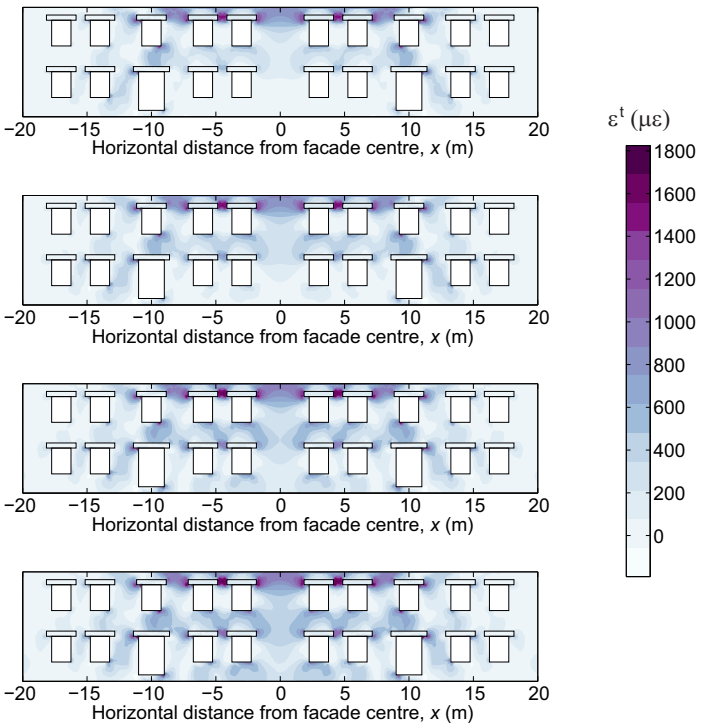


Figure 6.29: Major principal strains ε^{t} in facades of height $H = 8$ m induced by twin tunnels with various friction coefficients in the contact model adopted for the soil-footing interface. From top to bottom: $\mu = [0, 0.3, 0.6, \infty]$

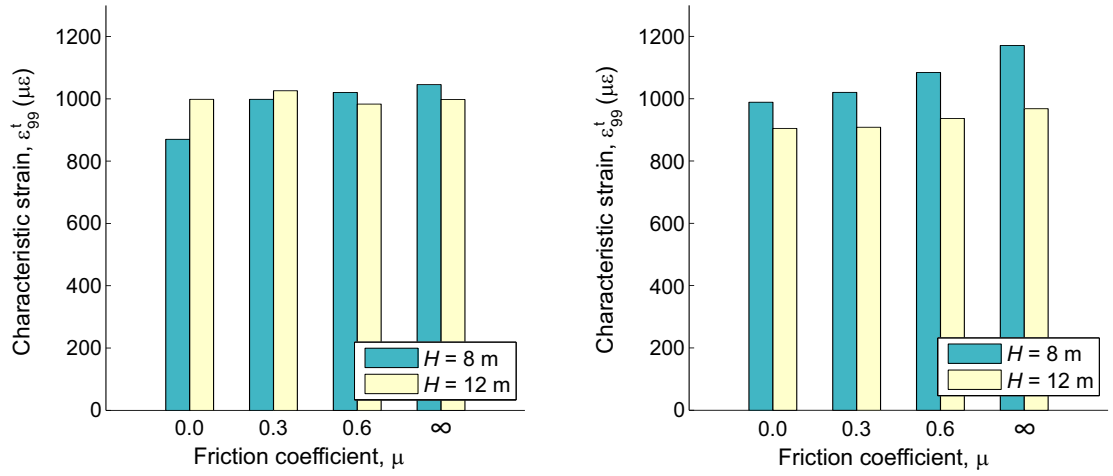


Figure 6.30: Characteristic strains ε_{99}^{t} induced in facades of height $H = 8, 12$ m with different friction coefficients for the soil-footing interaction model: (a) single tunnel; (b) twin tunnels

The significance of the value of friction coefficient employed in the analysis in the context of building damage assessment is illustrated in terms of the characteristic strains, ε_{99}^{t}, in Fig. 6.30. For the facade with $H = 8$ m in both tunnel configurations, the ε_{99}^{t} increases gradually with increasing friction coefficient. However, the ε_{99}^{t} for the facade with $H = 12$ m is relatively insensitive to the variation of the friction coefficient.

It is noted that the ε_{99}^{t} generally increases as the friction coefficient increases, although the vertical differential displacements and the horizontal strains tend to decrease. This might indicate that higher tensile strains develop around the facade openings with larger friction coefficient (and the mesh-dependent extreme values computed at the corners of the openings have been discounted using the characteristic strain approach). However, considering that the values of ε_{99}^{t} remain in the same building damage category (Category 2: $750 - 1500\mu\varepsilon$), the surface roughness is regarded to have a relatively small effect on the building damage. This suggests that uncertainties in frictional characteristics of the soil-foundation interface are likely to be relatively unimportant for practical assessment purposes. Adopting a fully rough interface may provide a conservative and convenient estimate of tensile strains for the purpose of tunnelling-induced building damage assessments, if the displacements and strains at the soil-footing interface are not the main concerns.

In the other calculations of the current work, the friction coefficient of 0.3 is still employed. Analyses with this value ($\mu = 0.3$) are demonstrated to compute horizontal movements of the foundation and the soil that agree with previous field monitoring and centrifuge test data (Section 6.3.1).

6.3.6 Evaluation of elastic beam assessment (EBA) method

In the phased procedures of building damage assessments (Section 2.3.4), buildings that are identified likely to be affected by tunnel construction in the initial greenfield assessment (Phase 1) are preliminarily assessed using a relatively simple analytical approach in which the building is modelled as an elastic beam (Burland & Wroth 1975, Boscardin & Cording 1989) (Phase 2). This procedure is referred to the elastic beam assessment (EBA) method in the thesis. The EBA method and the 3D isolated facade analysis approach share the assumptions of (i) the building in concern being independent of other structures and (ii) the severity of damage being correlated with the tensile strain developed in the building as determined from the model. The finite element analysis results therefore provide a basis for understanding the nature and impact of some of the simplifications and assumptions inherent in the EBA method, at least for the particular tunnelling scenarios investigated here. The conventional EBA calculation approach is denoted by EBA_A. A modified procedure, referred to EBA_B, is developed from the EBA_A approach to diagnose the effect of some assumptions.

6.3.6.1 Conventional EBA_A approach

The assumptions in the EBA method (Burland 2001) include that

1. the building is modelled as a rectangular beam of length L and height H_{EBA} (taken as the height from foundation level to the roof),
2. the beam conforms to the greenfield tunnel-induced ground movements that are estimated to occur at foundation level,
3. the length of the building beyond $2.5i$ (where $S_\text{v}/S_{\text{v,max}} \approx 0.44$) of the settlement trough is not taken into account,

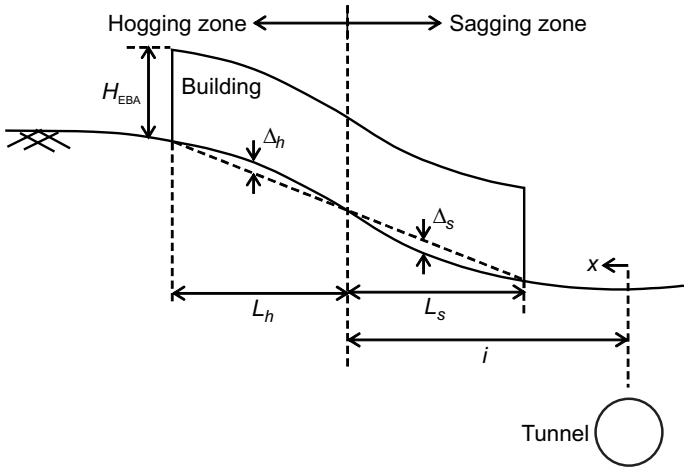


Figure 6.31: Building deformation assumed in the elastic beam assessment method (after Burland 2001)

4. the points of inflection of the settlement profile partition the beam into hogging and sagging sections, with length L_{h} and L_{s} respectively (Fig. 6.31),
5. each beam section is simply supported and under a central point load, resulting in a deflection, Δ_{h} or Δ_{s}, which is defined as the maximum settlement with respect to a straight line joining the two ends of the beam section (Fig. 6.31).

When deformation is imposed on the beam, it is likely that bending and shearing occur simultaneously. To calculate a single value of tensile strain representative of the possible extent of damage in the building (referred to the 'maximum tensile strain, $\varepsilon_{\mathrm{max}}^{\mathrm{t,EBA}}$'), each hogging and sagging beam section is considered for two extreme deformations, (i) bending only (about a neutral axis at the bottom of the beam for hogging and about a neutral axis at the centre of the beam for sagging), and (ii) shearing only.

The maximum bending strain, $\varepsilon_{\mathrm{b,max}}$, and the maximum diagonal strain, $\varepsilon_{\mathrm{d,max}}$, (which is equivalent to half of the engineering shear strain) are computed for each hogging and sagging beam section using the equations derived from the beam theory (Timoshenko 1957, Burland & Wroth 1975) as follows.

$$\varepsilon_{\mathrm{b,max}} = \frac{\Delta}{L} \Bigg/ \left(\frac{L}{12t} + \frac{3I}{2tLH_{\mathrm{EBA}}} \frac{E}{G} \right) \tag{6.3}$$

$$\varepsilon_{\mathrm{d,max}} = \frac{\Delta}{L} \Bigg/ \left(1 + \frac{H_{\mathrm{EBA}} L^2}{18I} \frac{G}{E} \right) \tag{6.4}$$

where Δ/L is also known as the deflection ratio, t is the distance from the neutral axis to the edge of the beam in tension ($t = H_{\mathrm{EBA}}$ for hogging and $t = H_{\mathrm{EBA}}/2$ for sagging), I is the second moment of area, E is the Young's modulus, and G is the shear modulus.

Horizontal strain from the settlement, ε_{h}, is incorporated to the beam in tension due to bending using simple superposition (Boscardin & Cording 1989). The ε_{h} used here is the average horizontal strain calculated from the total difference in horizontal displacement over the hogging section, instead of the local horizontal strain. The resultant bending strain, $\varepsilon_{\mathrm{b,r}}$, and the resultant diagonal tensile strain, $\varepsilon_{\mathrm{d,r}}$ are given by the following equations.

$$\varepsilon_{\mathrm{b,r}} = \varepsilon_{\mathrm{b,max}} + \varepsilon_{\mathrm{h}} \tag{6.5}$$

$$\varepsilon_{\mathrm{d,r}} = \varepsilon_{\mathrm{h}}\left(\frac{1-\nu}{2}\right) + \sqrt{\varepsilon_{\mathrm{h}}^2\left(\frac{1+\nu}{2}\right)^2 + \varepsilon_{\mathrm{d,max}}^2} \tag{6.6}$$

where ν is the Poisson's ratio. Finally, the maximum tensile strain, $\varepsilon_{\mathrm{max}}^{\mathrm{t,EBA}}$, is the greater of $\varepsilon_{\mathrm{b,r}}$ and $\varepsilon_{\mathrm{d,r}}$.

The horizontal strain of the soil under sagging is compressive and thus beneficial in restraining the beam from tensile damage. The ε_{h} in sagging section is ignored in the $\mathrm{EBA_A}$ procedure here.

6.3.6.2 Modified $\mathrm{EBA_B}$ approach

Two major assumptions in the $\mathrm{EBA_A}$ approach are that (i) the building follows the greenfield ground movements at foundation level, and (ii) the horizontal tensile strain is imposed additively for sections in tension. However, the results from the finite element analyses have demonstrated that the presence of the building modifies the ground movement as a consequence of its structural action (Fig. 6.10) and the foundation of the building experiences substantially lower horizontal strains than the surrounding soil (Fig. 6.11). Consistent findings are observed from the finite element analysis even when a smooth (uncoupled) soil-foundation interface is assumed, that the vertical differential displacements and the horizontal strains of the building are significantly smaller than

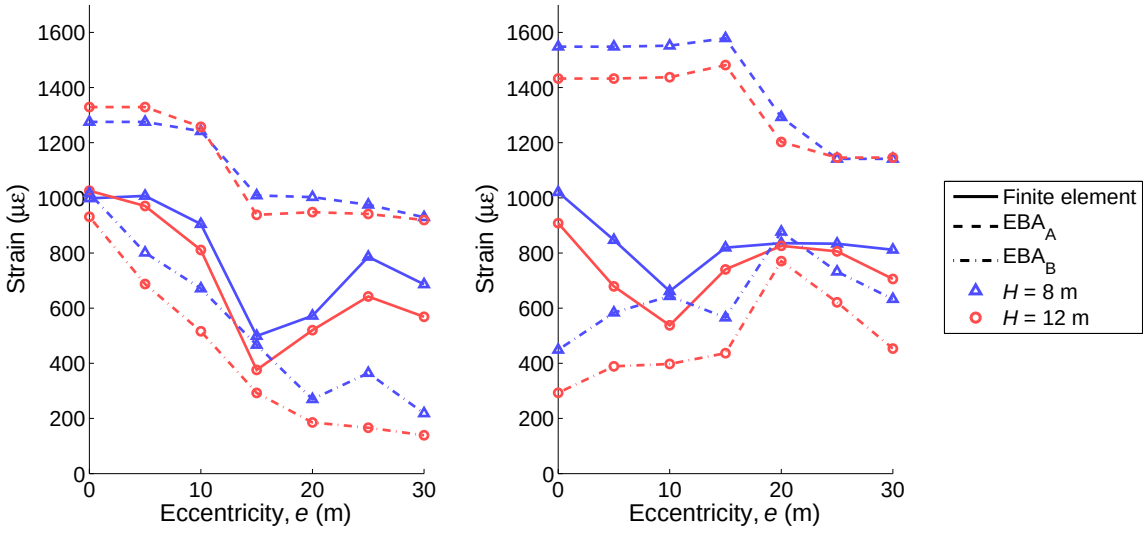
the greenfield values (Fig. 6.25 and Fig. 6.27).

A modified approach, $\mathrm{EBA_B}$, is developed in which the vertical displacements computed at the base of the foundation of the isolated facade from the finite element analysis are applied to the EBA beam model, and no additional ground horizontal strain is imposed on the beam. The $\mathrm{EBA_B}$ approach accounts for the reduced differential settlements and horizontal strains that are likely to be more realistic in a coupled scenario.

6.3.6.3 Comparison with finite element analysis results

The conventional EBA approach ($\mathrm{EBA_A}$) and the modified procedure ($\mathrm{EBA_B}$) are compared with the finite element analysis with a facade with openings for both single- and twin-tunnel cases with a range of tunnel eccentricities. In the EBA method, the full height of the facade down to foundation level is employed, i.e. $H_{\mathrm{EBA}} = 9$ m for $H = 8$ m and $H_{\mathrm{EBA}} = 13$ m for $H = 12$ m. The length of the building is $L = 40$ m; L_{h} and L_{s} vary with eccentricity. The elastic properties of the masonry are adopted for the elastic beam, with $E = 3$ GPa and $\nu = 0.2$, giving an isotropic beam with $E/G = 2.4$ in the EBA procedure. In the $\mathrm{EBA_A}$ method, the greenfield settlement profiles computed from the finite element calculations TSA-GF-T{1,2} (green dash-dot lines in Fig. 6.20) are applied to the beam. For the $\mathrm{EBA_B}$ method, the vertical displacement profiles at the base of the footing of the models TSA-F{08,12}O-T{1,2}e{00,05,10,15,20,25,30} (blue and red lines in Fig. 6.20) are adopted.

The values of the maximum tensile strain, $\varepsilon_{\mathrm{max}}^{\mathrm{t,EBA}}$, determined using the $\mathrm{EBA_A}$ and $\mathrm{EBA_B}$ methods are plotted in Fig. 6.32. Also shown are the characteristic tensile strain, $\varepsilon_{99}^{\mathrm{t}}$, computed from the finite element analysis using the isolated facade with openings (extracted from Fig. 6.21). It is clear from Fig. 6.32 that the $\varepsilon_{\mathrm{max}}^{\mathrm{t,EBA}}$ from $\mathrm{EBA_A}$ invariably exceed the $\varepsilon_{99}^{\mathrm{t}}$ obtained from the finite element analysis. This is an expected outcome (due to the relatively large greenfield differential settlements employed in $\mathrm{EBA_A}$) and is a reassuring confirmation of the conservatism inherent in the $\mathrm{EBA_A}$ method. In contrast, the $\varepsilon_{\mathrm{max}}^{\mathrm{t,EBA}}$ from $\mathrm{EBA_B}$ typically fall below the finite element data.



(a) (b)

Figure 6.32: Comparison of the maximum tensile strain, $\varepsilon_{\max}^{t,EBA}$, determined from the EBA methods and the characteristic strain, ε_{99}^{t}, obtained from the finite element analysis for facades with openings of height $H = 8$ m and 12 m, varying with eccentricity: (a) single tunnel; (b) twin tunnels

The significance of this can be understood in terms of the strain distributions in the facade. Although the vertical displacements at foundation level applied to the EBA_B model are identical to those that occur in the finite element model, the presence of the window and door openings in the finite element model (not accounted for in the EBA method) causes strain concentrations to occur around the internal corners, as shown in Figs 6.15(c) and (d) and Figs 6.16(c) and (d).

When the finite element analysis is used in the combined tunnel-soil-building system, the effect of the structural action of the building as well as the redistribution of bearing pressures on the base of the foundation are accounted automatically. The finite element results show that ground vertical displacements are modified by the building (Fig. 6.10) and the horizontal coupling between the foundation and the ground is relatively weak (Fig. 6.11). This contrasts with the conventional EBA method, which adopts the ground settlement and superposes horizontal strains from the ground to the building. The models in this study illustrate the conservative nature of the EBA_A approach. This suggests that predictions of the severity of damage are systematically overestimated

when the EBA_A method is employed. The absence of the strain localisation effect around the window and door openings in the EBA method, nevertheless, reduces the reliability of assessments using this approach.

6.4 Short-term complete building analysis

The usefulness of the isolated facade modelling approach are verified with selected 3D complete building analyses with orthogonal tunnels. Moreover, a case of a single skew tunnel is conducted using the complete building approach, as a demonstration of a scenario where direct application of the isolated facade approach is less trivial.

6.4.1 Orthogonal tunnel

Calculations with the complete building are conducted for building heights of $H = 8$ m and $H = 12$ m, considering both single and twin tunnels orthogonal to the building with zero tunnel eccentricity (models TSA-B{08,12}O-T{1,2}e00). The case $e = 0$ is selected because it causes the most severe building damage in the isolated facade analysis (Fig. 6.21). The results of complete building analyses are compared with the corresponding isolated facade calculations TSA-F{08,12}O-T{1,2}e00. The meshes of models TSA-B08O-T1e00 and TSA-B12O-T2e00 are shown in Figs 6.3(a) and (b).

The computed principal tensile strains in the front facade of the complete building of $H = 8$ m for the single-tunnel case with $e = 0$ are shown in Fig. 6.33(a). The magnitude and distribution of these strains are similar to those obtained from the corresponding isolated facade analysis (Fig. 6.15(c)). The computed vertical and horizontal displacements of the footing of the front facade are compared with the corresponding isolated facade data in Figs 6.33(b) and (c) (note that the magnitude of horizontal displacements in Fig. 6.33(c) is small); again, the two sets of data are similar.

Figs 6.33(d) and (e) show the vertical and horizontal displacements of the internal wall and the end wall of the complete building. Although the differential settlements experienced by these walls are small and may not be important in building damage

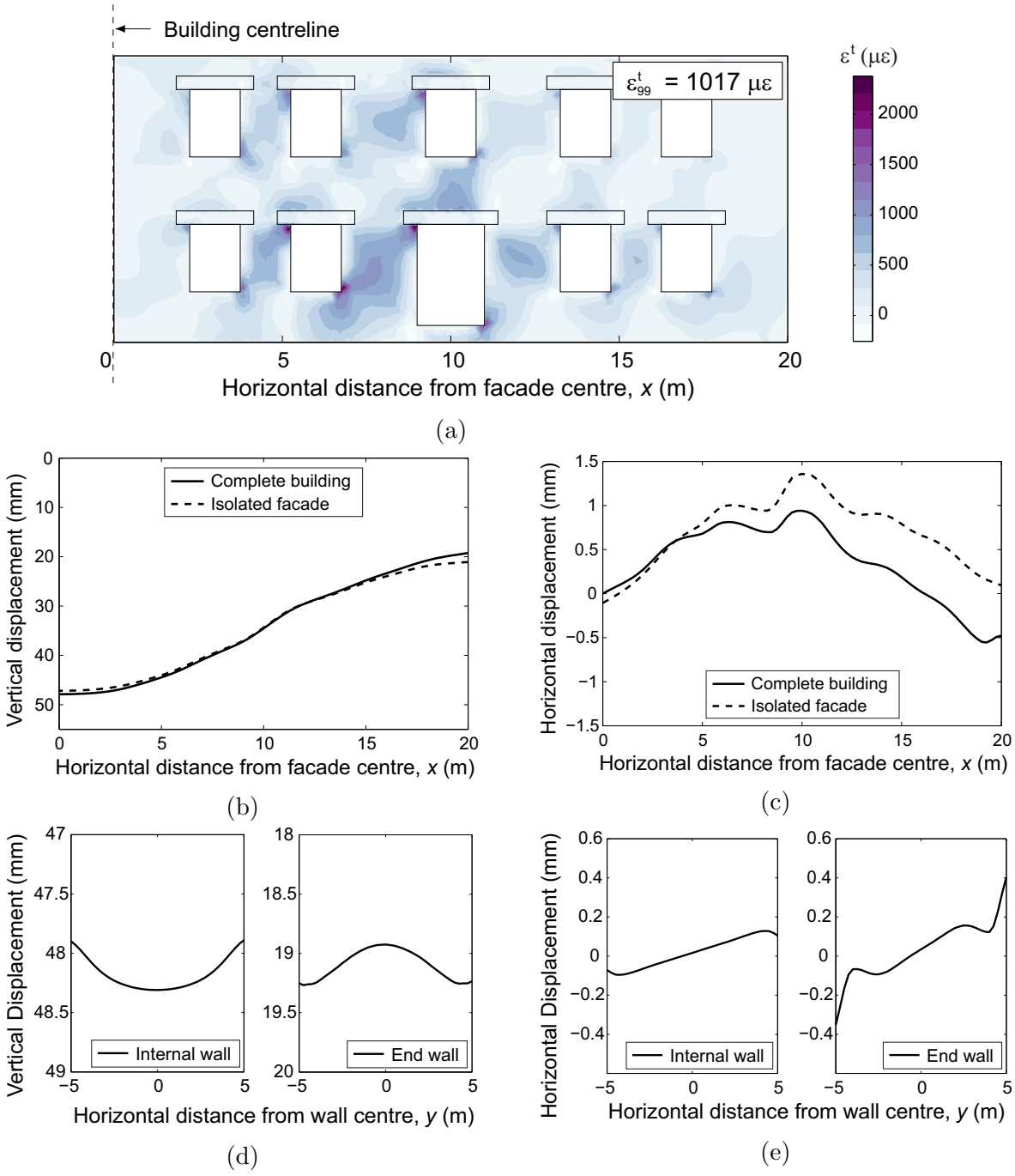


Figure 6.33: Data from complete building analysis with $H = 8$ m for single tunnel with $e = 0$, compared with data from corresponding isolated facade analysis: (a) major principal strains ε^t in the front facade (same scale as in Fig. 6.15(c)) and characteristic strain ε^t_{99}; (b) vertical displacement of the base of footing of the front facade; (c) horizontal displacement of the base of footing of the front facade; (d) vertical displacement of the base of footing of the internal and end walls; (e) horizontal displacement of the base of footing of the internal and end walls

assessments, the tendency of their movements provide more understanding about the 3D geometric effects of the building. As the internal wall is directly above the tunnel centre along the tunnel alignment in the single-tunnel case, the total vertical displacements of the internal wall are relatively large. The two ends of the internal wall are restrained by the foundations and facades perpendicular to the internal wall, resulting in the sagging shape of the vertical displacement profile and the outward horizontal movement towards the front and rear facades. In contrast, the end wall is away from the tunnel and acts to restrain the front and the rear facades from settling, resulting in the hogging shape in the vertical displacement profile of the end wall. As the internal wall tends to drag the facades and the end wall contributes in holding the facades in place, the front and rear facades are expected to settle more around $x = 0$ and settle less at about $x = 20$ m, compared to an isolated facade without the internal and end walls. This explains the difference, although relatively insignificant, between the vertical displacement profile of the front facade of the complete building and that of the isolated facade in Fig. 6.33(c).

The results for the twin-tunnel case with $e = 0$ is shown in Fig. 6.34. The tensile strain field of the front facade of the complete building in Fig. 6.34(a) is similar to the that of the isolated facade (Fig. 6.15(d)). The vertical and horizontal displacements at the base of the footing of the front facade in Fig. 6.34(b) and (c) are also comparable to the isolated facade. The influence of the internal and end walls are shown to be smaller in the twin-tunnel case than in the single-tunnel case.

The damage bar charts of the front facades of the complete building analysis are compared with the corresponding isolated facade analysis for both the single- and twin-tunnel cases and building heights of $H = 8, 12$ m in Fig. 6.35. For all the four scenarios considered here, the percentages of the area of facade in each damage category computed for the two modelling approaches are almost identical. The characteristic strains of the front facade and walls for the four complete building analyses and the corresponding isolated facade analyses are compared in Fig. 6.36. The $\varepsilon_{99}^{\mathrm{t}}$ computed for the front facade using the two modelling approaches are comparable. The influence

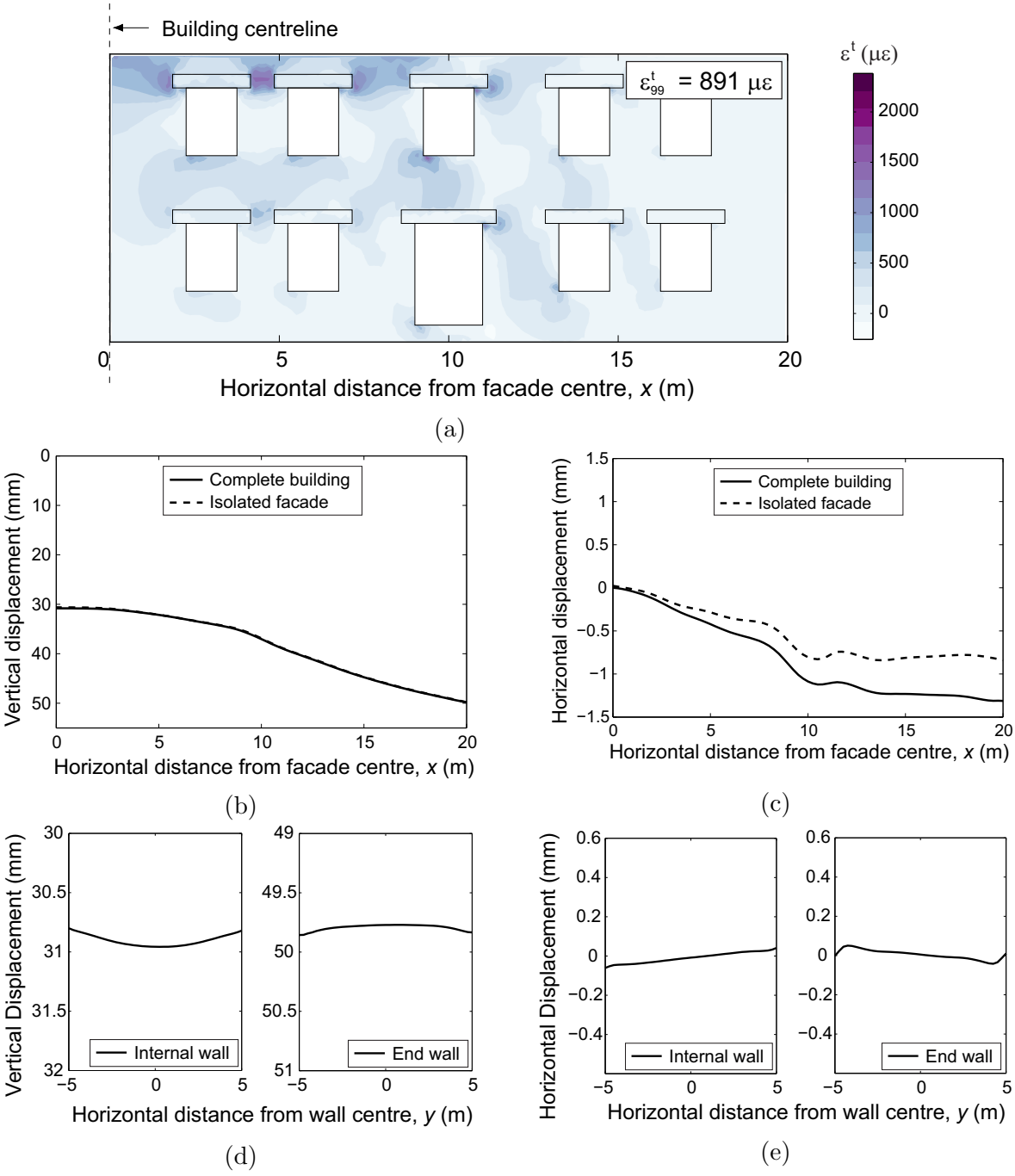
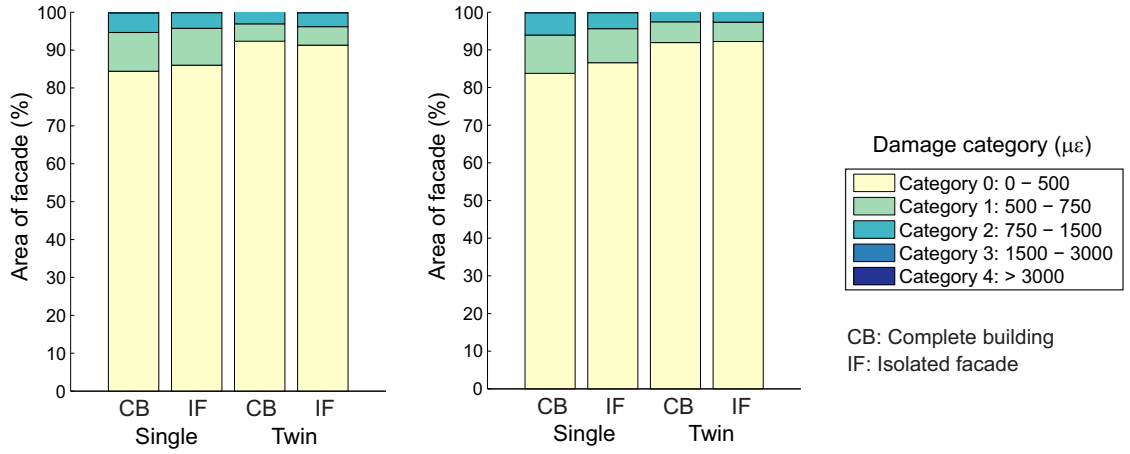
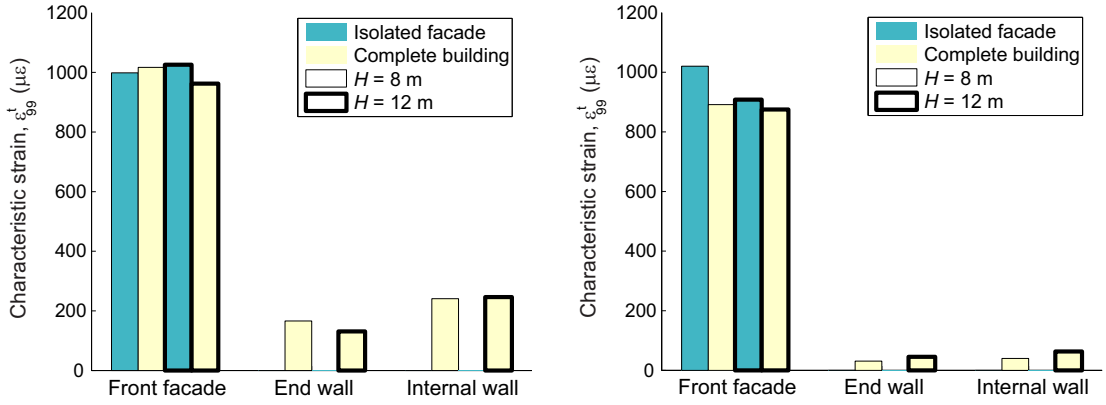


Figure 6.34: Data from complete building analysis with $H = 8$ m for twin tunnels with $e = 0$, compared with data from corresponding isolated facade analysis: (a) major principal strains ε^t in the front facade (same scale as in Fig. 6.15(d)) and characteristic strain ε^t_{99}; (b) vertical displacement of the base of footing of the front facade; (c) horizontal displacement of the base of footing of the front facade; (d) vertical displacement of the base of footing of the internal and end walls; (e) horizontal displacement of the base of footing of the internal and end walls



(a) (b)

Figure 6.35: Building damage bar charts for the front facade of the complete building for single- and twin-tunnel cases with $e = 0$, compared with data from corresponding isolated facade analysis: (a) building height $H = 8$ m; (b) building height $H = 12$ m



(a) (b)

Figure 6.36: Comparison of characteristic strains induced in individual facades (and return walls) of height $H = 8$ m and 12 m, obtained from complete building and isolated facade analyses for tunnels with $e = 0$: (a) single tunnel; (b) twin tunnels

of the internal wall, end walls and foundations running parallel to the tunnel axis appears to be relatively insignificant in the context of building damage assessment. This suggests that, at least for tunnel-building configurations similar to those considered here, isolated facade models are likely to be sufficiently detailed for the purpose of building damage assessments.

6.4.2 Skew tunnel

The 3D complete building finite element analysis allows modelling of complex geometric tunnel-building configurations which may not be plausible to model using the 3D

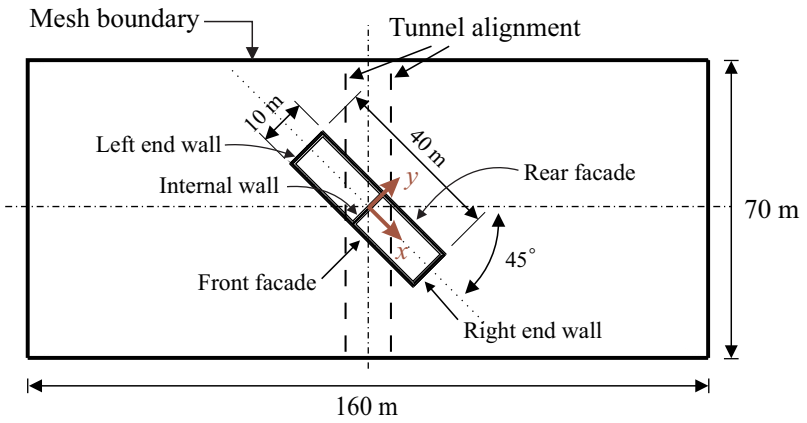


Figure 6.37: Plan view of the mesh showing relative position of the complete building and the skew tunnel. Also showing the coordinate axes used in this case

isolated facade approach. A skew tunnel case is modelled as an example. Analyses are conducted with a complete building with height $H = 8, 12$ m and a single tunnel aligned at 45° to the building facades and zero eccentricity to the centre of the building (models TSA-B{08,12}O-T1e00s45). The plan view of the model and its coordinate axes are shown in Fig. 6.37 and the mesh for the case of $H = 8$ m is displayed in Fig. 6.3(c). The results are compared with those obtained from the complete building analysis with the single orthogonal tunnel with zero eccentricity (models TSA-B{08,12}O-T1e00).

The computed principal tensile strains in the front facade of the building with $H = 8$ m are shown in Fig. 6.38(a). Strain concentrations are observed close to the right end (i.e. the region above the tunnel). Fig. 6.38(b) shows the damage bar chart of the front facade in the single skew tunnel case and that in the single orthogonal tunnel case. Comparisons of the results obtained from the cases of skew tunnel and orthogonal tunnel (Fig. 6.38(a) with Fig. 6.33(a), and also in Fig. 6.38(b)) indicate that the front facade experiences less damage when the tunnel is skewed. Fig. 6.38(c) shows the vertical displacements at the footing base of the front and rear facades in the skew tunnel case, and those in the single orthogonal tunnel case. The slope of the settlements in the skew tunnel case is slightly flatter than that in the orthogonal tunnel case. The horizontal displacements at the footing base of the front and rear facades are plotted in Fig. 6.38(d) and those for the return walls are shown in Fig. 6.38(f). The positive horizontal movements of the front facade and the left end wall, and the

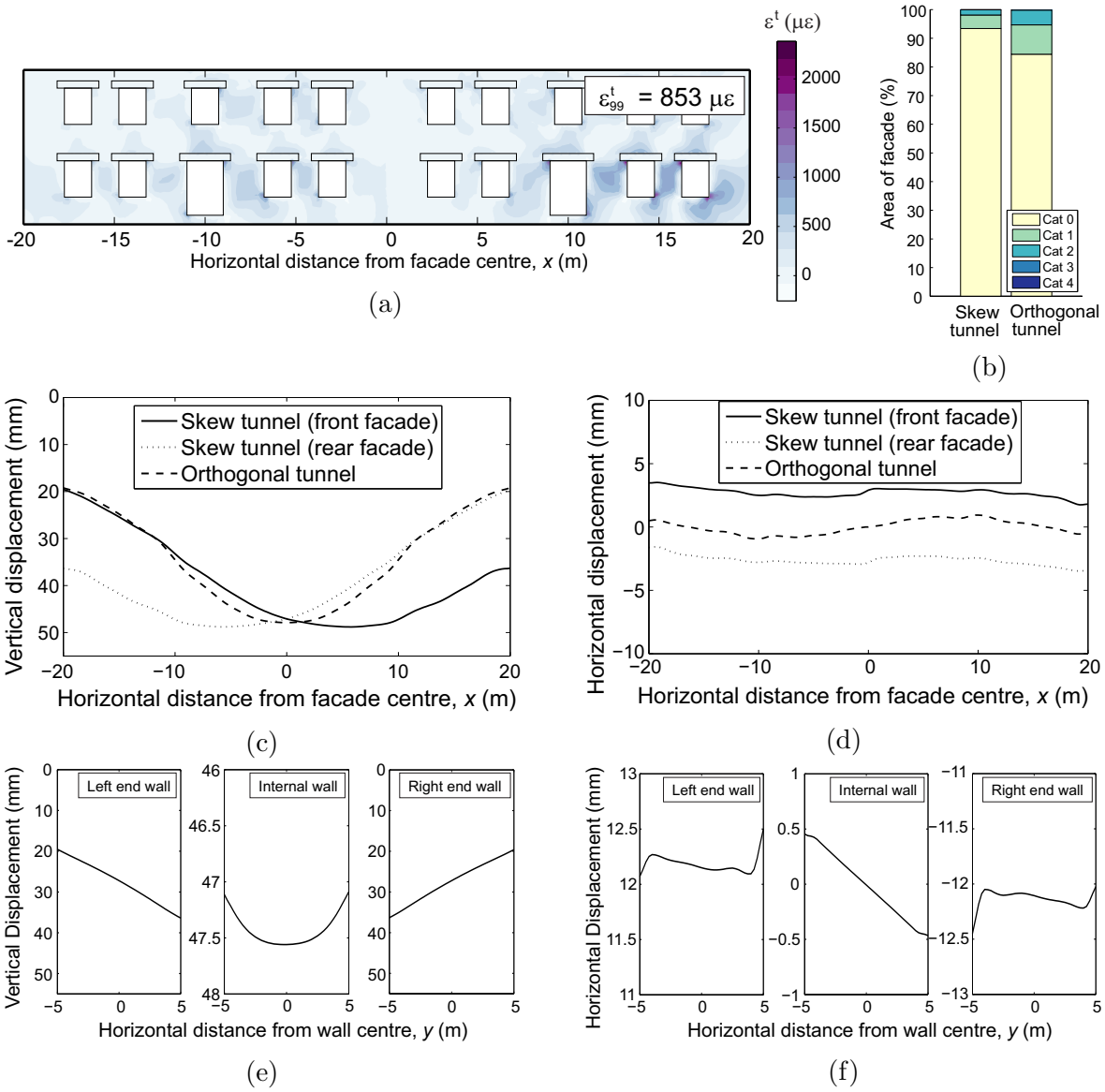


Figure 6.38: Data from complete building analysis with $H = 8$ m for skew single tunnel at 45°, compared with data from complete building analysis with $H = 8$ m and orthogonal single tunnel with $e = 0$: (a) major principal strains ε^t in the front facade (same scale as in Fig. 6.33(a)) and characteristic strain ε^t_{99}; (b) building damage bar chart of the front facade; (c) vertical displacement of the base of footing of the front and rear facades; (d) horizontal displacement of the base of footing of the front and rear facades; (e) vertical displacement of the base of footing of the return walls; (f) horizontal displacement of the base of footing of the return walls

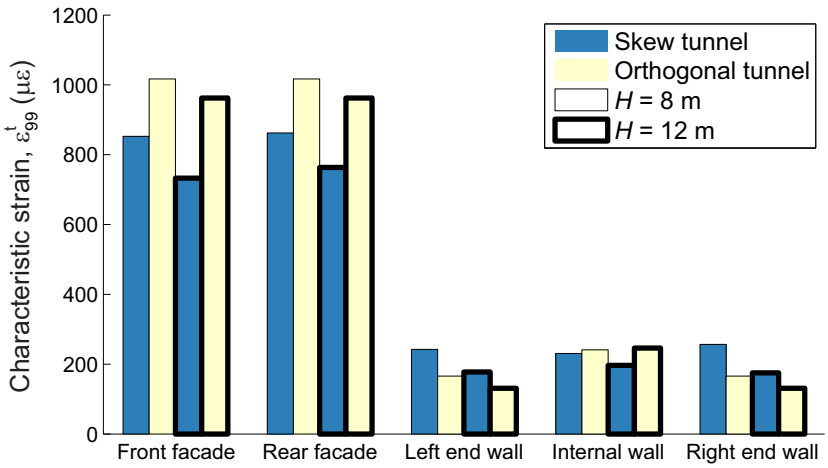


Figure 6.39: Comparison of characteristic strains induced in the facades and return walls obtained from complete building analyses, with height $H = 8$ m and $H = 12$ m, for single skew tunnel at 45° and single orthogonal tunnel

negative horizontal movements of the rear facade and the right end wall indicate that the building is twisted in the clockwise direction considered from the plan view.

Fig. 6.39 compares the characteristic strain, $\varepsilon_{99}^{\mathrm{t}}$, for each individual facade and wall of the complete buildings with $H = 8, 12$ m for the single skew tunnel case and the single orthogonal tunnel case. The $\varepsilon_{99}^{\mathrm{t}}$ computed from the front and rear facades in the skew tunnel case are less than those in the orthogonal tunnel case. Although data for the end walls indicate slightly larger tensile strains in the skew tunnel case, their damage categories remain in Category 0 $(0 - 500\mu\varepsilon)$. On the basis of this comparison, the orthogonal tunnel case appears to provide a more conservative damage estimate.

It is noted that transient effects associated with incremental tunnel construction are not included in the current model. Transient effects could be particularly significant for skew configurations in which complex twisting deformation modes may be induced in the building as the tunnel heading passes beneath it (Pickhaver et al. 2010).

6.5 Concluding remarks

The general trends indicated by the finite element analyses presented in this chapter are consistent with the expected behaviour: (i) the presence of the building tends to modify the local ground movements, (ii) reducing the building height or incorporating

openings for windows and doors leads to more severe damage, (iii) the footing details and contact models affect the deformation mechanism of the building, and (iv) the dominant mode of deformation of the building is affected by tunnel eccentricity.

The strain concentrations that develop around internal corners of facades with openings have a significant influence on the magnitude of the computed strains. The characteristic strain approach and the building damage bar chart proposed are demonstrated as practical result processing procedures.

Additionally, the analyses with appropriate frictional contact model at the soil-footing interface reproduce the commonly observed finding from field measurements that the horizontal strains in a building at foundation level are typically smaller than those in the adjacent ground, and substantially less than would be implied by the commonly used elastic beam assessment (EBA) method. This phenomenon, which is identified as being associated with slippage at the soil-foundation interface, suggests that the current assessment methods in which greenfield horizontal strains are imposed directly on a beam model of the building may be unrealistic. Detailed comparisons between the results obtained from the finite element analyses and the EBA method suggest that, in general, the EBA approach is likely to be conservative. However, modifications to the EBA method in which differential settlements are reduced on account of building stiffness may be unconservative, as a result of the negligence of strain concentrations at the corners of any facade openings in the standard EBA method.

For the orthogonal tunnel-building scenarios considered in this study, the 3D isolated facade analyses and 3D complete building analyses provide similar displacement profiles and tensile strains. The 3D complete building analysis with a skew tunnel predicts less damage than the orthogonal single tunnel case. This suggests that the 3D isolated facade modelling approach may provide a potentially useful tool within the hierarchical phased assessment approach that has evolved to facilitate the assessment of large numbers of buildings that may be affected by urban tunnelling operations.

Chapter 7

Effective stress analysis of building response to tunnelling

Long-term ground and building movements after tunnel construction are expected to be caused by at least three time-dependent mechanisms: (i) consolidation in the soil, (ii) creep in the soil, and (iii) creep in the masonry. The current work focuses on consolidation in the soil, which is due to changes in the effective stresses via dissipation of the tunnelling-induced excess pore pressures. Creep effects (further increase in strain as a result of long-term exposure to stress) are neglected in the current model. Effective stress analysis (ESA) is employed to study the long-term behaviour of the ground and the building after tunnel construction. The isolated facade analysis approach, with single and twin tunnels at zero eccentricity, is adopted for the coupled analysis.

The modelling procedures for effective stress analysis are described in Section 3.9. Drained conditions are assumed for the geological history, whereas the tunnel excavation is modelled by the nodal force reduction method under undrained conditions. The consolidation process after tunnel construction takes place under drained conditions and the drainage is affected by the permeability of the tunnel lining. The London Clay is represented by the M2-SKH model (Chapter 5), calibrated using the procedures in Section 5.3. The constitutive models for the Terrace Gravel and masonry are the EMC model and the non-linear concrete damaged plasticity model respectively.

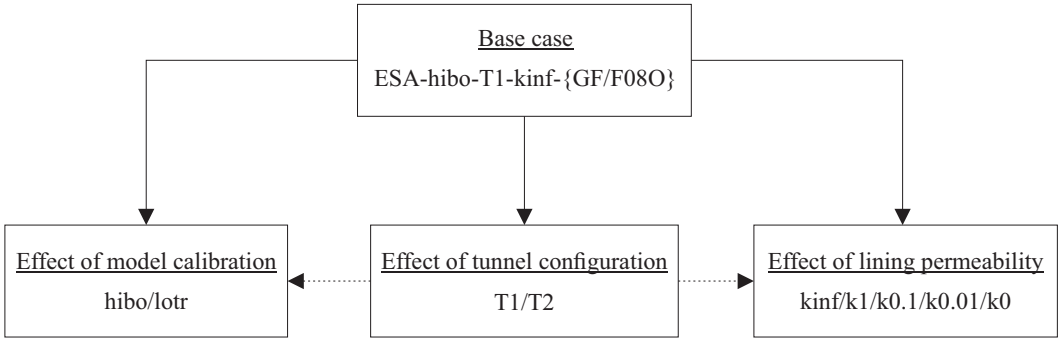


Figure 7.1: Structure of the parametric studies of the long-term effect of tunnelling using greenfield analysis and isolated facade analysis

7.1 List of calculations and meshes

Greenfield analysis is conducted to understand the long-term ground movements induced by tunnelling, before the building response is studied through coupled tunnel-soil-building analysis. Fig. 7.1 summarises the study plan for each set of analyses. The time effect on the ground response is first explored under greenfield conditions in the 'base case', where the single-tunnel configuration is used, the lining is assumed to be fully permeable and the 'high both' calibration is employed for the M2-SKH model. This is followed by an analysis with the twin-tunnel case. Further studies are conducted with both tunnel cases to consider the effect of the relative lining-soil permeability and the significance of the calibration of parameters adopted in the M2-SKH model. The building response over time is investigated via the isolated facade analysis approach, where an isolated facade with openings and a height of 8 m is employed with the tunnel(s) at zero eccentricity (eccentricity defined in Fig. 3.4). The parametric studies of the effects of tunnel configuration, lining permeability and M2-SKH model calibration are repeated for the coupled analysis.

A series of simulation codes are also shown in Fig. 7.1. Firstly, all calculations in this chapter are denoted by 'ESA' to indicate that the modelling procedures developed for effective stress analysis are employed. This is followed by the set of model parameters used in the M2-SKH model. The 'high both' calibration is denoted by 'hibo' and a few calculations are conducted using the 'low triaxial' calibration (code 'lotr') for comparison (Table 5.7). The scenarios of single tunnel and twin tunnels are denoted by

Table 7.1: Numbers of elements employed in the finite element models

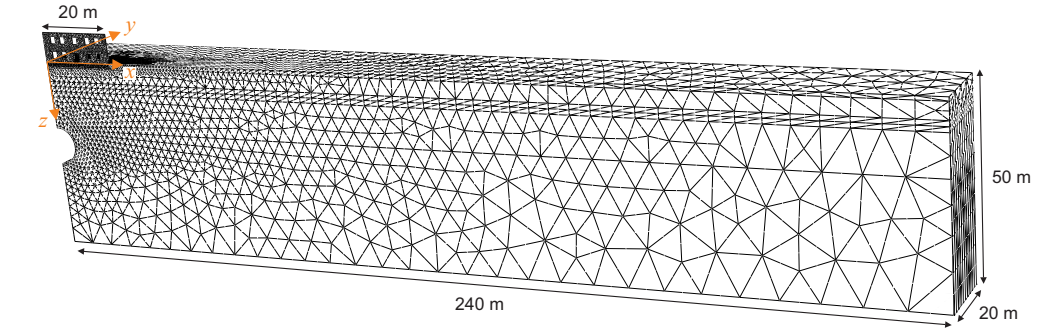
	Tunnel case	
Part	single tunnel	twin tunnels
Isolated facade	1392	
Footing	441	
Gravel (upper layer)	20081/ 20522*	18975/ 19416*
Gravel (lower layer)	7156	6346
Clay	38540	52974
Tunnel lining	2165	4119

* in greenfield analysis

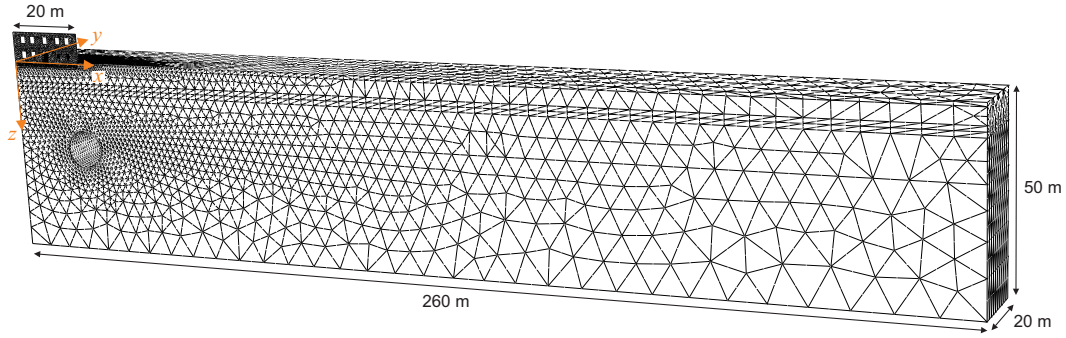
'T1' and 'T2' respectively in the third part of the code. The tunnel lining permeability, k_{L}, is quantified relative to the permeability of the adjacent soil, k_{S}, such that $k_{\mathrm{L}} = \xi k_{\mathrm{S}}$. The fourth part of the code indicates the tunnel lining permeability in terms of ξ. The considered cases of the lining permeability are fully permeable lining ($\xi = \infty$, code 'kinf'), same as that of the soil ($\xi = 1$, code 'k1'), 10% of that of the soil ($\xi = 0.1$, code 'k0.1'), 1% of that of the soil ($\xi = 0.01$, code 'k0.01'), and impermeable lining ($\xi = 0$, code 'k0'). The fifth part of the code indicates whether the simulation is a greenfield analysis (code 'GF') or a coupled, isolated facade analysis (code 'F08O'). A full list of the simulations conducted is included in Table 7.2.

The meshes with the isolated facade for the single- and twin-tunnel cases are shown in Figs 7.2(a) and (b) respectively. The meshes for the ESA analyses are longer in the x-direction than the ones used for TSA (Fig. 6.2) in order to deal with the hydraulic boundary conditions. The planes of symmetry about the mid-plane and the mid-span of the facade are exploited in the model. Fig. 7.2(c) displays the mesh details around the facade and the tunnel lining. The numbers of elements employed in the meshes are given in Table 7.1. The element types adopted are listed in Table 3.2.

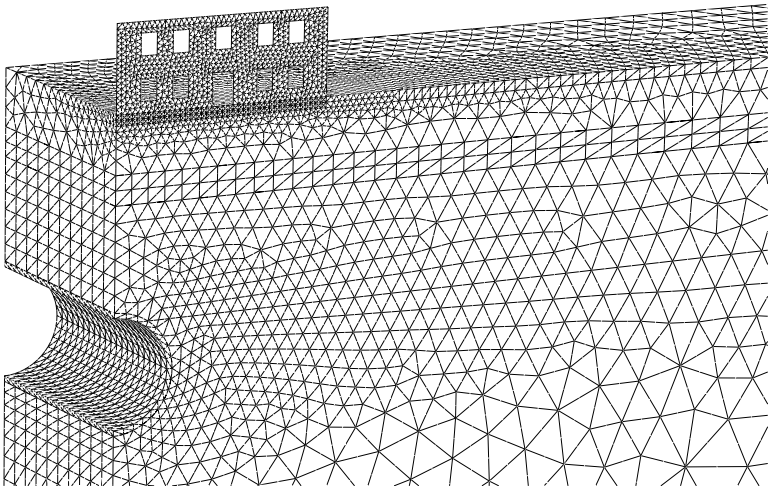
The tunnel excavation is modelled by the nodal force reduction method, which generally cannot achieve the exact target volume loss (Section 3.9.2). The force reduction was performed using automatic time incrementation in Abaqus, where the initial increment was prescribed to correspond to unloading of 0.1% of the forces exerted by the soil elements inside the tunnel, and the maximum size of a time increment was



(a)



(b)



(c)

Figure 7.2: Mesh employed for effective stress analyses, also showing coordinate axes (elements internal to the tunnels have been removed for clarity): (a) model ESA-T1-F08O; (b) model ESA-T2-F08O; (c) mesh detail of the facade and the tunnel in model ESA-T1-F08O

Table 7.2: Tunnel volume loss, V_L^T, and percentage of force unloading in each simulation (target $\widetilde{V}_L^T = 1.5\%$)

	GF		F08O	
Simulation	V_L^T (%)	Unloading (%)	V_L^T (%)*	Unloading (%)
ESA-hibo-T1-kinf	1.50	27.0	1.53/1.46	28.4
ESA-hibo-T1-k1	1.50	26.9	1.52/1.45	28.2
ESA-hibo-T1-k0.1	1.51	27.1	1.51/1.44	28.2
ESA-hibo-T1-k0.01	1.53	27.2	1.56/1.49	28.6
ESA-hibo-T1-k0	1.50	27.0	1.53/1.46	28.4
ESA-hibo-T2-kinf	1.49	26.4	1.53/1.49	27.4
ESA-hibo-T2-k1	1.54	26.7	1.51/1.48	27.3
ESA-hibo-T2-k0.1	1.54	26.7	1.53/1.50	27.4
ESA-hibo-T2-k0.01	1.54	26.7	1.50/1.46	27.1
ESA-hibo-T2-k0	1.51	26.0	1.52/1.49	27.4
ESA-lotr-T1-kinf	1.47	13.5	1.52/1.44	14.4
ESA-lotr-T1-k0	1.52	13.7	1.48/1.41	14.3
ESA-lotr-T2-kinf	1.49	12.5	1.52/1.49	13.7
ESA-lotr-T2-k0	1.49	12.5	1.52/1.49	13.7

* computed away from facade at $y = 20$ m/ directly beneath facade at $y = 0$

set equivalent to unloading of 0.5% of the forces. Table 7.2 shows the adopted tunnel volume loss, V_L^T, computed nearest to the target volume loss, $\widetilde{V}_L^T$, of 1.5% and the corresponding percentage of unloading of the forces of all the simulations conducted. In the isolated facade analysis, the adopted V_L^T for monitoring was evaluated well away from the facade (at $y = 20$ m).

Also shown in Table 7.2 is the V_L^T computed directly underneath the facade ($y = 0$) in the isolated facade analysis. The V_L^T at $y = 0$ is shown to be lower than that at $y = 20$ m, which is consistent with the effect of building load on the volume loss found in Franzius et al. (2004). This suggests that the effect of the increase in soil strength owing to the self-weight of the facade outweighs the effect of the increase in the forces being removed around the tunnel periphery directly beneath the facade.

7.2 Greenfield analysis

The short-term (immediate) results are obtained immediately after the tunnel construction process (Step 9 in Section 3.9.3). Two sets of results for long-term consolidation under greenfield conditions are obtained by transient analysis for 100 years (Step 11T to 17T in Section 3.9.3) and by steady state analysis (Step 11S in Section 3.9.3) .

7.2.1 Base case

The base case (model ESA-hibo-T1-kinf-GF) consists of a single tunnel with fully permeable lining and adopts the 'high both' parameter set for the M2-SKH model.

The total vertical displacement profiles at the level of the expected foundation ($z = 1$ m) obtained from the transient analysis over 100 years after tunnel construction are shown in Fig. 7.3. The magnitude of maximum settlement triples in the first year after tunnel construction, with significant increases in slope and trough width. The increase in the magnitude of settlement remains substantial in the following four years, although there is only a mild rise in the slope. The incremental development of settlement diminishes over time as expected, with the net increase of maximum settlement during the next 95 years similar to that occurring in the first year. The slope has little variation after 10 years from tunnel construction as a wider trough develops with greater settlement. Based on the vertical displacement profiles, the consolidation process reaches steady state at a time between 60 and 100 years after tunnel construction.

A separate steady state analysis is conducted (Step 11S). In this approach, an uncoupled pore pressure-stress procedure is adopted. The steady state pore pressures are first computed and imposed according to the prescribed boundary conditions. Then the effective stresses and the consequential deformations are determined based on the out-of-balance forces. This procedure is evidenced by the pore pressure distribution, as shown in Fig. 7.4. Fig. 7.4(a) shows the pore pressures at the beginning of Step 11S, which are resulted from the excess pore pressure generated from tunnelling and a short period of transient consolidation involved in Step 10. Fig. 7.4(b) shows the pore

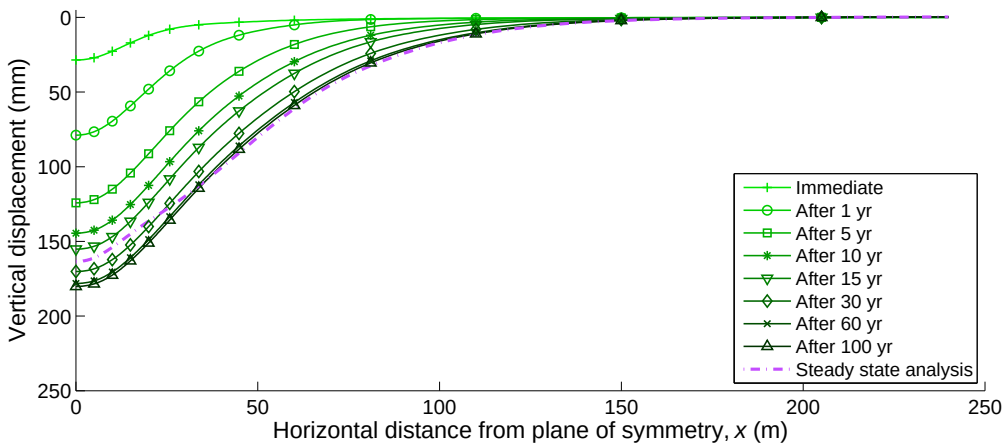
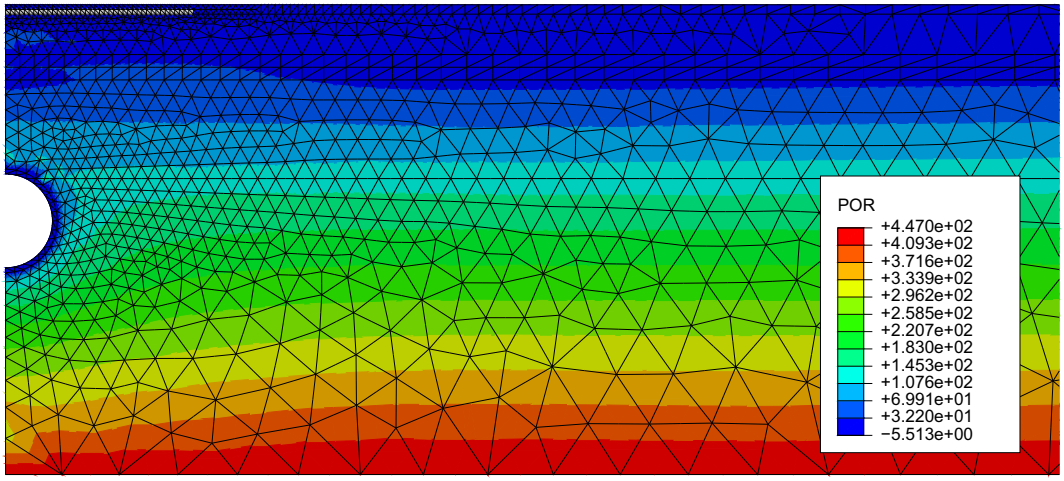


Figure 7.3: Greenfield vertical displacements at $z = 1$ m induced by single tunnel with fully permeable lining over 100 years, with results from steady state analysis

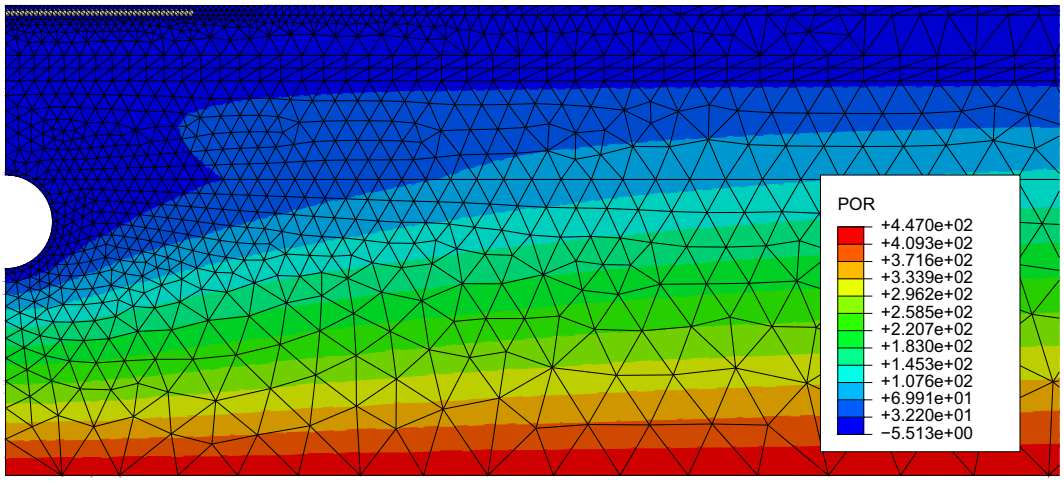
pressure distribution at the end of the first increment of Step 11S, which remains the same throughout Step 11S while changes in the effective stresses and strains continue to be computed in the consecutive increments of Step 11S. The pore pressure distribution in the steady state analysis (Fig. 7.4(b)) is shown to be identical to that reached at the end of Step 17T in the transient analysis (Fig. 7.4(c)).

Also plotted in Fig. 7.3 are the vertical displacements obtained from the steady state analysis. The trough width agrees with the final state reached in the transient analysis, although the settlement trough is shallower and hence the slope is comparatively smaller. As the transient analysis involves coupled pore pressure-stress procedures whereas the steady state analysis adopts an uncoupled approach, the discrepancy of the profiles between the final state of the transient analysis and the steady state analysis is probably a result of different stress paths experienced by the soil, noting that inelastic soil models are used. Nevertheless, both analysis approaches present a clear distinction between the short-term and long-term ground movements in terms of maximum settlement, slope and trough width.

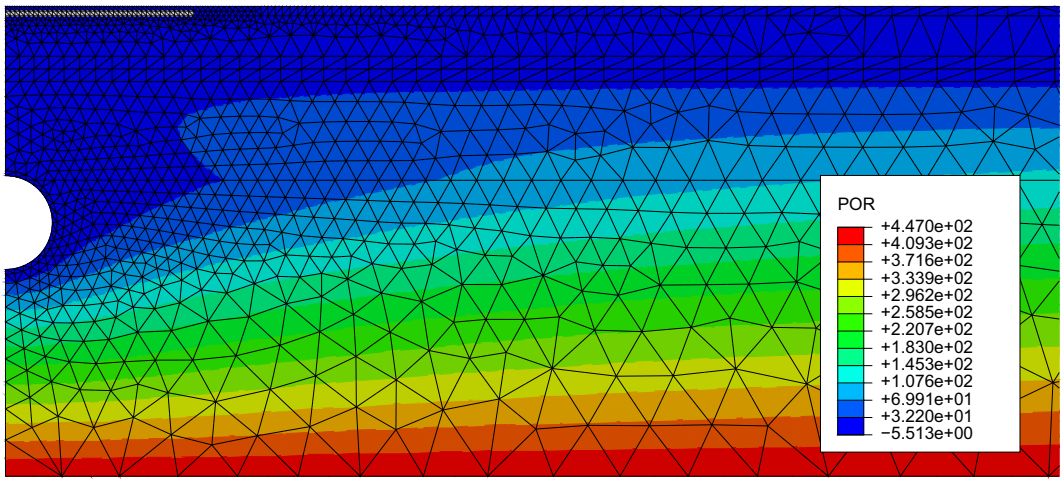
The cumulative horizontal displacements of the ground at the level of the expected foundation ($z = 1$ m) over time are shown in Fig. 7.5. In the long term, more soil is mobilised and moves further towards the tunnel axis, and the location of maximum horizontal displacement shifts outwards. The data obtained from the steady state analysis display a matching magnitude with the final state of the transient analysis,



(a)



(b)



(c)

Figure 7.4: Contours of pore pressure (POR) in greenfield analyses after tunnelling: (a) at the start of the consolidation step in the steady state analysis (Step 11S in Section 3.9.3); (b) at the end of each increment of Step 11S; (c) at the end of Step 17T in the transient analysis (after 100 years). The figure displays the undeformed mesh with x-coordinates from 0 to +111 m

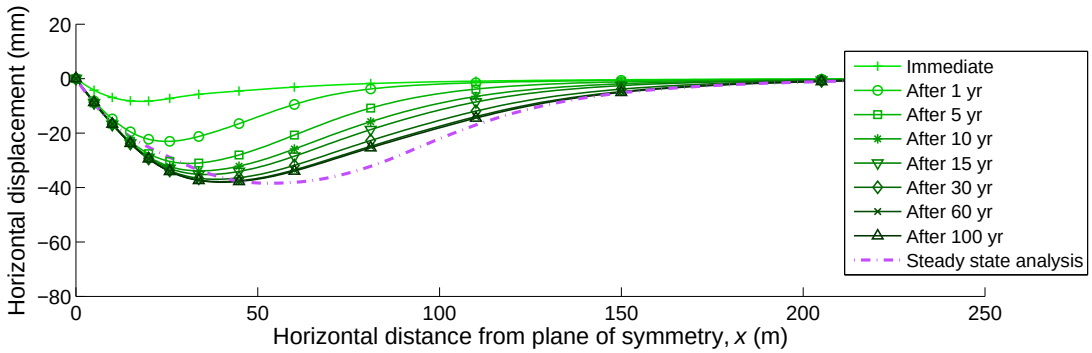


Figure 7.5: Greenfield horizontal displacements at $z = 1$ m induced by single tunnel with fully permeable lining over 100 years, with results from steady state analysis

although the maximum horizontal displacement in the steady state analysis is located further away from the tunnel axis.

Fig. 7.6 shows the total horizontal strains developed in the soil at the expected foundation level ($z = 1$ m). Both the magnitude and the shape of the strain profiles vary over time. The maximum horizontal strains (in compression above the tunnel and in tension at a distance from the tunnel) nearly double after one year since tunnel construction, and the maximum strains are greatest after 5 years. The strains then gradually redistribute, and the profiles for 5 years and subsequent years of the transient analysis cross at point A and point B in Fig. 7.6 — more compressive between point A and point B and more tensile beyond point B. The location of maximum horizontal strain at a given time shifts away from the tunnel axis, consistent with the inflection points of the horizontal displacement profiles in Fig. 7.5. The results from the steady state analysis exhibit a fairly different shape as a consequence of the discrepancy in the horizontal displacements (Fig. 7.5) being amplified in horizontal strains. It is noted that the profile of the steady state analysis also passes close to point A and point B.

7.2.2 Effect of tunnel configuration

A pair of tunnels 40 m apart is modelled, with the use of symmetry, to study the effect of twin tunnels (model ESA-hibo-T2-kinf-GF).

The total vertical displacement profiles at $z = 1$ m are shown in Fig. 7.7. The settlement trough computed immediately after tunnel construction exhibits twin troughs

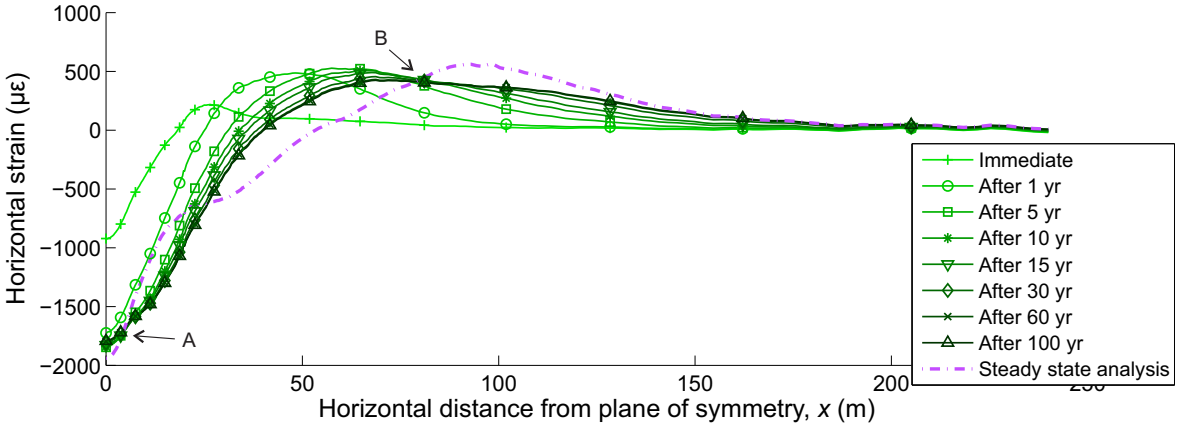


Figure 7.6: Greenfield horizontal strains at $z = 1$ m induced by single tunnel with fully permeable lining over 100 years, with results from steady state analysis

(symmetry applies) directly above the tunnel centres. The settlement then becomes one merged, wider trough one year after tunnelling owing to tunnel-tunnel interaction. The hogging region between the twin tunnels observed in the short term becomes sagging in the long term. A merged settlement trough induced by twin tunnels was also obtained from previous field measurements and numerical analyses such as those regarding the JLE at St James's Park (Nyren (1998), Laver (2010), and Fig. 5.21 in this thesis) where an asymmetric single settlement trough is observed after the two tunnels at different depths are excavated sequentially. In the current study, the assumption of simultaneous excavation of twin tunnels at the same depth results in a symmetric settlement trough as shown in Fig. 7.7. The trends of variation of the settlement, slope and trough width over time in the twin-tunnel case generally agree with those in the single-tunnel case, though the resultant settlement in the twin-tunnel case is greater than the single-tunnel case because two tunnels with $\widetilde{V}_{\mathrm{L}}^{\mathrm{T}} = 1.5\%$ each are assumed in the twin-tunnel case. The time required to reach steady state in the transient analysis of the twin-tunnel case is similar to that in the single-tunnel case. The results from the steady state analysis predict a trough with similar width to, and shallower maximum settlement than, the profile obtained from the transient analysis after 100 years.

The horizontal displacement and horizontal strain profiles at $z = 1$ m are plotted in Figs 7.8 and 7.9 respectively. As a consequence of the tunnel-tunnel interaction, the soil generally moves towards the mid-point of the two tunnels instead of towards the

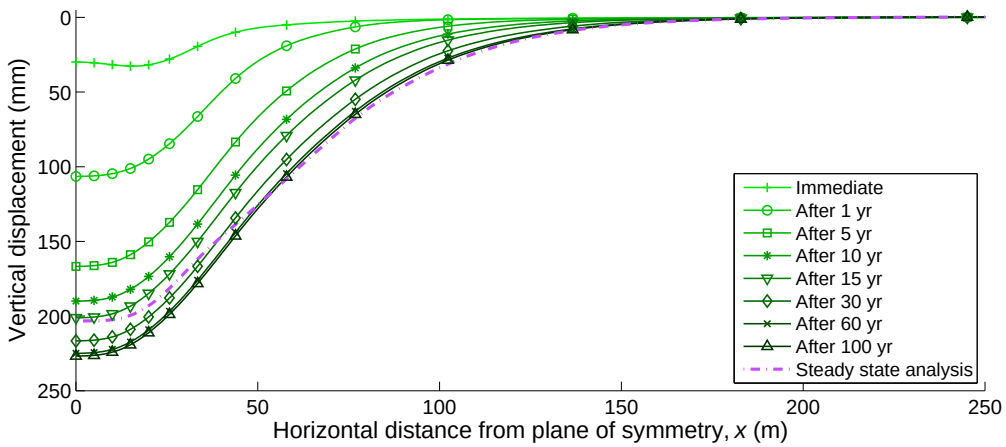


Figure 7.7: Greenfield vertical displacements at $z = 1$ m induced by twin tunnels with fully permeable lining over 100 years, with results from steady state analysis

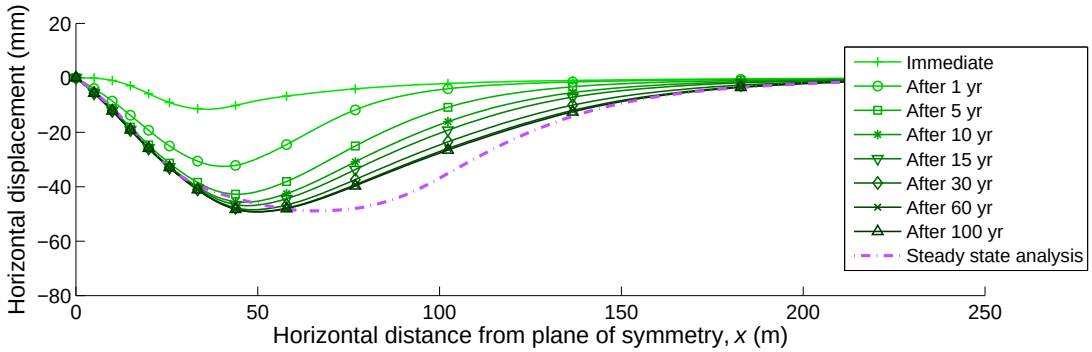


Figure 7.8: Greenfield horizontal displacements at $z = 1$ m induced by twin tunnels with fully permeable lining over 100 years, with results from steady state analysis

centres of the individual tunnels after one year since tunnel construction. The magnitudes of horizontal displacement in the twin-tunnel case are greater than those in the single-tunnel case. Compressive horizontal strains are found between the two tunnels (Fig. 7.9), illustrating a strong interaction between the two tunnels. Compared to the single-tunnel case, the twin-tunnel case results in a smaller maximum compressive horizontal strain and a greater maximum tensile horizontal strain.

7.2.3 Effect of lining permeability

The effect of the permeability of the tunnel lining on the long-term ground response is investigated by varying the lining permeability relative to that of the soil adjacent to the tunnel ($k_{\mathrm{L}} = \xi k_{\mathrm{S}}$). Five cases of differing lining permeability are considered in the single- and twin-tunnel cases (models ESA-hibo-T{1, 2}-k{inf, 1, 0.1, 0.01, 0}-GF).

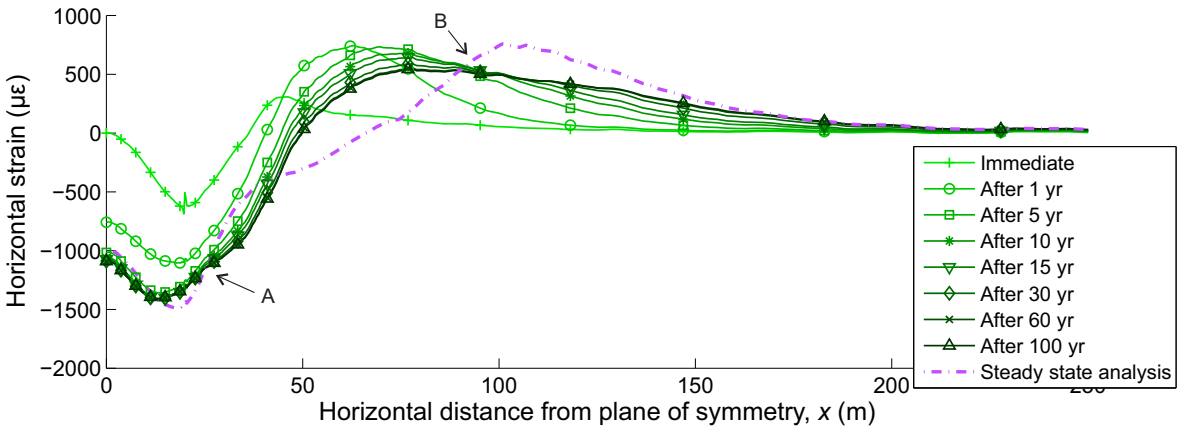
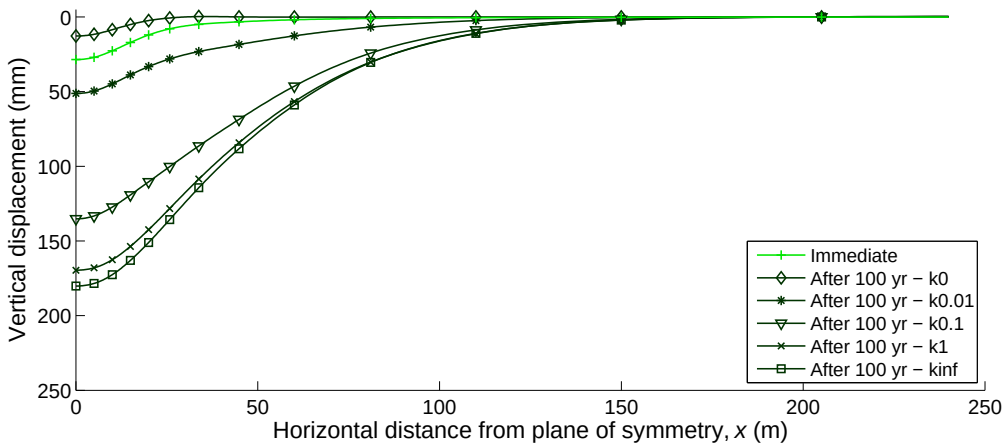


Figure 7.9: Greenfield horizontal strains at $z = 1$ m induced by twin tunnels with fully permeable lining over 100 years, with results from steady state analysis

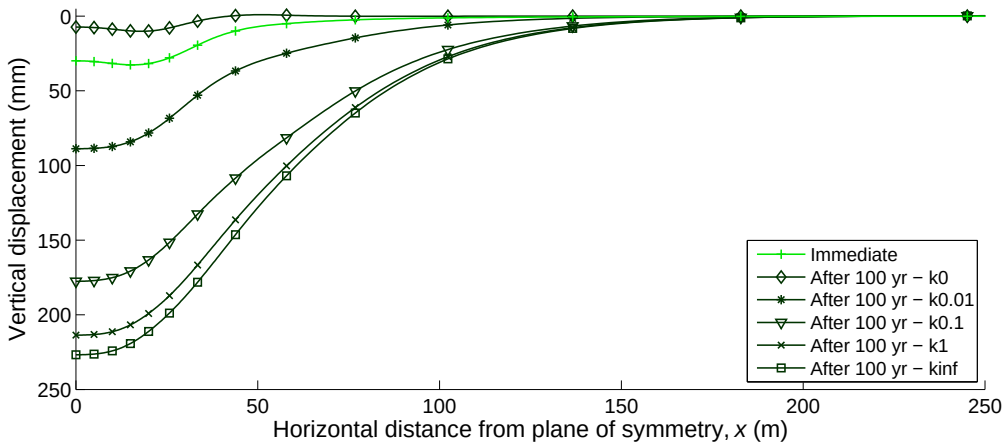
Fig. 7.10 shows the greenfield vertical displacements in the long term at steady state resulting from different lining permeabilities (using the data of 100 years after tunnel construction from the transient analysis), together with the settlements immediately after tunnel construction. In both tunnel cases, the long-term settlements, slopes and trough widths are greatest when the lining is fully permeable, and these quantities reduce for less permeable linings. The relationship of increasing maximum settlement with increasing lining permeability is consistent with the finite element analysis results presented in Wongsaroj et al. (2013) and Avgerinos et al. (2018). When the lining is impermeable, incremental heave occurs in the long term (Fig. 7.10). The result of reduced total settlements in the long term in the case of impermeable tunnel lining was also observed in the simulations conducted by Shin et al. (2002).

The effect of reducing the lining permeability from $\xi = 0.1$ to 0.01 is much greater than from $\xi = 1$ to 0.1, and the lining with $\xi = 1$ results in a settlement profile similar to the $\xi = \infty$ case. The prediction of long-term vertical displacements is shown to be particularly sensitive to lining permeabilities below 10% of that of the soil permeability ($\xi \leq 0.1$). This suggests that the assumed permeability of the tunnel lining is a critical parameter in predicting long-term tunnelling-induced ground movements.

Consistent effects of lining permeability are observed in the long-term horizontal displacements, which are plotted in Fig. 7.11. When the lining is more permeable (for $\xi \geq 0.01$), the horizontal movements towards the tunnel axis in the single-tunnel case,

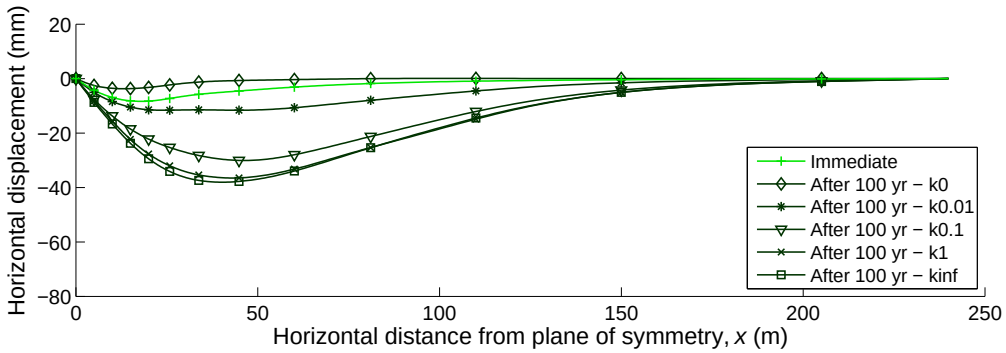


(a)

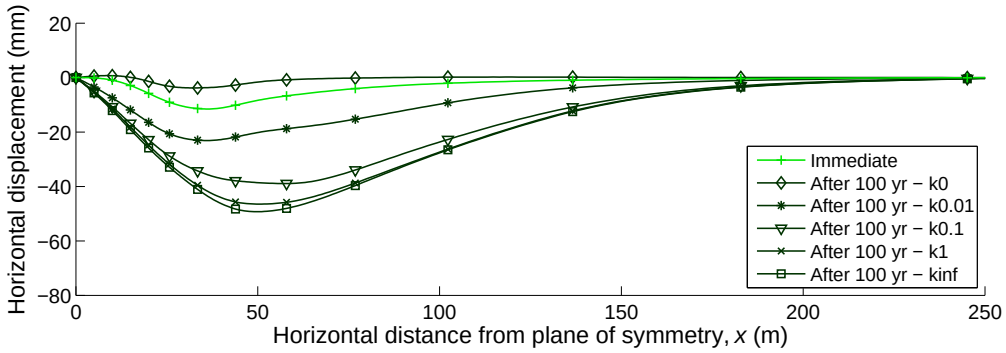


(b)

Figure 7.10: Greenfield vertical displacements at steady state of the transient analysis varying with tunnel lining permeability, also showing the short-term data: (a) single tunnel; (b) twin tunnels



(a)



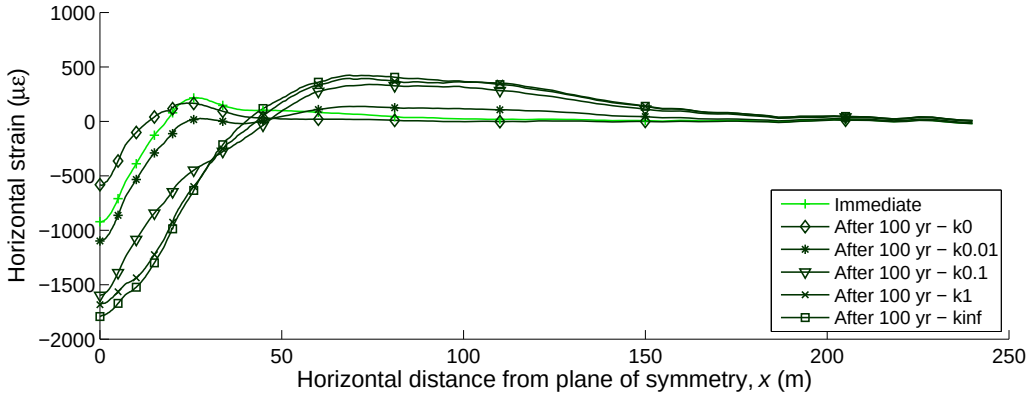
(b)

Figure 7.11: Greenfield horizontal displacements at steady state of the transient analysis varying with tunnel lining permeability, also showing the short-term data: (a) single tunnel; (b) twin tunnels

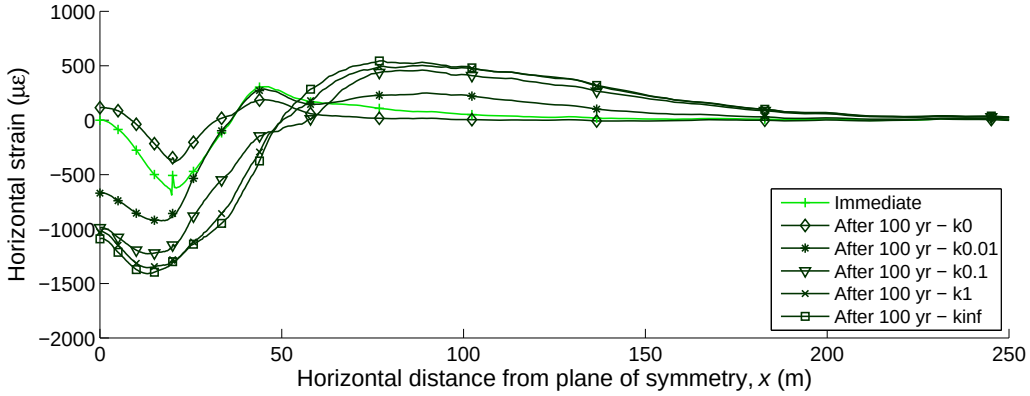
and towards the mid-point between the tunnels in the twin-tunnel case, are larger. When the lining is completely impermeable ($\xi = 0$), however, incremental long-term horizontal displacements develop in the reverse direction compared to the immediate displacements, resulting in reduced total horizontal displacements. The corresponding horizontal strains developed in the soil are shown in Fig. 7.12. For $\xi \geq 0.01$, the horizontal strains become more compressive directly above the tunnel and more tensile at a distance away from the tunnel in the long term, and the extent increases with the lining permeability. The impermeable lining ($\xi = 0$) is a special case where the horizontal strains above the tunnel become more tensile in the long term.

7.2.4 Effect of model calibration

The 'high both' calibration is employed in the M2-SKH model in the base case because it provides the most satisfactory prediction of the long-term ground movements



(a)



(b)

Figure 7.12: Greenfield horizontal strains at steady state of the transient analysis varying with tunnel lining permeability, also showing the short-term data: (a) single tunnel; (b) twin tunnels

in Avgerinos et al. (2016) and Section 5.4 of this thesis, while the 'low triaxial' calibration performs the best in predicting short-term ground movements. To illustrate the significance of the constitutive model parameter selection, additional studies are conducted using the 'low triaxial' calibration in the M2-SKH model, for fully permeable and completely impermeable tunnel linings in single- and twin-tunnel cases (models ESA-lotr-T{1,2}-k{inf,0}-GF).

The tunnel-induced vertical displacement profiles at the expected foundation level ($z = 1$ m) over 100 years computed using the 'low triaxial' parameters are plotted in Fig. 7.13, overlaid with the 'immediate' and 'after 100 years' data from the analyses using the 'high both' calibration. Although the short-term settlements obtained using the 'low triaxial' calibration are shallower and wider than those obtained when the 'high both' parameters are used, the predicted long-term settlements in the case of

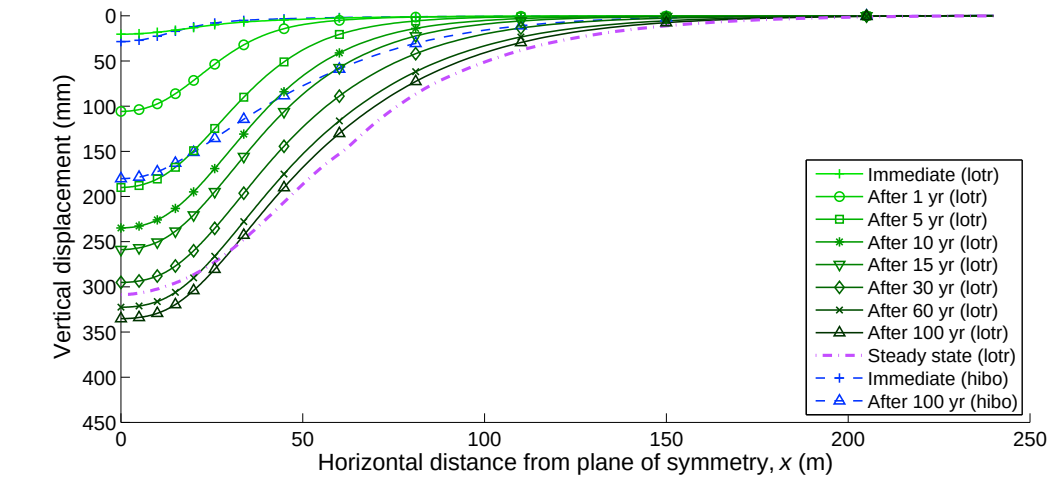
a fully permeable lining are steeper, and the maximum magnitude after 100 years is nearly twice greater (Figs 7.13(a) and (b)). The ratio of the long-term to short-term maximum settlements in the 'low triaxial' analysis is larger than that in the 'high both' analysis, which agrees with the results obtained from previous applications of the M2-SKH model to tunnelling in Avgerinos et al. (2016) and Fig. 5.21 of this thesis. However, the consolidation in the 'low triaxial' analysis has not reached steady state at 100 years after tunnel construction as there is a noticeable increase in consolidation from 60 years to 100 years, although they are close to the data obtained from the steady state analysis. The 'low triaxial' parameters also lead to larger long-term horizontal displacements than those obtained from with 'high both' parameters in the case of a fully permeable lining, as shown in Figs 7.14(a) and (b). The observation that the 'low triaxial' analysis computes more severe response than the 'high both' analysis might be because the 'low triaxial' calibration corresponds to soil with a lower elastic stiffness and a higher rate of stiffness degradation with strain.

In the case of an impermeable tunnel lining, the extent of swelling of the ground in the long term is more substantial in the results obtained using the 'low triaxial' calibration than with the 'high both' calibration, as indicated in Figs 7.13(c) and (d). Net heave is observed in the twin-tunnel case at steady state (Fig. 7.13(d)). The total horizontal displacements induced by tunnelling, displayed in Figs 7.14(c) and (d), recover to nearly zero in the long term.

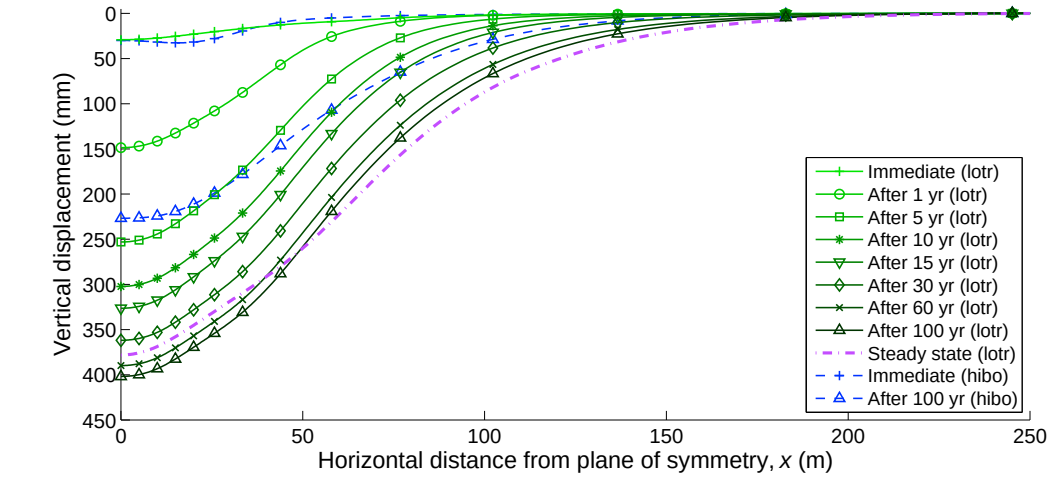
7.3 Isolated facade analysis

The response of a masonry building to the long-term ground movements induced by tunnelling is explored by including an isolated facade and its continuous strip footing in the finite element model prior to tunnel excavation (refer to the simulation steps in Section 3.9.3). An isolated facade with openings and a height of 8 m, with zero tunnel eccentricity, is adopted and modelled with symmetries along the mid-span and mid-plane of the facade (Fig. 7.2).

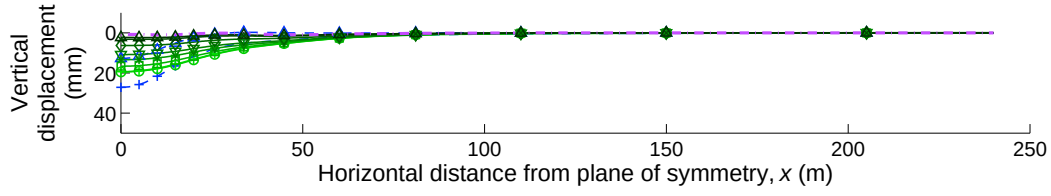
Only the results of steady state analysis (Step 11S) are presented for the isolated



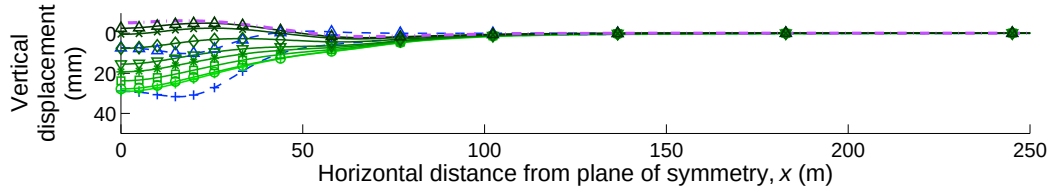
(a)



(b)

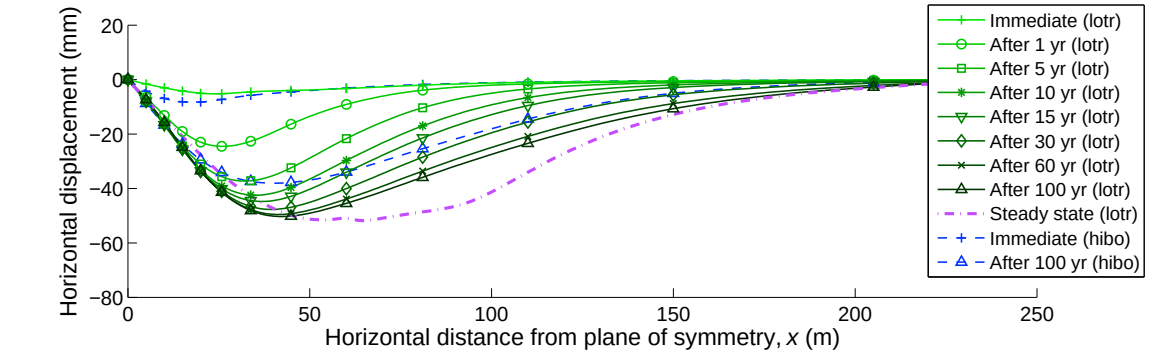


(c)

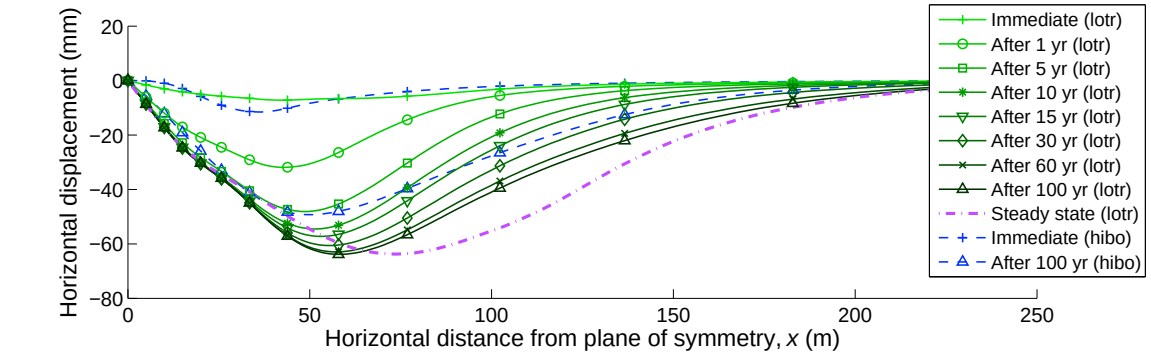


(d)

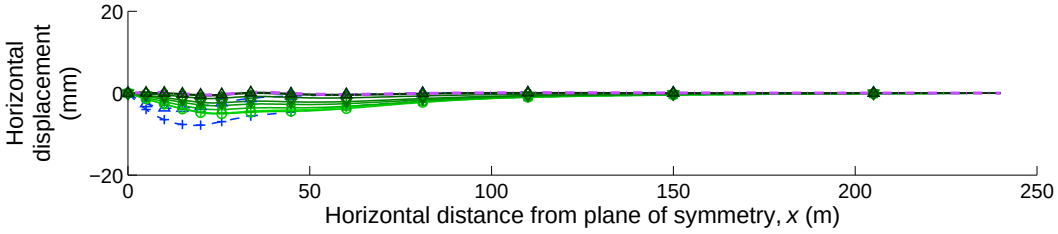
Figure 7.13: Greenfield vertical displacements induced by tunnelling computed with 'low triaxial' calibration in the M2-SKH model, compared with results obtained using 'high both' calibration: (a) fully permeable lining, single tunnel; (b) fully permeable lining, twin tunnels; (c) impermeable lining, single tunnel; (d) impermeable lining, twin tunnels



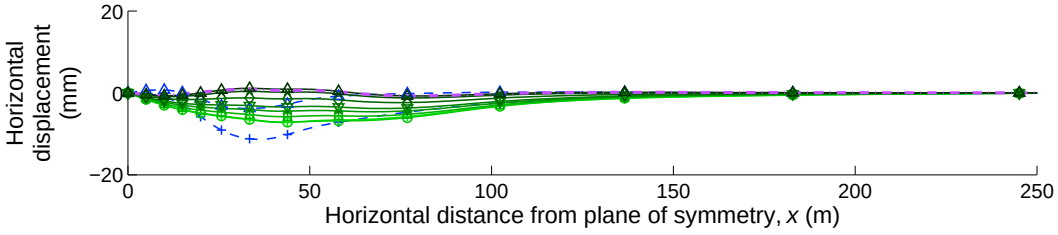
(a)



(b)



(c)



(d)

Figure 7.14: Greenfield horizontal displacements induced by tunnelling computed with 'low triaxial' calibration in the M2-SKH model, compared with results obtained using 'high both' calibration: (a) fully permeable lining, single tunnel; (b) fully permeable lining, twin tunnels; (c) impermeable lining, single tunnel; (d) impermeable lining, twin tunnels

facade analysis because the corresponding transient analysis experienced numerical convergence problems. In the consolidation step of the transient analysis (Step 11T), warning was issued by Abaqus to indicate that the plasticity algorithm did not converge at some integration points in the facade elements, although attempts had been made to vary the size of time increments. A separate transient analysis with the facade modelled with linear elasticity converges, suggesting that the relatively low tensile strength adopted in the masonry constitutive model (Section 3.6.1) might be a cause of the non-convergence in the current transient analysis.

For consistency, the greenfield analysis data used for reference in this section are the results from steady state analysis. There are small differences in the tunnel volume loss between the greenfield analysis and the isolated facade analysis (Table 7.2).

7.3.1 Base case

The base case features a single tunnel at zero eccentricity with a fully permeable tunnel lining and employs the 'high both' parameter set for the M2-SKH model (model ESA-hibo-T1-kinf-F08O).

The total vertical and horizontal displacements, and the horizontal strains at the base of the foundation and in the adjacent soil (z = 1 m) are plotted in Fig. 7.15. Results are shown for the short term (immediately after tunnel construction) and in the long term at steady state. The vertical displacement profiles (Fig. 7.15(a)) indicate localised settlement modification due to the presence of the facade, particularly near the edges of the facade. No gapping is observed at the soil-footing interface, suggesting that the building modelled is flexible relative to the soil in the current configuration. In spite of the considerable increase in total settlements of the facade in the long term, there is only a moderate increase in differential settlements. Moreover, the location experiencing the maximum increase in slope over time appears to be at some distance away from the tunnel axis (e.g. at x = 50 m). This suggests that buildings offset from the tunnel axis may suffer from greater incremental damage induced by long-term consolidation, although the long-term building response resulting from eccentric

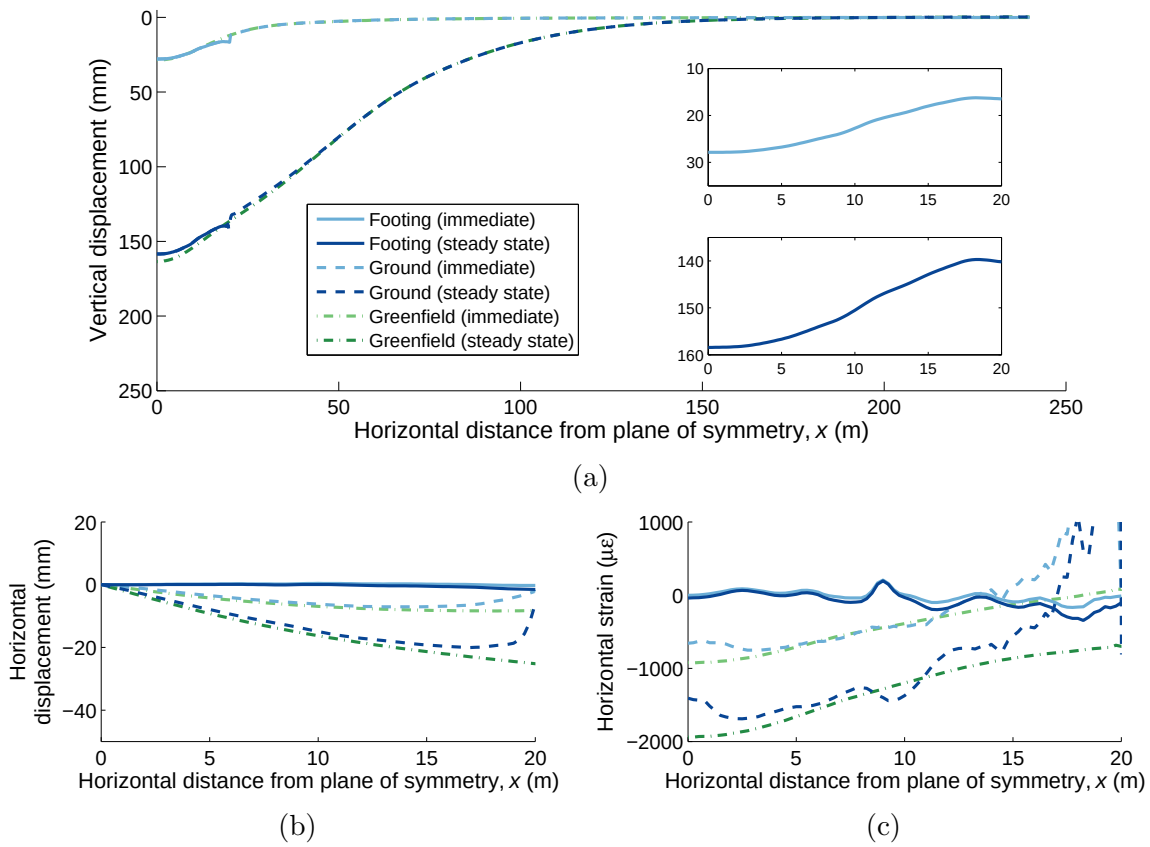
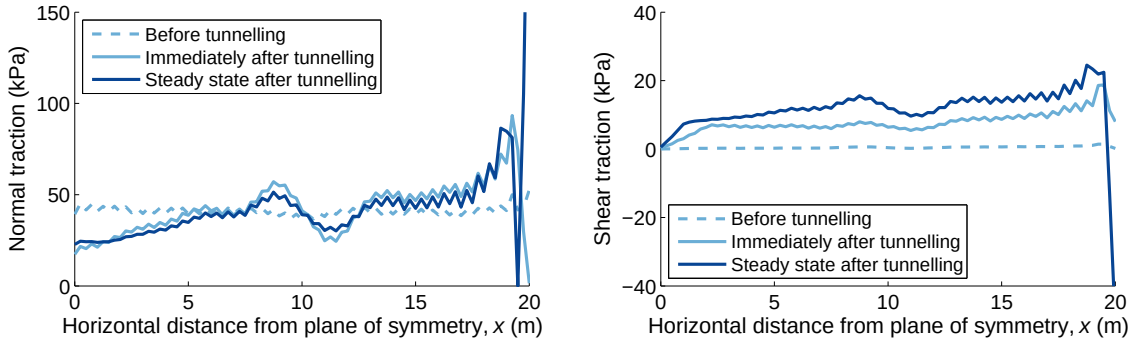


Figure 7.15: Data at the base of the foundation and in the adjacent soil (z = 1 m) in the short term and at steady state for the case of a single tunnel with fully permeable lining using 'high both' M2-SKH parameters, compared with the data from greenfield analysis: (a) vertical displacement, with close-ups of the footing data; (b) horizontal displacement; (c) horizontal strain

tunnelling was not considered in the current scope. Also, as the trough widens over time, the influenced area extends and the number of buildings at risk may increase.

The horizontal displacements and horizontal strains, shown in Figs 7.15(b) and (c), indicate that these quantities at the base of the footing do not vary much in the long term, with only small incremental compressive horizontal strains developed in the footing. However, the displacements and strains in the adjacent soil progress similarly to the values obtained in the greenfield analysis. Sliding occurs at the soil-footing interface and the extent of sliding increases over time.

Fig. 7.16 shows the normal and shear tractions developed on the base of the footing before tunnelling, shortly after tunnelling and at steady state. The normal tractions redistribute towards the edges of the facade immediately after tunnelling, as expected, and remain approximately the same in the long term. The magnitude of the shear



(a) (b)

Figure 7.16: Contact tractions on the base of the foundation before and after tunnelling for the case of a single tunnel with fully permeable lining using 'high both' M2-SKH parameters: (a) normal traction; (b) shear traction

tractions increases in the long term.

The contours of major principal strain induced in the facade immediately after tunnel construction and in the long term at steady state are displayed in Figs 7.17(a) and (b) respectively. Diagonal patterns of high tensile strain areas are exhibited, and these develop further in the long term. In particular, high strains are observed at the bottom of the facade at around $x = 12$ m at steady state, coinciding with the point of inflection of the settlement trough (Fig. 7.15(a)). The increase in building damage is unlikely to be attributable to the horizontal strains at the base of the footing, which barely vary in the long term (Fig. 7.15(c)).

Fig. 7.17(c) shows the damage bar charts which categorise the area of the facade into damage categories based on the major principal strains. Comparing the short-term and the long-term results, there is a clear increase in building damage in terms of an increased area of the facade being in higher damage categories in the long term. Also shown in Figs 7.17(a) and (b) are the characteristic strains, $\varepsilon^{\mathrm{t}}_{99}$, induced in the facade, suggesting a substantial increase in $\varepsilon^{\mathrm{t}}_{99}$ over time.

7.3.2 Effect of tunnel configuration

The case of twin tunnels at zero eccentricity is considered using the model ESA-hibo-T2-kinf-F08O.

The vertical displacement profiles at the base of foundation and in the adjacent soil

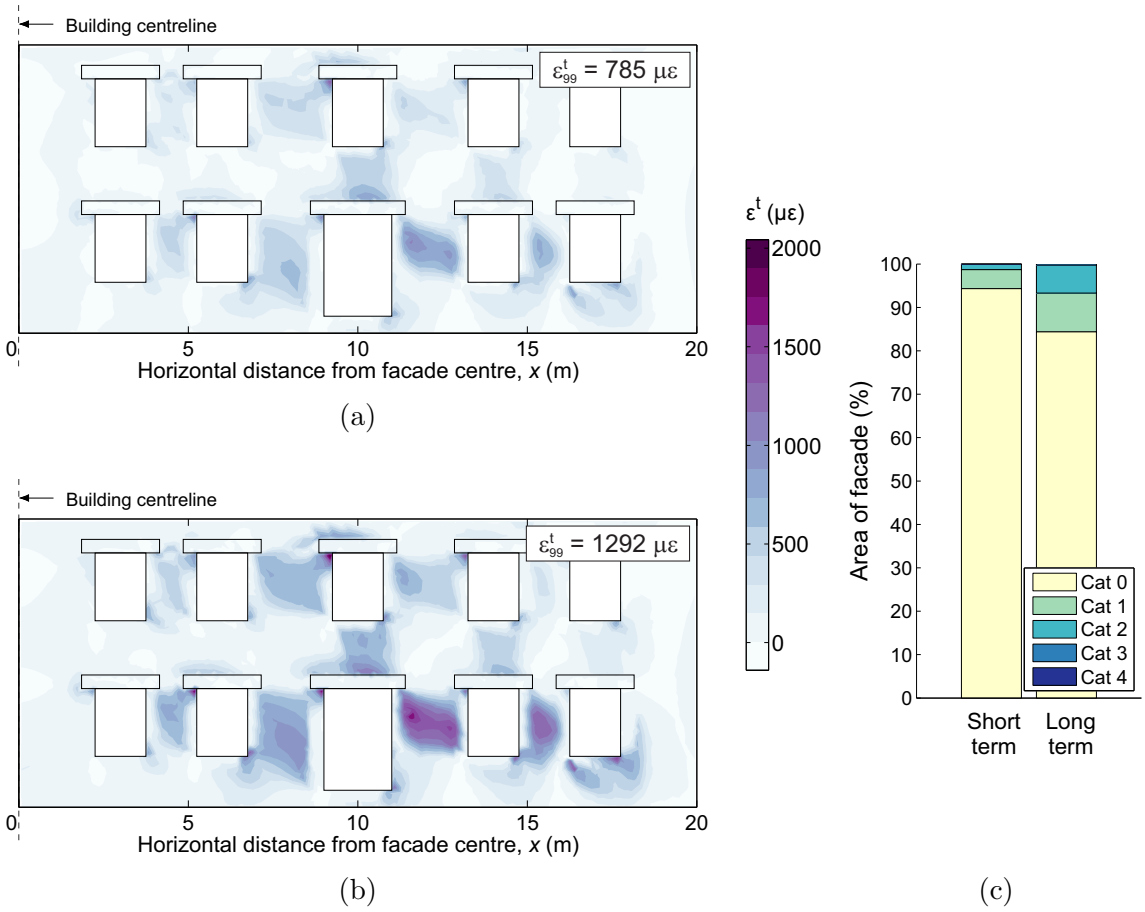


Figure 7.17: Major principal strain induced in the facade for the case of a single tunnel with fully permeable lining using 'high both' M2-SKH parameters: (a) strain field and ε_{99}^t immediately after tunnelling; (b) strain field and ε_{99}^t at steady state; (c) damage bar chart

in the isolated facade analysis are shown in Fig. 7.18(a), together with the greenfield results. Immediately after tunnel construction, the footing deforms predominantly in hogging. As the tunnel-tunnel interaction develops in the long term, however, the adjacent soil tends to settle more at the mid-point between the two tunnels than above the centres of the tunnels. As a result, the inclination of the footing changes direction and a hint of sagging is noticed at around $x = 10$ m at steady state.

The horizontal displacements and the horizontal strains along the footing length are plotted in Figs 7.18(b) and (c). Similar to the single-tunnel case, the horizontal movements of the footing in the twin-tunnel case are negligible, and sliding develops more at the soil-footing interface over time. The horizontal strains induced in the footing are also minimal.

Fig. 7.19 shows the contact tractions on the base of the footing before and after

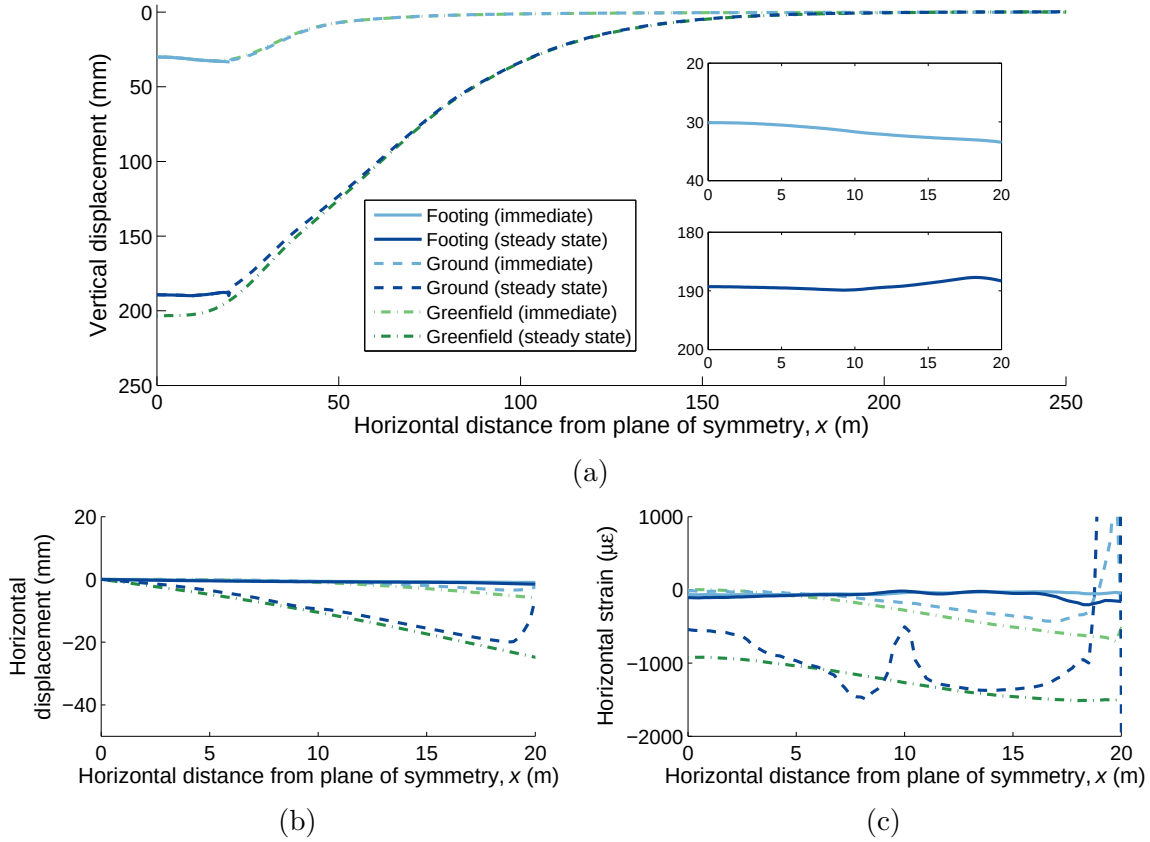
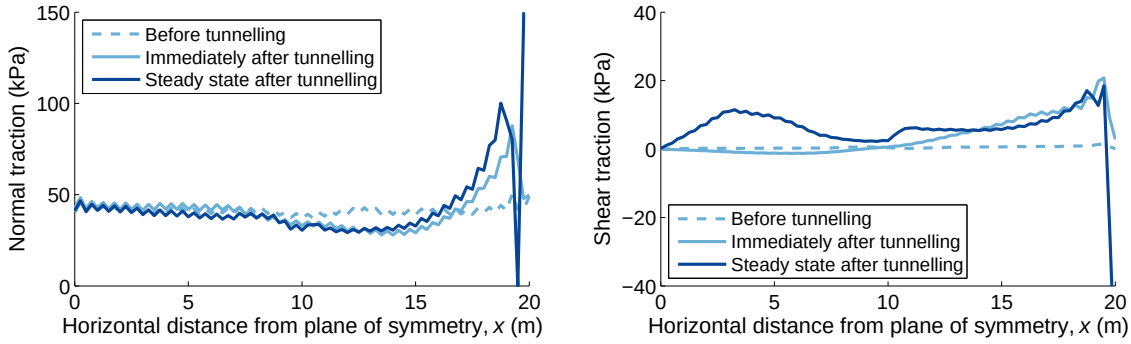


Figure 7.18: Data at the base of the foundation and in the adjacent soil ($z = 1$ m) in the short term and at steady state for the case of twin tunnels with fully permeable lining using 'high both' M2-SKH parameters, compared with the data from greenfield analysis: (a) vertical displacement, with close-ups of the footing data; (b) horizontal displacement; (c) horizontal strain



(a) (b)

Figure 7.19: Contact tractions on the base of the foundation before and after tunnelling for the case of twin tunnels with fully permeable lining using 'high both' M2-SKH parameters: (a) normal traction; (b) shear traction

tunnelling. The normal tractions along 9 m $\leq x \leq$ 16 m redistribute mainly to the edges of the footing after tunnelling, and the extent of redistribution increases in the long term. The small negative shear tractions induced after tunnelling near the mid-span of the footing ($0 \leq x \leq 10$ m) become positive in the long term.

The major principal strains induced in the facade in the short and long term after tunnelling are contoured in Figs 7.20(a) and (b). Immediately after tunnelling, concentrations of tensile strain are found at the top of the mid-span of the facade, indicating that the facade deformation is dominated by hogging. In the long term, however, the magnitude of these concentrations at the top middle of the facade reduces, and high tensile strains develop towards the edges of the bottom part of the facade. The shift of strain concentrations in the facade evidences a change in the dominant deformation mode from hogging to sagging. The ε_{99}^{t} values in Figs 7.20(a) and (b) and the damage bar chart in Fig. 7.20(c) indicate negligible damage to the facade induced by twin tunnels in both the short term and long term for the building configuration considered.

7.3.3 Effect of lining permeability

The effect of lining permeability on building response is investigated by analysing the models ESA-hibo-T{1, 2}-k{inf, 1, 0.1, 0.01, 0}-F08O.

The profiles of vertical displacement, horizontal displacement and horizontal strain at the base of the footing in the long term at steady state are plotted in Fig. 7.21 for

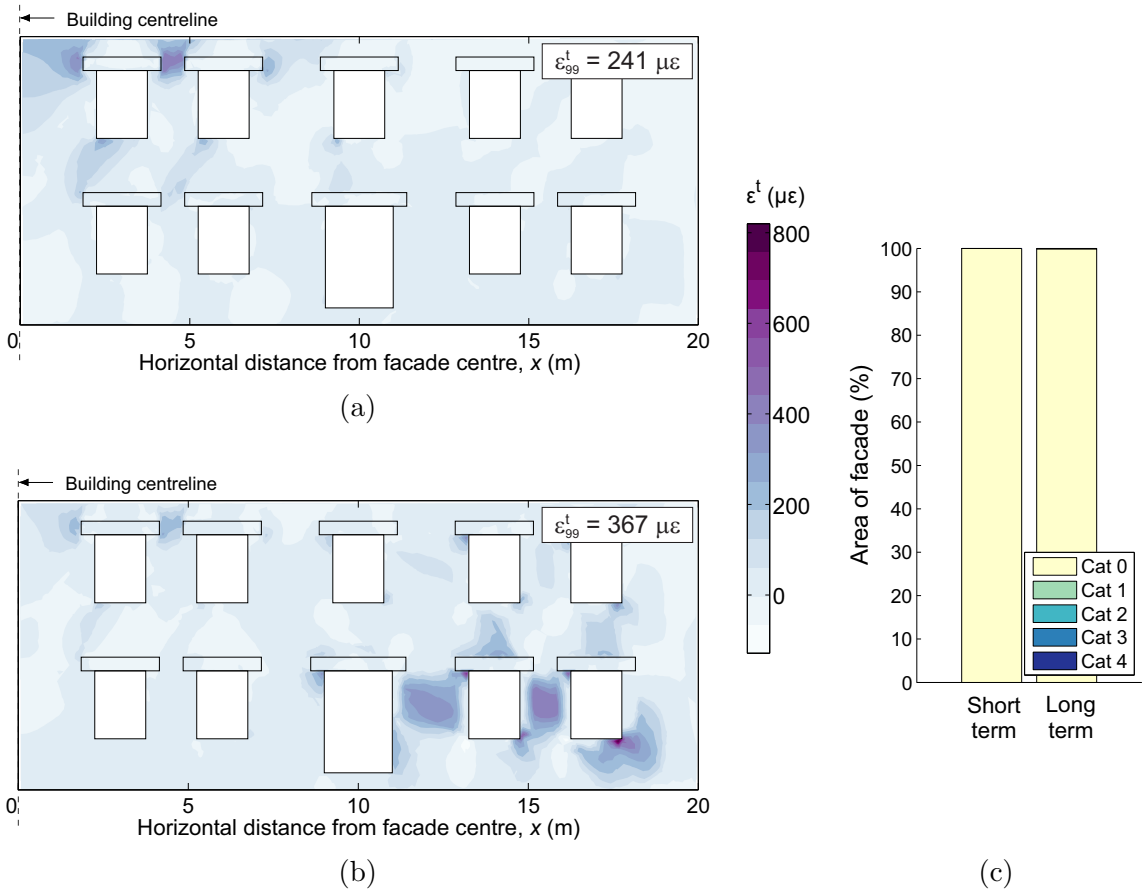


Figure 7.20: Major principal strain induced in the facade for the case of twin tunnels with fully permeable lining using 'high both' M2-SKH parameters: (a) strain field and ε^t_{99} immediately after tunnelling; (b) strain field and ε^t_{99} at steady state; (c) damage bar chart

various tunnel lining permeabilities. In both tunnel cases, the total settlement of the facade is greatest in the case of a fully permeable lining, and the settlement reduces as the lining is made less permeable. In the case of a completely impermeable lining, the total settlement in the long term is smaller than that in the short term. This correlation between the total settlement and the lining permeability agrees with that of the ground in the greenfield analysis (Fig. 7.10). The vertical displacements also vary over a large extent for cases from $\xi = 0.01$ to 0.1 in $k_{\mathrm{L}} = \xi k_{\mathrm{S}}$. In the single-tunnel case, the slope of the long-term settlement is flatter with lower ξ, while in the twin-tunnel case, the footing settlements are comparatively flat in all cases.

For $\xi \geq 0.01$, the horizontal movements and horizontal strains in the footing at steady state are insensitive to the value of the lining permeability, as shown in Figs 7.21(c) to (f). However, in the case of a completely impermeable lining ($\xi = 0$), these quantities develop in the other direction from the short-term data compared to the results computed with permeable linings.

The effect of the relative lining-soil permeability on long-term damage induced in the facade is shown in terms of the characteristic strains, $\varepsilon_{99}^{\mathrm{t}}$, in Fig. 7.22. The values of the short-term $\varepsilon_{99}^{\mathrm{t}}$ obtained immediately after tunnel construction differ slightly among the analyses with the same tunnel configuration because of the small difference in the tunnel volume loss attained in each analysis (Table 7.2). In the single-tunnel case, the increase in $\varepsilon_{99}^{\mathrm{t}}$ in the long term is greatest when $\xi = \infty$. As the lining becomes less permeable, the increase in $\varepsilon_{99}^{\mathrm{t}}$ in the long term is smaller, which aligns with the smaller increase in the slope of the settlement profile in the long term (Fig. 7.21(a)). In the case of $\xi = 0$, where the vertical displacement profile in the long term is even flatter than the short-term one, the total $\varepsilon_{99}^{\mathrm{t}}$ decreases in the long term.

For the twin-tunnel configuration considered, although the values of $\varepsilon_{99}^{\mathrm{t}}$ are comparatively small, the $\varepsilon_{99}^{\mathrm{t}}$ in the long term is also greatest for $\xi = \infty$ and smallest for $\xi = 0$. The influence of the tunnel lining permeability on the current twin-tunnel case is not monotonic as the dominant mode of deformation of the facade in the long term changes with different values of lining permeability (Fig. 7.21(b)).

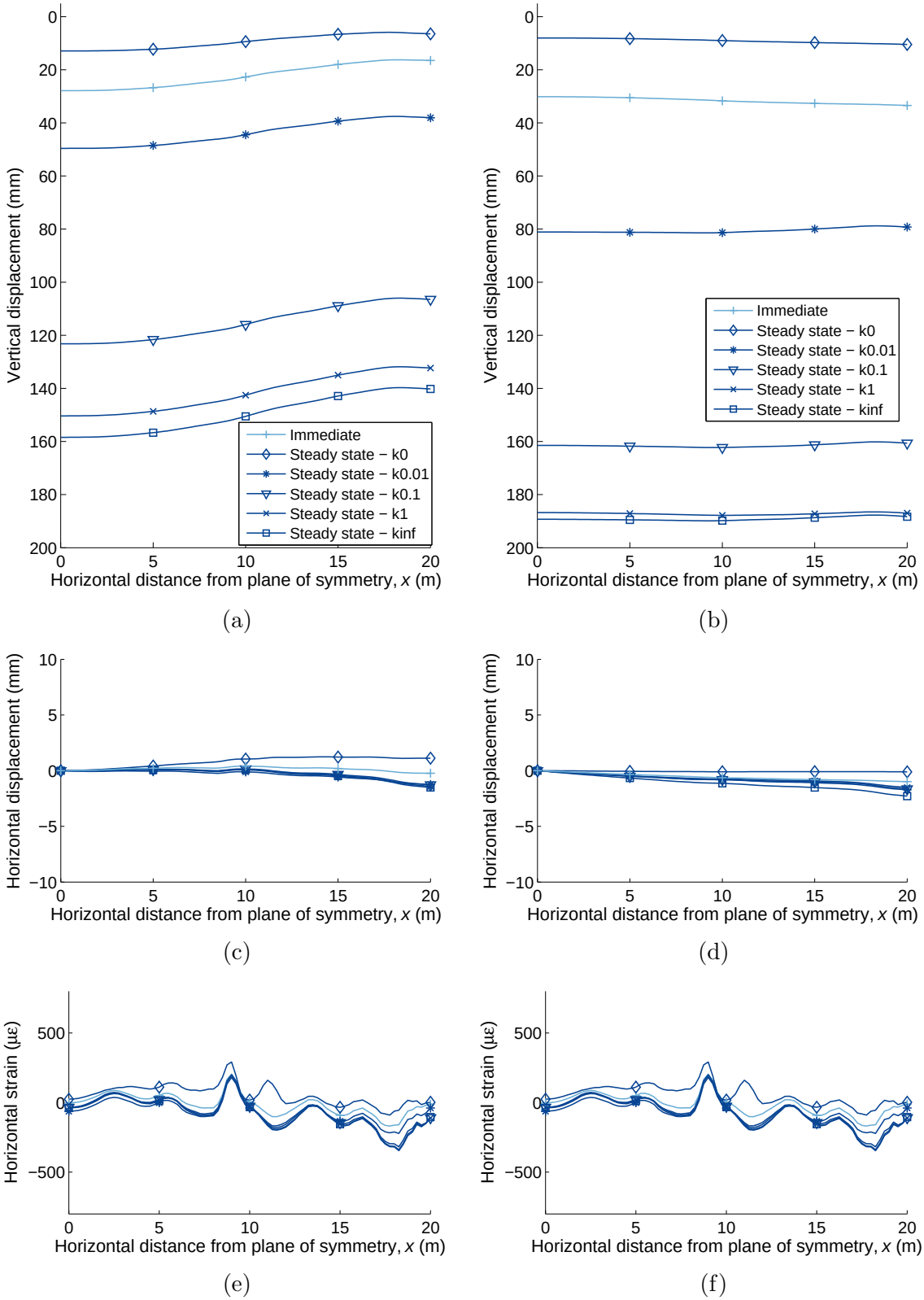


Figure 7.21: Data at the base of the foundation of the facade at steady state using 'high both' M2-SKH parameters and varying the permeability of the tunnel lining, compared with the data immediately after tunnelling: (a) vertical displacement, single tunnel; (b) vertical displacement, twin tunnels; (c) horizontal displacement, single tunnel; (d) horizontal displacement, twin tunnels; (e) horizontal strain, single tunnel; (f) horizontal strain, twin tunnels

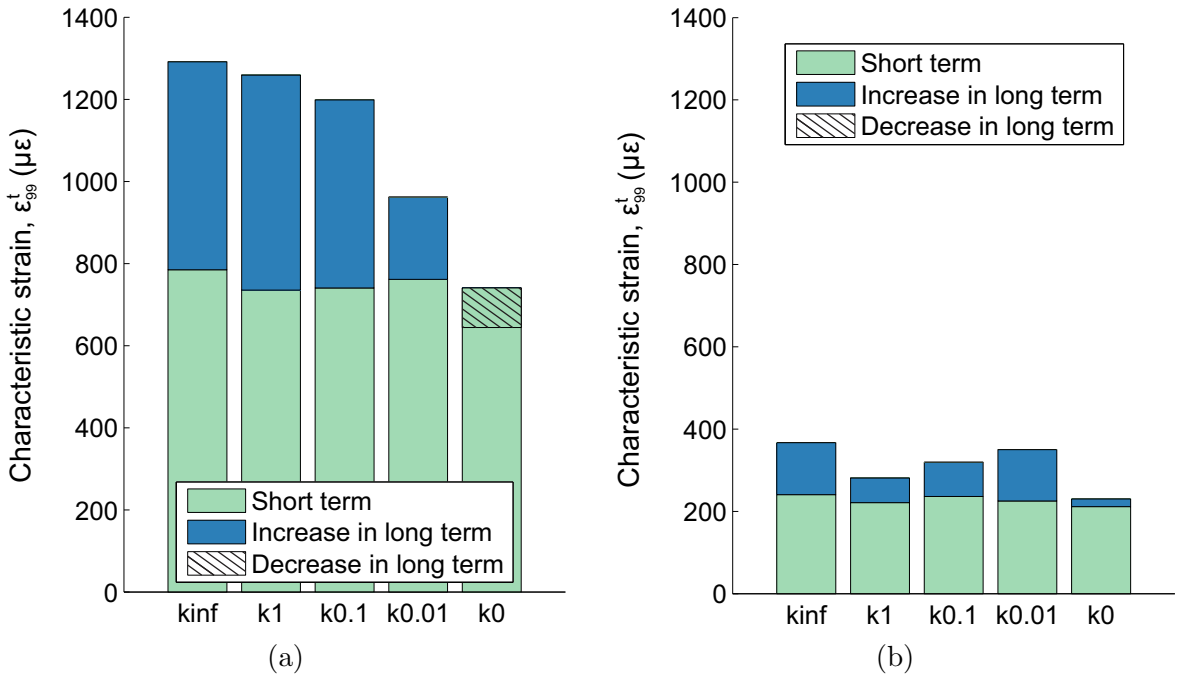


Figure 7.22: Effect of the relative lining-soil permeability on characteristic strain, ε_{99}^{t}, induced in the facade in the long term: (a) single tunnel; (b) twin tunnels

7.3.4 Effect of model calibration

The prediction of tunnelling-induced consolidation was shown to be sensitive to the calibration of the soil model in the greenfield analysis (Section 7.2.4). The study of the significance of the calibration of the M2-SKH model is now continued in the context of building damage assessment. The 'low triaxial' calibration is applied to the models ESA-lotr-T{1, 2}-k{inf, 0}-F08O. The results are compared with those of the main study where the 'high both' calibration is employed.

The vertical displacements at the base of the footing immediately after tunnel construction and at steady state, computed using the 'low triaxial' calibration, are compared with those obtained using the 'high both' calibration in Fig. 7.23. In the single-tunnel case, the short-term settlements computed using the 'low triaxial' parameters are shallower than those using the 'high both' parameters (Figs 7.23(a) and (c)). In the twin-tunnel case, the footing in the 'low triaxial' analysis deforms in sagging about the mid-point of the tunnels immediately after tunnel construction, instead of hogging as in the 'high both' analysis. This indicates that a greater effect of tunnel-tunnel interaction is realised in the soil calibrated against the 'low triaxial' data.

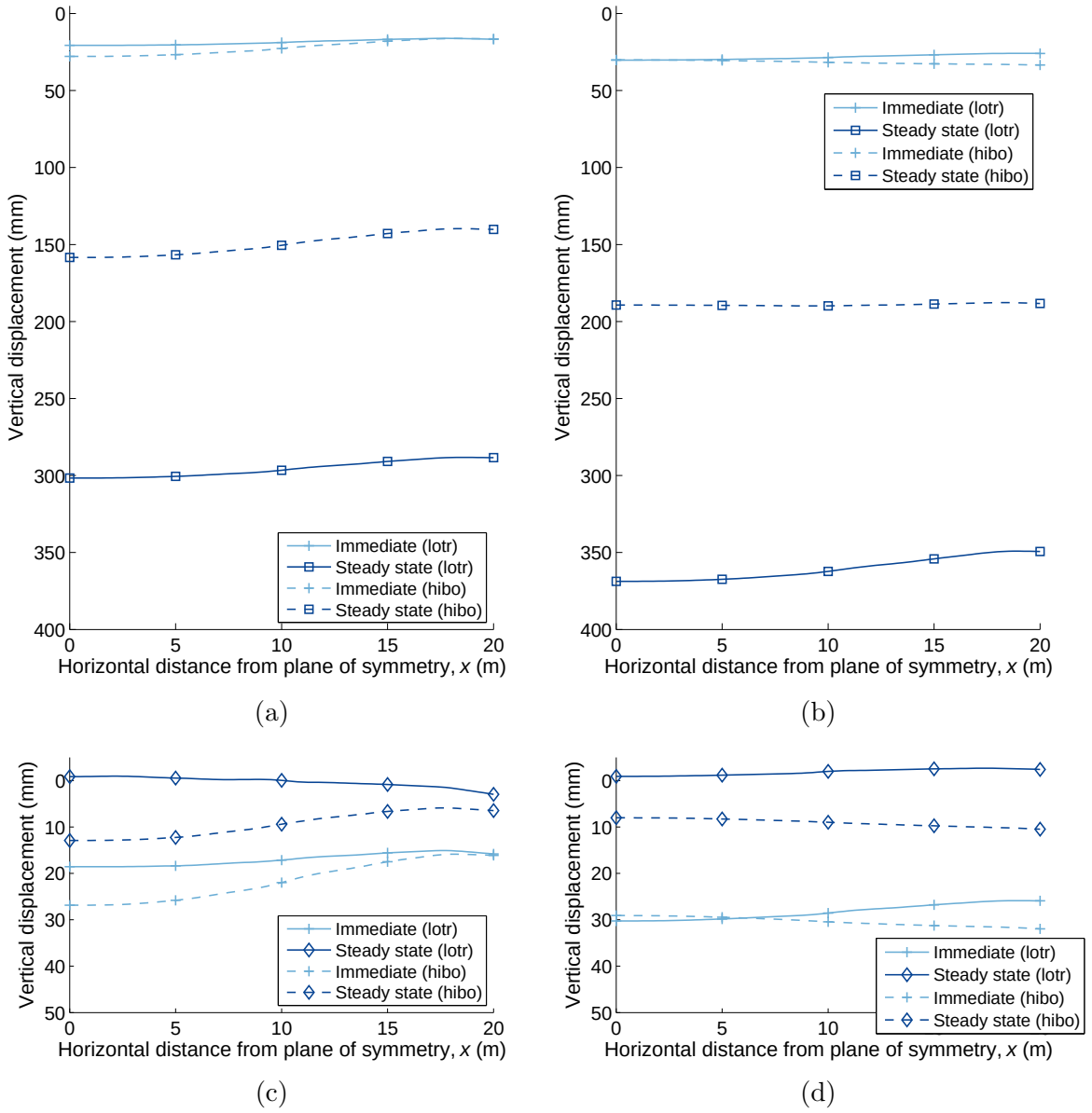


Figure 7.23: Vertical displacements at the base of the foundation of the facade in the short and long term computed with 'low triaxial' parameters in the M2-SKH model, compared with the results using 'high both' parameters: (a) fully permeable lining, single tunnel; (b) fully permeable lining, twin tunnels; (c) impermeable lining, single tunnel; (d) impermeable lining, twin tunnels

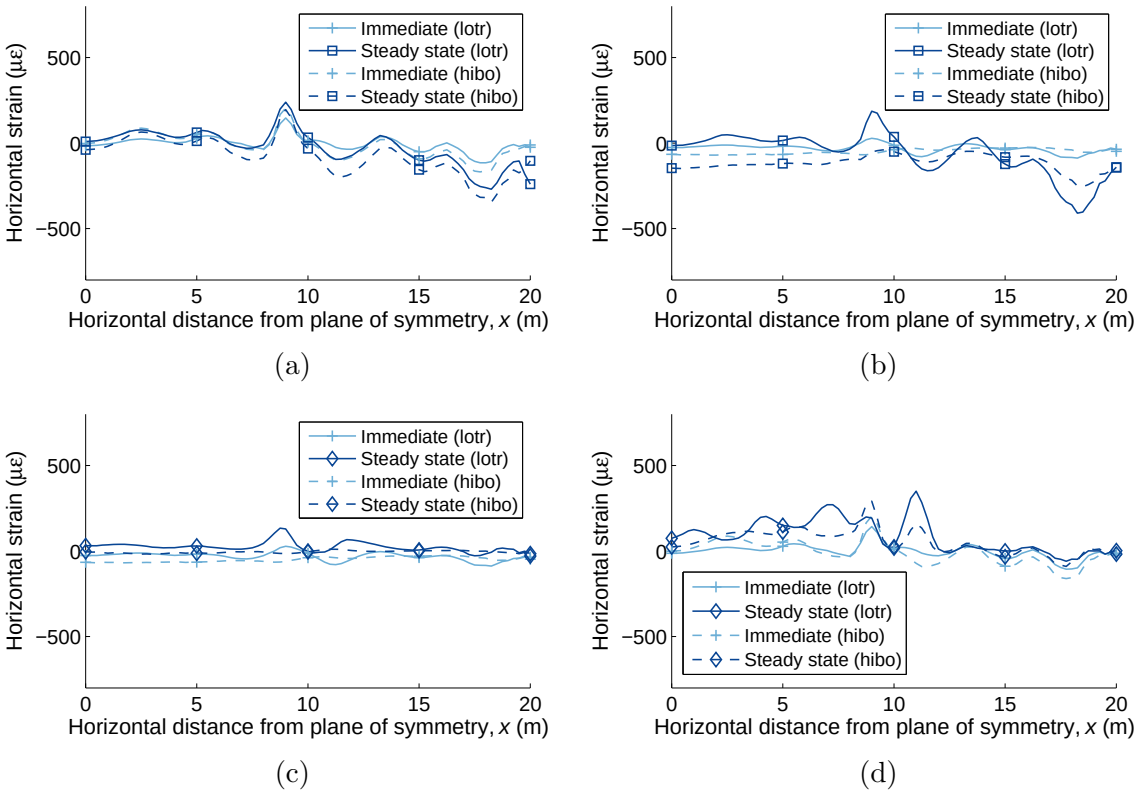


Figure 7.24: Horizontal strains at the base of the foundation of the facade in the short and long term computed with 'low triaxial' parameters in the M2-SKH model, compared with the results using 'high both' parameters: (a) fully permeable lining, single tunnel; (b) fully permeable lining, twin tunnels; (c) impermeable lining, single tunnel; (d) impermeable lining, twin tunnels

In the long term, with fully permeable tunnel lining assumed (Figs 7.23(a) and (b)), the footing settlements computed using the 'low triaxial' calibration are greater than those using the 'high both' calibration. With the impermeable lining, in the 'low triaxial' analysis, the soil heaves and the footing in the single-tunnel case experiences hogging across the full span (Fig. 7.23(c)), while the footing in the twin-tunnel case sags with a reduced slope (Fig. 7.23(d)). These behaviours are different from the results computed using the 'high both' calibration.

The horizontal strains developed in the base of the footing are shown in Fig. 7.24. The 'low triaxial' calibration generally results in greater maximum tensile strains than the 'high both' parameters in all cases considered, although the magnitudes of the horizontal strains are still relatively small.

The major principal strains induced in the facade in the short term and long term

computed using the 'low triaxial' calibration for the case of fully permeable lining (models ESA-lotr-T{1, 2}-kinf-F08O) are similar in pattern, with smaller magnitude, to that of the 'high both' results in Figs 7.17(a) and (b). The similarity is because the facade in these cases deforms in sagging and the settlement slope increases over time.

Figs 7.25 and 7.26 show the strain fields and damage bar charts for the case of a completely impermeable tunnel lining, computed using the 'low triaxial' parameters for the single-tunnel and twin-tunnel cases respectively. In the single-tunnel case (Fig. 7.25), where the dominant deformation mode changes from sagging immediately after tunnelling to hogging in the long term (Fig. 7.23(c)), the strain concentration shifts from the bottom edges to the top middle correspondingly, even though traces of the high strain areas around the bottom edges can still be observed at steady state. The damage bar chart in Fig. 7.25(c) indicates that a notable proportion of the area of facade ($\approx 5\%$) experiences one category higher damage in the long term. For the twin-tunnel case (Fig. 7.26), as the slope of the footing settlement profile is flattened upon swelling in the long term (Fig. 7.23(d)), the strain field indicates a relief of tensile strains in the facade over time. The $\varepsilon_{99}^{\mathrm{t}}$ value (and the damage bar chart) suggests the building damage in this scenario is negligible.

The characteristic strain, $\varepsilon_{99}^{\mathrm{t}}$, induced in the facade in the short and long term after tunnelling computed using the 'low triaxial' calibration are compared with those obtained from the 'high both' calibration in Fig. 7.27. In the single-tunnel case, the values of $\varepsilon_{99}^{\mathrm{t}}$ immediately after tunnelling computed in the 'low triaxial' analysis are lower than that of 'high both' because the differential settlements are smaller in the 'low triaxial' analysis (Figs 7.23(a) and (c)). The incremental increase in $\varepsilon_{99}^{\mathrm{t}}$ in the long term in the case of fully permeable lining using the 'low triaxial' calibration is significant, and the increase is comparable with that in the corresponding 'high both' analysis. The impermeable lining scenario (in the single-tunnel case) results in a bigger contrast. While the 'high both' calibration results in a decrease in $\varepsilon_{99}^{\mathrm{t}}$ at steady state, there is a substantial increase in $\varepsilon_{99}^{\mathrm{t}}$ in the long term when the 'low triaxial' calibration is used. This could be a consequence of the difference in the transition of the dominant

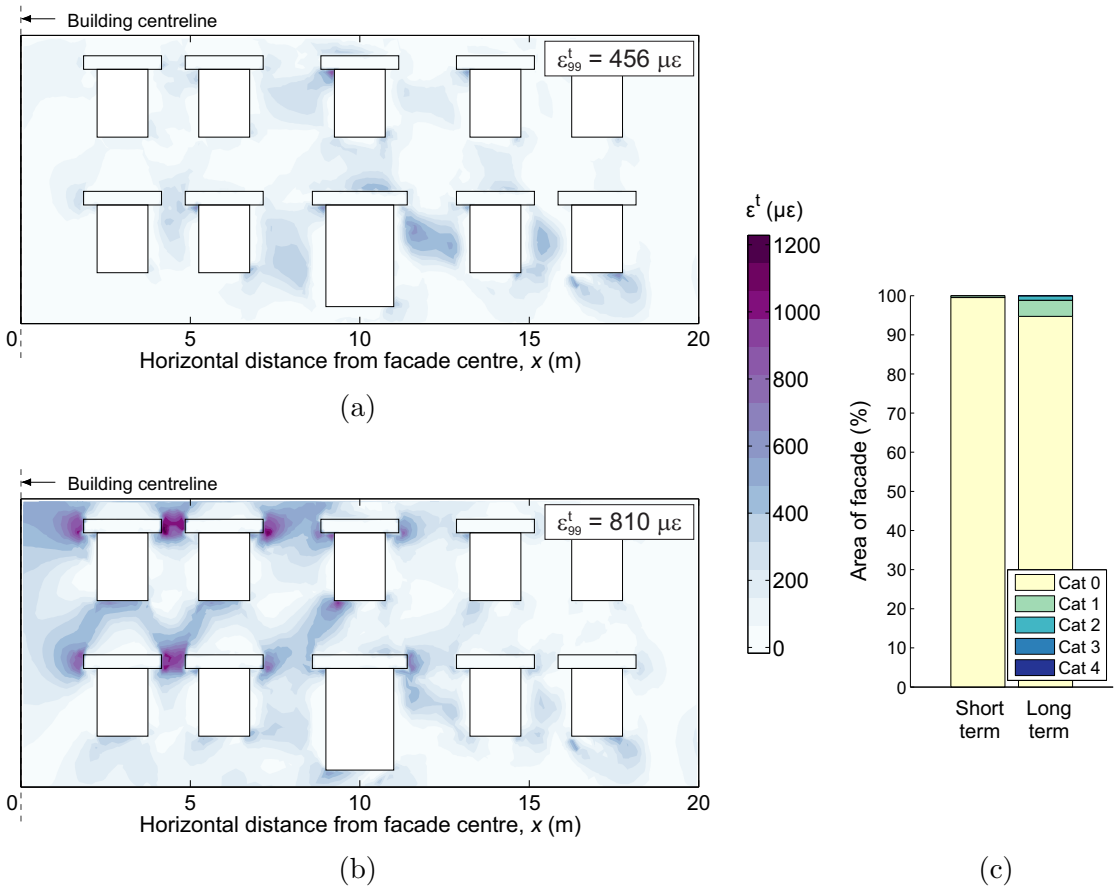


Figure 7.25: Major principal strain induced in the facade for the case of a single tunnel with impermeable lining using 'low triaxial' M2-SKH parameters: (a) strain field and ε^t_{99} immediately after tunnelling; (b) strain field and ε^t_{99} at steady state; (c) damage bar chart

deformation mode of the facade, from sagging to less sagging in the 'high both' analysis, and from sagging to hogging in the 'low triaxial' analysis.

For the case of twin tunnels (Fig. 7.27(b)), although the values of the short-term ε^t_{99} obtained using the 'low triaxial' calibration are similar to those using the 'high both' calibration, the dominant modes of deformation of the facade are different (sagging in the 'low triaxial' analysis and hogging in the 'high both' analysis, Figs 7.23(b) and (d)). In the case of a fully permeable lining, the 'low triaxial' analysis predicts an escalation of ε^t_{99} in the long term, remarkably greater than the increase in ε^t_{99} in the 'high both' analysis. In the impermeable lining case, there is a reduction in ε^t_{99} in the long term when the 'low triaxial' calibration is used, while a small rise in ε^t_{99} is computed when the 'high both' calibration is used.

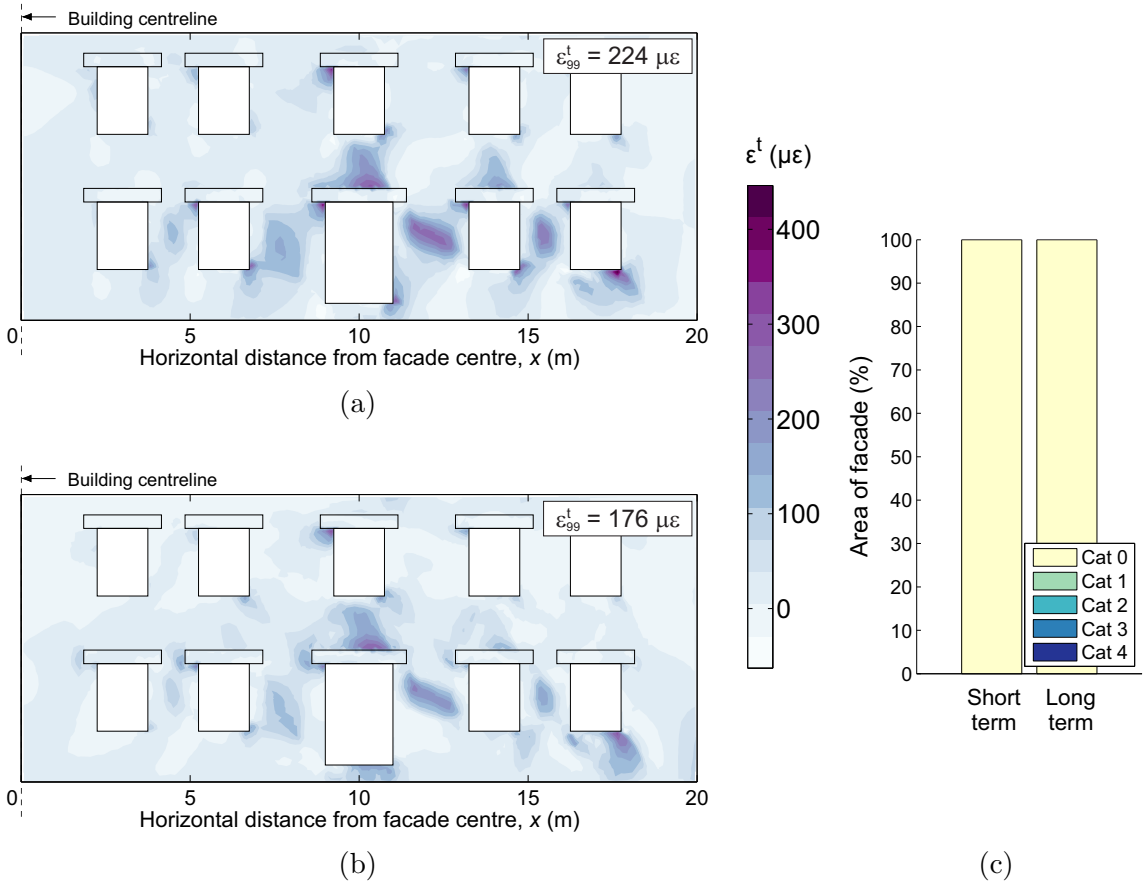


Figure 7.26: Major principal strain induced in the facade for the case of twin tunnels with impermeable lining using 'low triaxial' M2-SKH parameters: (a) strain field and ε^t_{99} immediately after tunnelling; (b) strain field and ε^t_{99} at steady state; (c) damage bar chart

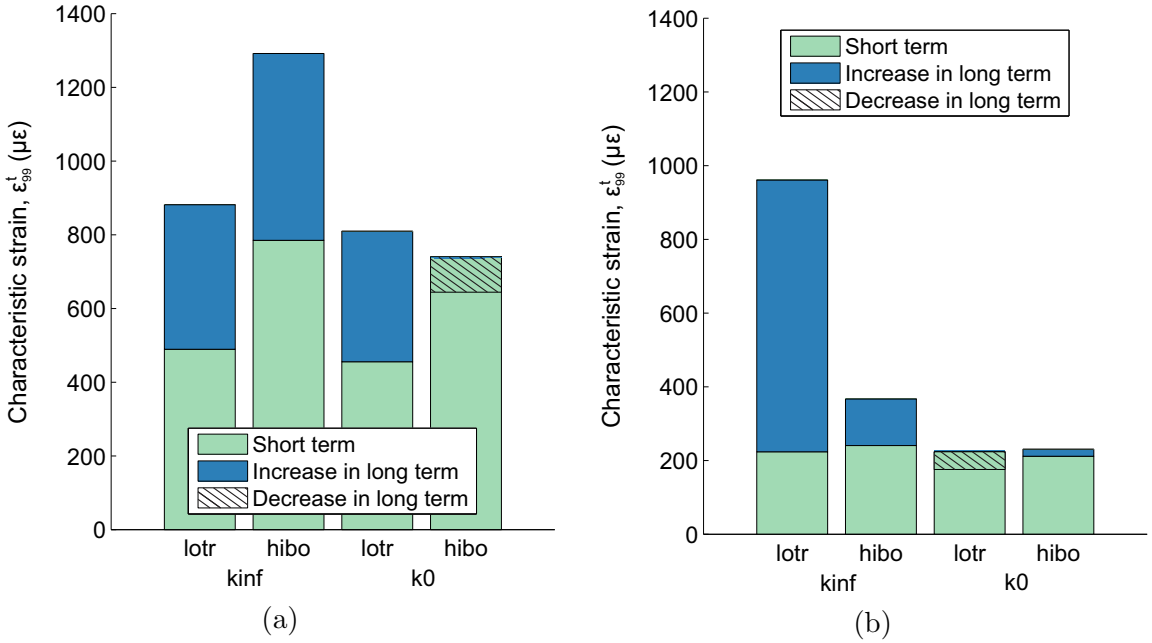


Figure 7.27: Effect of the calibration of the M2-SKH model, 'low triaxial' and 'high both', on characteristic strain, ε^t_{99}, induced in the facade, in the cases of fully permeable and impermeable tunnel linings: (a) single tunnel; (b) twin tunnels

7.4 Concluding remarks

The trends obtained from the greenfield analyses are consistent with expectations: (i) the rate of increase in settlement, slope and trough width (in the case of a permeable tunnel lining) are greatest immediately after tunnel construction, and (ii) the long-term settlements are greater when the lining is more permeable. Moreover, the long-term ground movements are shown to be particularly sensitive to the lining permeability for $\xi < 1$. Time-dependent tunnel-tunnel interaction is observed in the twin-tunnel case, where two separate settlement troughs merge into one as time elapses after tunnel construction.

Results of the building damage assessments for the combined soil-building analyses are strongly influenced by the chosen calibration of the M2-SKH model. Two plausible calibrations of the M2-SKH model induce considerably different short-term and long-term values of ε_{99}^{t} in the facade. The ε_{99}^{t} value, particularly for the single-tunnel case, is also sensitive to the permeability of the tunnel lining. The tunnel-tunnel interaction arising in the twin-tunnel case alters the dominant deformation mode of the building located between the twin tunnels over time — from hogging immediately after tunnel construction to sagging after a period of time. These results suggest that the long-term building damage induced by tunnelling is significantly case-specific.

Although a high long-term ε_{99}^{t} value is obtained in the isolated facade analysis with a single tunnel and fully permeable lining, the current study suggests that there is no urgent need to include calculations of long-term building response in the building damage assessment procedures. This is drawn on the basis that (i) the finite element results are highly sensitive to the soil model calibration for London Clay and further work is needed to enhance its reliability, (ii) the platform tunnels being modelled are likely to be built with sprayed concrete lining, which has relatively low permeability, and (iii) the computed long-term ε_{99}^{t} is likely to reduce when the effect of creep in the soil and masonry is included.

Chapter 8

Conclusions

This thesis develops the use of 3D finite element analysis for assessing the likely severity and extent of damage to a masonry building induced by tunnel construction in the short term and the long term. Finite element modelling procedures have been established systematically for analysing an example scenario of urban tunnelling in typical central London conditions in which layered soils are considered. The key contributions of this thesis and recommendations for further work are summarised below.

8.1 Contributions

8.1.1 Implementation of advanced constitutive models

Two advanced soil constitutive models, the extended Mohr-Coulomb (EMC) model developed by Doherty & Muir Wood (2013) and the modified two-surface kinematic hardening (M2-SKH) model by Grammatikopoulou et al. (2006), have been implemented for the Terrace Gravel and the London Clay respectively in the current work.

i. The compatibility of the EMC model and the explicit modified Euler integration scheme with substepping and stress correction (Sloan et al. 2001) is reviewed. Some numerical issues encountered with the scheme described in Sloan et al. (2001) are identified, and alternative solutions are implemented. Some challenges due to the nature of the EMC model, such as the singularities of the yield surface

at triaxial stress conditions, are also addressed. The EMC model is calibrated against another model used in Jurečič et al. (2013) for Terrace Gravel.

ii. The M2-SKH model is implemented with a modified measure of the proximity of the yield surface to the bounding surface. The substepping stress update algorithm with the explicit Runge-Kutta-Dormand-Prince integration scheme and the stress state correction described in Sloan et al. (2001) is adapted to the specific, two-surface model. The implemented algorithm consists of an elastic update routine, a yield surface update routine and a bounding surface update routine as sequential operations.

iii. The implemented M2-SKH model is calibrated for London Clay against the 'high both' and 'low triaxial' calibrations of the M2-SKH model used in Avgerinos et al. (2016). The overburden stress assumed in the geological history and the hardening parameter of the model are adjusted in the implemented M2-SKH model to match the K_0 profile after simulation of the geological history in Avgerinos et al. (2016). The model parameters of the 'high both' calibration, which accounts for both triaxial compression test and oedometer test data, are validated for the prediction of long-term ground movements induced by tunnelling.

8.1.2 Understanding of tunnel-soil-building interaction

3D finite element analyses performed in terms of total stress, with an isolated facade, have revealed the mechanisms that are active in the interaction in terms of the settlement, deformation mode and strain distribution of the facade. The main findings include the following.

i. The presence of a building tends to modify the local tunnelling-induced ground movements. The normal tractions on the base of the footing redistribute after tunnelling. Reducing the building height lowers the overall stiffness of the building and leads to more severe damage.

ii. The dominant mode of deformation of the building depends on the tunnel configuration (e.g. single tunnel or twin tunnels) and the tunnel eccentricity. In

both single- and twin-tunnel cases, the characteristic strain, ε_{99}^{t}, is greatest when the building is located at zero tunnel eccentricity, and another maximum ε_{99}^{t} is obtained when the building is located slightly beyond the point of inflection.

iii. The presence of openings for windows and doors in the facade reduces the overall stiffness of the facade and introduces internal corners. Higher damage is predicted in a facade with openings than in a plain facade. The facade with openings exhibits a frame-like action, with significant concentrations of strain developing around the corners of the openings, whereas the strains in the plain facade correspond broadly to beam action.

iv. The contact behaviour between the soil and the building foundation affects the deformation mechanisms of the building. Gapping and sliding at the soil-footing interface are allowed by modelling the continuous strip footing explicitly with 3D continuum elements and defining a no-tension frictional soil-footing contact model. The damage induced in the facade is also affected by footing width and embedment depth.

v. The tunnel-induced horizontal strains developed at the base of a building with shallow foundations are substantially lower in magnitude than those in the adjacent ground. When a moderate friction coefficient (e.g. $\mu = 0.3$) is employed in the soil-footing frictional contact model, the influence of the horizontal strains in the soil, combined with the beam action of the building via shear at the soil-footing interface, cause the horizontal strains in the footing to be approximately zero. The sliding occurring at the interface indicates that the horizontal coupling between the foundation and the ground is relatively weak. This finding aligns with published data from field measurements in London.

In addition, 3D finite element analyses with a complete building have demonstrated 3D geometrical effects associated with the internal and end walls connected to facades. The building as a whole tends to restrain individual facades and walls from differential settlements. Additional 3D effects such as twisting of the building have been illustrated in the complete building analysis with a skew tunnel.

8.1.3 Understanding of time-dependent effects on ground and building response

The long-term ground and building responses caused by the dissipation of excess pore pressure after tunnel construction have been evaluated using 3D finite element analyses in terms of effective stress. The main results are summarised below.

i. The greenfield transient analysis after tunnel construction indicates that the long-term ground movement converges in around 60 years for the configuration considered. The changes in the magnitude of settlement, trough width and slope are most significant in the first 10 years.

ii. The long-term ground movement is correlated with the permeability of the tunnel lining. The vertical displacements (magnitude, trough width and slope), horizontal displacements, and horizontal strains are greatest when the lining is fully permeable. These values decrease as the relative lining-soil permeability decreases. The case of a completely impermeable lining results in the soil swelling in the long term, leaving to surface heave. The relationship between the variation of these quantities and the relative lining-soil permeability is non-linear.

iii. Tunnel-tunnel interaction is apparent in the greenfield analysis of consolidation following the construction of twin tunnels. The two settlement troughs computed immediately after tunnel construction merge into one wider trough within one year. This kind of tunnel-tunnel interaction with a merged settlement trough has previously been observed in field measurements.

iv. The analysis of an isolated facade with a single tunnel at zero eccentricity shows that the additional damage induced in the facade due to long-term consolidation is greatest when the tunnel lining is fully permeable. When the lining is impermeable, the settlement profile of the facade becomes even flatter than the one computed in the short term, resulting in a smaller severity of damage at steady state than immediately after tunnel construction.

v. The building response to long-term ground movements induced by twin tunnels is influenced by the tunnel-tunnel interaction. The analysis of an isolated facade

located between twin tunnels with permeable linings shows that the dominant deformation mode of the facade changes from hogging to sagging over time. The variation of the long-term characteristic strain induced in the facade with the lining permeability is not monotonic in the twin-tunnel case.

8.1.4 Finite element analysis for building damage assessment in practice

This research work has established 3D finite element modelling procedures that support certain simplifications of the tunnel-soil-building interaction problem, while providing results that are useful for practical assessment purposes, with suggested methods for data processing.

i. Modelling procedures for both total stress analysis (TSA) and effective stress analysis (ESA) are developed. Deep and narrow settlement troughs are obtained from the TSA, where the tunnel excavation is modelled using the displacement field method and the London Clay is represented by the multiple yield surface kinematic hardening model (Houlsby 1999). In the ESA, the nodal force reduction method is employed to model the tunnel construction process and the behaviour of the London Clay is described by the M2-SKH model, allowing the development and dissipation of excess pore pressure to be simulated. It is noted that different predictions of the short-term building damage and ground movement are obtained using the TSA and ESA approaches.

ii. Several data interpretation methods for the results computed from finite element analysis are developed and demonstrated as practical result processing procedures. The characteristic strain, ε_{99}^{t}, the damage bar chart and the major principal strain field provide information about the extent and the distribution of the tensile strains induced in the facade, with increasing levels of detail. In particular, the ε_{99}^{t} value offers a potentially useful mesh-independent single metric for quantifying the likely highest severity of building damage.

iii. Some features are identified as necessary to capture the tunnel-soil-building in-

teraction with sufficient realism. The openings in the facade, the tunnel configuration and the tunnel eccentricity are all shown to influence the deformation mechanisms of the building. The explicitly modelled building foundation with no-tension frictional contact is needed to allow for possible gapping and sliding at the soil-footing interface. The value assumed for the relative tunnel lining-soil permeability is crucial for predicting long-term ground movements.

iv. Adopting a rough soil-footing interface provides a conservative and convenient estimate of tensile strains in the facade for the purpose of building damage assessments, if the deformation mechanisms of the building are not the main concern as the contact behaviour at the soil-footing interface is important for capturing the coupling of stresses and strains between the soil and the building.

v. Appropriate geometric simplifications for the purpose of building damage assessments are achieved based on the example scenarios. For the orthogonal tunnel-building configuration considered, the 3D isolated facade analysis and the 3D complete building analysis predict similar results in the facade. The 3D complete building analysis with an orthogonal tunnel provides more conservative results than that with a skew tunnel, although details of the actual building response differ considerably. This suggests that the 3D isolated facade modelling approach may offer a simplified and reliable numerical procedure that could potentially be useful within a hierarchical phased building damage assessment.

vi. Some simplification of constitutive models for the purpose of building damage assessment is feasible with careful model calibration. The linear elastic, perfectly plastic Mohr-Coulomb model, which is calibrated in a similar manner to the EMC model for the Terrace Gravel and incorporates a reduction in elastic shear modulus to account for the small-strain stiffness degradation, is shown to perform as well as the EMC model in the current analyses. However, the results are strongly influenced by the calibration of the M2-SKH model employed for the London Clay in the effective stress analyses. Two plausible calibrations, which are adopted from previous literature, provide significantly different predictions

for the short-term and long-term ground and building response.

8.1.5 Evaluation of the current building damage assessment procedure

The limitations of the conventional elastic beam assessment (EBA) approach have been reviewed. On one hand, the EBA procedure overestimates the severity of damage to the facade by superimposing greenfield horizontal strains in the soil directly on the structural strains derived from the beam model of the building. On the other hand, the EBA method neglects the strain localisation effect at the corners of the openings in the facade. Although detailed comparisons with the finite element results suggest that the EBA approach is likely to be conservative in general, this simple and fast approach should be used with caution if detailed and accurate damage predictions are required.

8.2 Recommendations for future work

i. **Transient effect of tunnel excavation.**

   As a tunnel heading approaches beneath a building, twisting deformation may be induced in the building. This transient effect of the tunnel construction process is neglected in the present thesis, in which the tunnel excavation is modelled as a single-stage process. Future analysis could consider the transient effect of tunnelling using the step-by-step tunnel excavation method, although the computational cost would be higher. This effect might be more significant in the 3D complete building analysis than in the 3D isolated facade analysis.

ii. **Sequential construction of twin tunnels.**

   Twin tunnels are likely to be constructed sequentially, such that the soil movements induced by the second tunnel may be influenced by the presence of the first tunnel. The tunnel-tunnel interaction in sequential construction is not considered in this thesis, where the process is simplified by modelling simultaneous tunnel excavation. Further work could be conducted to determine whether the

tunnel-tunnel interaction during sequential construction is important for building damage assessment purposes.

iii. **Creep of the materials.**

Creep is likely to occur in the soil and the masonry in the long term. If creep is accounted for in the soil, the soil beneath the building would be expected to deform further in the long term such that the total settlements of the footing increase, but its differential settlements decrease. Moderate creep in the masonry might be beneficial in relieving tensile cracking in the building. It is suggested that these creep effects may have a substantial influence on the prediction of long-term building damage. Further research on the effect of creep in the tunnel-soil-building interaction requires deeper knowledge of the material properties, and use of more sophisticated constitutive models.

iv. **Eccentric tunnel scenarios for long-term building damage.**

The greatest additional ground differential settlements induced by long-term consolidation are found to occur at some distance away from the tunnel centre. This suggests that buildings eccentric to the tunnel could be more sensitive to long-term ground movements, whereas the most severe building damage in the short term is predicted at zero tunnel eccentricity. Further effective stress analyses with isolated facades and eccentric tunnels could be conducted to identify the relative position of the building associated with the greatest increase in building damage in the long term. The results could also be used to advise on the extended influence areas affected by tunnel construction in the long term, which could be useful for building monitoring purposes.

v. **Stress paths in soil.**

The mechanisms involved in the tunnel-soil-building interaction problem could be further understood by studying the short-term and long-term stress paths in the soil at various locations. The study of stress paths could also allow better targeting of laboratory tests for the calibration of constitutive models that strongly influence the finite element results (e.g. the M2-SKH model for London Clay).

References

Abbo, A. J. (1997), Finite element algorithms for elastoplasticity and consolidation, PhD thesis, University of Newcastle, Australia.

Addenbrooke, T. I. & Potts, D. M. (1996), Twin tunnel construction - ground movements and lining behaviour, *in* 'Proc. International Symposium on Geotechnical Aspects of Underground Construction in Soft Ground', pp. 441–446.

Addenbrooke, T. I. & Potts, D. M. (2001), 'Twin tunnel interaction: surface and subsurface effects', *International Journal of Geomechanics* **1**(2), 249–271.

Addenbrooke, T. I., Potts, D. M. & Puzrin, A. M. (1997), 'The influence of pre-failure soil stiffness on the numerical analysis of tunnel construction', *Géotechnique* **47**(3), 693–712.

Al-Tabbaa, A. & Muir Wood, D. (1989), An experimentally based 'bubble' model for clay, *in* '3rd International Symposium on Numerical Models in Geomechanics (NUMOG III)', pp. 91–99.

Amorosi, A., Boldini, D., de Felice, G., Malena, M. & Sebastianelli, M. (2014), 'Tunnelling-induced deformation and damage on historical masonry structures', *Géotechnique* **64**(2), 118–130.

Atkinson, J. H. (2000), 'Non-linear soil stiffness in routine design', *Géotechnique* **50**(5), 487–507.

Atkinson, J. H. & Mair, R. J. (1981), 'Soil mechanics aspects of soft ground tunnelling', *Ground Engineering* **14**(5), 20–28.

Atkinson, J. H., Richardson, D. & Stallebrass, S. E. (1990), 'Effect of recent stress history on the stiffness of overconsolidated soil', *Géotechnique* **40**(4), 531–540.

Attewell, P. B., Yeates, J. & Selby, A. R. (1986), *Soil movements induced by tunnelling and their effects on pipelines and structures*, Blackie, Glasgow.

Augarde, C. E. & Burd, H. J. (2001), 'Three-dimensional finite element analysis of lined tunnels', *International Journal for Numerical and Analytical Methods in Geomechanics* **25**(3), 243–262.

Avgerinos, V. (2014), Numerical investigation of tunnelling beneath exisiting tunnels, PhD thesis, Imperial College London.

Avgerinos, V., Potts, D. M. & Standing, J. R. (2016), 'The use of kinematic hardening models for predicting tunnelling-induced ground movements in London Clay', *Géotechnique* **66**(2), 106–120.

Avgerinos, V., Potts, D. M., Standing, J. R. & Wan, M. S. P. (2018), 'Predicting tunnelling-induced ground movements and interpreting field measurements using numerical analysis: Crossrail case study at Hyde Park', *Géotechnique* **68**(1), 31–49.

Bilotta, E., Paolillo, A., Russo, G. & Aversa, S. (2017), 'Displacements induced by tunnelling under a historical building', *Tunnelling and Underground Space Technology* **61**, 221–232.

Bloodworth, A. G. (2002), Three-dimensional analysis of tunnelling effects on structures to develop design methods, DPhil thesis, University of Oxford.

Bloodworth, A. G. & Houlsby, G. T. (2017), 'Analysis of pre-vault tunnelling interaction with buildings', *Proceedings of the Institution of Civil Engineers - Geotechnical Engineering* **170**(2), 99–116.

Boscardin, M. D. & Cording, E. J. (1989), 'Building response to excavation-induced settlement', *Journal of Geotechnical Engineering* **115**(1), 1–21.

Bowers, K. H., Hiller, D. M. & New, B. M. (1996), Ground movement over three years at the Heathrow Express Trial Tunnel, *in* R. J. Mair & R. N. Taylor, eds, 'Proc. International Symposium on Geotechnical Aspects of Underground Construction in Soft Ground', CRC Press, pp. 647–652.

Brown, P. T. & Booker, J. R. (1985), 'Finite element analysis of excavation', *Computers and Geotechnics* **1**(3), 207–220.

Burd, H. J., Houlsby, G. T., Augarde, C. E. & Liu, G. (2000), 'Modelling tunnelling-induced settlement of masonry buildings', *Proceedings of the Institution of Civil Engineers - Geotechnical Engineering* **143**(1), 17–29.

Burland, J. B. (2001), Assessment methods used in design, *in* 'Building Response to Tunnelling: Case Studies from Construction of the Jubilee Line Extension, London', Vol. 1, Thomas Telford, pp. 23–43.

Burland, J. B., Broms, B. B. & de Mello, V. F. B. (1977), Behavior of foundations and structures on soft ground, *in* '9th International Conference on Soil Mechanics and Foundation Engineering', Vol. Session 2, pp. 495–546.

Burland, J. B., Chapman, T., Skinner, H. D. & Brown, M. (2012), *ICE Manual of Geotechnical Engineering*, Thomas Telford Ltd.

Burland, J. B., Mair, R. J. & Standing, J. R. (2004), Ground performance and building response due to tunnelling, *in* R. J. Jardine, D. Potts & K. G. Higgins, eds, 'Proc. Advances in Geotechnical Engineering: The Skempton Conference', Vol. 1, pp. 291–342.

Burland, J. B., Standing, J. R. & Jardine, F. M., eds (2001), *Building Reponse to Tunnelling - Case Studies from Construction of the Jubilee Line Extension, London*, Thomas Telford.

Burland, J. B. & Wroth, C. P. (1975), *Settlement of Buildings and Associated Damage*, Building Research Establishment, Department of the Environment.

Chow, L. (1994), The prediction of surface settlements due to tunnelling in soft ground, Master's thesis, University of Oxford.

Clausen, J., Damkilde, L. & Andersen, L. (2007), 'An efficient return algorithm for non-associated plasticity with linear yield criteria in principal stress space', *Computers and Structures* **85**(23/24), 1795–1807.

Clough, G. W., Sweeney, B. P. & Finno, R. J. (1983), 'Measured soil response to EPB shield tunneling', *Journal of Geotechnical Engineering* **109**(2), 131–149.

Crossrail Ltd (2008), D12 - ground settlement, *in* 'Crossrail Information Paper', Crossrail Ltd.

Dimmock, P. S. & Mair, R. J. (2007), 'Volume loss experienced on open-face London Clay tunnels', *Proceedings of the Institution of Civil Engineers - Geotechnical Engineering* **160**(1), 3–11.

Dimmock, P. S. & Mair, R. J. (2008), 'Effect of building stiffness on tunnelling-induced ground movement', *Tunnelling and Underground Space Technology* **23**(4), 438–450.

Doherty, J. P. & Muir Wood, D. (2013), 'An extended Mohr-Coulomb (EMC) model for predicting the settlement of shallow foundations on sand', *Géotechnique* **63**(8), 661–673.

Dong, Y. P. (2014), Advanced finite element analysis of deep excavation case histories, DPhil thesis, University of Oxford.

Dong, Y. P., Burd, H. J. & Houlsby, G. T. (2016), 'Finite-element analysis of a deep excavation case history', *Géotechnique* **66**(1), 1–15.

Dulake, C. (2011), 'Crossrail – design and construction / Crossrail – Entwurf, Bemessung und Ausführung', *Geomechanics and Tunnelling* **4**(5), 592–604.

Fargnoli, V., Gragnano, C. G., Boldini, D. & Amorosi, A. (2015), '3D numerical modelling of soil-structure interaction during EPB tunnelling', *Géotechnique* **65**(1), 23–37.

Farrell, R. P., Mair, R. J., Sciotti, A. & Pigorini, A. (2014), 'Building response to tunnelling', *Soils and Foundations* **54**(3), 269–279.

Franzius, J. N. (2003), Behaviour of buildings due to tunnel induced subsidence, PhD thesis, Imperial College London.

Franzius, J. N., Potts, D. M., Addenbrook, T. I. & Burland, J. B. (2004), 'The influence of building weight on tunnelling-induced ground and building deformation', *Soils and Foundations* **44**(1), 25–38.

Franzius, J. N., Potts, D. M. & Burland, J. B. (2005*a*), 'The influence of soil anisotropy and K_0 on ground surface movements resulting from tunnel excavation', *Géotechnique* **55**, 189–199.

Franzius, J. N., Potts, D. M. & Burland, J. B. (2005*b*), 'The response of surface structures to tunnel construction', *Proceedings of the Institution of Civil Engineers - Geotechnical Engineering* **158**, 1–15.

Frischmann, W. W., Hellings, J. E., Gittoes, G. & Snowden, C. (1994), 'Protection of the Mansion House against damage caused by ground movements due to the Docklands Light Railway extension', *Proceedings of the Institution of Civil Engineers - Geotechnical Engineering* **107**(2), 65–76.

Furtmuller, T. & Adam, C. (2011), 'Numerical modeling of the in-plane behaviour of historical brick masonry walls', *Acta Mechanica* **221**, 65–77.

Gajo, A. & Muir Wood, D. (1999), 'Severn-Trent sand: a kinematic-hardening constitutive model: the *q-p* formulation', *Géotechnique* **49**(5), 595–614.

Gakis, A., Salak, P. & St. John, A. (2014), Geotechnical risk management for sprayed concrete lining tunnels in Farringdon Crossrail Station, *in* M. Black, C. Dodge & U. Lawrence, eds, 'Crossrail project: Infrastructure design and construction', ICE Publishing, pp. 349–362.

Galli, G., Grimaldi, A. & Leonardi, A. (2004), 'Three-dimensional modelling of tunnel excavation and lining', *Computers and Geotechnics* **31**(3), 171–183.

Geotechdata.info (2013), 'Geotechnical parameter'. Accessed 14 December, 2017. `http://www.geotechdata.info/parameter/parameter.html`.

Giardina, G., DeJong, M. J. & Mair, R. J. (2015a), 'Interaction between surface structures and tunnelling in sand: Centrifuge and computational modelling', *Tunnelling and Underground Space Technology* **50**, 465–478.

Giardina, G., Hendriks, M. A. N. & Rots, J. G. (2010), 'Numerical analysis of tunnelling effects on masonry buildings: the influence of tunnel location on damage assessment', *Advanced Materials Research* **133-134**, 289–294.

Giardina, G., Hendriks, M. A. N. & Rots, J. G. (2015b), 'Damage functions for the vulnerability assessment of masonry buildings subjected to tunneling', *Journal of Structural Engineering* **141**(9), 04014212.

Giardina, G., Ritter, S., DeJong, M. J. & Mair, R. J. (2017), Influence of building geometry on bending and shear deformations of buildings subject to tunnelling subsidence: numerical modelling, *in* 'Proc. IV International Conference on Computational Methods in Tunneling and Subsurface Engineering', ECCOMAS, Austria.

Giardina, G., van de Graaf, A. V., Hendriks, M. A. N., Rots, J. G. & Marini, A. (2013), 'Numerical analysis of a masonry facade subject to tunnelling-induced settlements', *Engineering Structures* **54**, 234–247.

Grammatikopoulou, A., Zdravković, L. & Potts, D. M. (2006), 'General formulation of two kinematic hardening constitutive models with a smooth elastoplastic transition', *International Journal of Geomechanics* **6**, 291–302.

Grammatikopoulou, A., Zdravković, L. & Potts, D. M. (2007), 'The effect of the yield and plastic potential deviatoric surfaces on the failure height of an embankment', *Géotechnique* **57**, 795–806.

Grammatikopoulou, A., Zdravković, L. & Potts, D. M. (2008), 'The influence of previous stress history and stress path direction on the surface settlement trough induced by tunnelling', *Géotechnique* **58**, 269–281.

Grant, R. J. & Taylor, R. N. (1996), Centrifuge modelling of ground movements due to tunnelling in layered ground, *in* R. J. Mair & R. N. Taylor, eds, 'Proc. International Symposium on Geotechnical Aspects of Underground Construction in Soft Ground', Balkema, London, pp. 507–512.

Guedes de Melo, P. F. M. & Santos Pereira, C. (2000), The role of k_0 value in numerical analysis of shallow tunnels, *in* Kusakabe, Fujita & Miyazaki, eds, 'Proc. International Symposium on Geotechnical Aspects of Underground Construction in Soft Ground', Balkema, Rotterdam, pp. 379–384.

Gupta, S. C., Viggiani, G. & Standing, J. R. (2001), Great George Street - south side, *in* 'Building Response to Tunnelling: Case Studies from Construction of the Jubilee Line Extension, London', Vol. 2, Thomas Telford, pp. 433–452.

Harris, D. I. (2001), Compensation grouting for the Royal Automobile Club building, *in* 'Building Response to Tunnelling: Case Studies from Construction of the Jubilee Line Extension, London', Vol. 2, Thomas Telford, pp. 367–385.

Harris, D. I. (2002), Long term settlement following tunnelling in overconsolidated London Clay, *in* Kastner, Emeriault, Dias & Guilloux, eds, 'Proc. International Symposium on Geotechnical Aspects of Underground Construction in Soft Ground', pp. 393–398.

Harris, D. I. & Franzius, J. N. (2006), Settlement assessment for running tunnels – a generic approach, *in* 'Proc. 5th International Symposium on Geotechnical Aspects of Underground Construction in Soft Ground', Amsterdam, pp. 225–230.

Hight, D. W., Gasparre, A., Nishimura, S., Minh, N. A., Jardine, R. J. & Coop, M. R. (2007), 'Characteristics of the London Clay from the Terminal 5 site at Heathrow Airport', *Géotechnique* **57**(1), 3–18.

Hills, D. A. & Dini, D. (2011), 'Characteristics of the process zone at sharp notch roots', *International Journal of Solids and Structures* **48**(14), 2177–2183.

Houlsby, G. T. (1999), A model for the variable stiffness of undrained clay, *in* 'Proc. 2nd International Symposium on Pre-Failure Deformation Characteristics of Geomaterials', Vol. 1, Turin, Italy, pp. 443–450.

Houlsby, G. T., Liu, G. & Augarde, C. E. (2000), 'A tying scheme for imposing displacement constraints in finite element analysis', *Communications in Numerical Methods in Engineering* **16**(10), 721–732.

Hover, E., Psomas, S. & Eddie, C. (2015), 'Short- and long-term tunnelling-induced settlments at Whitechapel Station', *Ground Engineering* **December**, 30–40.

Jardine, R. J., Potts, D. M., Fourie, A. B. & Burland, J. B. (1986), 'Studies of the influence of non-linear stress-strain characteristics in soil-structure interaction', *Géotechnique* **36**(3), 377–396.

Jefferies, M. G. (1993), 'Nor-Sand - a simple critical state model for sand', *Géotechnique* **43**(1), 91–103.

Jurečič, N., Zdravković, L. & Jovičić, V. (2013), 'Predicting ground movements in London Clay', *Proceedings of the Institution of Civil Engineers - Geotechnical Engineering* **166**(5), 466–482.

Karakus, M. (2007), 'Appraising the methods accounting for 3D tunnelling effects in 2D plane strain FE analysis', *Tunnelling and Underground Space Technology* **22**(1), 47–56.

Karakus, M. & Fowell, R. J. (2003), 'Effects of different tunnel face advance excavation on the settlement by FEM', *Tunnelling and Underground Space Technology* **18**(5), 513–523.

Kasper, T. & Meschke, G. (2004), 'A 3D finite element simulation model for TBM', *International Journal for Numerical and Analytical Methods in Geomechanics* **28**, 1441–1460.

Kovacevic, N., Edmonds, H. E., Mair, R. J., Higgins, K. G. & Potts, D. M. (1996), Numerical modelling of the NATM and compensation grouting trials at Redcross Way, *in* 'Proc. International Symposium on Geotechnical Aspects of Underground Construction in Soft Ground', A a Balkema, Rotterdam, pp. 553–559.

Lade, P. V. & Duncan, J. M. (1975), 'Elastoplastic stress-strain theory for cohesionless soil', *Journal of Geotechnical and Geoenvironmental Engineering* **101**(GT10), 1037–1053.

Laver, R. G. (2010), Long-term behaviour of twin tunnels in London Clay, PhD thesis, University of Cambridge.

Laver, R. G., Li, Z. & Soga, K. (2017), 'Method to evaluate the long-term surface movements by tunneling in London Clay', *Journal of Geotechnical and Geoenvironmental Engineering* **143**(3), 06016023.

Lee, J. & Fenves, G. L. (1998), 'Plastic-damage model for cyclic loading of concrete structures', *Journal of Engineering Mechanics* **124**(8), 892–900.

Lee, K. M. & Rowe, R. K. (1989), 'Deformations caused by surface loading and tunnelling - the role of elastic-anisotropy', *Géotechnique* **39**(1), 125–140.

Liu, G., Houlsby, G. T. & Augarde, C. E. (2000), '2-dimensional analysis of settlement damage to masonry buildings caused by tunnelling', *Structural Engineer* **79**(1), 19–25.

Losacco, N., Burghignoli, A. & Callisto, L. (2014), 'Uncoupled evaluation of the structural damage induced by tunnelling', *Géotechnique* **64**(8), 646–656.

Mair, R. J. (2008), 'Tunnelling and geotechnics: new horizons', *Géotechnique* **58**(9), 695–736.

Mair, R. J. & Taylor, R. N. (1993), Prediction of clay behaviour around tunnels using plasticity solutions, *in* 'Predictive Soil Mechanics: Proceedings of the Wroth Memorial Symposium', Oxford, pp. 449–463.

Mair, R. J. & Taylor, R. N. (1999), Theme lecture: Bored tunnelling in the urban environment, *in* 'Proc. 14th International Conference on Soil Mechanics and Foundation Engineering', Vol. 4, pp. 2353–2385.

Mair, R. J. & Taylor, R. N. (2001), Settlement predictions for Neptune, Murdoch, and Clegg Houses and adjacent masonry walls, *in* 'Building Response to Tunnelling: Case Studies from Construction of the Jubilee Line Extension, London', Vol. 1, Thomas Telford, pp. 217–228.

Mair, R. J., Taylor, R. N. & Burland, J. B. (1996), Prediction of ground movements and assessment of risk of building damage due to bored tunnelling, *in* 'Proc. 4th International Symposium on Geotechnical Aspects of Underground Construction in Soft Ground', AA Balkema, pp. 713–718.

Marshall, A., Farrell, R. P., Klar, A. & Mair, R. J. (2012), 'Tunnels in sands: the effect of size, depth and volume loss on greenfield displacements', *Géotechnique* **62**(5), 385.

Matsuoka, H. & Nakai, T. (1974), 'Stress-deformation and strength characteristics of soil under three different principal stresses', *Proceedings of the Japan Society of Civil Engineers* **232**, 59–70.

Menétrey, P. & Willam, K. J. (1995), 'Triaxial failure criterion for concrete and its generalization', *ACI Structural Journal* **92**(3), 311–318.

Miliziano, S., Soccodato, F. M. & Burghignoli, A. (2002), Evaluation of damage in masonry buildings due to tunnelling in clayey soils, *in* Kastner, Emeriault, Dias & Guilloux, eds, 'Proc. International Symposium on Geotechnical Aspects of Underground Construction in Soft Ground', pp. 335–340.

Mitaritonna, G., Amorosi, A. & Cotecchia, F. (2014), 'Experimental investigation of the evolution of elastic stiffness anisotropy in a clayey soil', *Géotechnique* **64**(6), 463–475.

Mroueh, H. & Shahrour, I. (2003), 'A full 3-D finite element analysis of tunneling-adjacent structures interaction', *Computers and Geotechnics* **30**(3), 245–253.

Muir Wood, D. (2004), *Geotechnical modelling*, Spon Press.

Nyren, R. (1998), Field measurements above twin tunnels in London Clay, PhD thesis, Imperial College London.

Nyren, R. J., Standing, J. R. & Burland, J. B. (2001), Surface displacement at St James's Park greenfield reference site above twin tunnels through the London Clay, *in* 'Building Response to Tunnelling: Case Studies from Construction of the Jubilee Line Extension, London', Vol. 2, Thomas Telford, pp. 387–400.

O'Reilly, M. P., Mair, R. J. & Alderman, G. H. (1991), Long-term settlements over tunnels: an eleven-year study at Grimsby, *in* 'Tunnelling '91', pp. 55–64.

O'Reilly, M. P. & New, B. M. (1982), Settlements above tunnels in the United Kingdom-their magnitude and prediction, *in* 'Tunnelling '82', pp. 173–181.

Ottosen, N. S. & Ristinmaa, M. (2005), 13 - nonlinear kinematic hardening laws, *in* N. S. Ottosen & M. Ristinmaa, eds, 'The Mechanics of Constitutive Modeling', Elsevier Ltd, Oxford, pp. 321 – 355.

Panet, M. & Guenot, A. (1982), Analysis of convergence behind the face of a tunnel, *in* 'Tunnelling '82', pp. 197–204.

Peck, R. B. (1969), Deep excavations and tunnelling in soft ground, *in* 'Proc. 7th International Conference on Soil Mechanics and Foundation Engineering', Vol. State of the Art, Hamburg, pp. 225–290.

Petrova, S., Standing, J. R. & Taylor, G. R. (2001), London Bridge Post Office, *in* 'Building Response to Tunnelling: Case Studies from Construction of the Jubilee Line Extension, London', Vol. 2, Thomas Telford, pp. 631–656.

Pickhaver, J. B. (2006), Numerical Modelling of Building Response to Tunnelling, DPhil thesis, University of Oxford.

Pickhaver, J. B., Burd, H. J. & Houlsby, G. T. (2010), 'An equivalent beam method to model masonry buildings in 3D finite element analysis', *Computers and Structures* **88**(19/20), 1049–1063.

Potts, D. M. & Addenbrooke, T. I. (1997), 'A structure's influence on tunnelling-induced ground movements', *Proceedings of the Institution of Civil Engineers - Geotechnical Engineering* **125**(2), 109–125.

Potts, D. M. & Zdravković, L. (1999), *Finite element analysis in geotechnical engineering : theory*, Thomas Telford, London.

Potts, D. M. & Zdravković, L. (2001), *Finite element analysis in geotechnical engineering : application*, Thomas Telford, London.

Puzrin, A. M., Burland, J. B. & Standing, J. R. (2012), 'Simple approach to predicting ground displacements caused by tunnelling in undrained anisotropic elastic soil', *Géotechnique* **62**(4), 341.

Rankin, W. J. (1988), Ground movements resulting from urban tunnelling: predictions and effects, *in* 'Engineering Geology of Underground Movements. Proc. of the 23rd Annual Conference of the Engineering Group of the Geological Society', Vol. 5, pp. 79–92.

Ritter, S., Giardina, G., DeJong, M. J. & Mair, R. J. (2017*a*), 'Influence of building characteristics on tunnelling-induced ground movements', *Géotechnique* **67**(10), 926–937.

Ritter, S., Giardina, G., DeJong, M. J. & Mair, R. J. (2017*b*), The role of building dimensions and position on the response of buildings to tunnelling subsidence: Centrifuge modelling, *in* A. Negro & M. O. Cecílio, Jr., eds, 'Proc. 9th International Symposium on Geotechnical Aspects of Underground Construction in Soft Ground', Brazil, pp. 277–286.

Roscoe, K. H. & Burland, J. B. (1968), On the generalized stress-strain behaviour of wet clay, *in* 'Engineering Plasticity', pp. 535–609.

Rowe, R. K., Lo, K. Y. & Kack, G. J. (1983), 'A method of estimating surface settlement above tunnels constructed in soft ground', *Canadian Geotechnical Journal* **20**(1), 11–22.

Shin, J. H., Addenbrooke, T. I. & Potts, D. M. (2002), 'A numerical study of the effect of groundwater movement on long-term tunnel behaviour', *Géotechnique* **52**(6), 391–403.

Skinner, H., Potts, V., St. John, A. & McGirr, D. (2014), Stabilisation of soil pillar adjacent to Eastern Ticket Hall at Bond Street Crossrail Station, *in* M. Black, C. Dodge & U. Lawrence, eds, 'Crossrail project: Infrastructure design and construction', ICE Publishing, pp. 419–431.

Sloan, S. W., Abbo, A. J. & Sheng, D. (2001), 'Refined explicit integration of elastoplastic models with automatic error control', *Engineering Computations* **18**(1/2), 121–154.

Sloan, S. W. & Booker, J. R. (1986), 'Removal of singularities in Tresca and Mohr-Coulomb yield functions', *Communications in Applied Numerical Methods* **2**, 173–179.

Soga, K., Laver, R. G. & Li, Z. (2017), 'Long-term tunnel behaviour and ground movements after tunnelling in clayey soils', *Underground Space* **2**(3), 149–167.

Stallebrass, S. E. & Taylor, R. N. (1997), 'The development and evaluation of a constitutive model for the prediction of ground movements in overconsolidated clay', *Géotechnique* **47**(2), 235–253.

Standing, J. R. & Burland, J. B. (2006), 'Unexpected tunnelling volume losses in the Westminster area, London', *Géotechnique* **56**, 11–26.

Standing, J. R. & Selemetas, D. (2013), 'Greenfield ground response to EPBM tunnelling in London Clay', *Géotechnique* **63**(12), 989–1007.

Timoshenko, S. (1957), *Strength of materials – Part 1*, van Nostrand.

Truong-Hong, L. & Laefer, D. F. (2013), 'Impact of modeling architectural detailing for predicting unreinforced masonry response to subsidence', *Automation in Construction* **30**, 191–204.

University of the West of England (2009), 'Evolution of building elements'. Accessed 22 November, 2017. `https://fet.uwe.ac.uk/conweb/house_ages/elements/section1.htm`.

Urciuoli, G., Russo, C., Desideri, A. & Picarelli, L. (1996), Pore pressure generation and equalization around a circular tunnel in soft clays, *in* 'Proc. International Symposium on Geotechnical Aspects of Underground Construction in Soft Ground', Balkema, pp. 621–625.

van Eekelen, H. A. M. (1980), 'Isotropic yield surfaces in three dimensions for use in soil mechanics', *International Journal for Numerical and Analytical Methods in Geomechanics* **4**(1), 89–101.

Viggiani, G. & Atkinson, J. H. (1995), 'Stiffness of fine-grained soil at very small strains', *Géotechnique* **45**(2), 249–265.

Viggiani, G. & Standing, J. R. (2001), The Treasury, *in* 'Building Response to Tunnelling: Case Studies from Construction of the Jubilee Line Extension, London', Vol. 2, Thomas Telford, pp. 401–432.

Vorster, T. E. B., Klar, A., Soga, K. & Mair, R. J. (2005), 'Estimating the effects of tunneling on existing pipelines', *Journal of Geotechnical and Geoenvironmental Engineering* **131**(11), 1399–1410.

Wan, M. S., Standing, J. R., Potts, D. & Burland, J. B. (2017), 'Measured short-term ground surface response to EPBM tunnelling in London Clay', *Géotechnique* **67**(5), 420–445.

Ward, W. H. & Pender, M. J. (1981), Tunnelling in soft ground: general report, *in* 'Proc. 10th International Conference on Soil Mechanics and Foundation Engineering', Vol. 4, Stockholm, pp. 261–275.

Whittle, A. J. & Kavvadas, M. J. (1994), 'Formulation of MIT-E3 constitutive model for overconsolidated clays', *Journal of Geotechnical Engineering* **120**(1), 173–198.

Wisser, C., Augarde, C. E. & Burd, H. J. (2005), 'Numerical modelling of compensation grouting above shallow tunnels', *International Journal for Numerical and Analytical Methods in Geomechanics* **29**(5), 443–471.

Withers, A. D. (2001*a*), Keetons Estate, Bermondsey, *in* 'Building Response to Tunnelling: Case Studies from Construction of the Jubilee Line Extension, London', Vol. 2, Thomas Telford, pp. 755–774.

Withers, A. D. (2001*b*), Murdoch, Neptune and Clegg Houses in Moodkee Street, Rotherhithe, *in* 'Building Response to Tunnelling: Case Studies from Construction of the Jubilee Line Extension, London', Vol. 2, Thomas Telford, pp. 811–828.

Withers, A. D. (2001*c*), Surface displacements at three surface reference sites above twin tunnels through the Lambeth Group, *in* 'Building Response to Tunnelling: Case Studies from Construction of the Jubilee Line Extension, London', Vol. 2, Thomas Telford, pp. 735–752.

Withers, A. D., Page, D. P. & Linney, L. F. (2001), Geology and geotechnical properties, *in* 'Building Response to Tunnelling: Case Studies from Construction of the Jubilee Line Extension, London', Vol. 1, Thomas Telford, pp. 57–81.

Wongsaroj, J. (2005), Three-dimensional finite element analysis of short and long-term ground response to open-face tunnelling in stiff clay, PhD thesis, University of Cambridge.

Wongsaroj, J., Soga, K. & Mair, R. J. (2007), 'Modelling of long-term ground response to tunnelling under St James's Park, London', *Géotechnique* **57**(1), 75–90.

Wongsaroj, J., Soga, K. & Mair, R. J. (2013), 'Tunnelling-induced consolidation settlements in London Clay', *Géotechnique* **63**(13), 1103–1115.

Yiu, W. N., Burd, H. J. & Martin, C. M. (2017*a*), 'Finite element modelling for the assessment of tunnel-induced damage to a masonry building', *Géotechnique* **67**(9), 780–794.

Yiu, W. N., Burd, H. J. & Martin, C. M. (2017*b*), Soil-building interaction in finite element analysis of tunnelling-induced building damage, *in* 'Proc. IV International Conference on Computational Methods in Tunneling and Subsurface Engineering', ECCOMAS, Austria, pp. 381–388.

Yiu, W. N., Burd, H. J. & Martin, C. M. (2018), Soil-foundation contact models in finite element analysis of tunnelling-induced building damage, *in* A. S. Cardoso, J. L. Borges, P. A. Costa, A. T. Gomes, J. C. Marques & C. S. Vieira, eds, 'Proc. 9th European Conference on Numerical Methods in Geotechnical Engineering (NUMGE 2018)', ISSMGE, SPG, Portugal, pp. 989–998.

Zytynski, M., Randolph, M. F., Nova, R. & Wroth, C. P. (1978), 'On modelling the unloading-reloading behaviour of soils', *International Journal for Numerical and Analytical Methods in Geomechanics: Short Communications* **2**(1), 87–93.